Design and Modelling of Axially-Laminated Interior Permanent Magnet Motor Drives for Field-Weakening Applications

Wen Liang Soong

A Thesis Submitted to
the Department of Electronics and Electrical Engineering
of the University of Glasgow
in Partial Fulfilment of the Requirements
for the Degree of
Doctor of Philosophy

September 1993

ProQuest LLC.
789 East Eisenhower Parkway
P.O. Box 1346
Ann Arbor, MI 48106 – 1346

Abstract

This thesis is concerned with the design of AC motors to operate at constant shaft power over the widest possible speed range from an inverter of fixed volt-ampere rating. In particular, it examines and validates the reputation of the interior permanent magnet motor drive of having a wide speed range at constant power (field-weakening range). The design and construction of a 7.5kW axially-laminated interior permanent magnet motor showing a constant-power speed range exceeding 7.5:1 is described. This result cannot be matched by any other motor type.

Vector-controlled induction motor drives are widely used for field-weakening applications. They offer a constant-power speed range of up to about 4:1. Higher values can be obtained only by oversizing the drive or by using a winding changeover technique. Combined with improvements in low-speed dynamic performance, the inherently wider constant-power speed range makes the interior permanent magnet motor drive a serious contender for applications such as machine tool main spindle drives and traction.

The thesis consists of two parts. The first part examines the theoretical and practical limitations to the field-weakening performance of the three types of brushless synchronous AC motor : the surface permanent magnet, the synchronous reluctance and the interior permanent magnet motor. It is shown that high-saliency interior permanent magnet motor drives should offer the best practical field-weakening performance. The axially-laminated (as opposed to the conventional radially-laminated) construction offer the highest saliency ratios.

The second part describes the modelling and design of an axially-laminated interior permanent magnet motor drive for optimal field-weakening performance. The effect of varying the design parameters on the drive's field-weakening performance is analysed. A 7.5kW axially-laminated synchronous reluctance and a 7.5kW axially-laminated interior permanent magnet motor were built. The interior permanent magnet motor drive shows an extremely wide constant-power speed range which exceeds 7.5:1.

Contents

List of Figures

List of Tables

Acknowledgements

Firstly I thank my supervisor and mentor, Professor T.J.E. Miller for his guidance and encouragement. I acknowledge the financial support of the Commonwealth Scholarship Commission in the United Kingdom. I also thank the Scottish Power Electronics and Electric Drives Consortium (SPEED) and the Glasgow University Electronic and Electrical Engineering Department for providing the facilities to allow me to carry out this research.

I thank all the members of the department and especially the members of the SPEED group for their friendliness and help over the years. Special acknowledgement is due to Dave Staton for his help with the finite-element analysis and the machine design; Rolf Lagerquist for his help with the software packages; Peter Miller for building the 7.5kW inverter; and to Jimmy Kelly and Wilson McDougall who are undoubtably the world's experts at building axially-laminated interior permanent magnet rotors.

Finally I thank my family, colleagues, officemates and flatmates for their support during the good and the bad times over the last three years.

Nomenclature

a	rotor insulation ratio : $w_{ins}/(w_{ins} + w_{lam})$	
AC	alternating current	
α	electrical pole-arc	[deg or rad]
α	parameter used in saturation model	
B	magnetic flux density	[T]
B_r	permanent magnet remanence	[T]
CPSR	constant-power speed range : w_p/w_k	
D_{major}	bolt major diameter	[m]
D_{minor}	bolt minor diameter	[m]
DC	direct current	
DQ	direct and quadrature axis reference frame	
E_q	magnet-induced back-emf voltage	[V rms]
η	efficiency	
ϵ	winding chording angle	[deg or rad]
f	frequency	[Hz]
F	force	[N]
F_B	force per bolt	[N]
g	mechanical radial airgap	[m]
g''	effective radial airgap : $k_c g$	[m]
γ	electrical slot pitch angle	[deg or rad]
γ	electrical current-angle between I and q-axis	[deg or rad]
γ_i	internal (magnetising) current-angle	[deg or rad]
γ_m	maximum-torque-per-ampere current-angle	[deg or rad]
γ_{mi}	internal maximum-torque-per-ampere current-angle	[deg or rad]
γ_p	maximum constant-power speed current-angle	[deg or rad]

γ_t	Mode III transition current-angle	[deg or rad]
γ_v	maximum power-factor current-angle	[deg or rad]
H	magnetic field strength	[A/m]
H_c	coercivity	[A/m]
H_{ci}	intrinsic coercivity	[A/m]
I	current	[A rms]
I_c	rated stator current	[A rms]
I_F	field current	[A rms]
I_m	magnetising stator current	[A rms]
I_o	base stator current	[A rms]
IM	induction motor	
IPM	interior permanent magnet motor	
k_c	Carter's airgap extension factor	
k_{d1}	fundamental distribution factor	
k_{p1}	fundamental pitch factor	
k_{s1}	fundamental skew factor	
k_{w1}	fundamental winding factor	
κ	inverter utilisation	
κ_R	inverter utilisation including R_s	
κ_T	inverter utilisation including R_s and R_{fe}	
l	stack length	[m]
l_{bs}	length of bolt embedded in shaft	[m]
l_s	edge length of square shaft	[m]
L	inductance per phase	[H]
L_d	d-axis synchronous inductance : $L_{dm} + L_l$	[H]
L_{dm}	magnetising d-axis synchronous inductance	[H]
L_{di}	intrinsic d-axis synchronous inductance	[H]
L_{dmi}	intrinsic magnetising d-axis synchronous inductance	[H]

L_{end}	stator endwinding inductance	[H]
L_l	stator leakage inductance : $L_{end} + L_{slt}$	[H]
L_m	round-rotor machine magnetising inductance	[H]
L_q	q-axis synchronous inductance : $L_{qm} + L_l$	[H]
L_{qm}	magnetising q-axis synchronous inductance	[H]
L_s	synchronous inductance (SPM)	[H]
L_{slt}	stator slot-leakage inductance	[H]
m	number of phases	
M	mutual inductance	[H]
N_b	number of bolts per pole	
N_{ph}	number of series turns per phase	
N_s	number of effective sine-distributed turns per phase	
p	pole-pairs	
P	power	[W]
P_a	asymptotic high-speed power output	[W]
P_{fe}	iron loss	[W]
P_k	rated output power	[W]
P_o	base output power	[W]
P_s	slot permeance ratio	
PM	permanent magnet	
ϕ	power-factor angle between V and I	[deg or rad]
ϕ_i	internal power-factor angle between V and I	[deg or rad]
Φ	magnetic flux	[Wb]
Φ_m	flux due to magnets	[Wb]
Ψ	flux-linkage	[Vs rms]
Ψ_m	flux-linkage due to magnets	[Vs rms]
q	number of slots per pole per phase	

r	radius	[m]
r_1	rotor radius	[m]
ρ	density	[kgm^{-3}]
ρ_l	density of lamination material	[kgm^{-3}]
R	resistance	[Ω]
R_s	stator phase resistance	[Ω]
R_c	effective core-loss resistance	[Ω]
S_1	number of stator slots	
SPM	surface permanent magnet motor	
SYNCHREL	synchronous reluctance motor	
σ	Carter's coefficient	
σ_o	Carter's coefficient for open slots	
σ_{sc}	Carter's coefficient for semi-closed slots	
σ	constant-power speed range	
σ	mechanical stress	[MPa]
σ_{yb}	yield stress of bolt material	[MPa]
σ_{ys}	yield stress of shaft material	[MPa]
σ	skew angle	[deg or rad]
T	torque	[Nm]
T_k	rated output torque	[Nm]
θ	mechanical rotor angle	[deg or rad]
V	voltage	[V rms]
V_c	rated phase voltage	[V rms]
V_m	magnetising phase voltage	[V rms]
V_o	base phase voltage	[V rms]
VA	volt amperes	[V A]
w	width	[m]
w_{ins}	thickness of non-magnetic rotor layers	[m]

w_{lam}	thickness of magnetic rotor layers	[m]
w_s	slot opening width	[m]
w_t	tooth width	[m]
ω	angular speed	[rad/s]
ω_k	rated speed	[rad/s]
ω_o	base speed	[rad/s]
ω_p	highest speed at which $P \geq P_k$	[rad/s]
ω_t	transition speed between Mode II and III	[rad/s]
ω_v	speed at which the power-factor is maximum under the optimal torque control strategy	[rad/s]
ω_x	maximum voltage-limited operating speed	[rad/s]

ξ	saliency ratio : L_q/L_d
ξ_i	intrinsic saliency ratio : $L_m/L_{di} = r_1/pg$
ξ_m	magnetising saliency ratio : L_{qm}/L_{dm}
ξ_{mi}	intrinsic magnetising saliency ratio : $L_m/L_{dmi} = ar_1/(pg)$
ξ_s	saturated saliency ratio
ξ_u	unsaturated saliency ratio

ζ	minimum magnet operating point

Subscripts

1	fundamental
A	armature
A, B, C	phase numbers
c	core loss
c	rated
d	direct axis
F	field
i	internal
i	intrinsic

k	at the knee speed (rated)
m	magnetising
m	maximum-torque-per-ampere
m, M	magnet
m	mechanical
n	normalised
o	base quantity
p	at the constant-power speed
q	quadrature axis
r	rotor
r	radial
s	synchronous
s	saturated
s, S	stator
t	at the transistion between Mode II and III
t	tangential
T	total
T	torque producing
u	unsaturated
v	maximum power-factor

Superscripts

$\hat{}$	peak

Chapter 1

Introduction to Field-Weakening

Chapter One introduces the concept of field-weakening, compares the field-weakening performance of common motor drives, examines the requirements of applications requiring a large field-weakening range and describes the structure of the remainder of the thesis. It includes references to previous work concerned with field-weakening and outlines the original content of the thesis.

1.1 Background

Electric motors generate torque by the interaction of magnetic flux and electric current. In the simple example shown in Fig. 1.1 these quantities are controlled independently. The *magnetic flux* Φ is produced by the *field current* I_F. The flux is proportional to the field current if magnetic saturation is neglected. The *armature current* I_A interacts with the flux to produce the *torque* T. This is proportional to the product of the flux and the armature current [1], that is :

$$T \propto \Phi I_A \tag{1.1}$$

The induced voltage and hence the required *terminal voltage* V is proportional to the product of the flux and the *angular speed* ω (neglecting resistance) :

$$V \propto \Phi\omega \tag{1.2}$$

Thus to a first approximation, if the flux is constant then the torque is dependent only on the armature current, and the required terminal voltage is dependent only on the speed.

A *motor drive* consists of a motor, a power electronic inverter and a controller as shown in Fig. 1.2. This thesis is concerned with the *steady-state* field-weakening

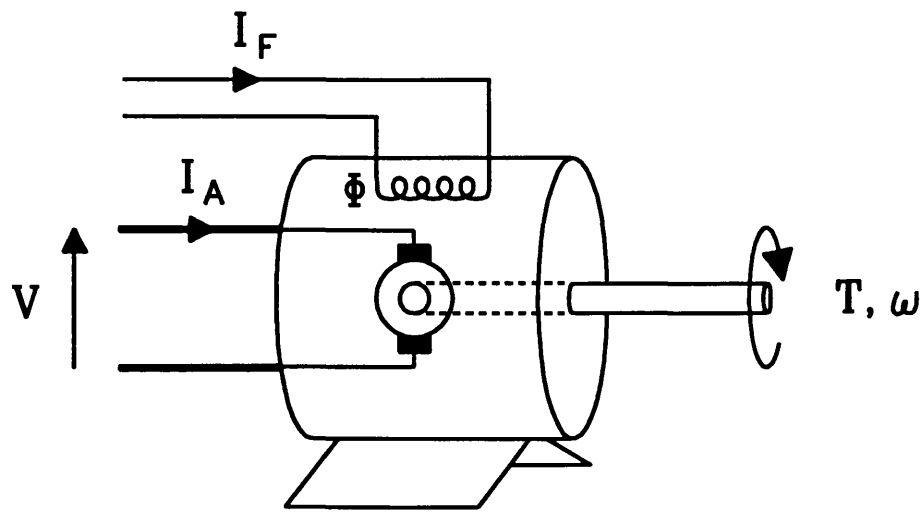

Figure 1.1: *Simple DC electric motor model.*

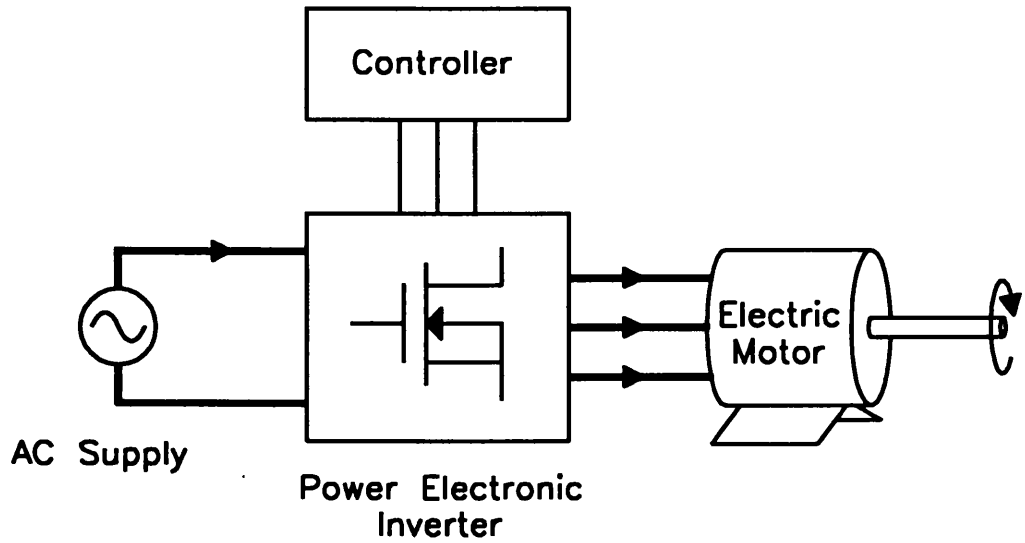

Figure 1.2: *A motor drive.*

performance of motor drives. At a given speed this is limited by the supply/inverter capabilities or by thermal, electromagnetic (eg. saturation) or mechanical (eg. commutator) motor limitations. To a first approximation, the maximum power can be calculated from a model of the motor by assuming a limited voltage and current are available from the inverter. This is a common approximation [2, 3, 4, 5] as it is simple but still allows useful comparisons between motor types.

Much of this thesis is concerned with determining the maximum speed range at constant power which is available from a motor drive within a given inverter voltage and current rating. It is inherently assumed that at any speed the drive is controlled in such a way to maximise the output torque. It is useful to examine first the operating limits of an ideal motor drive as shown in Fig. 1.3. *Rated torque*[1] T_k is the maximum torque which can be obtained with *rated current* I_c. For the DC motor in Fig. 1.1, (1.1) shows that maximum torque is obtained with maximum flux. For brushless synchronous AC motors such as the interior permanent magnet motor, the maximum torque is obtained by appropriately controlling the stator current phasor orientation.

[1]Rated torque can be maintained up to the rated speed. The rated speed is also termed the *knee-speed*, thus the subscript "k" in T_k.

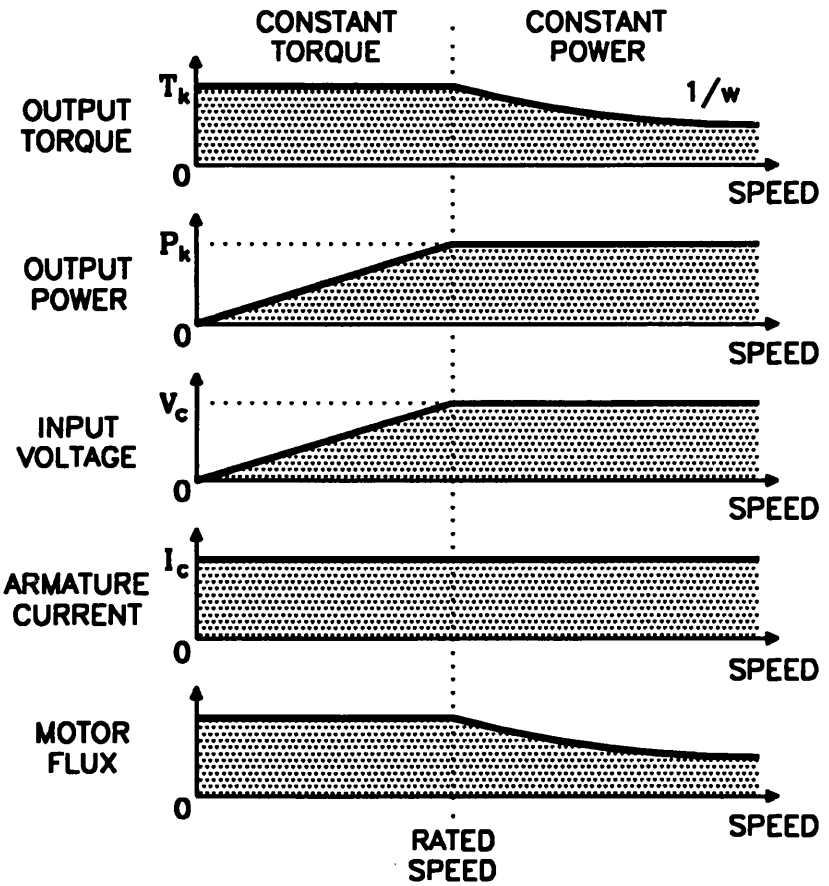

Figure 1.3: *Ideal motor drive field-weakening characteristics.*

This is described in more detail later.

The *rated speed* ω_k is defined as the speed at which the required terminal voltage equals the *rated voltage* V_c with rated current and rated torque. The last point is important as the rated speed will change if the input power-factor [6, 7] or the motor efficiency is maximised instead of the output torque. Rated output torque can be maintained from zero speed up to rated speed. This is called the *constant torque operating region.* Note that the terminal voltage and the output power both rise linearly with increasing speed in this region.

At the rated speed, the motor delivers *rated output power* P_k. In order to operate above rated speed while still maintaining the rated terminal voltage, from (1.2) it is necessary to reduce the flux by reducing or *weakening* the field current inversely

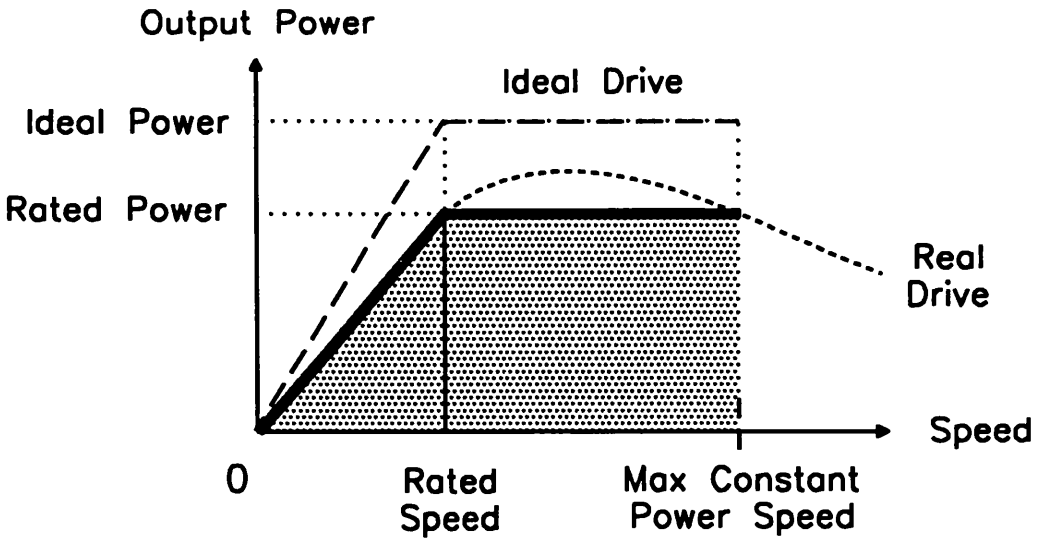

Figure 1.4: *Definition of field-weakening parameters.*

proportionally to the speed. If the armature current is kept at its rated value, then from (1.1) the output torque will fall inversely with speed. The output power is constant as it is equal to the product of the torque and speed (see Fig. 1.3). This is called the *field-weakening* or the *constant-power operating region.*

The field-weakening performance of a practical motor drive can be characterised by two parameters (see Fig. 1.4). The *inverter utilisation* κ is the ratio of the rated output power to the ideal motor drive output power at rated speed. The constant-power speed range (CPSR) is the speed range over which the output power is greater or equal to the rated power. It is given by the ratio of the maximum constant-power speed ω_p to the rated speed. Fig. 1.3 shows that an ideal field-weakening drive has unity inverter utilisation and infinite constant-power speed range.

The majority of applications such as fans, pumps, compressors and servo drives do not require field-weakening operation and thus most motor drives only operate in the constant torque region. However certain types of loads such as washing machines, machine tool spindle drives and traction drives have the constant-power characteristic shown in Fig. 1.5. The required constant-power speed range varies from about 1.5:1 for electric locomotives [8] up to 30:1 for domestic washing machines [9].

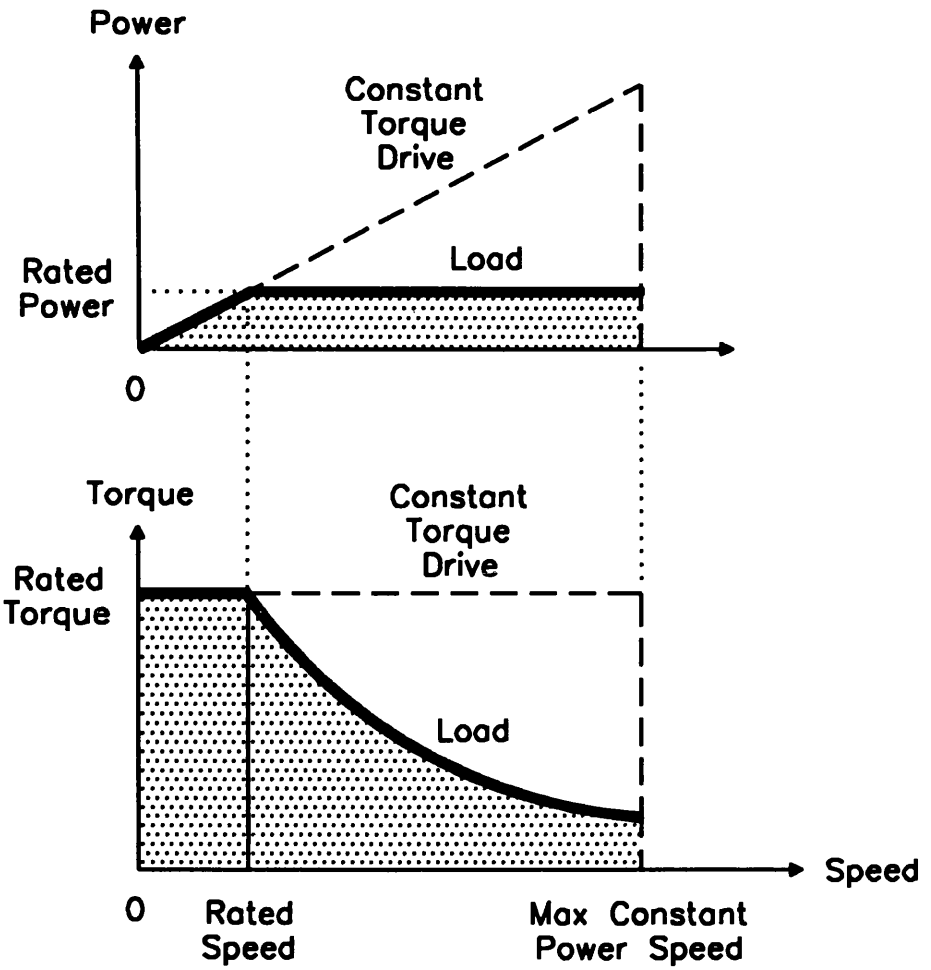

Figure 1.5: *A load requiring a wide constant-power speed range.*

It is most cost-effective to match the drive's capabilities to the load's characteristics. For a constant-power load characteristic, using a drive only capable of constant torque operation would require it to be capable of delivering rated torque up to the maximum speed (see dashed line in Fig. 1.5). This is clearly a considerable over-specification of the required drive output power and would be prohibitively expensive. A better approach would be to use a drive capable of delivering rated torque at rated speed with the required constant-power speed range.

The concept of field-weakening was illustrated above for a simple motor which allowed independent control of the motor flux by the field current and the torque by the armature current. This is the case in the separately-excited DC commutator motor

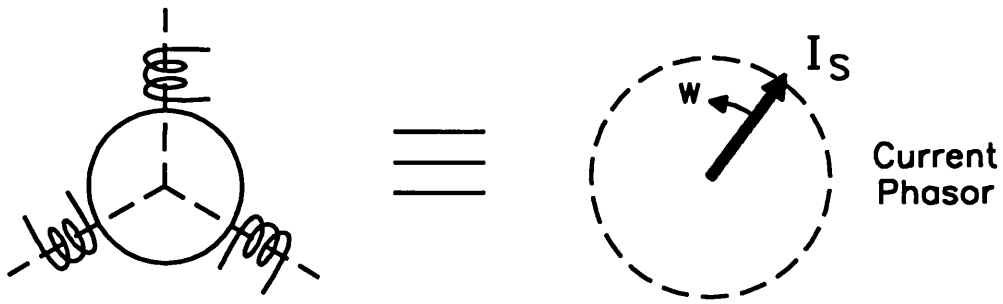

Figure 1.6: *The AC stator winding.*

and it is from this that the term field-weakening originated. However field-weakening is now generally used to describe the operation of any type of motor above rated speed, despite the lack of any physical separation between the "field current" and the "armature current" in some of these motors.

A three-phase stator winding is generally used in brushless AC motors such as the induction motor, the surface permanent magnet motor and the synchronous reluctance motor. This consists of three coils whose magnetic axes are separated by 120° as shown in Fig. 1.6. These are fed by three-phase currents which are 120° phase shifted with respect to one another in time. The physical phase shift between the coils and the time phase shift between the currents combine such that the *resultant* field generated by all three coils is of constant magnitude and rotates at a constant (synchronous) speed. This is equivalent to a current phasor I_S rotating at synchronous speed.

The stator current phasor can be effectively split into two orthogonal components : the field current or magnetising current I_F which controls the airgap flux Φ in the motor and the torque producing component I_T which interacts with this flux (see Fig. 1.7). Operation above rated speed is obtained by reducing the airgap flux in the motor by appropriately controlling the amplitude and sign of the magnetising current I_F. In the synchronous reluctance and the induction motors, the airgap flux is produced purely by the magnetising current and so this component is decreased above rated speed. In permanent magnet machines the flux is mainly produced by the magnets. The "magnetising" current generates a flux Φ_F which *opposes* the magnet flux Φ_M and

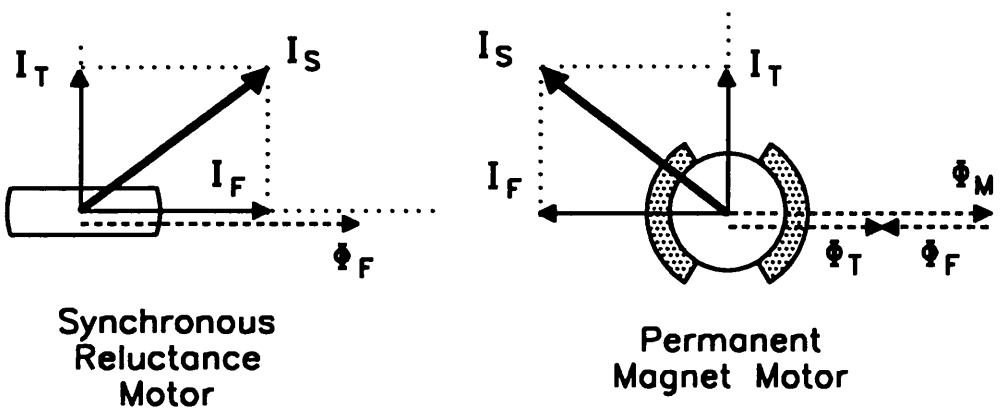

Figure 1.7: *Field-weakening of reluctance and permanent magnet motors.*

hence *reduces* the total airgap flux Φ_T. In these motors the required demagnetising current increases with speed.

To describe general motor operation above rated speed, the term "flux-weakening" has been suggested [2] as being more accurate and descriptive than the traditional "field-weakening". Both these terms will be used interchangeably in this thesis.

1.2 Field-Weakening Characteristics

Figure 1.8 shows the development of the major motor classes over time [1, 10, 11] and how they correspond to important developments in related areas. The history of motor science began with the discovery of electromagnetic induction by Michael Faraday in 1831. The next half century saw the development of the three "classical" motors : the DC commutator motor, the synchronous motor and the induction motor. These were characterised by their ability to start and run without an electronic controller [12]. Of these, only the DC commutator motor was suitable for variable-speed drives.

Brushless variable-speed drives became possible with the development of modern "power" semiconductors, beginning with the introduction of the silicon-controlled rectifier (SCR) in 1957 [10]. They were also aided by the introduction of the microprocessor in 1971.

Permanent magnet motors became practical with the discovery of Alnico in the 1930s. This was followed by the introduction of ferrites in the 1950s and rare-earth magnets in the 1970s.

Table 1.1 summarises the field-weakening characteristics of each of the main motor types [12, 13, 14]. The oldest motor is the wound-field DC commutator motor. When used in the separately-excited configuration it offers independent control of the flux and the torque with DC currents (see Fig. 1.1). This motor is important not only because of its "ideal" field-weakening characteristics (see Fig. 1.3) but also because it is the basis of DQ axis theory (vector control) for AC motors. Unfortunately the excellent theoretical field-weakening characteristics cannot be realised due to practical commutation limitations at high speeds. This usually limits the achievable constant-power speed range to less than 4:1 [14]. Presently it tends to be used mainly in high power drives (up to 10MW) but is gradually being replaced by induction motors in applications such as locomotive traction [15]. These offer faster dynamic response and a more rugged construction.

The AC commutator or universal motor is basically a wound-field DC commutator motor with the field winding in series with the armature winding. It can operate from

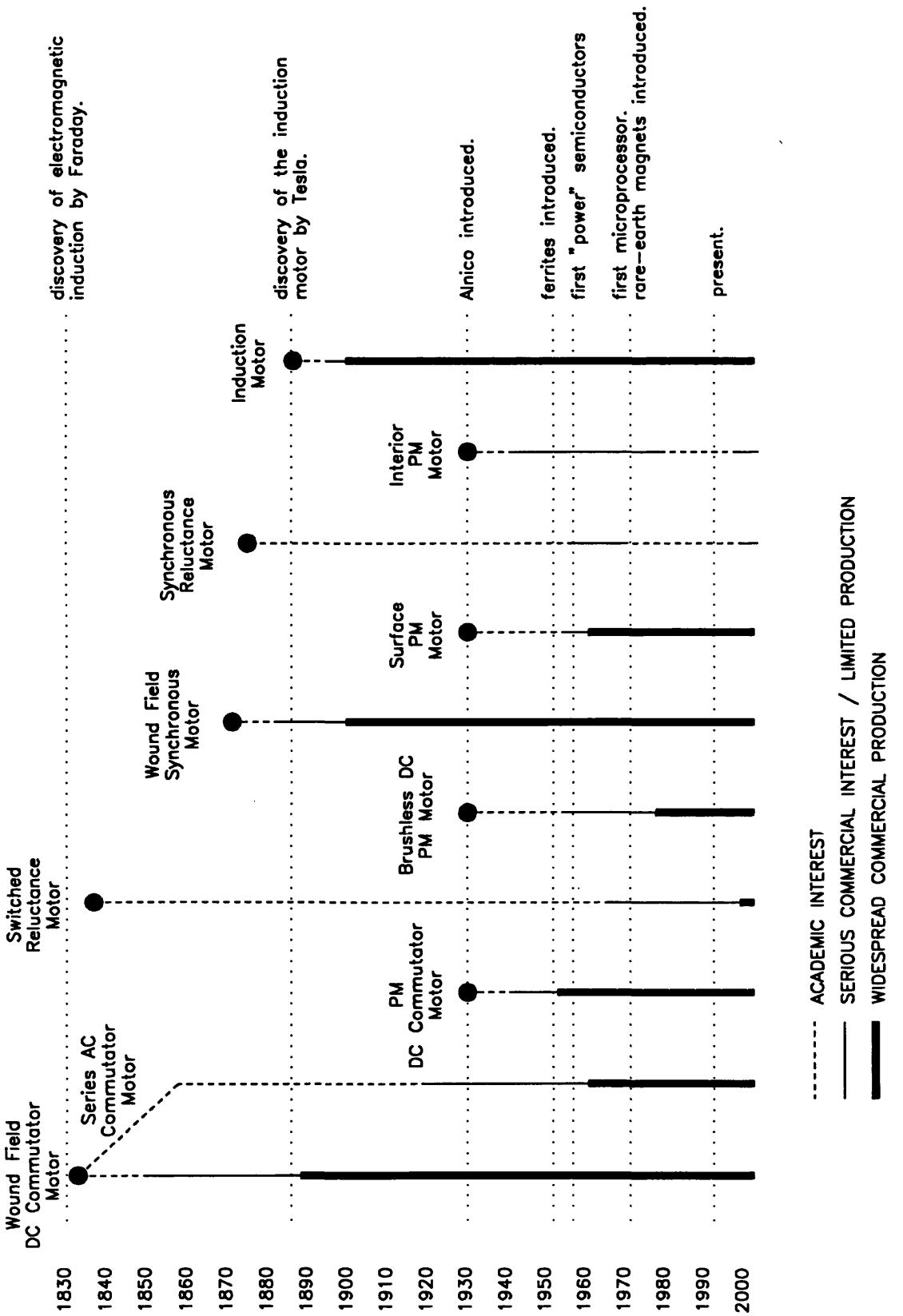

Figure 1.8: *The development of the major motor types over time.*

Table 1.1: *Field-weakening characteristics of common motor types.*

Motor Type	Power Range	CPSR			Torque Ripple		Power Density	Eff.
		Ideal	Typ.	Best	Low Speed	Field Wkg		
DC Wound Field	1kW–10MW	∞	1.5–3	4	low	low	low	med
AC Commutator	10W–1kW	1	1	1	high	–	high	med
DC PM	1W–10kW	1	1	1	low	–	med	high
Switched Rel.	10W–100kW		2–3		med	high	high	high
Wound Field Synch.	1kW–10MW	∞	5		low	low	med	med
Brushless DC PM	1W–10kW		1–2		med	high	high	high
Brushless AC PM	10W–50kW		1–2		low	low	high	high
Synchronous Rel.	100W–10kW	5	1.5–3		low	low	med	med
Interior PM	1kW–30kW	∞	2–4	>7.5	low	low	high	high
Induction Motor	100W–10MW		2–3	4	low	low	med	med

both AC and DC, has a high starting torque and a high power density [16]. The output power naturally reduces inversely with speed and so it has a limited constant-power speed range. Despite this, it is widely used in domestic appliances such as washing machines and electric drills.

The DC PM commutator motor behaves similarly to the wound-field motor with a fixed field current. It is perhaps the simplest motor to control and drive and is widely used for general purpose variable-speed servo drives up to the integral kW range. Due to the lack of the control over the excitation, this motor has a very limited field-weakening range.

The switched-reluctance motor is one of the earliest motor types (see Fig. 1.8) but it did not become practical until the development of suitable power electronic controllers in the 1960s and 70s as it cannot start or run from a pure AC or DC voltage source. Its main advantages are its high torque to volume ratio, high torque to inertia ratio, high speed capability and fault tolerance [12]. These characteristics give it some potential for use in domestic appliances and aerospace applications. It has a moderate degree of torque ripple below rated speed. With fixed firing angles and a fixed supply voltage,

the switched-reluctance motor has an inverse power characteristic similar to that of the AC commutator motor [10]. A constant-power speed range of 2 to 3:1 can generally be achieved by phase advancing the firing angles at the cost of an increase in the torque ripple.

The brushless DC PM motor is basically a DC PM commutator motor turned inside out. It generates a trapezoidal back-emf waveform which allows it to produce a relatively smooth output torque when driven with rectangular currents. It offers a high power density and high efficiency. The use of rectangular currents eliminates the need for accurate shaft position sensing. This greatly simplifies the control and makes the motor ideal for low power, cost sensitive applications such as in computer peripherals and fans. A field-weakening range of about 2:1 can be obtained by phase advancing the firing angles in a similar way to the switched-reluctance motor. Note that this increases the output torque ripple [17, 18].

The wound-field synchronous motor is similar to an inside-out wound-field DC commutator motor except that the armature currents are sinusoidal instead of DC. It is generally used in large sizes (> 100kW) for power-factor correction in industrial plants due to its ability to operate at a leading power-factor. Like the wound-field DC commutator motor, it has an ideal infinite field-weakening range. Its practical field-weakening range is somewhat greater than that of the DC commutator motor as it uses slip-rings instead of a commutator, but it is still brush limited.

The surface permanent magnet AC motor is similar to the brushless DC PM motor except it is designed to have a sinusoidal back-emf and is operated from sinusoidal currents. It offers a high output torque density, fast dynamic response, high efficiency, low torque ripple and a large overload capability. Rare-earth magnets are used to obtain the best performance, although these are expensive. The surface permanent magnet motor is widely used for industrial servo drives [19]. As with all true sinusoidally-driven AC motors, it has low torque ripple both below rated speed and in the field-weakening region. Its constant-power speed range is generally limited to below 2:1 for conventional designs. The reasons for this are explored in the next chapter.

The synchronous reluctance motor has a long history and in fact predates the

induction motor [20]. Early versions were line-start motors and required a starting cage which compromised their synchronous performance. They were used in the 1950s and 1960s for applications such as fibre-spinning which required several motor drives running in synchronism from a single inverter [7], but have subsequently been replaced by vector-controlled surface permanent magnet motor drives.

The synchronous reluctance motor theoretically offers simple control, fast dynamic response, high efficiency and a wide field-weakening range. In the last few years there has been increasing interest in it as an alternative to the induction motor for high performance drives. In particular there has been considerable interest in the axially-laminated form of construction which has been shown to offer the best performance of all types of synchronous reluctance motor [21].

The interior permanent magnet motor was one of the first brushless permanent magnet motors to be developed. This was due to its ability to utilise the early, low-coercivity Alnico magnets [22]. Improved materials in later years led to the development of integral kW machines using a squirrel-cage for line-starting and an interior permanent magnet geometry for efficient steady-state operation.

Variable-speed interior permanent magnet motor drives offer a wide field-weakening range, fast dynamic response and relatively simple control compared to the induction motor. They are well suited to field-weakening applications such as spindle drives. Despite the rapid acceptance of the surface permanent magnet motor drive for (constant torque) servo applications, the interior permanent magnet motor drive has been slow to establish itself. It is only recently that interior permanent magnet spindle drives have become commercially available [23]. These offer a constant-power speed range of 4:1. It will be shown later than an axially-laminated interior permanent magnet motor can achieve a constant-power speed range exceeding 7.5:1.

Last but certainly not least is the squirrel-cage induction motor. It offers a simple and rugged construction, low cost when manufactured in sufficient volume, and good efficiency in large sizes. It is widely used in industry for fixed-speed applications such as fans and pumps. Variable-speed induction motor drives were the first AC variable-speed drives to be developed and are now widely used for high power drives up to

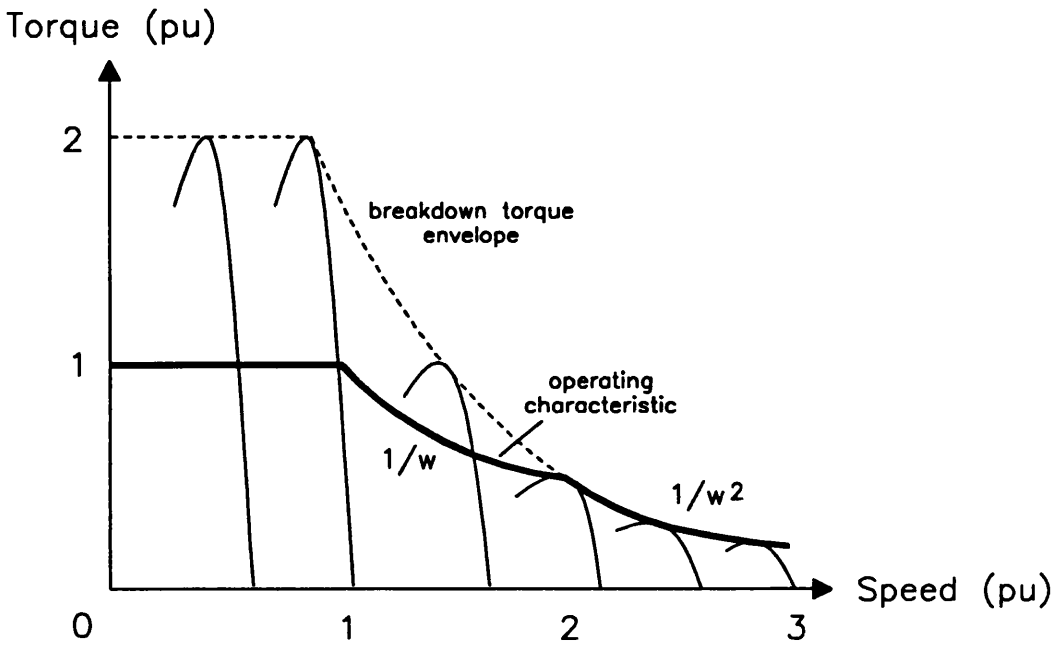

Figure 1.9: *Typical induction motor field-weakening characteristics [10].*

10MW. Vector-control (field-orientation) allows separate control of the torque and flux in the motor in the same way as the separately-excited DC motor [10].

The constant-power speed range obtainable with an induction motor drive is approximately given by the ratio of the breakdown torque[2] to the rated torque [24]. This is because under constant voltage operation the breakdown torque decreases as the square of the speed, while for constant-power operation the required torque decreases only inversely with the speed (see Fig. 1.9). They are equal at the limit of the constant-power speed range.

The breakdown torque and hence the constant-power speed range is primarily determined by the motor leakage inductance. However the direct-on-line starting inrush current is also affected by the leakage inductance. Standard induction motors are designed to have a limited starting current and consequently are restricted to constant-power speed ranges of 2 to 3:1 [24]. Special low-leakage motors designed for inverter operation can offer constant-power speed ranges of up to 4:1 [25]. Higher values can be

[2]This is the maximum output torque at any speed with a given supply voltage and frequency.

obtained by oversizing the inverter or by using a winding changeover switch [26]. The latter technique involves switching the stator winding in a similar way to star/delta starting to obtain a constant-power speed range of up to 12:1. An electromagnetic switch (relay) is used to perform the switching operation. These are simple and low cost however they take tens of milliseconds to switch-over and so restrict the drive's dynamic performance. This could be avoided by using semiconductor switches but the cost would be prohibitive. This technique could also be applied to any motor type to extend the constant-power speed range.

1.3 Field-Weakening Applications

As mentioned earlier, the majority of variable-speed applications do not require field-weakening operation. However for applications such as traction and spindle drives which require a wide constant-power speed range, using a constant torque drive would be prohibitively expensive due to the oversizing required (see Fig. 1.5 on page 32).

Four common applications requiring a wide field-weakening range are traction, machine tool main spindle drives, rolling mills and washing machines. Typical specifications for these drives are given in Table 1.2 [5, 8, 15]. Electric motors have been used in traction applications for over a century. These require a high torque at low speeds to overcome stiction and to allow inclines to be climbed at reasonable speeds, and low torque at high speeds to overcome friction and windage [15].

For trains, output powers in the MW region and constant-power speed ranges of between 1.5 and 3 are required. Wound-field DC commutator motors were used extensively in the past because of their simple control, but are slowly being replaced by the more rugged, lower-cost and lighter induction motors. Wound-field synchronous

Table 1.2: *Typical field-weakening requirements.*

	Traction		Main	Rolling	Washing
	Car	Train	Spindle	Mills	Machines
Power Range	20–60kW	1–10MW	5–50kW	1–10MW	1kW
Base Speed	25kmph	60kmph	1500rpm	250rpm	50rpm
CPSR	4	1.5–3	4–12	3–4	15–30
allowable torque ripple ...					
low-speed	med	med	low	low	high
high-speed	high	high	low	med	high
motor types used ...					
in the past		DC	DC, IM	DC	IM
presently		DC, IM	IM	DC, Syn, IM	universal
the future?	IM, SR, IPM	IM	IM, IPM	IM	SR

motors offer unity power-factor and higher efficiency than induction motors but still require brushes and have a less rugged rotor.

Electric cars represent an immense future market for the "right" electric drive. With legislation practically forcing their use in the future, there is considerable research being carried out to develop a suitable drive [27]. The main requirements are : a constant-power speed range of about 4:1, a high power/weight ratio, a high overload capacity (200%) and high efficiency [5]. The allowable torque ripple is relatively high. DC motors would be the simplest to control, but AC motors are smaller and lighter for the same output power. Possible contenders are the induction motor (IM), the switched-reluctance motor (SR) and the interior permanent magnet motor (IPM).

Main spindle drives are used in machine tools to rotate the workpiece during turning operations and also increasingly to hold the workpiece stationary in a particular position while drilling and tapping operations are performed by a separate tool spindle [23]. This is called c-axis operation. Machining processes are inherently constant-power operations, requiring high torque at low speeds and low torque at high speeds. Low torque ripple is critical, especially at low speeds in order to achieve good positioning performance. In the past, variable gear ratios were used to achieve the required constant-power speed range, however the trend is now to use a fixed gear ratio with a motor with the required field-weakening range. It is also desirable to eliminate the gearing completely and use a *direct drive* to improve the static and dynamic performance. DC motors and fixed-speed induction motors were used in the past and presently vector-controlled induction motors are widely used. Recently interior permanent magnet spindle drives have become commercially available [23]. These offer similar constant-power speed ranges (about 4:1) and improved low-speed and positioning dynamics compared to the induction motor.

Rolling mills are used to roll metal ingots into strip or sheet [28]. Considerable torque is required on the slow initial passes but higher speeds and lower torque are used as the material becomes thinner. The process requires high power (MW) motors with a constant-power speed range of about 4:1. DC commutator motors have been used in the past. Synchronous and induction motors are however gradually taking over

because they are available in larger sizes (reducing the number of motors which have to be paralleled to achieve the desired output), are more rugged, and have lower inertia and hence faster dynamic response. This gives better control over the quality of the finished sheet [29].

Washing machine main drive motors are required to operate with high torque at 50rpm during the wash cycle in order to reverse the drum rotation every 5 to 15 secs, yet be capable of spinning the drum up to 1500rpm with sufficient torque to overcome friction and windage losses [9]. In the past, a 2/24 pole-changing induction motor was used in combination with a fixed gear, however this had a low maximum spin speed and little control over the acceleration. The latter point is necessary as it is important to allow the clothes time to distribute themselves evenly over the drum prior to reaching the maximum spin speed. Presently a universal motor is used and variable-speed control is obtained with a single, low-cost triac. Due to the cost-sensitive nature of the product, it is unlikely that more sophisticated drives would be used in the future except perhaps switched-reluctance drives.

1.4 Thesis Structure

Fig. 1.10 shows how this thesis is split into two major parts. The first part examines the theoretical and practical limitations to the field-weakening performance of the three main types of brushless synchronous AC motor : the surface permanent magnet motor, the synchronous reluctance motor and the interior permanent magnet motor. The results are validated using a custom-built controller. Using a new *interior permanent magnet motor drive parameter plane* approach, it is shown that a high-saliency interior permanent magnet motor drive should offer the best practical field-weakening performance. Note that the axially-laminated construction offers the highest saliency ratios [21].

The second part of this thesis examines the design, modelling and testing of a new axially-laminated interior permanent magnet motor drive in order to validate and extend the results of the first part. First the importance of the DQ inductance characteristics in determining the drive performance is shown and the calculation and measurement of these characteristics are discussed. Next the design of a 7.5kW axially-laminated synchronous reluctance and interior permanent magnet motor drive for optimal field-weakening performance is described. Experimental results are given showing that the interior permanent magnet motor drive can achieve an extremely wide constant-power speed range which exceeds 7.5:1. This cannot be matched by any other type of motor and makes this drive a serious contender for applications such as machine tool main spindle drives and traction.

The original content of this thesis can be summarised as follows. Firstly the new concept of the interior permanent magnet parameter plane is introduced. It is used to show the optimal field-weakening performance limit and also how to design brushless synchronous AC motor drives to achieve it. Next an original analysis of the effect of copper loss, magnetic saturation and iron loss on the field-weakening performance is performed. This showed that saturation severely restricts the field-weakening performance of synchronous reluctance drives. Then a complete design procedure for a new type of axially-laminated interior permanent magnet motor is described. The motor

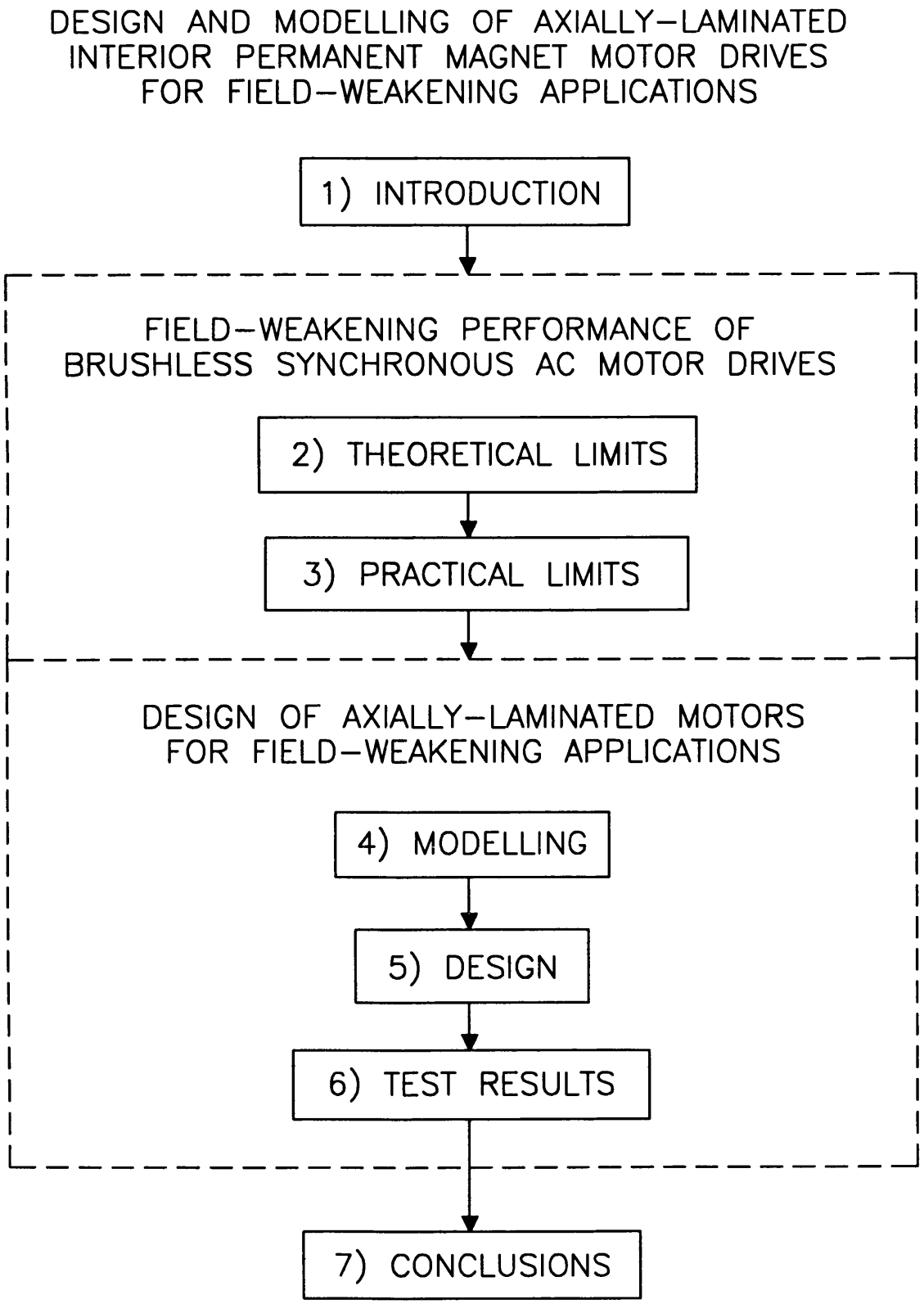

Figure 1.10: *Flow-chart showing structure of thesis.*

was built and comprehensive test results illustrating the extremely wide constant-power speed range are given. The achieved constant-power speed range exceeded all previously published test results[3] known to the author for any motor type.

[3]When no special mechanical motor winding switching arrangements are used.

Part I

Field-Weakening Performance of Brushless Synchronous AC Motors

Chapter 2

Theoretical Limitations

Chapter Two examines the theoretical limitations to the field-weakening performance of the three types of brushless synchronous AC motor when driven from an inverter with a limited voltage and current capability. Using a lossless linear model it is shown that five classes of motor drive can be defined based on whether or not there is a theoretical maximum speed limitation due to the voltage and current-limit constraints. The circle diagram is used to show the similarities between the optimal field-weakening control strategies for the five drive classes.

The new concept of the *interior permanent magnet motor drive parameter plane* is introduced. This provides a convenient graphical means for visualising the effect of parameter changes on the field-weakening performance. It is also used to determine the optimal field-weakening performance and to show what parameters are required to achieve it. High-saliency synchronous reluctance and interior permanent magnet motor drives appear to be the most promising. The effects of practical factors such as copper loss, magnetic saturation and iron loss on these ideal characteristics are examined in the next chapter.

2.1 Introduction

Brushless synchronous AC motors operate with sinusoidal currents and use a standard quasi-sinusoidally distributed AC stator winding and inverter. The three main types are the surface permanent magnet motor (SPM), the interior permanent magnet motor (IPM) and the synchronous reluctance motor (SYNCHREL). Cross-sections of the three types are shown in Fig. 2.1, where the dotted areas represent steel and the solid areas represent permanent magnets. As the permeability of ferrite and rare-earth magnets is close to air, the surface permanent magnet motor is non-salient and operates purely on magnet alignment torque. The synchronous reluctance motor operates purely on reluctance torque. The interior permanent magnet motor is a hybrid of the surface permanent magnet and synchronous reluctance motors in terms of torque production [22]. The latter two motors can be considered to be special cases of the interior permanent magnet motor.

The torque versus speed characteristic of a lossless, constant parameter interior permanent magnet motor drive is determined by seven parameters : the number of phases m, the number of pole-pairs p, the rated voltage V_c, the rated current I_c, the d-axis inductance L_d, the q-axis inductance L_q and the magnet flux-linkage Ψ_m. As will be shown later, only the latter four affect the shape of the *normalised* torque versus

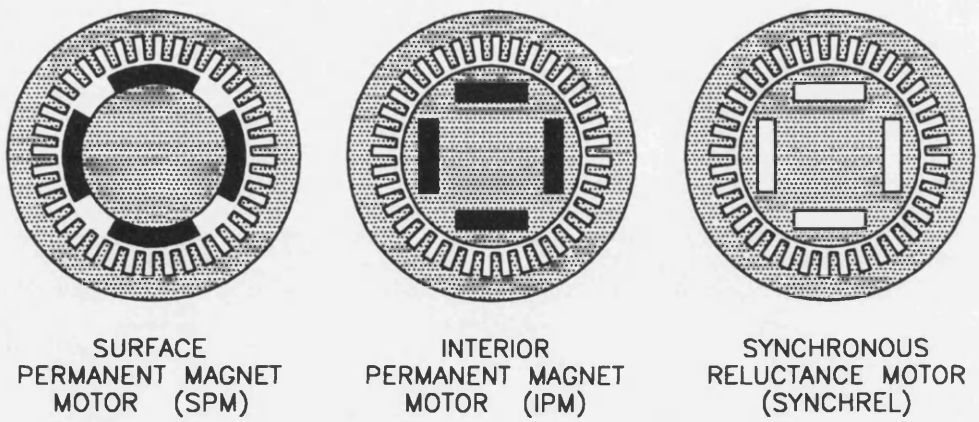

Figure 2.1: *Motor cross-sections.*

speed characteristic.

As the cost of the inverter is typically three to five times that of the motor [21], the ability of a motor drive to utilise a given inverter voltage and current capability is important.

The analysis in this chapter is based on three major assumptions which were discussed in Sec. 1.1. Firstly, a lossless, steady-state, constant parameter DQ model is used. This clearly neglects the effect of practical factors such as stator resistance, iron loss and magnetic saturation. Second, a limited inverter capacity is assumed with maximum voltage and current ratings and pure sinusoidal waveforms at any frequency and current-angle. Finally the motor drive is assumed to be operated to deliver maximum torque at any speed.

Five classes of brushless synchronous AC motor drive can be defined based on whether there is a *theoretical* finite maximum speed limit due to *voltage-limit* constraints. These are :

1. the finite maximum speed SPM drive.
2. the infinite maximum speed SPM drive.
3. the infinite maximum speed SYNCHREL drive.
4. the finite maximum speed IPM drive.
5. the infinite maximum speed IPM drive.

All synchronous reluctance motor drives have no theoretical speed limitation as they lack any magnet flux, however the output power at high speed may be very low. Surface and interior permanent magnet motors by themselves cannot be classified as infinite or finite maximum speed as this depends on the inverter ratings. Only motor drives can be classified.

Early work concerning the field-weakening performance of interior permanent magnet motor drives dealt with the analysis and control of existing machines [2, 22, 30].

It is only recently that the selection and effect of the drive parameters on the field-weakening performance has started to be explored.

One of the first papers on this topic was by Sebastian and Slemon [3]. They showed that inset (interior) permanent magnet motor designs offered more torque and a better field-weakening range compared to conventional surface permanent magnet motor designs.

This was followed by a landmark paper by Schiferl and Lipo [4] which made the first serious attempt at examining the effect on the field-weakening performance of varying the parameters. Unfortunately they were hampered by two factors. Firstly though they used a unity inverter kVA normalisation, they did not normalise the drive parameters for unity rated speed (see Sec. 2.2.1). This left them with three independent parameters instead of two. The effect of a single independent parameter is simple to demonstrate, the effect of two independent parameters is more difficult but can be coped with, however the effect of three independent parameters is extremely difficult to describe. Secondly, they did not understand the optimal control of infinite maximum speed drives and in particular the existence of a "Mode III" form of operation (see Sec. 2.2.4). Despite these problems, their work laid the foundation for later analysis and they were also the first to describe the main design criterion for optimal field-weakening performance. This is to make the magnet flux-linkage equal to the maximum d-axis stator flux-linkage :

$$\Psi_m = L_d I_c \tag{2.1}$$

The normalisation of the DQ equations to unity rated speed to reduce the number of independent drive parameters is described in [12, 31, 32]. It was applied by Adnanes [5, 33] to investigate the field-weakening performance of the finite maximum speed SPM drive. Betz [6] also used a normalised model to analyse the field-weakening performance of the synchronous reluctance motor drive. It should be noted that the normalised torque versus speed characteristics of the surface permanent magnet and synchronous reluctance motor drives can both be characterised by a single parameter.

The optimal control of infinite maximum speed IPM drives was later comprehen-

sively analysed using the circle diagram (see Sec. 2.2.2) in a paper by Morimoto, Takeda, Hirasa and Taniguchi [34]. They showed that the infinite maximum speed SPM drive has a true constant-power characteristic in the high speed region and also investigated the effect of magnet operating point limitations.

This chapter has a similar aim to Schiferl and Lipo's work. This is to explore the effect of varying the motor drive parameters on the field-weakening performance of interior permanent magnet motor drives. It achieves more useful results as it fully normalises the field-weakening characteristics and uses the optimal control strategies for infinite maximum speed drives.

The field-weakening performances of surface permanent magnet and synchronous reluctance motor drives are considered first. This is useful as these motor drives represent simpler cases of the interior permanent magnet motor drive and so give insight into its fundamental limitations. Next the interior permanent magnet motor drive is examined and the new concept of the IPM parameter plane is introduced as a means for graphically illustrating the effect of varying the parameters on the field-weakening performance. The IPM parameter plane is used to to show that the optimal field-weakening performance gives maximum output power up to infinite speeds but is restricted to an inverter utilisation below about 0.7 at rated speed. This optimal field-weakening performance can be achieved by a large number of designs and practical factors will determine which is the most feasible.

2.2 Surface Permanent Magnet Motor Drives

The surface permanent magnet brushless AC motor (SPM) has a standard three-phase AC stator and a non-salient iron rotor with projecting magnets (see Fig. 2.1 on pg. 52). These magnets can either be glued in position or held in place by an enclosing can or binding. Its construction is similar to the brushless DC PM motor except that it operates with sinusoidal currents instead of rectangular currents.

The performance of the finite maximum speed SPM drive has been comprehensively analysed by Adnanes [5, 33]. The infinite maximum speed SPM drive has received little attention but the optimal control characteristics have been analysed by Morimoto et al. [34].

The surface permanent magnet motor drive is the easiest of the three brushless synchronous AC motors to analyse and its equivalent circuit and phasor diagram are shown in Fig. 2.2 [12]. The equivalent circuit consists of the *synchronous inductance* L_s in series with the magnet-induced *back-emf voltage* E_q which is given by the product of

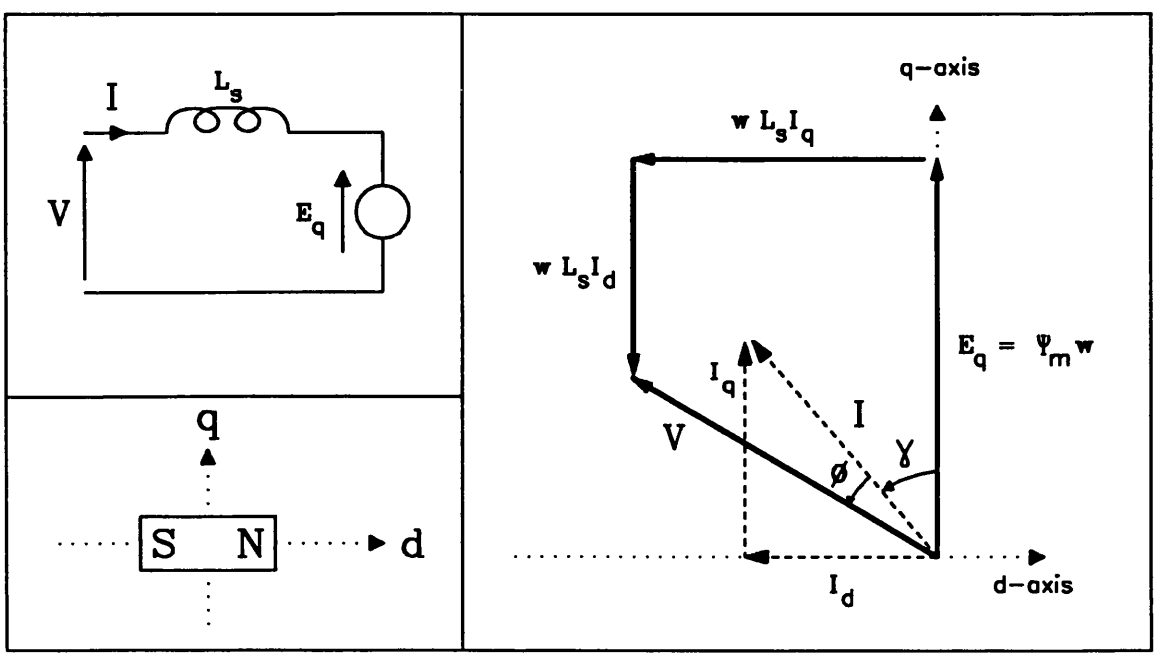

Figure 2.2: *Surface permanent magnet motor phasor diagram.*

the magnet flux Ψ_m and the electrical speed w. The magnet flux lies along the positive d-axis and hence the back-emf phasor is along the positive q-axis. The *current-angle* γ is the angle by which the current leads the back-emf phasor and the input power-factor is $\cos\phi$ where the *power-factor angle* ϕ is the angle between the terminal voltage and the phase current.

In the phasor diagram in Fig. 2.2, the current-angle is greater than zero. This produces a component of stator current I_d along the negative d-axis which opposes the magnet flux, reduces the total airgap flux and hence reduces the terminal voltage. The further the current-angle is increased, the further the terminal voltage is reduced. This principle is used in flux-weakening the surface permanent magnet motor drive.

2.2.1 Normalised Equations

The conventional per-phase steady-state DQ equations for the surface permanent magnet motor drive can be obtained from the equivalent circuit in Fig. 2.2 as :

$$\left.\begin{aligned} V_d &= -\omega L_s I_q \\ V_q &= \omega L_s I_d + \omega \Psi_m \\ T &= \Psi_m I_q \end{aligned}\right\} \quad \text{where} \quad \begin{aligned} I &= \sqrt{I_d^2 + I_q^2} \leq I_c \\ V &= \sqrt{V_d^2 + V_q^2} \leq V_c \end{aligned} \tag{2.2}$$

where V_d, V_q, I_d and I_q are the d- and q-axis components of the stator voltage and current respectively, and V_c and I_c are the rated inverter phase voltage and current. The torque expression is obtained from energy conservation, $P = Tw = V_d I_d + V_q I_q$.

Equation 2.2 defines the maximum torque versus speed characteristic of the surface permanent magnet motor drive. It has four parameters : V_c, I_c, L_s and Ψ_m. In order to reduce the number of parameters the normalisation technique used by Schiferl and Lipo [4] is applied. This involves choosing the *base phase voltage* V_o and the *base phase current* I_o to be equal to be equal to the rated values, that is V_c and I_c. Note the use of the subscript "o" to indicate base quantities. The *base power* P_o is chosen to equal the output power with rated input voltage and current, and unity power-factor. This implies the following base quantities :

$$P_o = V_o I_o = T_o \omega_o \qquad L_o = \frac{V_o}{\omega_o I_o} \qquad \Psi_o = \frac{T_o}{I_o} \tag{2.3}$$

Following the method used by Betz [6], the normalised quantities can be defined in terms of the actual quantities and the base values as :

$$V_n \equiv \frac{V}{V_o} \qquad I_n \equiv \frac{I}{I_o} \qquad \omega_n \equiv \frac{\omega}{\omega_o} \qquad L_n \equiv \frac{L}{L_o} \qquad \Psi_n \equiv \frac{\Psi}{\Psi_o} \tag{2.4}$$

Using (2.3) and (2.4), (2.2) can be rewritten in normalised variables as :

$$\left.\begin{aligned} V_{dn} &= -w_n L_{sn} I_{qn} \\ V_{qn} &= w_n L_{sn} I_{dn} + w_n \Psi_{mn} \\ T_n &= \Psi_{mn} I_{qn} \end{aligned}\right\} \quad \text{where} \quad \begin{aligned} I_n &= \sqrt{I_{dn}^2 + I_{qn}^2} \leq 1 \\ V_n &= \sqrt{V_{dn}^2 + V_{qn}^2} \leq 1 \end{aligned} \tag{2.5}$$

where the subscript "n" is used to indicate normalised quantities. Note that normalisation has reduced the original four parameters to two parameters : L_{sn} and Ψ_{mn}.

Using the procedure described by Adnanes [5], the two parameters can be reduced to one by choosing the base speed ω_o to be equal to the rated speed. This makes the normalised rated speed ω_{kn} equal to unity. The rated speed was defined in Chapter 1 as the speed at which the terminal voltage equals its rated value when delivering rated torque. The terms base speed and rated speed will now be used interchangeably in this thesis. Note from the torque expression in (2.2) that the maximum torque is obtained with $I_q = I_c$ and $I_d = 0$, or in normalised variables, with $I_{qn} = 1$ and $I_{dn} = 0$. By applying this operating point to the voltage equations in (2.5) and solving for $V_n = 1$ at $\omega_n = 1$ it can be shown that the two normalised parameters Ψ_{mn} and L_{sn} are dependent where :

$$L_{sn} = \sqrt{1 - \Psi_{mn}^2} \tag{2.6}$$

Thus the shape of the normalised field-weakening characteristics of the surface permanent magnet motor drive can written in terms of one parameter. The choice of the parameter used is arbitrary, but it is convenient for the later analysis of the interior permanent magnet motor drive to use Ψ_{mn}. Using (2.6), (2.5) can written solely in terms of Ψ_{mn} as :

$$\left.\begin{aligned} V_{dn} &= -w_n \sqrt{1 - \Psi_{mn}^2} I_{qn} \\ V_{qn} &= w_n \sqrt{1 - \Psi_{mn}^2} I_{dn} + w_n \Psi_{mn} \\ T_n &= \Psi_{mn} I_{qn} \end{aligned}\right\} \quad \text{where} \quad \begin{aligned} I_n &= \sqrt{I_{dn}^2 + I_{qn}^2} \leq 1 \\ V_n &= \sqrt{V_{dn}^2 + V_{qn}^2} \leq 1 \end{aligned} \tag{2.7}$$

The d- and q-axis current components can be written in terms of the current-angle γ and I_n using the phasor diagram in Fig. 2.2 as :

$$I_{qn} = I_n \cos\gamma \qquad I_{dn} = -I_n \sin\gamma \tag{2.8}$$

This allows (2.7) to be written in terms of I_n and γ as :

$$\left.\begin{aligned} V_{dn} &= -w_n\sqrt{1-\Psi_{mn}^2}\,I_n\cos\gamma \\ V_{qn} &= -w_n\sqrt{1-\Psi_{mn}^2}\,I_n\sin\gamma + w_n\Psi_{mn} \\ T_n &= \Psi_{mn} I_n \cos\gamma \end{aligned}\right\} \quad \text{where} \quad \begin{aligned} I_n &\leq 1 \\ V_n &= \sqrt{V_{dn}^2 + V_{qn}^2} \leq 1 \end{aligned} \tag{2.9}$$

2.2.2 SPM Motor Drive Circle Diagram

The circle diagram is a well-known graphical technique to determine the optimal field-weakening control strategy for brushless synchronous AC motor drives [2, 4, 5, 12, 22, 34]. Brushless synchronous AC motors are usually current-controlled and so it is convenient to define their operating point in terms of I_{dn} and I_{qn} or I_n and γ. Each operating point can be represented by its position in the (I_{dn}, I_{qn}) plane.

A given operating point is termed *feasible* if it does not exceed the inverter voltage or current limits. The circle diagram shows how these limits restrict the feasible operating region in the (I_{dn}, I_{qn}) plane. The current-limit constraint, $I_{dn}^2 + I_{qn}^2 \leq 1$, forms a circle whose centre is at the origin with unity radius (see Fig. 2.3). Any operating point which lies on or within this circle will not exceed the inverter's current rating.

The voltage-limit locus can be obtained by applying the voltage constraint $V_{dn}^2 + V_{qn}^2 \leq 1$ to (2.5) which yields [12] :

$$\left[I_{dn} + \frac{\Psi_{mn}}{L_{sn}}\right]^2 + I_{qn}^2 \leq \frac{1}{(\omega_n L_{sn})^2} \tag{2.10}$$

This is the equation for a circle with its centre at $(-\Psi_{mn}/L_{sn}, 0)$ whose radius is inversely proportional to speed (see Fig. 2.3). This circle encloses all operating points where the terminal voltage does not exceed the rated voltage. All feasible operating points must lie on or within the intersection of the voltage and current-limit circles.

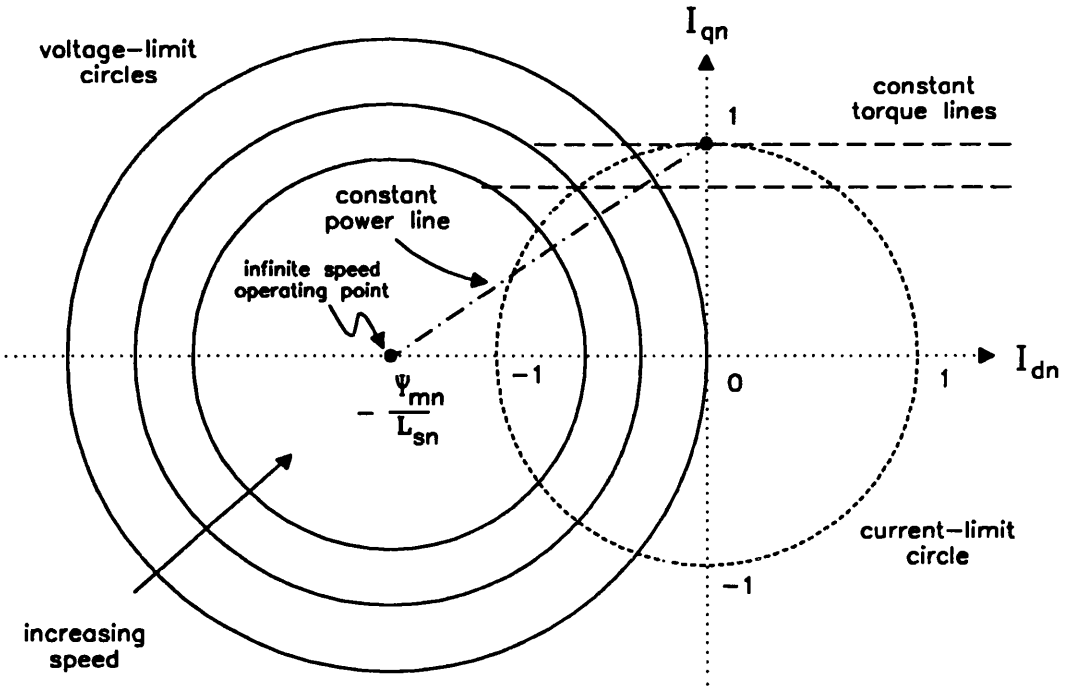

Figure 2.3: *Surface permanent magnet motor circle diagram.*

From (2.2), the output torque is directly proportional to I_q. This means that the loci of constant torque form straight lines parallel to the d-axis. At any speed the maximum torque is obtained at the feasible operating point with the maximum I_q. At low speeds the voltage-limit circle is large and completely encloses the current-limit circle. Hence the drive is purely current-limited and the maximum torque is obtained by operating at the top of the current-limit circle. As the speed increases, the voltage-limit circle contracts and the operating point is forced to converge towards its centre. This point is termed the *infinite speed operating point.* It lies on the current-limit circle when :

$$-\frac{\Psi_{mn}}{L_{sn}} = -\frac{\Psi_{mn}}{\sqrt{1-\Psi_{mn}^2}} = -1 \tag{2.11}$$

that is, when $\Psi_{mn} = 1/\sqrt{2}$. This corresponds to the optimal field-weakening criterion in (2.1).

There are two types of surface permanent magnet motor drive. These differ in the location of the infinite speed operating point. Finite maximum speed SPM drives

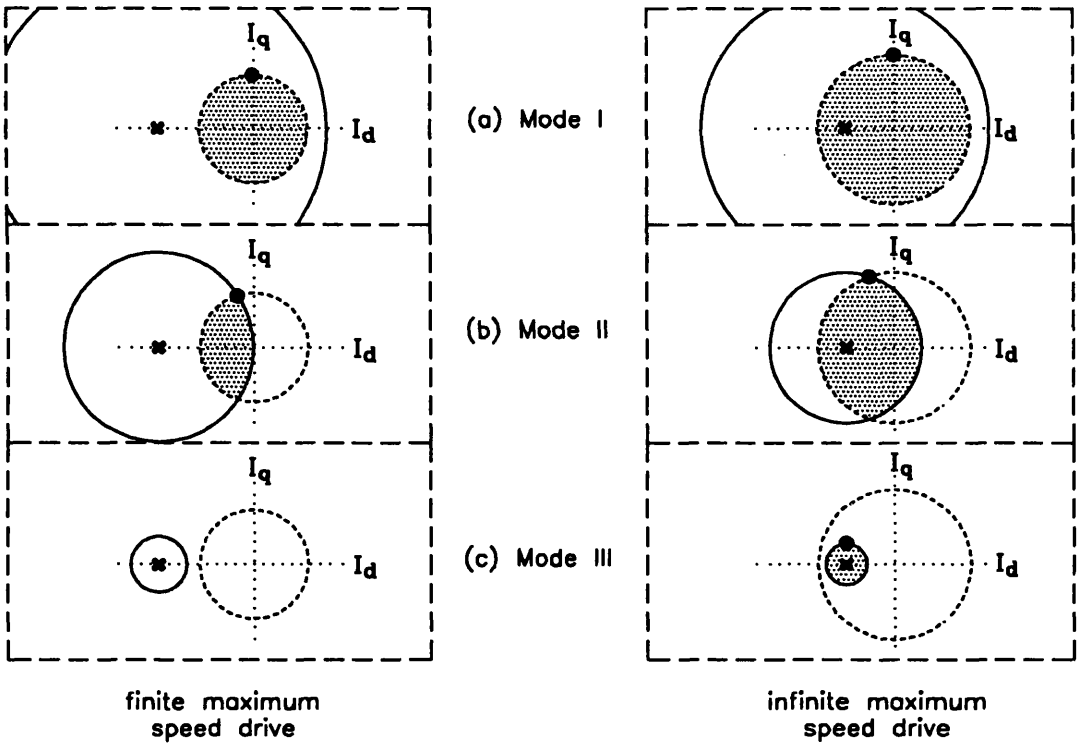

Figure 2.4: *Operating modes for finite and infinite maximum speed SPM drives.*

have an infinite speed operating point outside the current-limit circle ($\Psi_{mn} > 1/\sqrt{2}$). For these drives there will exist a maximum possible operating speed at which point the voltage and current-limit circles are tangential. At higher speeds the voltage and current-limit circles do not intersect and there are no feasible operating points.

Infinite maximum speed SPM drives have the infinite speed operating point on or within the current-limit circle ($\Psi_{mn} \leq 1/\sqrt{2}$). These drives have no theoretical maximum speed as at all speeds there are always feasible operating points. Note that infinite maximum speed drives do not necessarily have good field-weakening performance as the output power may be very low at high speeds.

Fig. 2.4 shows the current and voltage-limit loci for finite and infinite maximum speed SPM drives at low, medium and high speed. The infinite speed operating point is marked with a cross, the feasible operating region is shown shaded and the optimum operating point for maximum torque is shown by a "•". The optimum trajectories and

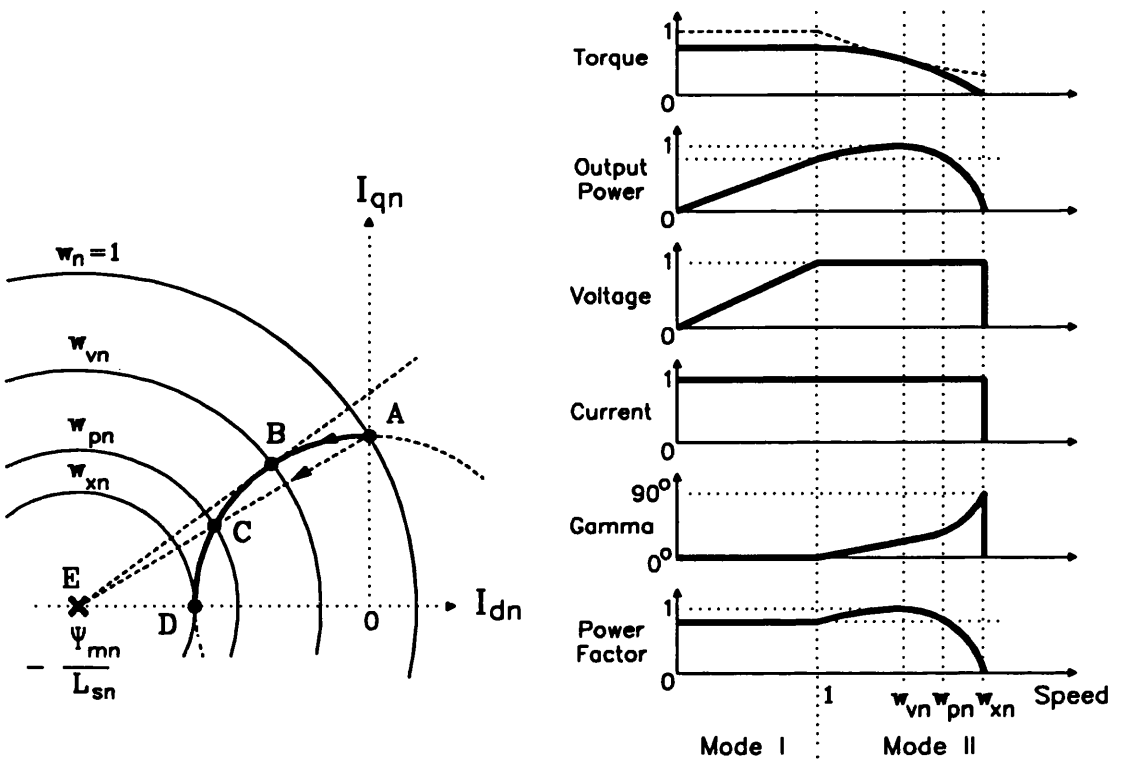

Figure 2.5: *The optimal torque trajectory for a finite maximum speed SPM drive.*

the three operating modes will now be discussed in detail.

2.2.3 Finite Maximum Speed SPM Motor Drives

Fig. 2.5 shows the optimum operating trajectory for maximum power output at any speed for a finite maximum speed SPM drive and the corresponding drive torque, power, voltage, current, current-angle and power-factor.

It was shown by Morimoto et al. [34] that in general, brushless synchronous AC motor drives have three operating modes or regions : Mode I, Mode II and Mode III. Mode I is the current-limited or constant torque region. This is the region from zero speed up to the rated speed where rated torque is obtained by operating with rated current at the *maximum-torque-per-ampere current-angle* γ_m. Geometrically this corresponds to operating at the point where the constant torque loci are tangent to the current-limit circle. From Fig. 2.4a it is clear that the maximum torque is obtained by

operating at the top of the current-limit circle, that is $\gamma_m = 0°$. This corresponds to point A in Fig. 2.5.

At the rated speed ($w_n = 1$) the voltage-limit circle intersects point A. At higher speeds, the drive transitions to Mode II. This is the current-and-voltage-limited region. Here the motor is operated with rated voltage and current at the minimum feasible current-angle. This corresponds to the intersection of the voltage and current-limit loci as shown in Fig. 2.4b.

In Mode II the current-angle γ increases monotonically as the speed increases and hence the voltage-limit circle shrinks. As the current-angle increases, I_q decreases, causing the torque to fall. Note that the dashed line in the torque graph in Fig. 2.5 shows the characteristic produced by an ideal field-weakening drive. The fall in torque is initially offset by the increase in speed and so the output power initially rises. The normalised power-factor and output power during Mode II operation increase until they reach unity at point B which corresponds to a speed of ω_{vn}. After this the power-factor and power decrease rapidly until they reach zero at the maximum operating speed ω_{xn} (point D) where $\gamma = 90°$. At this point the voltage and current-limit circles are tangential and operation at higher speeds is not possible without exceeding either constraint (see Fig. 2.4c). Mode III operation is not possible in finite maximum speed SPM drives. Note that due to the choice of normalisation and the use of a lossless model, the normalised output power equals the input power-factor during Mode II operation.

The surface permanent magnet motor drive has an interesting property regarding constant-power operation which was described by Morimoto et al. [35]. Consider a surface permanent magnet motor drive operated from a constant voltage source. From the circle diagram in Fig. 2.3 it can be seen that the operating speed is *inversely proportional* to the distance from its operating point to the infinite speed operating point. Now as torque is *proportional* to I_q thus operation along *any* straight line passing though the infinite speed operating point with a constant terminal voltage, corresponds to operating with constant-power output. The greater the slope of the line, the higher the output power.

This result can be usefully applied to the circle diagram. Consider point B in

Fig. 2.5. This lies on the line through the infinite speed operating point which is tangential to the current-limit circle. When operating with rated supply voltage and current, this point represents the maximum power output available from the motor drive at any speed as the line has the greatest possible slope and so the greatest output power.

The result can also be used to determine the constant-power speed range. At the rated speed with rated voltage and current the drive operates at point A and delivers rated output power. To maintain rated output power the operating point must move along a straight line from point A to the infinite speed operating point. The maximum operating speed at rated power is ω_{pn} (point C) where the rated power line intersects the current-limit circle again. The constant-power speed range is equal to the ratio of the lengths of the lines EA/EC.

2.2.4 Infinite Maximum Speed SPM Motor Drives

Infinite maximum speed SPM drives have received remarkably little attention in the literature and have only recently been analysed by Morimoto et. al. [34]. This is probably due to nearly all common surface permanent magnet motor drives being of the finite maximum speed variety. In order to produce an infinite maximum speed SPM drive it is generally necessary to add external inductance in series with the motor as suggested by Sebastian and Slemon [3].

Infinite maximum speed SPM drives have the infinite operating speed point within the current-limit circle. Operation in Mode I and the transition from Mode I to II is similar to that for the finite maximum speed drive (see Figs. 2.4 and 2.6). The main difference is that Mode III operation is now possible.

Mode III is a high speed, voltage-limited operating region where maximum torque is obtained by operating at the point where the constant torque locus is tangent to the voltage-limit locus. Note that the current is generally less than its rated value. For the surface permanent magnet motor drive, Mode III operation corresponds to the top of the voltage-limit circle (line BD in Fig. 2.6). The transition from Mode II to Mode

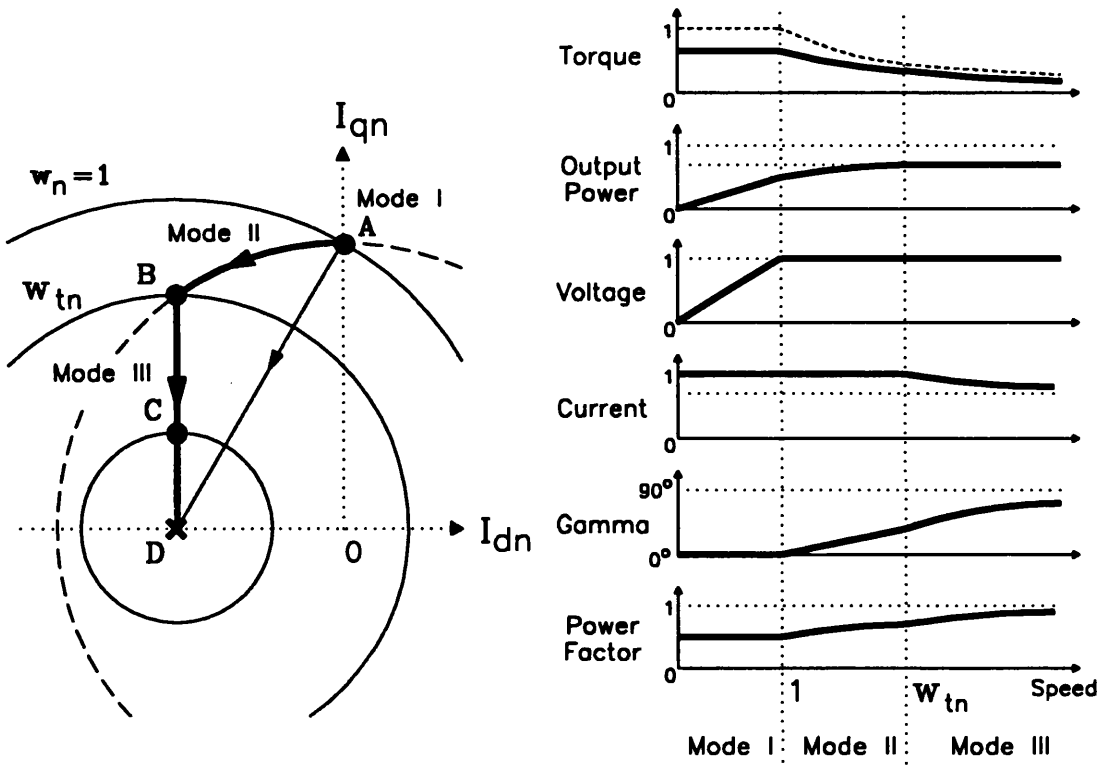

Figure 2.6: *The optimal torque trajectory for an infinite maximum speed SPM drive.*

III occurs at point B at ω_{tn} where the Mode III maximum-torque-with-limited-voltage trajectory intersects the current-limit circle.

Mode III operation for the surface permanent magnet motor drive corresponds to operating along a straight line passing through the infinite speed operating point. Thus the Mode III output power of the drive is *exactly* constant. In fact of all the five classes of brushless synchronous AC motor drive, the infinite maximum speed SPM drive is the only one with a perfectly flat high-speed output power versus speed characteristic (compare this with the finite maximum speed SPM drive in Fig. 2.5).

During Mode III operation the normalised current magnitude I_n asymptotes to Ψ_{mn}/L_{sn} while the power-factor increases towards unity. The two effects cancel and the output power remains precisely constant. The constant-power speed range is infinite as the output power increases monotonically with speed.

2.2.5 Calculated Characteristics

The circle diagram approach allows the identification of the optimal field-weakening control strategy. This control strategy can be combined with the motor drive equations (2.9) to calculate the drive's performance characteristics (see Table 2.1). The equations for the performance of finite maximum speed SPM drives are obtained using the method described by Adnanes [5].

The Mode I performance is obtained by substituting $I_n = 1$ and $\gamma = 0°$ into (2.9). The Mode II performance is obtained by solving the voltage equations in (2.9) with $V_n = 1$ and $I_n = 1$ giving an expression for $\sin\gamma$ in terms of ω_n (see Table 2.1). Substituting this into the torque expression in (2.9) gives an expression for torque in Mode II in terms of ω_n [5] :

$$T_n = \Psi_{mn}\sqrt{1 - \left(\frac{1-\omega_n^{-2}}{2\Psi_{mn}\sqrt{1-\Psi_{mn}^2}}\right)^2} \tag{2.12}$$

The constant-power speed range is obtained by solving for the speed at which the Mode II output power $T_n w_n$ equals the rated output power P_{kn}. The Mode III performance can be obtained from (2.7) with $I_{dn} = \Psi_{mn}/L_{sn}$ and $I_{qn} = 1/(w_n L_{sn})$ from (2.10).

The equations in Table 2.1 were used to calculate the performance characteristics of the surface permanent magnet motor drive. Figs. 2.7 and 2.8 show the variation in the normalised output torque, output power, power-factor and current-angle as a function of speed for surface permanent magnet motor drives with different values of Ψ_{mn}. For comparison, the ideal motor drive characteristic is superimposed on the torque and power graphs in Fig. 2.7 and on the torque graph in Fig. 2.8. Note that the normalised magnet flux-linkage Ψ_{mn} is equal to the ratio of the magnet-induced back-emf at the rated speed to the rated terminal voltage. The phasor diagram in Fig. 2.2 on pg. 56 shows that $\Psi_{mn} = 1$ when the synchronous inductance is zero. Such a motor drive has unity power-factor during Mode I operation, but Fig. 2.7 shows it has no field-weakening capability whatsoever.

As the synchronous inductance is increased, the voltage drop across it increases and so Ψ_{mn} falls. This causes a small decrease in the Mode I power-factor but a large

Table 2.1: *Summary of the characteristics of the surface permanent magnet motor drive under maximum torque operation.*

Parameter	Mode I	Mode II	Mode III
Speed			
$\Psi_{mn} \geq 1/\sqrt{2}$	$\omega_n \leq 1$	$1 \leq \omega_n \leq \frac{1}{\Psi_{mn}-\sqrt{1-\Psi_{mn}^2}}$	
$\Psi_{mn} \leq 1/\sqrt{2}$	$\omega_n \leq 1$	$1 \leq \omega_n \leq \frac{1}{\sqrt{1-2\Psi_{mn}^2}}$	$\omega_n \geq \frac{1}{\sqrt{1-2\Psi_{mn}^2}}$
Current-Angle	$\gamma = 0^\circ$	$\sin\gamma = \frac{\omega_n^2-1}{2\Psi_{mn}\omega_n^2\sqrt{1-\Psi_{mn}^2}}$	$\tan\gamma = \Psi_{mn}\omega_n$
Voltage	$V_n = \omega_n$	$V_n = 1$	$V_n = 1$
Current	$I_n = 1$	$I_n = 1$	$I_n = \sqrt{\frac{\omega_n^2\Psi_{mn}^2+1}{\omega_n^2(1-\Psi_{mn}^2)}}$
Torque	$T_n = \Psi_{mn}$	$T_n = \Psi_{mn}\sqrt{1-\left(\frac{1-\omega_n^{-2}}{2\Psi_{mn}\sqrt{1-\Psi_{mn}^2}}\right)^2}$	$T_n = \frac{\Psi_{mn}}{\omega_n\sqrt{1-\Psi_{mn}^2}}$
Power	$P_n = T_n\omega_n$	$P_n = T_n\omega_n$	$P_n = \frac{\Psi_{mn}}{\sqrt{1-\Psi_{mn}^2}}$
PF	$\cos\phi = \Psi_{mn}$	$\cos\phi = T_n\omega_n$	$\cos\phi = \frac{\omega_n\Psi_{mn}}{\sqrt{\omega_n^2\Psi_{mn}^2+1}}$
CPSR			
$\Psi_{mn} \geq 1/\sqrt{2}$		$\text{CPSR} = \frac{1}{2\Psi_{mn}^2-1}$	
$\Psi_{mn} \leq 1/\sqrt{2}$		$\text{CPSR} = \infty$	

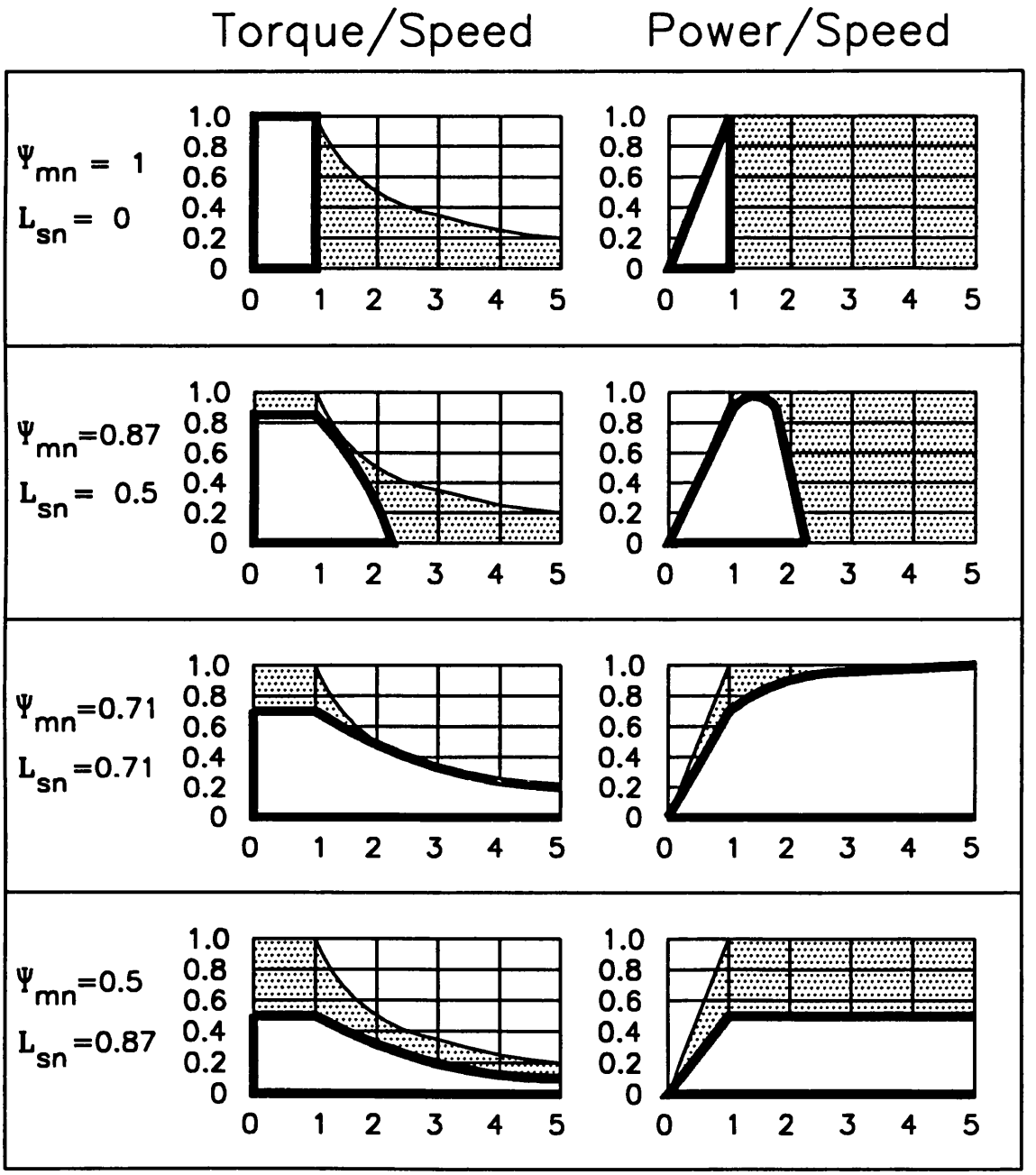

Figure 2.7: *Calculated SPM torque and power characteristics.*

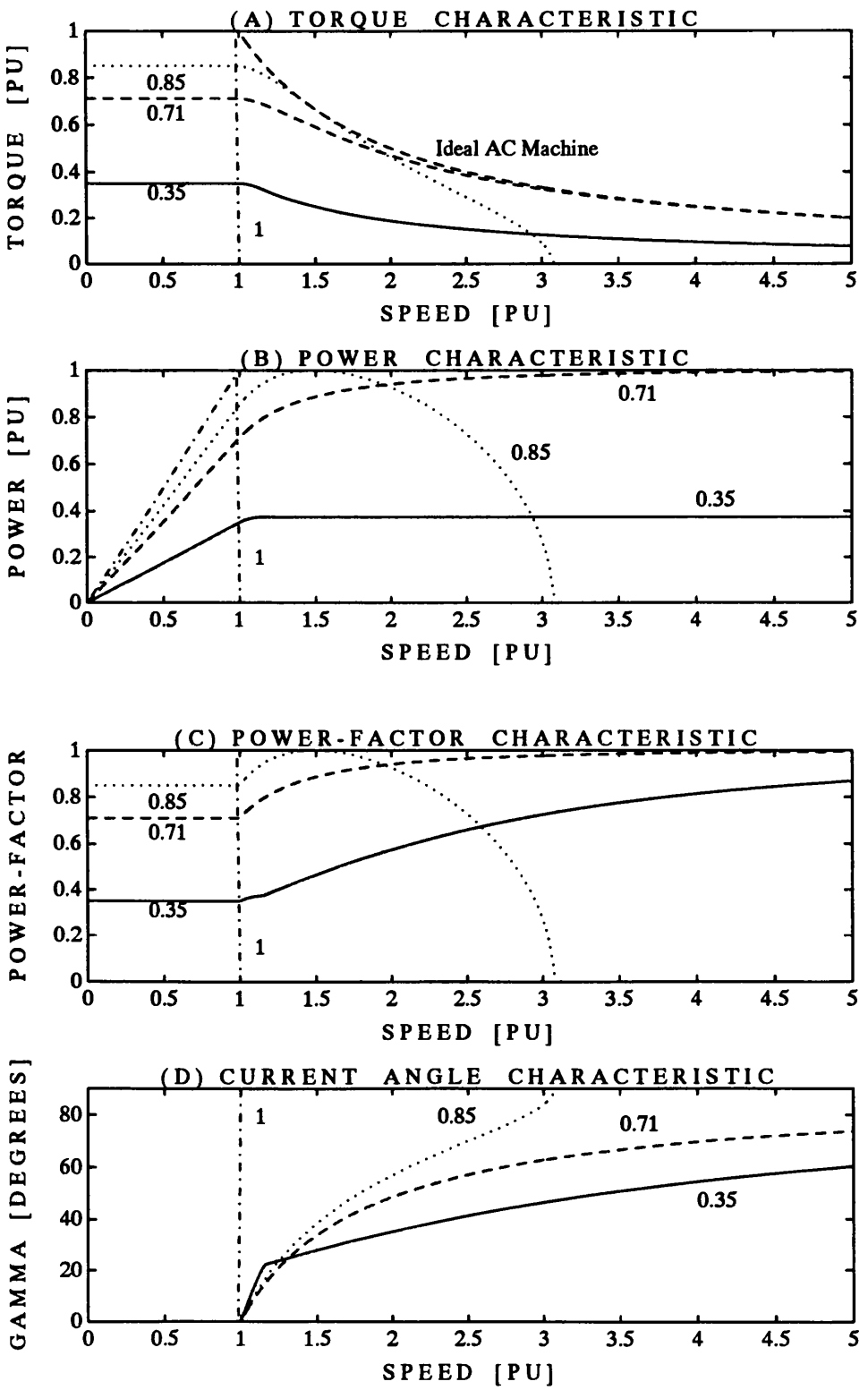

Figure 2.8: *Calculated SPM characteristics with Ψ_{mn} as a parameter.*

improvement in the field-weakening capability. The optimal field-weakening characteristic is obtained when $\Psi_{mn} = 1/\sqrt{2}$ at which point the drive can deliver full output power at infinite speed. Such a design is at the boundary between finite and infinite maximum speed drives. The price paid for this excellent field-weakening performance is an inverter utilisation of $1/\sqrt{2}$.

Increasing the inductance past the optimal point produces an infinite maximum speed motor drive with an exactly constant output power at high speed, however the lower Ψ_{mn} is, the lower the high speed output power. This equals $\Psi_{mn}/\sqrt{1-\Psi_{mn}^2}$.

Fig. 2.8c shows how the power-factor increases at the start of Mode II operation. Unity power-factor is reached at some speed ω_{vn} for finite maximum speed SPM drives and at infinite speed for infinite maximum speed SPM drives. This can be found by using (2.12) to solve $P_n = T_n w_n = 1$ for ω_{vn} giving :

$$\omega_{vn} = \frac{1}{\sqrt{2\Psi_{mn}^2 - 1}} \tag{2.13}$$

Note that this is the square root of the constant-power speed range. Thus the unity power-factor speed is the geometric mean of the rated speed and the maximum constant-power speed.

The current-angle versus speed characteristics in Fig. 2.8d show the monotonic increase in current-angle with speed. Note the abrupt change in slope at the transitions between the operating modes.

It should be noted that the normalisation method used does not give an intuitive picture of the effect of adding inductance to the motor drive. Adding extra inductance will not affect the rated torque but will cause the rated speed to fall. With the unity normalised rated speed method used here, this forces the normalised low-speed torque to drop instead. Thus it would be better to use a normalisation for unity rated torque. However the unity rated speed normalisation is best for the IPM parameter plane (see Sec. 2.5) and so it has been used for the surface permanent magnet motor drive for consistency.

The optimal field-weakening performance is obtained from a surface permanent magnet motor drive when $\Psi_{mn} = 1/\sqrt{2}$. It is clear that it is impossible for the surface

permanent magnet motor drive to ever match the ideal motor drive field-weakening performance as it is unable to maintain unity power-factor over its entire speed range. Common drive designs typically have values of Ψ_{mn} between 0.85 and 0.95. This limits the constant-power speed range to below about 2:1. Wider field-weakening performance can be obtained by adding external inductance to the motor [3]. This is at the cost of extra iron and copper losses in these inductances.

2.3 Synchronous Reluctance Motor Drives

The synchronous reluctance motor (SYNCHREL) does not contain magnets but instead relies on reluctance torque produced by the different inductances in the d- and q-axes. The ratio of these inductances is called the saliency ratio and is an important motor parameter.

A comprehensive analysis of the control of the synchronous reluctance motor drive has been performed by Betz [6]. He used a combined unity rated speed *and* unity rated torque normalisation. This type of normalisation is useful for normal control analysis, however for analysis of the field-weakening performance it is better to use the unity inverter kVA and unity rated speed normalisation. This shows more clearly how well the motor drive is utilising the inverter kVA rating. This type of normalisation was also used for the surface permanent magnet motor drive.

This section analyses the field-weakening characteristics of the synchronous reluctance motor drive using a lossless, steady-state, constant parameter DQ model. The

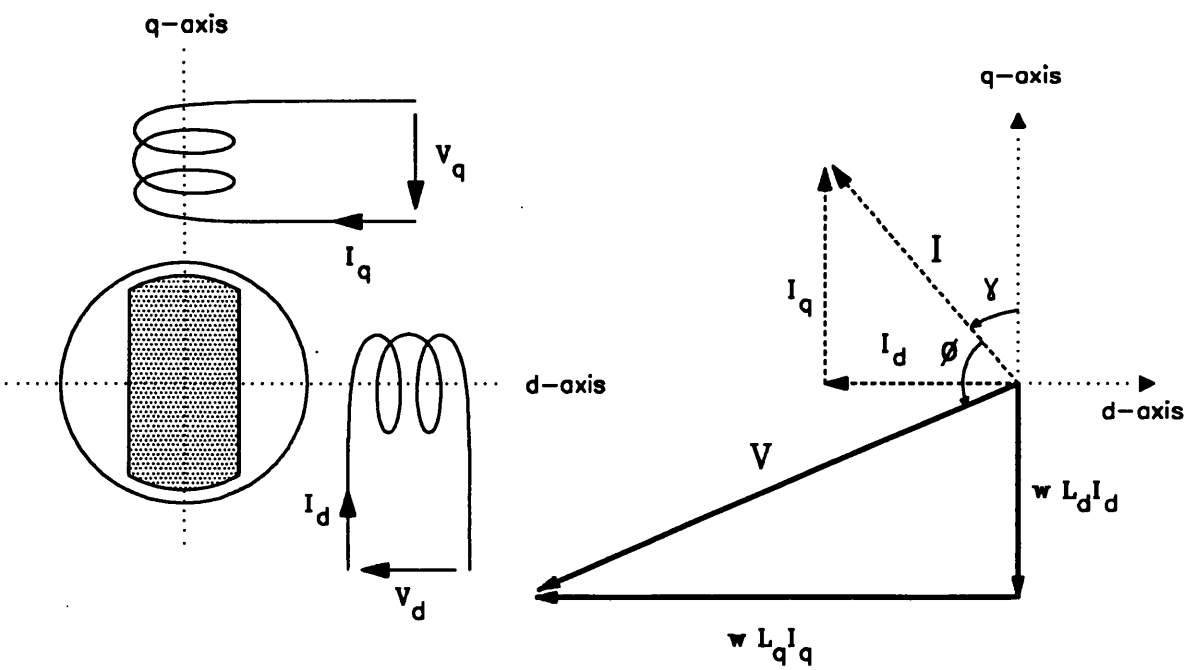

Figure 2.9: *Synchronous reluctance motor phasor diagram.*

q-axis is chosen to be the most inductive axis (see Fig. 2.9). This is opposite to the usual synchronous reluctance motor convention [6] but is normal for interior permanent magnet motor analysis [4, 34].

A synchronous reluctance motor drive can be characterised by its d-axis inductance L_d and q-axis inductance L_q. When the motor drive is normalised for unity rated speed the parameters become dependent and the shape of the torque versus speed characteristic can be described by a single parameter. The saliency ratio $\xi = L_q/L_d$ is chosen as it influences much of the control characteristics of the synchronous reluctance motor drive [6].

2.3.1 Normalised Equations

The conventional per-phase steady-state DQ equations for the synchronous reluctance motor drive can be obtained from the phasor diagram in Fig. 2.9 and the torque expression can be derived using energy conservation from $P = Tw = V_d I_d + V_q I_q$:

$$\left.\begin{aligned} V_d &= -\omega L_q I_q \\ V_q &= \omega L_d I_d \\ T &= -(L_q - L_d) I_d I_q \end{aligned}\right\} \quad \text{where} \quad \begin{aligned} I &= \sqrt{I_d^2 + I_q^2} \leq I_c \\ V &= \sqrt{V_d^2 + V_q^2} \leq V_c \end{aligned} \tag{2.14}$$

Using the same normalisation for base voltage, current and power that was used for the surface permanent magnet motor drive, and replacing L_q with ξL_d yields :

$$\left.\begin{aligned} V_{dn} &= -\omega_n \xi L_{dn} I_{qn} \\ V_{qn} &= \omega_n L_{dn} I_{dn} \\ T_n &= -(\xi - 1) L_{dn} I_{dn} I_{qn} \end{aligned}\right\} \quad \text{where} \quad \begin{aligned} I_n &= \sqrt{I_{dn}^2 + I_{qn}^2} \leq 1 \\ V_n &= \sqrt{V_{dn}^2 + V_{qn}^2} \leq 1 \end{aligned} \tag{2.15}$$

By applying the normalisation for unity rated speed to the voltage equations in (2.15) it can be shown that the two normalised parameters L_{dn} and L_{qn} are dependent. Thus like the surface permanent magnet motor drive, the field-weakening performance of the synchronous reluctance motor drive can be characterised by a single parameter. The saliency ratio is used in preference to either L_{dn} or L_{qn} as it is unchanged by normalisation.

Replacing I_{qn} with $I_n \cos\gamma$ and I_{dn} with $-I_n \sin\gamma$ in (2.15) yields :

$$\left.\begin{aligned} V_{dn} &= -\omega_n \xi L_{dn} I_n \cos\gamma \\ V_{qn} &= -\omega_n L_{dn} I_{dn} \sin\gamma \\ T_n &= \tfrac{1}{2}(\xi - 1) L_{dn} I_n^2 \sin 2\gamma \end{aligned}\right\} \quad \text{where} \quad \begin{aligned} I_n &\leq 1 \\ V_n &= \sqrt{V_{dn}^2 + V_{qn}^2} \leq 1 \end{aligned} \tag{2.16}$$

From this it is clear that maximum torque is obtained with $I_n = 1$ and $\gamma = 45^o$. Inserting this into the voltage equations in (2.16) and solving for $V_n = 1$ at $\omega_n = 1$ yields :

$$L_{dn} = \sqrt{2/(\xi^2 + 1)} \qquad L_{qn} = \xi L_{dn} \tag{2.17}$$

Substituting (2.17) into (2.15) yields :

$$\left.\begin{aligned} V_{dn} &= -\sqrt{\tfrac{2\xi^2}{\xi^2+1}}\omega_n I_n \cos\gamma \\ V_{qn} &= -\sqrt{\tfrac{2}{\xi^2+1}}\omega_n I_n \sin\gamma \\ T_n &= \tfrac{\xi-1}{\sqrt{2(\xi^2+1)}} I_n^2 \sin 2\gamma \end{aligned}\right\} \quad \text{where} \quad \begin{aligned} I_n &\leq 1 \\ V_n &= \sqrt{V_{dn}^2 + V_{qn}^2} \leq 1 \end{aligned} \tag{2.18}$$

2.3.2 SYNCHREL Motor Drive Circle Diagram

The circle diagram can be applied to the synchronous reluctance motor drive to determine the optimal field-weakening strategy in the same way as for the surface permanent magnet motor drive. The current-limit locus is again a circle. The voltage-limit locus can be obtained by applying the voltage constraint $V_{dn}^2 + V_{qn}^2 \leq 1$ to the voltage equations in (2.15) which yields :

$$I_{dn}^2 + (\xi I_{qn})^2 \leq \left(\frac{V_n}{\omega_n L_{dn}}\right)^2 \tag{2.19}$$

This is the equation of an ellipse, centred on the origin whose ellipticity is equal to the saliency ratio (see Fig. 2.10). Note that the infinite speed operating point lies at the origin and hence that synchronous reluctance motor drives have no inherent speed limitation.

From the torque equation in (2.15), the constant torque loci form hyperbolas in the (I_{dn}, I_{qn}) plane with the d- and q-axes as asymptotes.

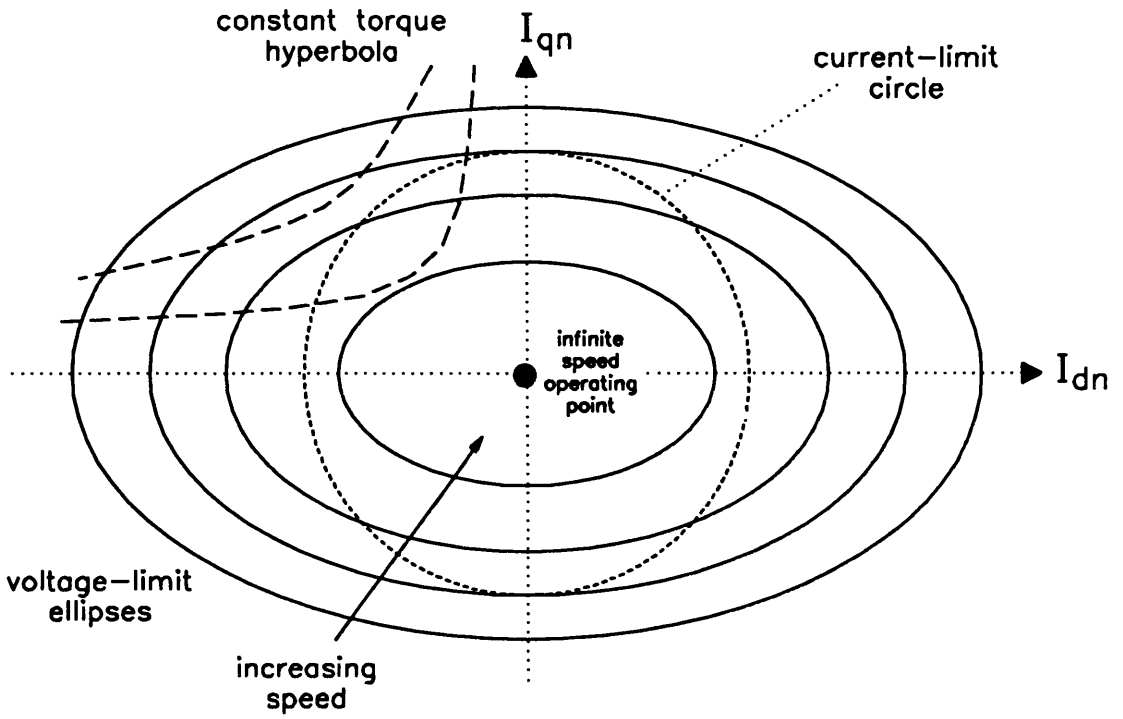

Figure 2.10: *The synchronous reluctance motor drive circle diagram.*

2.3.3 Infinite Maximum Speed SYNCHREL Motor Drives

Due to its infinite maximum speed capability, the synchronous reluctance motor drive shows operation in all three operating modes described in Sec. 2.2.3. This is illustrated in Figs. 2.11 and 2.12. Note that in Fig. 2.11 all feasible 2nd quadrant operating points are shown shaded.

In Mode I, the maximum-torque-per-ampere current-angle γ_m corresponds to the point where the constant torque hyperbola is tangent to the current-limit circle. This occurs with $\gamma = 45°$ in Fig. 2.11a and corresponds to point A in Fig. 2.12.

Above the rated speed the drive enters Mode II operation and the operating point moves along the current-limit circle. This is shown in Fig. 2.11b where the maximum torque is clearly obtained by operating at the intersection of the voltage and current-limit loci. This continues until the torque hyperbola becomes tangent to the voltage-limit ellipse at point B in Fig. 2.12 at ω_t. This is the transition speed to Mode III

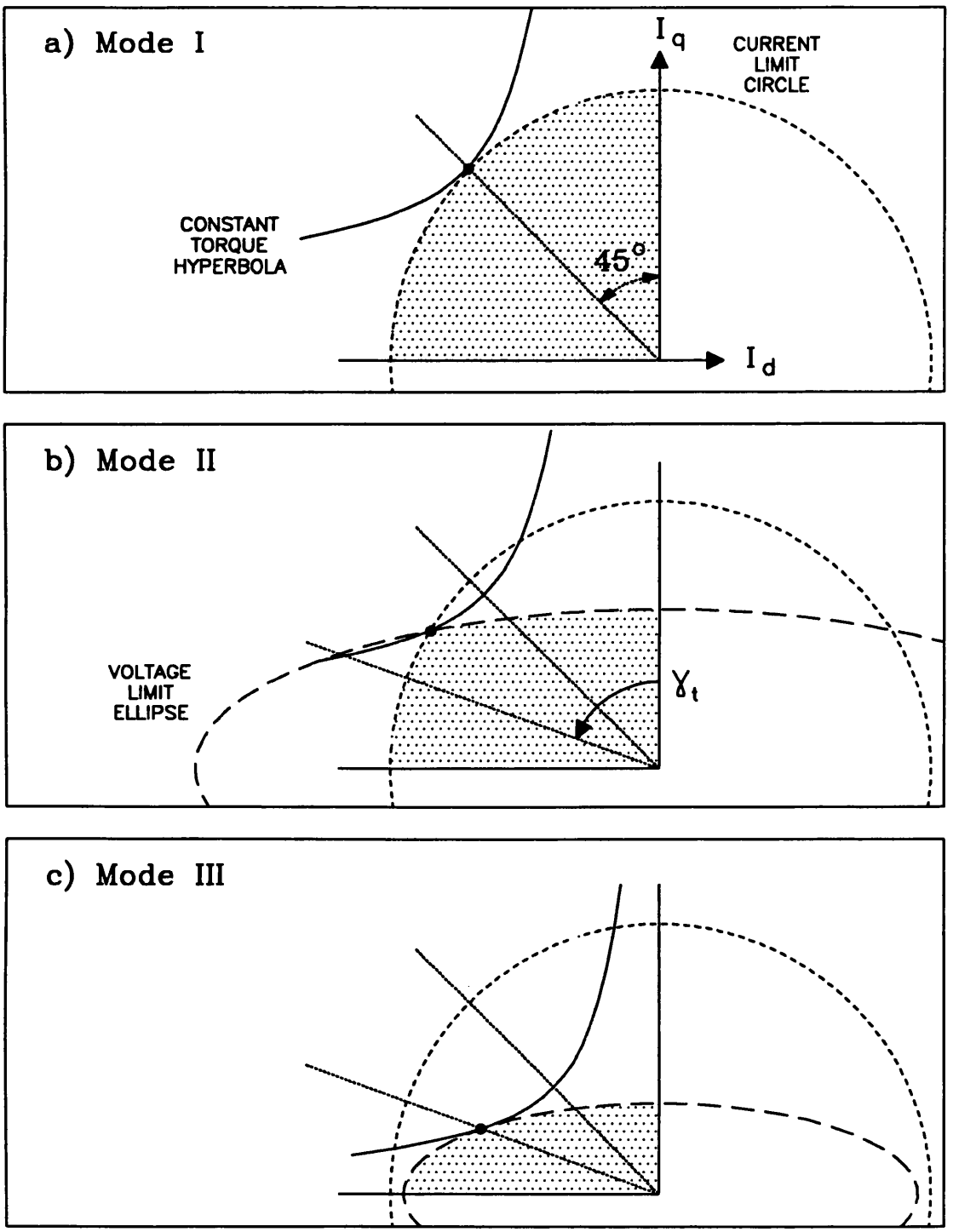

Figure 2.11: *SYNCHREL Mode I, II and III operation.*

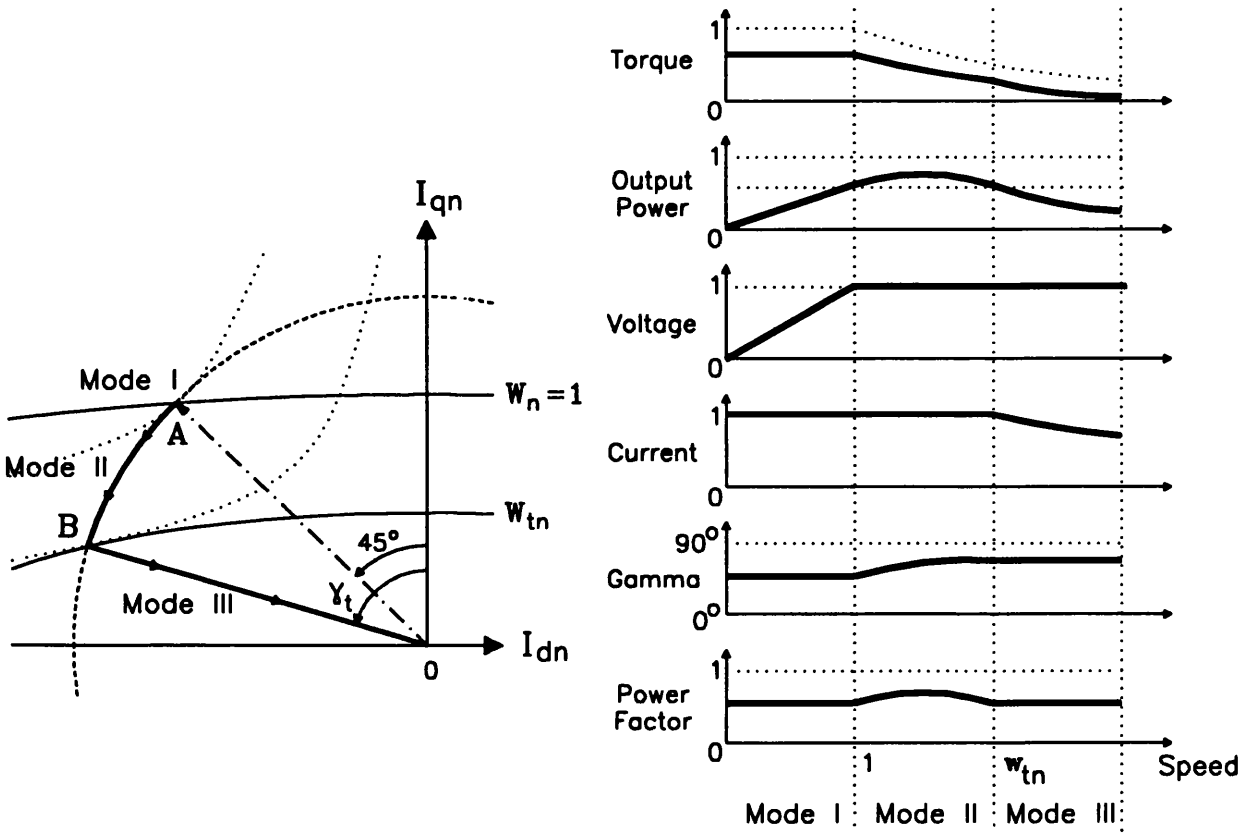

Figure 2.12: *Maximum torque operation of the synchronous reluctance motor drive.*

operation. From the operating equations it can be shown that the constant-power speed ω_p corresponds to the Mode III transition speed ω_t (see Fig. 2.12). Thus the constant-power speed range is equal to the the speed range in which the drive is in Mode II.

In Mode III, maximum output power is obtained by operating at a fixed current-angle γ_t with the maximum current possible, restricted by the voltage-limit constraint. The output power in this region falls inversely with speed. Thus the output power at very high speeds is small.

2.3.4 Calculated Characteristics

From the optimal torque trajectory derived above, the performance characteristics of the synchronous reluctance motor drive can be calculated using (2.18). The resulting equations are given in Table 2.2. From the Mode II power-factor expression it can be shown that the maximum power-factor is :

$$\cos\phi = \frac{\xi - 1}{\xi + 1} \tag{2.20}$$

which is achieved when $\gamma = \arctan\sqrt{\xi}$.

The equations in Table 2.2 are illustrated graphically in Figs. 2.13 and 2.14 which shows the normalised torque, power, power-factor and current-angle versus speed curves for synchronous reluctance motor drives with saliencies of 2, 4, 8 and 1000 (infinity). For comparison the saliency ratio of synchronous reluctance motors lie roughly in the range 2 to 4 for single-barrier designs and 6 to 20 for axially-laminated designs.

The performance of synchronous reluctance motor drives improve monotonically with increasing saliency. This is clearly shown from Fig. 2.13. For high values of ξ, the constant-power speed range is approximately equal to $\xi/2$ [6]. For instance from Fig. 2.13 the constant-power speed range of a synchronous reluctance motor drive with a saliency ratio of 8 is ideally about 4. Clearly the best field-weakening performance is obtained with an infinite saliency ratio. Note that like all pure reluctance machines, the synchronous reluctance motor drive features a natural inverse power versus speed characteristic in Mode III operation with fixed current-angles (cf. switched-reluctance motor drives).

Using the equations in Tables 2.1 and 2.2 it can be shown that the optimal field-weakening surface permanent magnet motor drive characteristic (with $\Psi_{mn} = 1/\sqrt{2}$) and the optimal synchronous reluctance characteristic (with $\xi = \infty$) have *exactly* the same torque (and hence power) versus speed characteristic :

$$T_n = \begin{cases} \dfrac{1}{\sqrt{2}} & 0 \leq w_n \leq 1 \\ \dfrac{1}{\omega_n}\sqrt{1 - \dfrac{1}{2\omega_n^2}} & w_n \geq 1 \end{cases} \tag{2.21}$$

Table 2.2: *Summary of the characteristics of the synchronous reluctance motor drive under maximum torque operation.*

Parameter	Mode I	Mode II	Mode III
Speed	$\omega_n \leq 1$	$1 \leq \omega_n \leq \frac{\xi^2+1}{2\xi}$	$\omega_n \geq \frac{\xi^2+1}{2\xi}$
Current Angle	$\gamma = 45^\circ$	$45^\circ \leq \gamma \leq \arctan \xi$	$\gamma = \arctan \xi$
		$\cos\gamma = \sqrt{\frac{\xi^2+1-2\omega_n^2}{(\xi^2-1)2\omega_n^2}}$	
Voltage	$V_n = \omega_n$	$V_n = 1$	$V_n = 1$
Current	$I_n = 1$	$I_n = 1$	$I_n = \frac{\xi^2+1}{2\xi}\frac{1}{\omega_n}$
Torque	$T_n = \frac{1}{\sqrt{2}}\frac{\xi-1}{\sqrt{\xi^2+1}}$	$T_n = \sqrt{\frac{(\xi-1)^2}{2(\xi^2+1)}}\sin 2\gamma$	$T_n = \frac{\xi-1}{2\sqrt{2}}\sqrt{\frac{\xi^2+1}{\xi^2}}\frac{1}{\omega_n^2}$
Power	$P_n = T_n\omega_n$	$P_n = \cos\phi$	$P_n = T_n\omega_n$
PF	$\cos\phi = \frac{1}{\sqrt{2}}\frac{\xi-1}{\sqrt{\xi^2+1}}$	$\cos\phi = \frac{\xi-1}{\sqrt{2}}\sqrt{\frac{\sin 2\gamma}{\tan\gamma+\xi^2\cot\gamma}}$	$\cos\phi = \frac{1}{\sqrt{2}}\frac{\xi-1}{\sqrt{\xi^2+1}}$
CPSR		$\text{CPSR} = \frac{\xi^2+1}{2\xi}$	

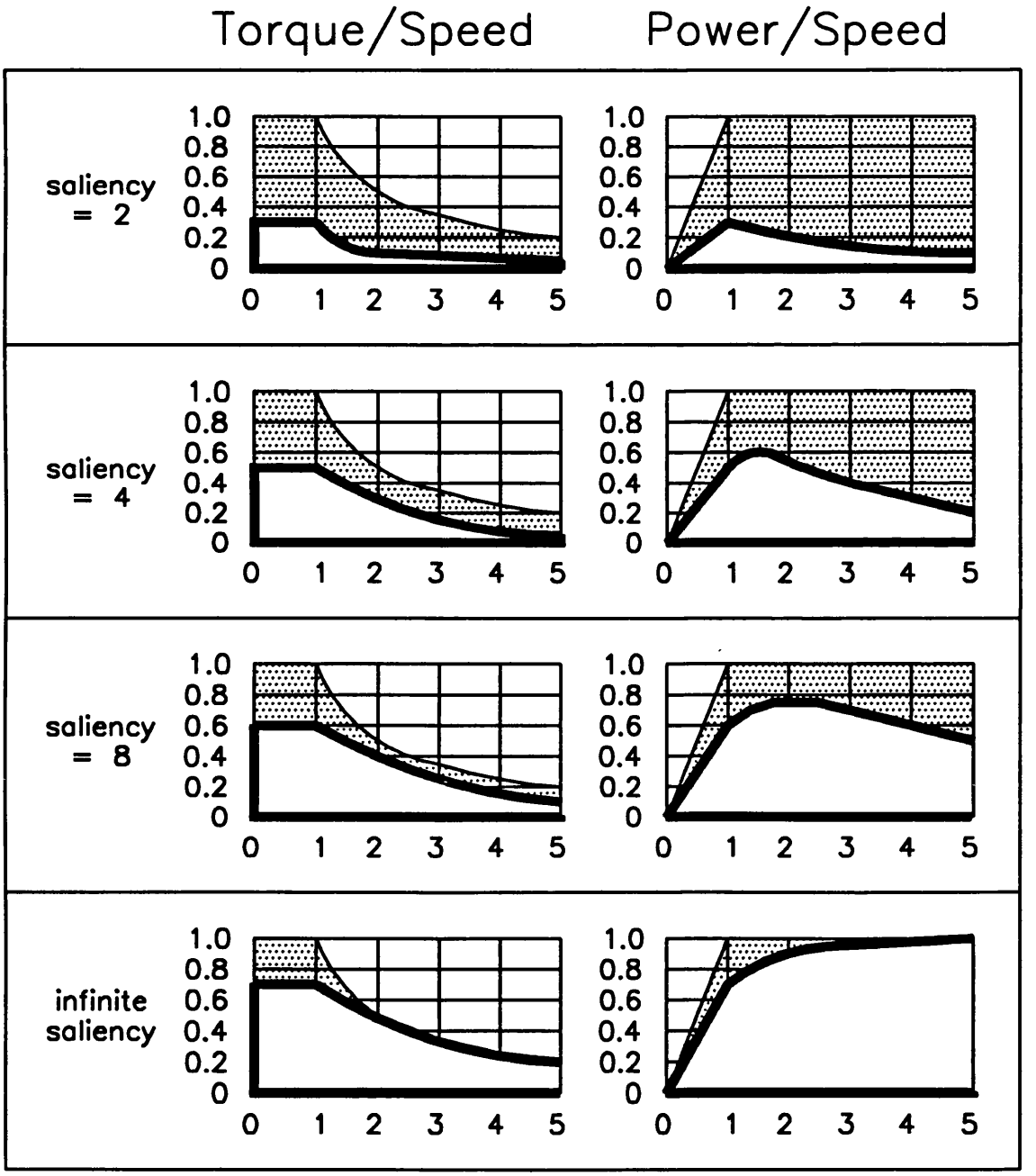

Figure 2.13: *SYNCHREL torque and power characteristics.*

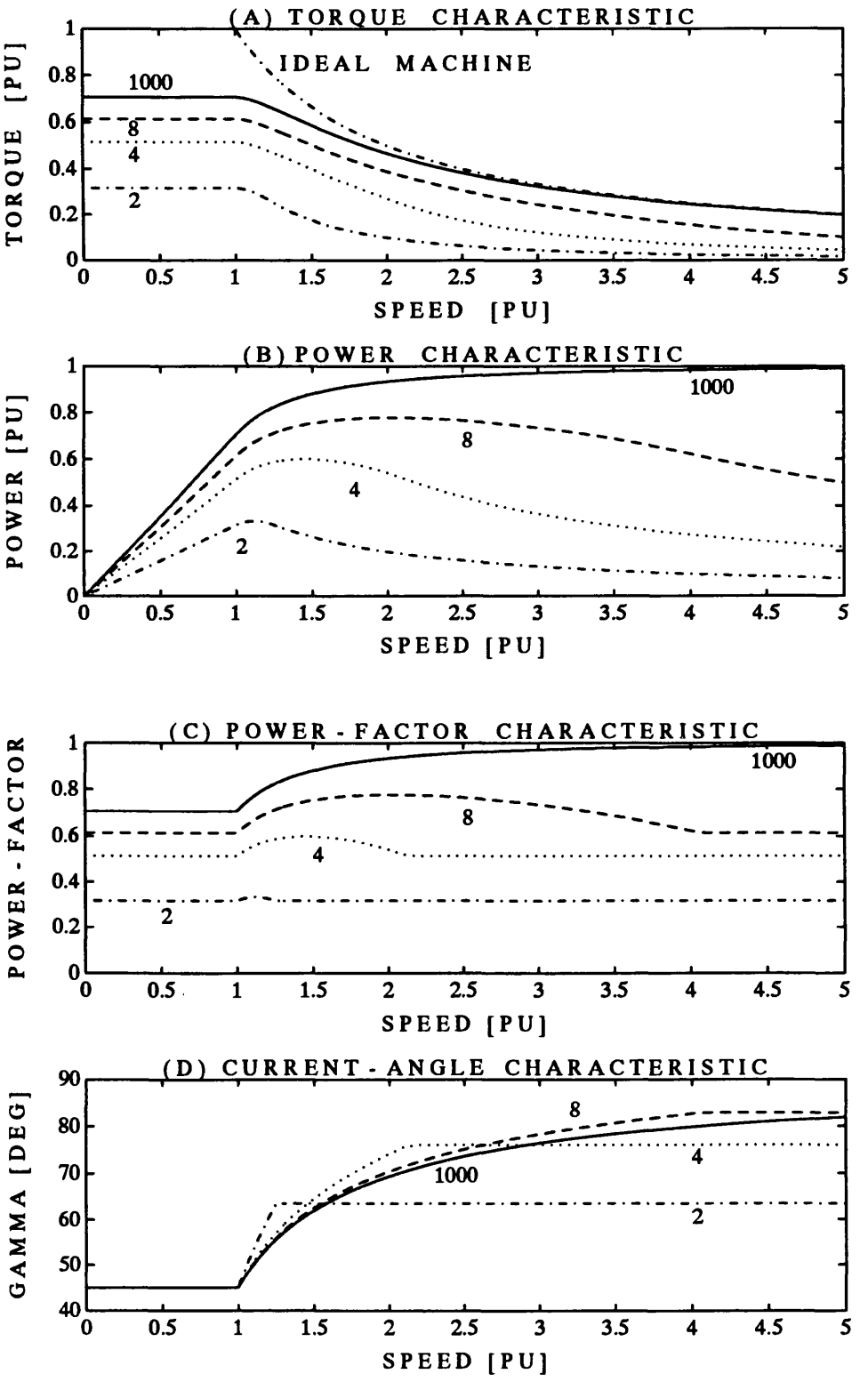

Figure 2.14: *Calculated synchronous reluctance motor drive characteristics.*

This is a rather surprising new result considering the completely different torque production mechanisms in the two motor drives. It illustrates an interesting *duality* between the surface permanent magnet motor drive and the synchronous reluctance motor drive which is reflected in the performance of the interior permanent magnet motor drive as will be seen later. It also gives some hint that this may be a fundamental limitation of interior permanent magnet motor drives and also perhaps of all brushless AC motor drives.

2.4 Interior Permanent Magnet Motor Drives

After examining the surface permanent magnet motor drive and the synchronous reluctance motor drive we are now ready to analyse the interior permanent magnet motor drive. As was pointed out by Jahns [22], this is really a hybrid of a permanent magnet motor and a reluctance motor. The main difficulty in its analysis is that it has two independent parameters instead of the one for the surface permanent magnet and synchronous reluctance motor drive.

2.4.1 Normalised Equations

The conventional per-phase steady-state voltage and torque DQ equations for the interior permanent magnet motor drive can be obtained from the phasor diagram in Fig. 2.15. Note that the torque equation is simply a combination of the surface per-

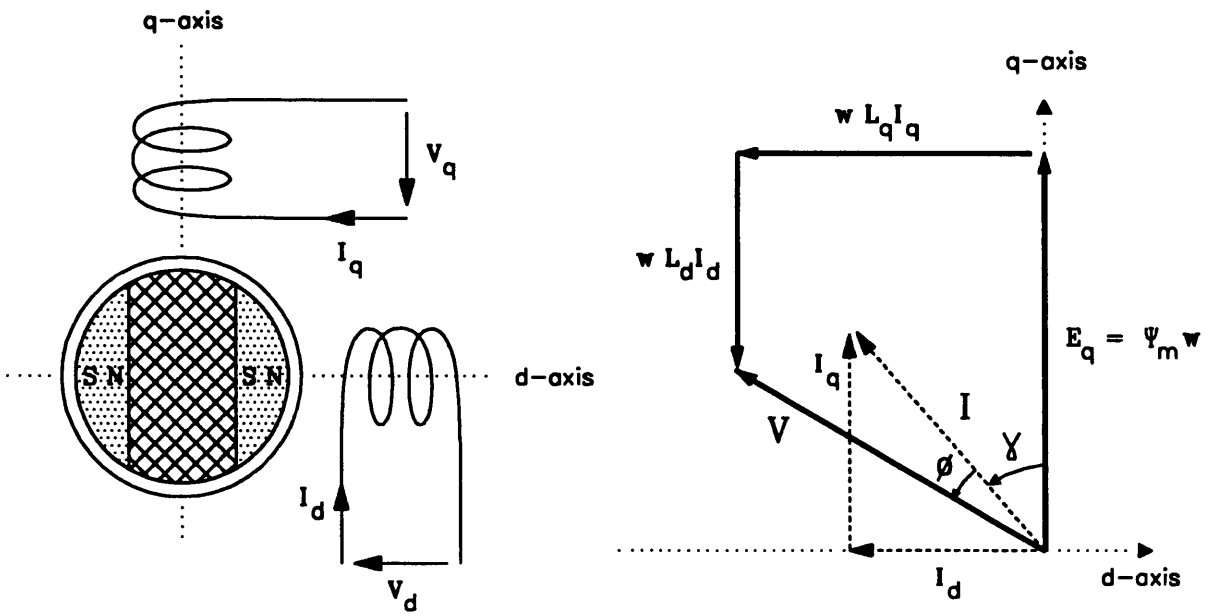

Figure 2.15: *The IPM phasor diagram.*

manent magnet (2.2) and synchronous reluctance (2.14) equations :

$$\left.\begin{aligned} V_d &= -wL_qI_q \\ V_q &= wL_dI_d + w\Psi_m \\ T &= \Psi_m I_q - (L_q - L_d)I_dI_q \end{aligned}\right\} \quad \text{where} \quad \begin{aligned} I &= \sqrt{I_d^2 + I_q^2} \leq I_c \\ V &= \sqrt{V_d^2 + V_q^2} \leq V_c \end{aligned} \tag{2.22}$$

Using the definition of $\xi = L_q/L_d$ yields :

$$\left.\begin{aligned} V_d &= -w\xi L_dI_q \\ V_q &= wL_dI_d + w\Psi_m \\ T &= \Psi_m I_q - (\xi - 1)L_dI_dI_q \end{aligned}\right\} \quad \text{where} \quad \begin{aligned} I &= \sqrt{I_d^2 + I_q^2} \leq I_c \\ V &= \sqrt{V_d^2 + V_q^2} \leq V_c \end{aligned} \tag{2.23}$$

From the phasor diagram, $I_d = -I\sin\gamma$ and $I_q = I\cos\gamma$. Thus :

$$\left.\begin{aligned} V_d &= -w\xi L_dI\cos\gamma \\ V_q &= -wL_dI\sin\gamma + w\Psi_m \\ T &= \Psi_m I\cos\gamma + \tfrac{1}{2}(\xi - 1)L_dI^2\sin 2\gamma \end{aligned}\right\} \quad \text{where} \quad \begin{aligned} I &\leq I_c \\ V &= \sqrt{V_d^2 + V_q^2} \leq V_c \end{aligned} \tag{2.24}$$

Applying the base voltage, current and power normalisation described in Sec. 2.2.1 to (2.23) and (2.24) yields :

$$\left.\begin{aligned} V_{dn} &= -w_n\xi L_{dn}I_{qn} \\ V_{qn} &= w_nL_{dn}I_{dn} + w_n\Psi_{mn} \\ T_n &= \Psi_{mn}I_{qn} - (\xi - 1)\,L_{dn}I_{dn}I_{qn} \end{aligned}\right\} \quad \text{where} \quad \begin{aligned} I_n &= \sqrt{I_{dn}^2 + I_{qn}^2} \leq 1 \\ V_n &= \sqrt{V_{dn}^2 + V_{qn}^2} \leq 1 \end{aligned} \tag{2.25}$$

$$\left.\begin{aligned} V_{dn} &= -w_n\xi L_{dn}I_n\cos\gamma \\ V_{qn} &= -w_nL_{dn}I_n\sin\gamma + w_n\Psi_{mn} \\ T_n &= \Psi_{mn}I_n\cos\gamma + \tfrac{1}{2}(\xi - 1)L_{dn}I_n^2\sin 2\gamma \end{aligned}\right\} \quad \text{where} \quad \begin{aligned} I_n &\leq 1 \\ V_n &= \sqrt{V_{dn}^2 + V_{qn}^2} \leq 1 \end{aligned} \tag{2.26}$$

These normalised equations have three parameters : Ψ_{mn}, ξ and L_{dn}. This can be reduced to two independent parameters by normalising the rated speed to unity. In order to do this it is necessary to calculate the maximum-torque-per-ampere current-angle. This is found by differentiating the torque equation in (2.26) with respect to γ

giving :

$$\sin\gamma_m = \begin{cases} 0 & \xi = 1 \\ \dfrac{-\Psi_{mn} + \sqrt{\Psi_{mn}^2 + 8(\xi-1)^2 L_{dn}^2}}{4(\xi-1)L_{dn}} & \xi \neq 1 \end{cases} \tag{2.27}$$

During Mode II operation, the speed ω_n as a function of γ at rated voltage ($V_n = 1$) and rated current ($I_n = 1$) is obtained from the voltage equations in (2.26) giving :

$$\omega_n = \frac{1}{\sqrt{(\xi L_{dn}\cos\gamma)^2 + (-L_{dn}\sin\gamma + \Psi_{mn})^2}} \tag{2.28}$$

From the torque equation in (2.26) this gives the output power in Mode II as :

$$P_n = T_n w_n = \frac{\Psi_{mn}\cos\gamma + \frac{1}{2}(\xi-1)L_{dn}\sin 2\gamma}{\sqrt{(\xi L_{dn}\cos\gamma)^2 + (-L_{dn}\sin\gamma + \Psi_{mn})^2}} \tag{2.29}$$

From the above normalisation, when $\gamma = \gamma_m$ in (2.28) then $w_n = 1$. This means ξ, Ψ_{mn} and L_{dn} must be dependent and thus there are only two independent parameters. The selection of the two interior permanent magnet motor drive parameters is important and is discussed in detail in Sec. 2.5.

2.4.2 IPM Motor Drive Circle Diagram

The voltage-limit constraint is obtained by setting $V_{dn}^2 + V_{qn}^2 \leq 1$ in (2.25). This yields :

$$\left(I_{dn} + \frac{\Psi_{mn}}{L_{dn}}\right)^2 + \xi^2 I_{qn}^2 \leq \left(\frac{1}{\omega_n L_{dn}}\right)^2 \tag{2.30}$$

which is an ellipse centred at $(-\Psi_{mn}/L_{dn}, 0)$ whose size is inversely proportional to speed (see Fig. 2.16). This is a combination of the surface permanent magnet motor drive's "offset" voltage-limit circle and the synchronous reluctance motor drive's voltage-limit ellipse. Thus not only is the interior permanent magnet motor drive a hybrid of the surface permanent magnet and synchronous reluctance motor drives in terms of torque, but also in terms of the voltage-limit constraint.

The constant torque locus is obtained from the torque equation in (2.25) as :

$$I_{qn} = \frac{T_n}{\Psi_{mn} - (\xi-1)L_{dn}I_{dn}} \tag{2.31}$$

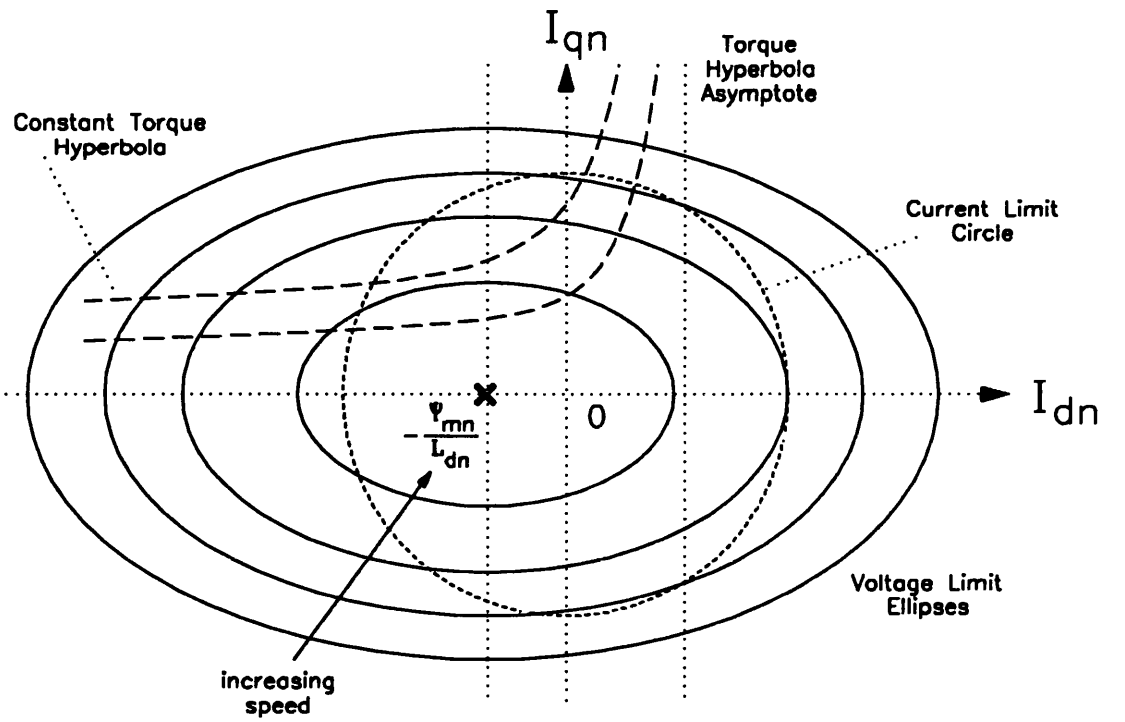

Figure 2.16: *The IPM circle diagram.*

which is a hyperbola whose asymptotes are the lines $I_{qn} = 0$ and the line $I_{dn} = \Psi_{mn}/(\xi - 1)L_{dn}$.

In a similar fashion to the surface permanent magnet motor drive, the finite maximum speed IPM drive has an infinite speed operating point outside the current-limit circle while the infinite maximum speed IPM drive has it within the current-limit circle.

2.4.3 Finite Maximum Speed IPM Motor Drives

The finite maximum speed IPM drive has a similar optimal control strategy and performance to the finite maximum speed SPM drive as shown by Figs. 2.17 and 2.18. It shows operation in Modes I and II. In Mode I the maximum-torque-per-ampere current-angle lies between 0° and 45°. This is represented by point A in Fig. 2.18 and corresponds to the point where the torque hyperbola is tangent to the current-limit circle.

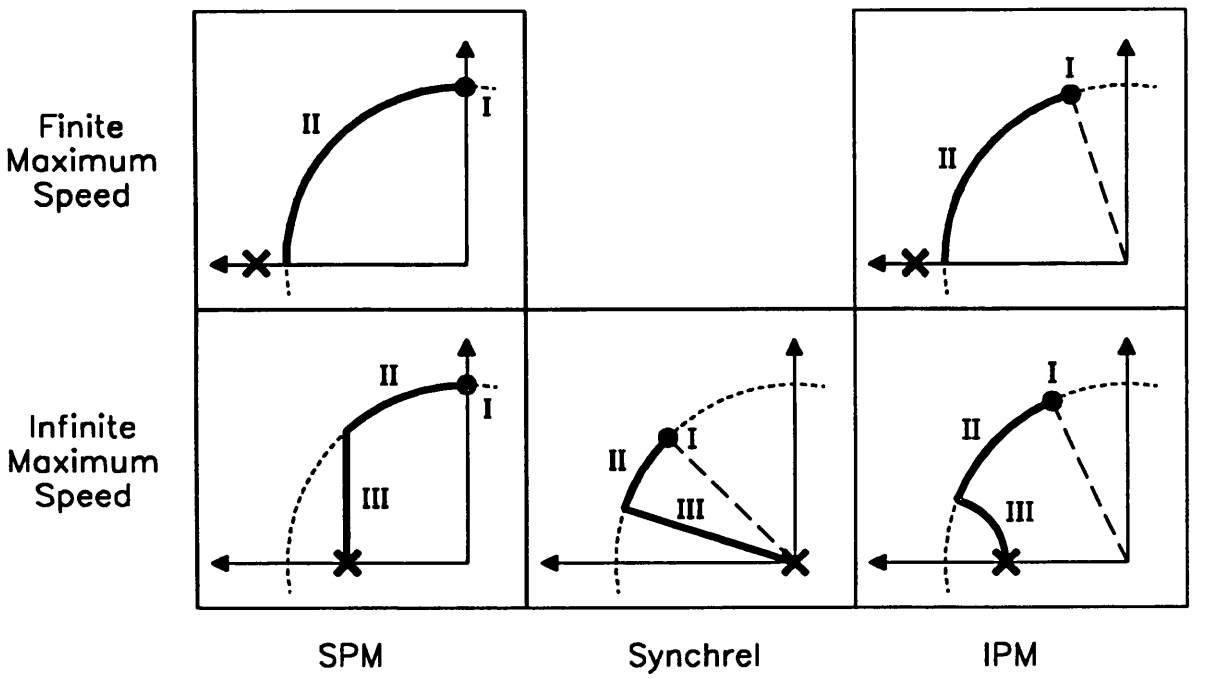

Figure 2.17: *The optimal control strategies for the five drive classes.*

It has been shown by Adnanes [5] that *for a given maximum normalised operating speed* ω_{xn}, the shape of the normalised finite maximum speed IPM drive torque versus speed characteristic is nearly identical to that of the corresponding finite maximum speed SPM drive.

2.4.4 Infinite Maximum Speed IPM Motor Drives

The hybrid nature of the interior permanent magnet motor drive is again clear from the optimal control strategy shown in Figs. 2.17 and 2.19. The control of the infinite maximum speed IPM drive is a cross between that of the infinite maximum speed SPM drive and the infinite maximum speed SYNCHREL drive. The main difference is that the Mode III trajectory is no longer a straight line in the circle diagram, but a curve representing the locus of the tangent between the constant torque hyperbola and the voltage-limit ellipse.

This yields similar torque versus speed characteristics to the infinite maximum speed

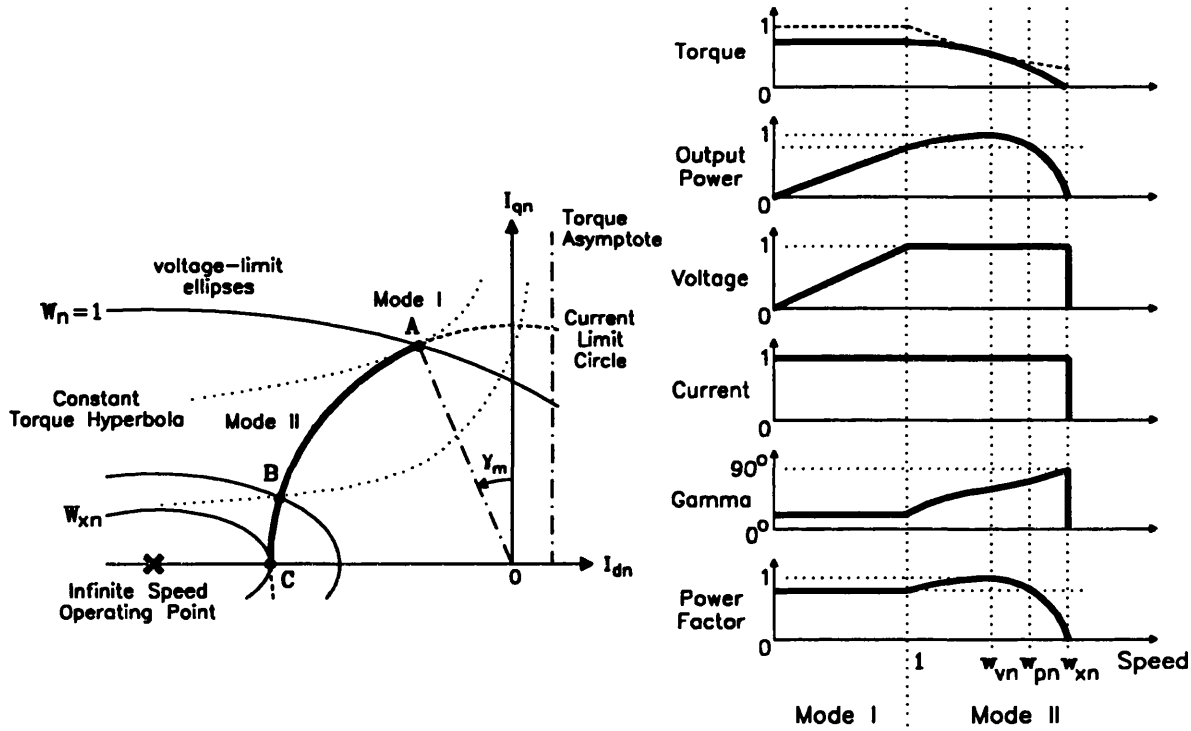

Figure 2.18: *The finite maximum speed IPM operating trajectory.*

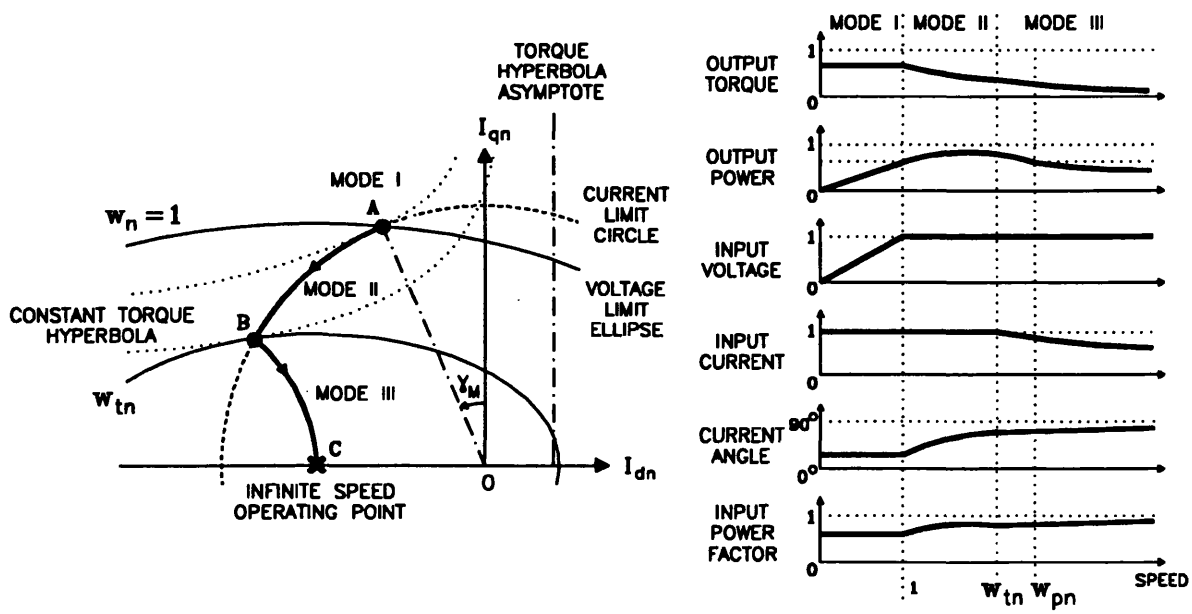

Figure 2.19: *The infinite maximum speed IPM operating trajectory.*

SPM drive. The main differences are that the output power in Mode III is no longer constant at Ψ_{mn}/L_{dn} but instead overshoots it during Mode I or II and then asymptotes towards it in Mode III. In general the constant-power speed ω_p occurs during Mode III operation instead of during Mode II operation as for the finite maximum speed IPM drive.

The Mode III (voltage-limited) trajectory is found by substituting the voltage-limit constraint ($V_{dn}^2 + V_{qn}^2 = 1$) into the torque equation in (2.25) and differentiating and equating to zero [34]. This yields the following expressions :

$$\left.\begin{aligned} I_{dn} &= -\frac{\Psi_{mn}}{L_{dn}} - \Delta I_{dn} \\ I_{qn} &= \frac{\sqrt{1/w_n^2 - (L_{dn}\Delta I_{dn})^2}}{\xi L_{dn}} \end{aligned}\right\} \quad \text{where} \quad \Delta I_{dn} = \frac{-\xi\Psi_{mn} + \sqrt{(\xi\Psi_{mn})^2 + 8(\xi-1)^2/w_n^2}}{4(\xi-1)L_{dn}} \tag{2.32}$$

2.5 IPM Parameter Plane

This section describes the new concept of the IPM parameter plane which allows the effect of parameter changes on all five drive classes to be examined using a single diagram.

The *shapes* of the surface permanent magnet and synchronous reluctance motor drive torque versus speed characteristics were both defined by a *single* parameter. It was thus straightforward to show how the shape of the field-weakening characteristic was affected by this parameter. On the other hand, the shape of the interior permanent magnet motor drive torque versus speed characteristic is defined by *two* parameters. This makes it difficult both to illustrate and to obtain a clear understanding of how changes in these parameters affect the drive's operating characteristic.

The IPM parameter plane is a new graphical technique which is based on contour plots. The two independent parameters are used as axes. The choice of these parameters is arbitrary but they should be as independent of each other and as physically meaningful as possible. One parameter should represent the interior permanent magnet motor drive's permanent magnet nature and the other its reluctance nature. A good choice is the parameters used earlier to characterise the surface permanent magnet and the synchronous reluctance motor drive, that is the normalised magnet flux-linkage Ψ_{mn} and the saliency ratio ξ. Note that the normalised magnet flux-linkage is equal to the ratio of the magnet-induced open-circuit back-emf voltage to the rated voltage at rated speed.

Fig. 2.20 shows the IPM parameter plane and the location of some common motor drive types. The dotted regions represent steel and the solid areas represent permanent magnets. All pure surface permanent magnet motor drive designs have $\xi = 1$ and lie on the x-axis while pure synchronous reluctance motor drive designs have $\Psi_{mn} = 0$ and lie on the y-axis. Single-barrier designs generally have saliencies in the range 2 to 4 while multiple-barrier designs (usually axially-laminated) have saliencies in the range 6 to 20.

The IPM parameter plane extends to infinite saliency ratios, however all the plots

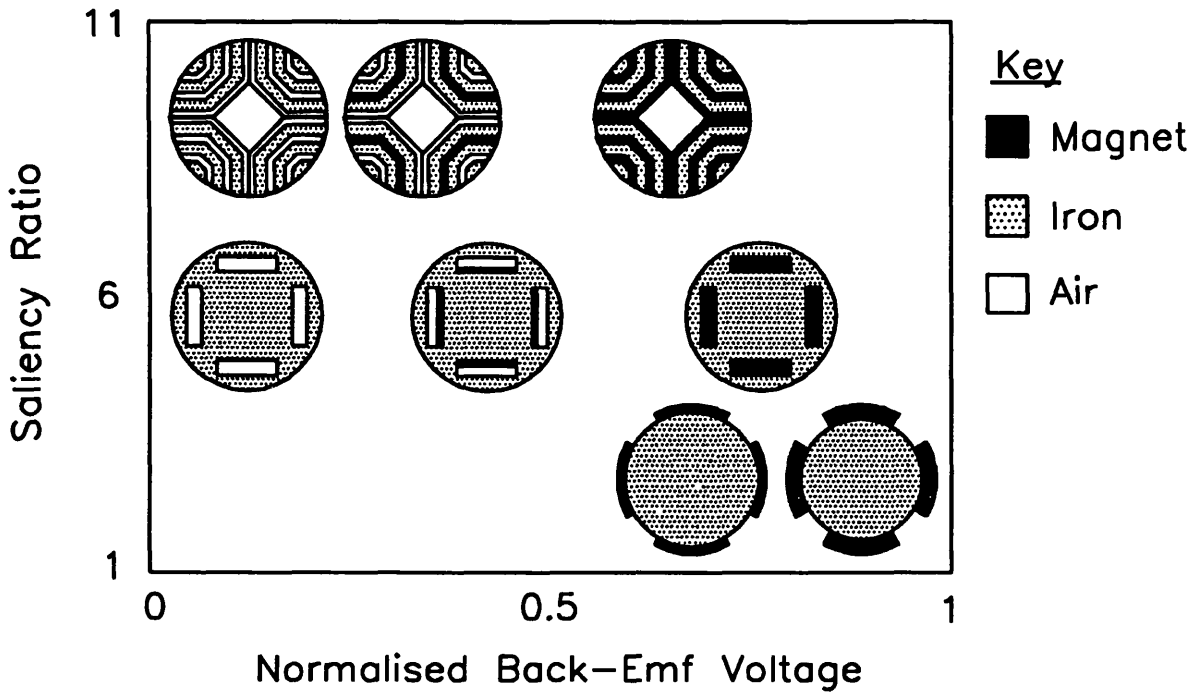

Figure 2.20: *The IPM parameter plane.*

shown in this section only cover $\xi \leq 11$ as most motor drive designs have saliencies in this range. A notable exception to this is a two-pole axially-laminated design described by Boldea [36] which had an saturated saliency ratio of about 14.

Fig. 2.20 also shows how adding permanent magnet material or improving its grade, increases the normalised magnet flux-linkage while not affecting the saliency ratio. As each point on the IPM parameter plane corresponds to a particular shape of torque versus speed characteristic, thus the performance of an interior permanent magnet motor drive can be "tailored" to some extent by adding or removing permanent magnet material.

Fig. 2.21 shows how the *normalised* torque and power versus speed characteristics vary with the location of the design on the IPM parameter plane (the equations are derived later). The dashed line represents the ideal motor drive field-weakening characteristic. It shows how the performance of synchronous reluctance motor drives (y-axis) improves monotonically with saliency. It also shows the ideal constant-power

characteristic of infinite maximum speed SPM drives (x-axis, $\Psi_{mn} \leq 0.7$).

Designs which have zero inductance have $\Psi_{mn} = 1$ and no field-weakening capability. As the motor inductance is increased, Ψ_{mn} will decrease until it is zero for pure synchronous reluctance motor drives. Ψ_{mn} also gives some idea of how much torque is produced by alignment (magnet) torque. In general, the further the design is to the right of the IPM parameter plane, the greater its permanent magnet nature while the closer it is to the left, the greater its reluctance nature.

Fig. 2.21 also shows that the boundary between finite and infinite maximum speed drives runs roughly diagonally from the top left to the bottom right of the IPM parameter plane. Designs which lie on this boundary appear to have excellent field-weakening characteristics. In order to investigate this phenomenum more closely it is useful to use contour plots of important field-weakening performance parameters such as the constant-power speed range. The remainder of this section discusses the calculation of the IPM parameter plane plots and evaluates the results obtained.

2.5.1 Calculation of IPM Parameter Plane Plots

In order to produce contour plots of the field-weakening performance characteristics of the interior permanent magnet motor drive it is necessary to calculate expressions for these in terms of the two independent parameters Ψ_{mn} and ξ. The first step is to calculate the third IPM parameter L_{dn} as a function of ξ and Ψ_{mn}. This is obtained by substituting (2.27) into (2.28) and solving for unity normalised rated speed giving :

$$\begin{aligned} 0 &= L_{dn}^4 \left[(\xi - 1)(\xi^2 + 1)^2\right] \\ &+ L_{dn}^2 \left[(3\xi^3 + \xi^2 - 4\xi + 2)\Psi_{mn}^2 - 4(\xi - 1)(\xi^2 + 1)\right] \\ &+ \left[(3\xi - 1)\Psi_{mn}^4 - (7\xi - 5)\Psi_{mn}^2 + 4(\xi - 1)\right] \end{aligned} \tag{2.33}$$

This has two positive real roots and substitution back into the original equations is required to determine the correct one.

Once L_{dn} has been calculated, the maximum-torque-per-ampere current-angle can be determined from (2.27). The normalised rated output power P_{kn} can be obtained

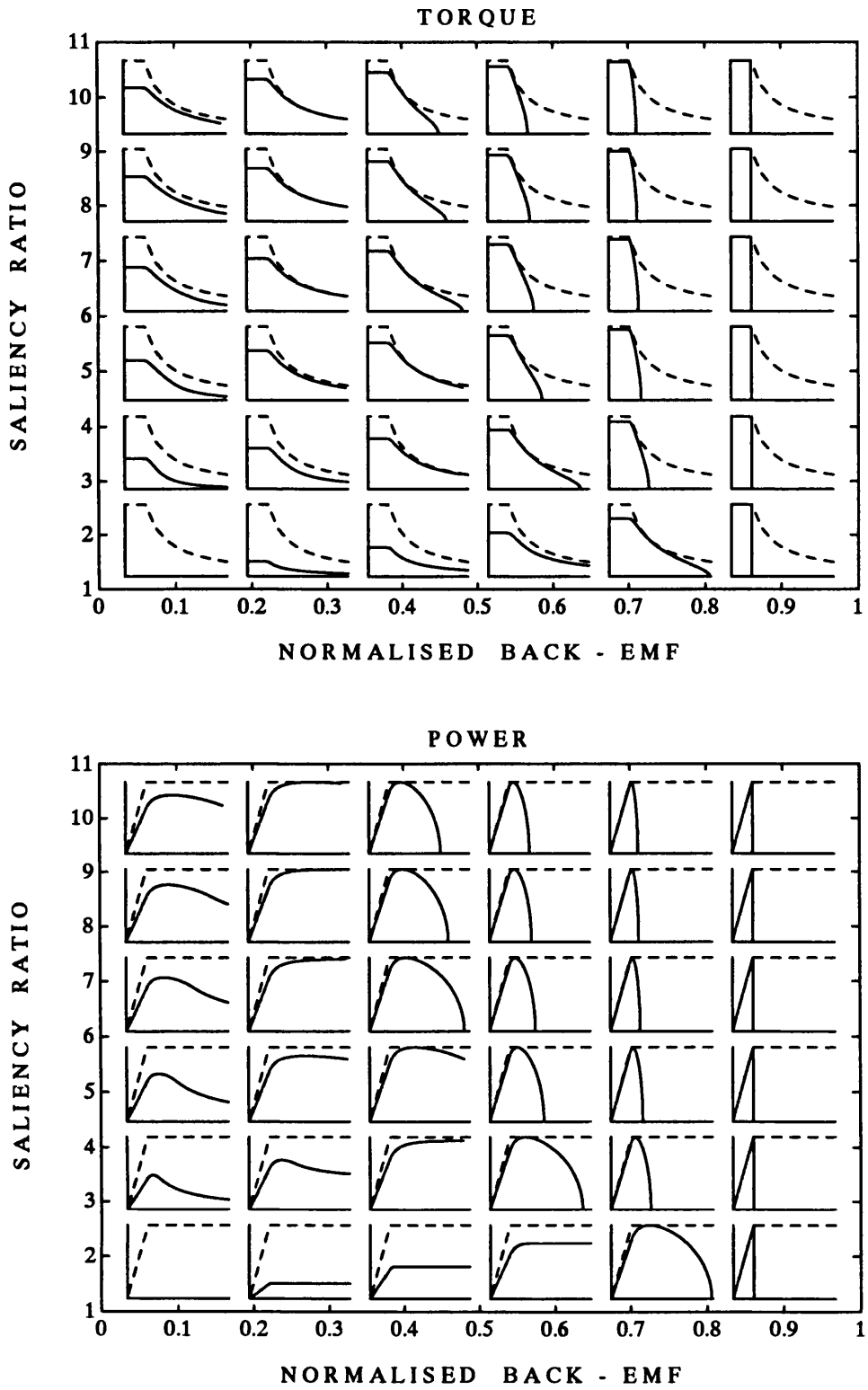

Figure 2.21: *Normalised torque and power versus speed characteristics.*

from (2.29) with $\gamma = \gamma_m$:

$$P_{kn} = \Psi_{mn} \cos\gamma_m + \frac{1}{2}(\xi - 1) L_{dn} \sin 2\gamma_m \tag{2.34}$$

The inverter utilisation κ is the ratio of the rated output power to the inverter kVA rating (see Sec. 1.1). This is equal to the normalised rated output power P_{kn}.

The normalised maximum operating speed ω_{xn} for finite maximum speed IPM drives is obtained by substituting $\gamma = 90^\circ$ into (2.28) :

$$\omega_{xn} = \frac{1}{\Psi_{mn} - L_{dn}} \qquad \text{where} \qquad \Psi_{mn} \geq L_{dn} \tag{2.35}$$

As the speed approaches infinity for an infinite maximum speed IPM drive, from (2.32) I_{dn} approaches $-\Psi_{mn}/L_{dn}$ and I_{qn} approaches $1/(\xi L_{dn} w_n)$. Substituting this into the torque equation in (2.25) yields the following expression for the normalised asymptotic output power at high speed P_{an} :

$$P_{an} = \begin{cases} 0 & \Psi_{mn} > L_{dn} \\ \Psi_{mn}/L_{dn} & \Psi_{mn} \leq L_{dn} \end{cases} \tag{2.36}$$

The constant-power speed range is calculated separately for finite and infinite maximum speed IPM drives. For finite maximum speed IPM drives, the constant-power speed ω_p occurs in Mode II. It is obtained by solving $P_n = P_{kn}$ with (2.29) and (2.34). This yields a quartic for $\sin\gamma_p$, the sine of the current-angle corresponding to the constant-power speed ω_p :

$$\begin{aligned} 0 \;=\; & \sin^4\gamma_p \,[(\xi - 1)^2 L_{dn}^2] \\ +\; & \sin^3\gamma_p \,[2\Psi_{mn}(\xi - 1) L_{dn}] \\ +\; & \sin^2\gamma_p \,[(1 - \xi^2) L_{dn}^2 P_{kn}^2 + \Psi_{mn}^2 - (\xi - 1)^2 L_{dn}^2] \\ +\; & \sin\gamma_p \,[-2\Psi_{mn} L_{dn} P_{kn}^2 - 2\Psi_{mn}(\xi - 1) L_{dn} - 2\Psi_{mn} L_{dn}(P_{kn}^2 + \xi - 1)] \\ +\; & [\xi^2 P_{kn}^2 L_{dn}^2 + P_{kn}^2 \Psi_{mn}^2 - \Psi_{mn}^2] \end{aligned} \tag{2.37}$$

This quartic can be rapidly solved numerically using eigenvalues [37] and generally yields only two real roots, one of which is $\sin\gamma_m$ and the other is $\sin\gamma_p$.

For infinite maximum speed IPM drives, ω_p occurs in Mode III (see Fig. 2.19 on pg. 88). The constant-power speed range can be obtained by solving the power equation

from (2.25) :

$$P_{kn} = T_n w_n = [\Psi_{mn} I_{qn} - (\xi - 1) L_{dn} I_{dn} I_{qn}] w_n \tag{2.38}$$

by substituting in the Mode III optimal torque trajectory equations (2.32). The resultant equation can be rearranged to yield :

$$Ax = \left[x - \left(\frac{B + \sqrt{C + Dx}}{E} \right)^2 \right] \left(F + \sqrt{C + Dx} \right)^2 \tag{2.39}$$

where :

$$\begin{aligned} x &= (1/w_{pn})^2 \\ A &= (4\xi L_{dn} P_{kn})^2 \\ B &= -\xi \Psi_{mn} \\ C &= (\xi \Psi_{mn})^2 \\ D &= 8(\xi - 1)^2 \\ E &= 4(\xi - 1) \\ F &= 3\xi \Psi_{mn} \end{aligned}$$

Rearranging (2.39) yields :

$$0 = (Gx^2 + Ix + K) + \sqrt{C + Dx}(Hx + J) \tag{2.40}$$

where :

$$\begin{aligned} G &= 4(\xi - 1)^2 \\ H &= 4\xi \Psi_{mn} \\ I &= 10\xi^2 \Psi_{mn}^2 - 16\xi^2 L_{dn}^2 P_{kn}^2 \\ J &= \xi^3 \Psi_{mn}^3 / 2(\xi - 1)^2 \\ K &= -\xi^4 \Psi_{mn}^4 / 2(\xi - 1)^2 \end{aligned}$$

Rearranging (2.40) yields :

$$\begin{aligned} 0 &= x^3[(\xi - 1)^4] \\ &+ x^2[\xi^2(\xi - 1)^2(-3\Psi_{mn}^2 - 8L_{dn}^2 P_{kn}^2)] \\ &+ x[\xi^4(3\Psi_{mn}^4 - 20L_{dn}^2 \Psi_{mn}^2 P_{kn}^2 + 16L_{dn}^4 P_{kn}^4)] \\ &+ [\xi^6 \Psi_{mn}^4 (L_{dn}^2 P_{kn}^2 - \Psi_{mn}^2)/(\xi - 1)^2] \end{aligned} \tag{2.41}$$

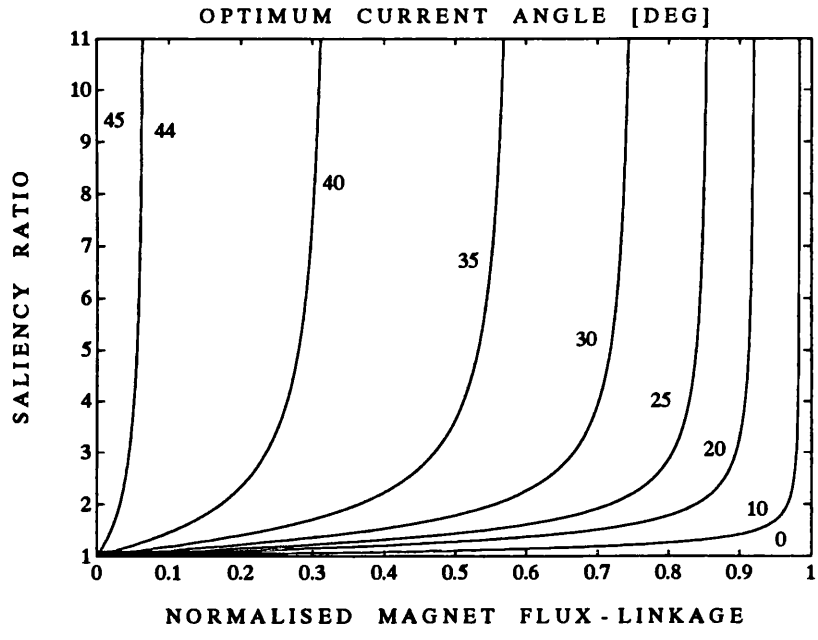

Figure 2.22: *Maximum-torque-per-ampere current-angle contour plot.*

This equation can be solved numerically as all the co-efficients are known. The correct root is found by substituting the roots back into the initial equations.

2.5.2 Discussion of Contour Plots

Using the above equations it is possible to calculate and produce contour plots of the maximum-torque-per-ampere current-angle γ_m, the inverter utilisation κ, the normalised maximum operating speed w_{xn}, the asymptotic high speed output power P_{an} and the constant-power speed range CPSR.

The maximum-torque-per-ampere current-angle contour plot (Fig. 2.22) shows how γ_m increases from 0° for surface permanent magnet motor drives along the x-axis to 45° for synchronous reluctance motor drives along the y-axis. It illustrates the point made earlier that designs to the right of the IPM parameter plane have a strong permanent magnet nature, while designs to the left have a strong reluctance nature.

The inverter utilisation κ contour plot is shown in Fig. 2.23. Since the motor drive is

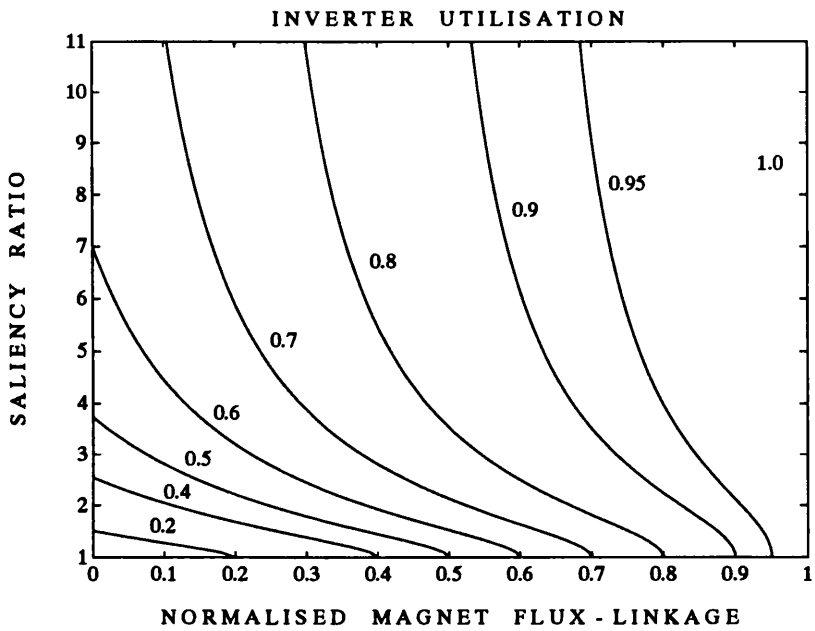

Figure 2.23: *Inverter utilisation (κ) contour plot.*

assumed lossless, this is equal to the power-factor at rated speed when delivering rated torque. The contour plot shows that the inverter utilisation improves monotonically with increasing saliency ratio and increasing magnet flux-linkage. Note that it was shown in Sec. 2.3.4 that a synchronous reluctance motor drive with an infinite saliency ratio has $\kappa = 1/\sqrt{2}$.

The normalised maximum operating speed w_{xn} contour plot (Fig. 2.24) shows that for a given saliency ratio, w_{xn} increases as the magnet flux-linkage is decreased until it reaches infinity at the *infinite maximum speed line.* This corresponds to the boundary between finite and infinite maximum speed drives. This matches closely but not exactly to the $\kappa = 1/\sqrt{2}$ line in Fig. 2.23.

The maximum operating speed contour plot is important as it allows the division of the IPM parameter plane into the five drive classes as shown in Fig. 2.25. The ability of the IPM parameter plane to represent all five classes on a single diagram is critical to allowing comparisons to be made.

The normalised asymptotic high speed output power P_{an} contour plot (Fig. 2.26)

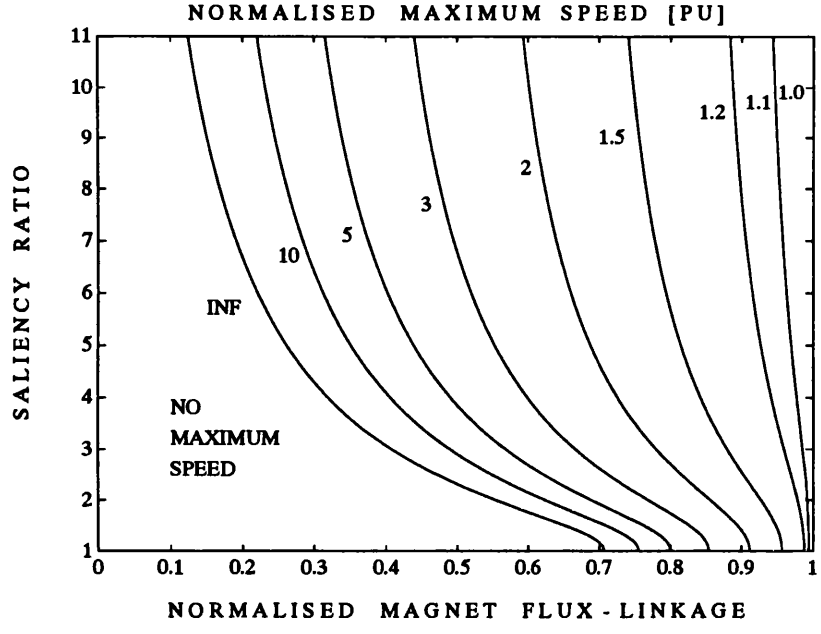

Figure 2.24: *Normalised maximum operating speed (ω_{xn}) contour plot.*

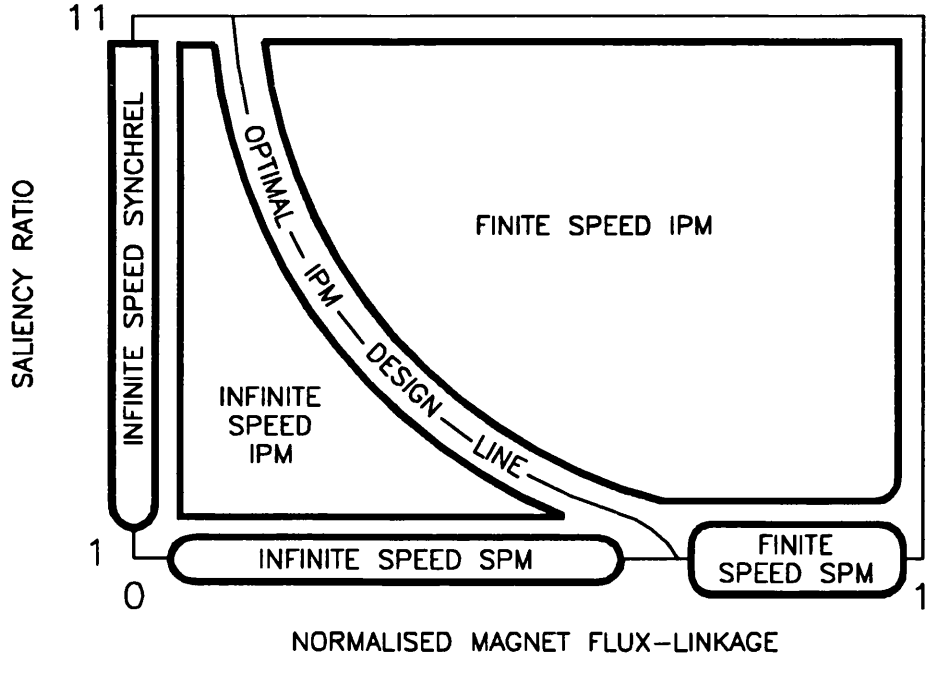

Figure 2.25: *The five drive classes.*

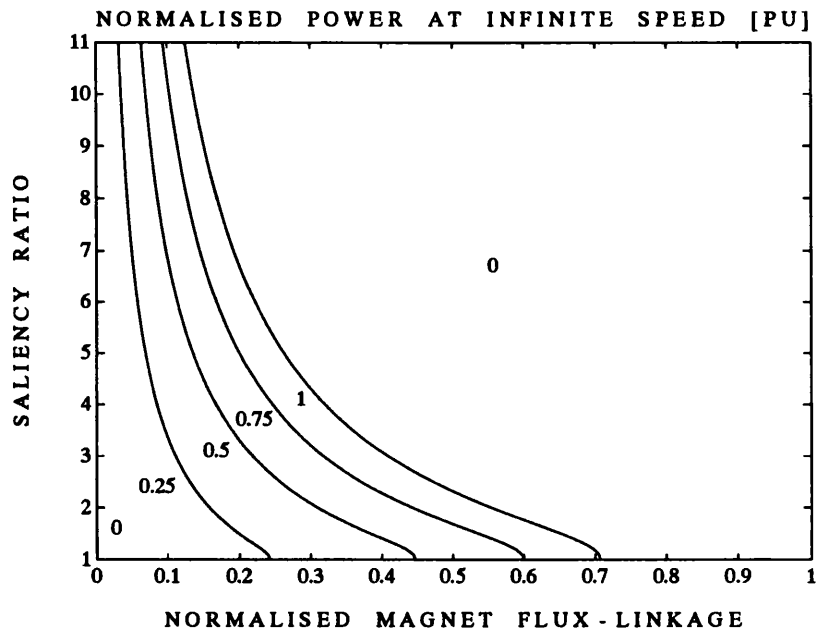

Figure 2.26: *Normalised asymptotic high speed output power (P_{an}).*

shows that finite maximum speed drives have zero output power at infinite speed. For infinite maximum speed drives P_{an} improves with increasing magnet flux-linkage up to the infinite maximum speed line, at which point it is unity.

The constant-power speed range (CPSR) contour plot in Fig. 2.27 is calculated using (2.37) and (2.41). For synchronous reluctance motor drives the constant-power speed range is approximately half the saliency ratio (see Sec. 2.3.4). For surface permanent magnet motor drives the constant-power speed range is unity with $\Psi_{mn} = 1$ and improves dramatically with decreasing Ψ_{mn} until it reaches infinity for $\Psi_{mn} \leq 1/\sqrt{2}$ (see Sec. 2.2.5). Finite maximum speed IPM drives clearly have a finite constant-power speed range however not all infinite maximum speed IPM drives have an infinite constant-power speed range. The designs that do, lie in a band bounded by the infinite maximum speed line on the right, and on the left by the line where the normalised asymptotic high speed output power (see Fig. 2.26) is equal to the normalised rated power or inverter utilisation (see Fig. 2.23).

A comparison of Figs. 2.27 and 2.23 shows that in order to obtain an infinite

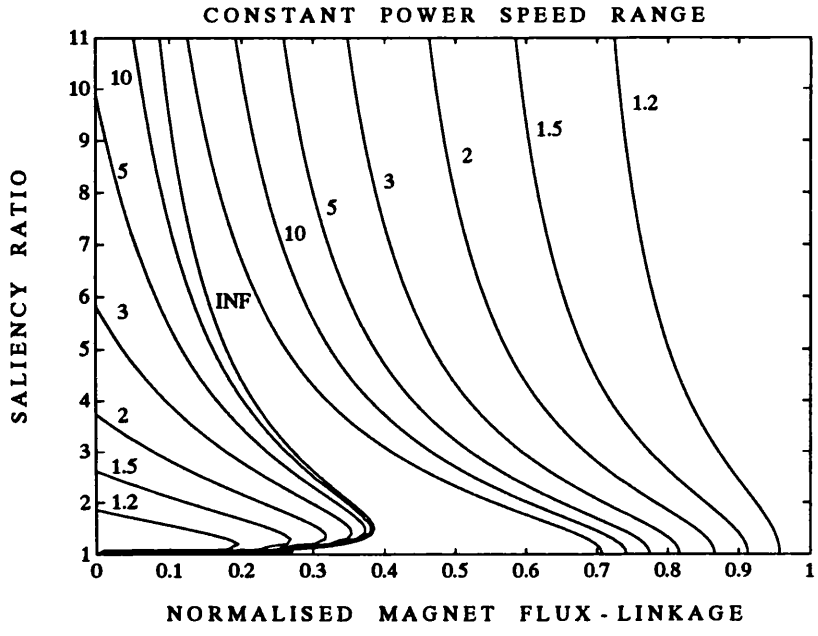

Figure 2.27: *Constant-power speed range (CPSR) contour plot.*

constant-power speed range it is necessary to have an inverter utilisation below about 0.7. The optimal field-weakening performance is obtained with designs on the infinite maximum speed line. This optimal performance corresponds to having unity normalised output power at infinite speeds and an infinite constant-power speed range, but is associated with an inverter utilisation of about 0.7. The infinite maximum speed line corresponds to Schiferl and Lipo's optimal design criterion (2.1) and will be now be referred to as the *optimal* IPM *design line.* Designs which lie on this line will be termed *optimal field-weakening* IPM *designs.*

The optimal surface permanent magnet and synchronous reluctance motor drive designs have identical field-weakening performance (see Sec. 2.3.4). Optimal interior permanent magnet motor drive designs have similar but not identical field-weakening performance. For instance the inverter utilisation of optimal surface permanent magnet and synchronous reluctance motor drives is 0.707. Optimal interior permanent magnet motor drives have inverter utilisations ranging from 0.707 to 0.721. The highest inverter utilisation is obtained with a saliency ratio of 2. For practical purposes the field-

weakening performance of all optimal designs is the same.

Demagnetisation withstand limits are critical for permanent magnet motor drives. Assuming zero airgap and no leakage for simplicity then the minimum magnet operating point ζ with rated stator current occurs when $I = I_c$ and $\gamma = 90^o$:

$$\zeta = \frac{\Psi_{mn} - L_{dn}}{\Psi_{mn}} \tag{2.42}$$

where unity represents operation at remanence and zero corresponds to zero flux in the magnet (see Fig. 2.28). It should be noted that using the rated stator current with the worst possible orientation is a conservative estimate and that the optimal field-weakening strategy will generally not require the magnet operating point to be brought so low. The minimum magnet operating point is inversely related to the field-weakening range and in optimal field-weakening IPM designs is equal to zero. Thus for good field-weakening performance it is necessary to use magnets with at least a linear 2nd quadrant demagnetisation curve [34]. In practice, stator leakage inductance will mean that not all the stator d-axis flux will pass through the magnet and this will increase the minimum magnet operating point.

2.5.3 Using the IPM Parameter Plane

The aim of the IPM parameter plane is to allow the visualisation of the effect of parameter changes on the field-weakening performance. This is what is explored in this section.

The shape of the normalised torque versus speed characteristic of a constant parameter, lossless interior permanent magnet motor drive is affected by four parameters : I_o, Ψ_m, L_d and L_q. Varying I_o or Ψ_m does not alter the saliency ratio and hence moves the design parallel to the Ψ_{mn} axis (see dotted lines in Fig. 2.29). Increasing I_o or decreasing Ψ_m decreases Ψ_{mn}. Varying L_q causes the design to move along the direction of the solid lines which roughly follow lines of constant ω_{xn} and P_{an}. This is because these parameters are mainly determined by L_d, Ψ_m and I_o. Varying L_d causes the design to move along the direction of the nearly vertical dashed lines. This is because for designs with a saliency above about two, $L_d \ll L_q$ and so L_d has little effect on

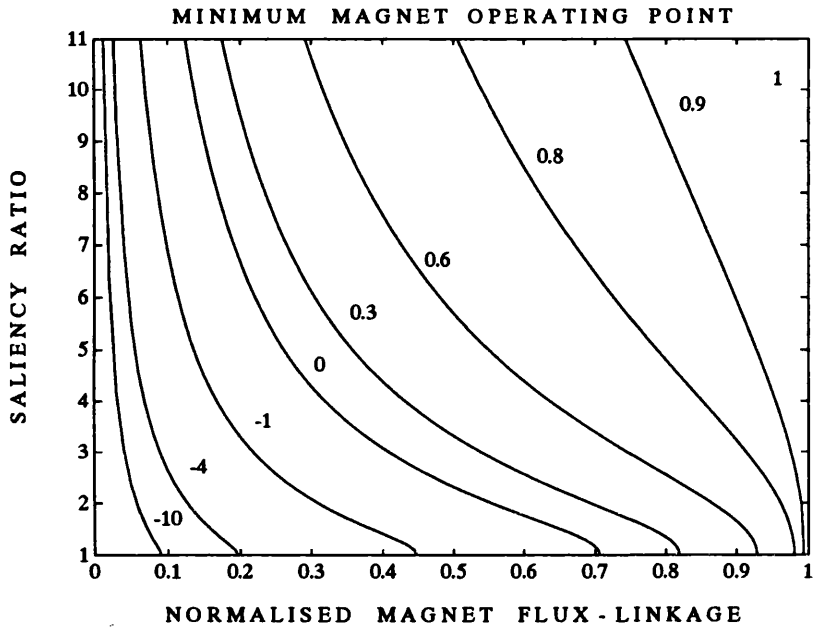

Figure 2.28: *Demagnetisation-withstand constraint contour plot.*

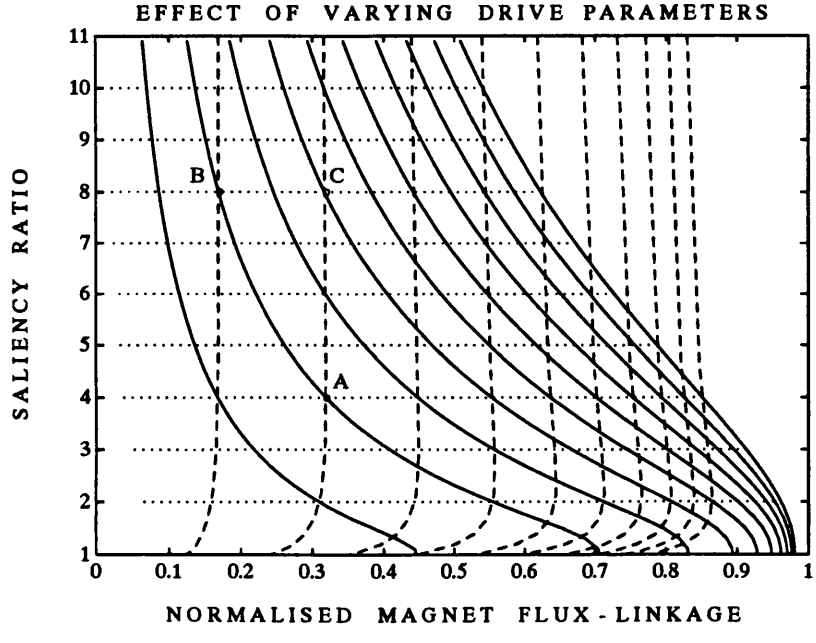

Figure 2.29: *Effect of varying L_q (solid), L_d (dashed), Ψ_m and I_o (dotted).*

ω_o and hence on Ψ_{mn}. The spacing between the solid lines and also that between the dashed lines correspond to equal increments in the *actual* magnet flux-linkage Ψ_m.

Consider a motor drive design corresponding to point A in Fig. 2.29 which has the *un-normalised* torque versus speed characteristic shown in Fig. 2.30 (also marked "A"). Note that it is a near optimal design showing excellent field-weakening performance.

Doubling L_q doubles the saliency ratio and moves it along the solid line in Fig. 2.29 to point B. Fig. 2.30 shows that this nearly doubles the low-speed torque and halves the rated speed but has little effect on the high speed performance and on the rated output power. As mentioned earlier, the high speed performance of designs with a significant permanent magnet nature is mainly determined by Ψ_m, L_d and I_o and is relatively independent of L_q. Thus saturation of L_q will mainly affect the low-speed performance and has little effect on the field-weakening performance. This has been noted earlier by Chalmers [38].

Doubling Ψ_m moves the design along a line of constant saliency to point C in Fig. 2.29. The doubling of the magnet flux only results in about a 20% increase in rated torque as this design is mainly a reluctance machine (note that the back-emf at rated speed is only just over 30% of the terminal voltage). The high speed performance of this design (shown as a dashed line in Fig. 2.30) is poor as the magnet flux is much greater than $L_d I_o$.

Finally, doubling L_d halves the saliency ratio and returns the design to point A. The new design (A') has exactly the same shaped torque versus speed characteristic as the original design, but has twice the rated torque and half the rated speed. This illustrates the concept of normalisation and shows that each point on the IPM parameter plane represents an infinite number of drive designs, each with identically shaped (normalised) field-weakening characteristics.

The IPM parameter plane is also useful for illustrating the effect of starting off with a given synchronous reluctance motor drive design and investigating the effect of adding magnet flux on the torque versus speed characteristics.

Figs. 2.31 and 2.32 show the effect on the torque and power versus speed character-

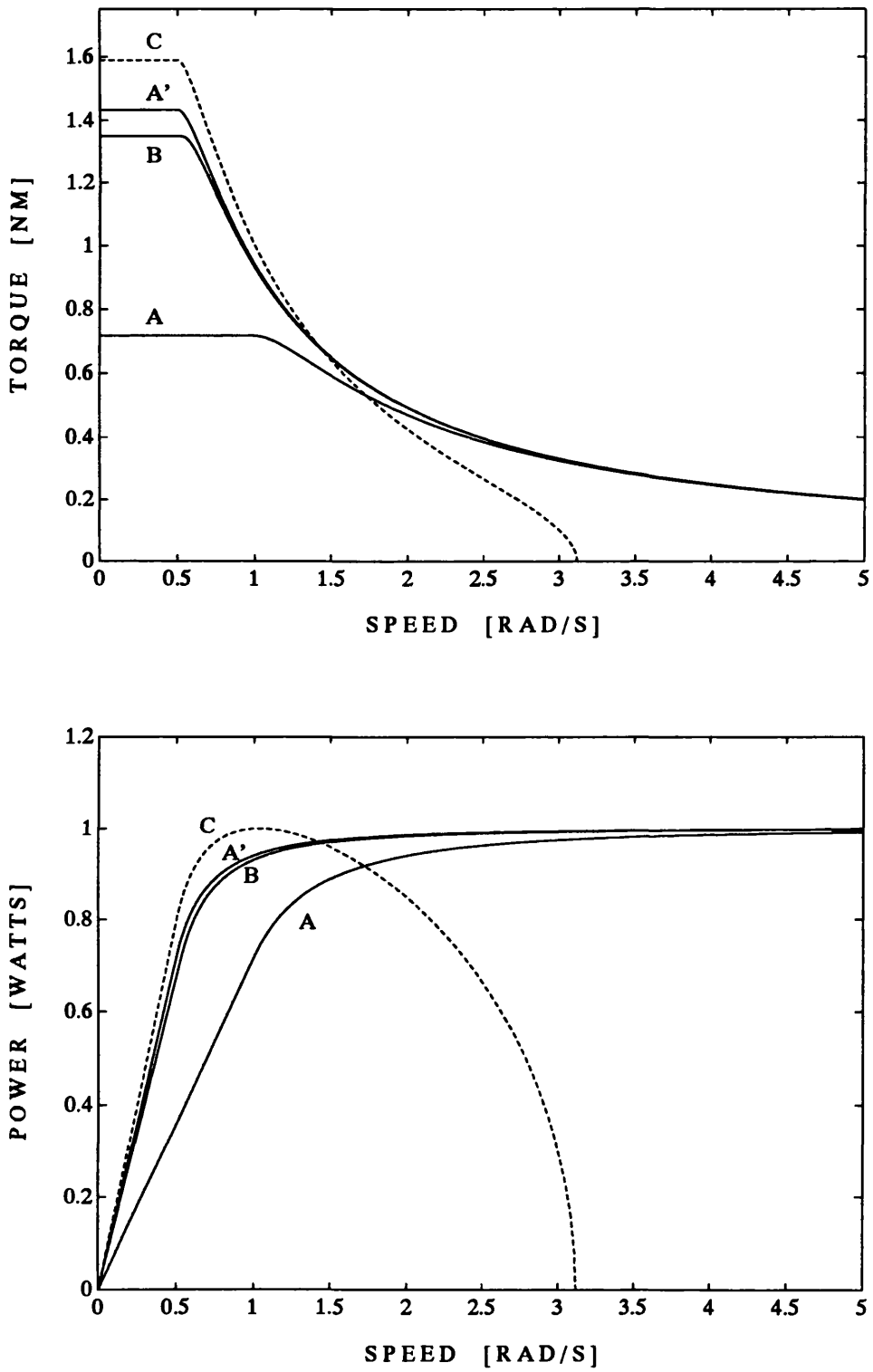

Figure 2.30: *Effect of parameter changes on the torque versus speed characteristic.*

istics of increasing the magnet flux in five equally-sized increments. "0" corresponds to a pure reluctance design, "2" corresponds to an optimal field-weakening design and "5" corresponds to a design with a strong permanent magnet nature. The drive in Fig. 2.31 has a saliency ratio of four and that in Fig. 2.32 has a saliency ratio of eight. Note that the optimal designs in Figs. 2.31 and 2.32 actually correspond to designs A and B respectively in Fig. 2.29.

Adding magnet flux improves the low-speed torque and decreases the rated speed. Initially the field-weakening performance improves with increasing magnet flux, however once the optimal design is reached further additions of magnet flux rapidly degrade the performance. For a high-saliency design the required optimal magnet flux is lower as L_d is lower and hence the increase in rated torque is smaller. Figs. 2.31 and 2.32 also show that the sensitivity of the field-weakening performance to variations in the magnet flux is lower with increased saliency. Thus a high a saliency ratio as possible should be used.

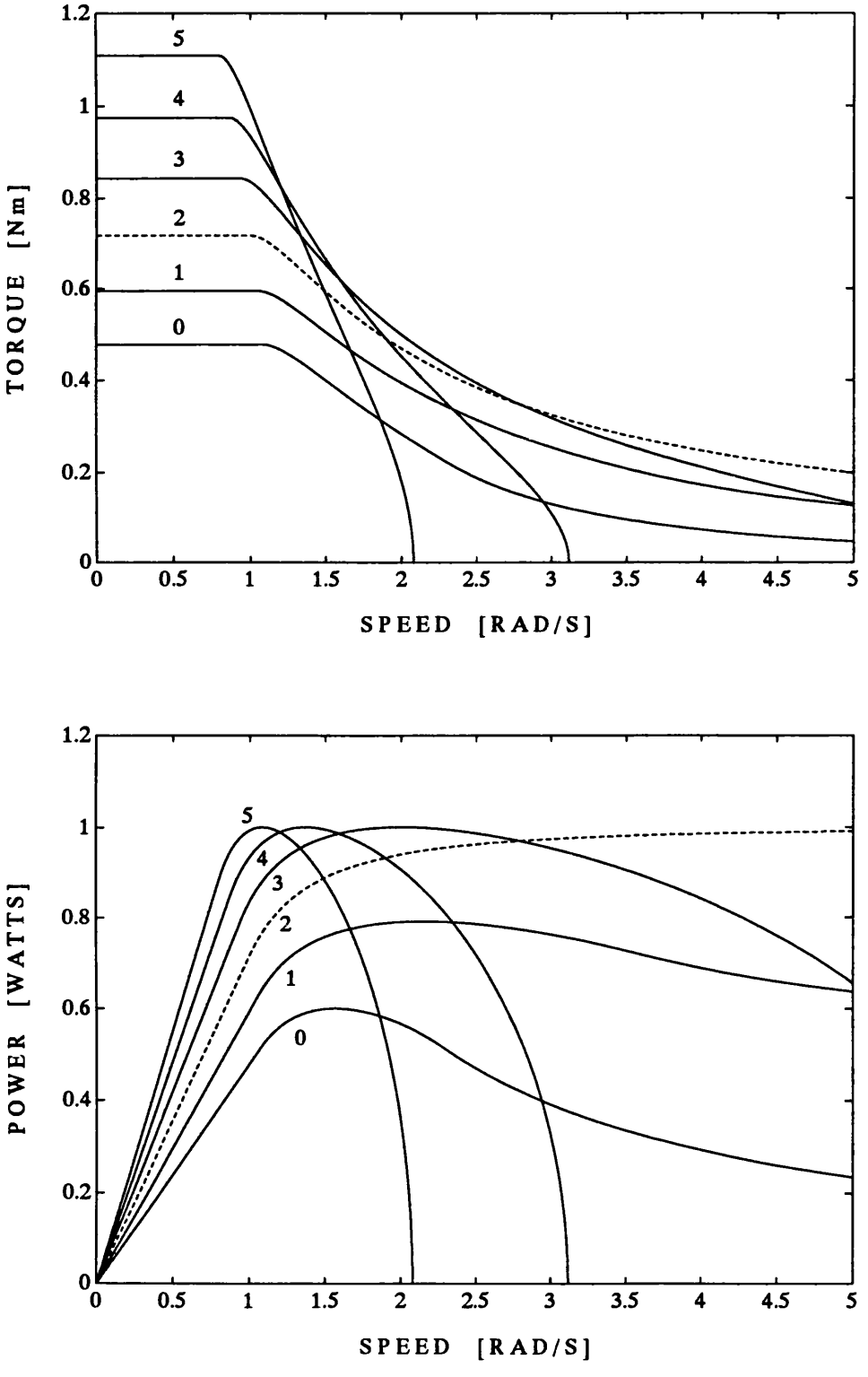

Figure 2.31: *Effect of adding magnet material to a* SYNCHREL *with* $\xi = 4$.

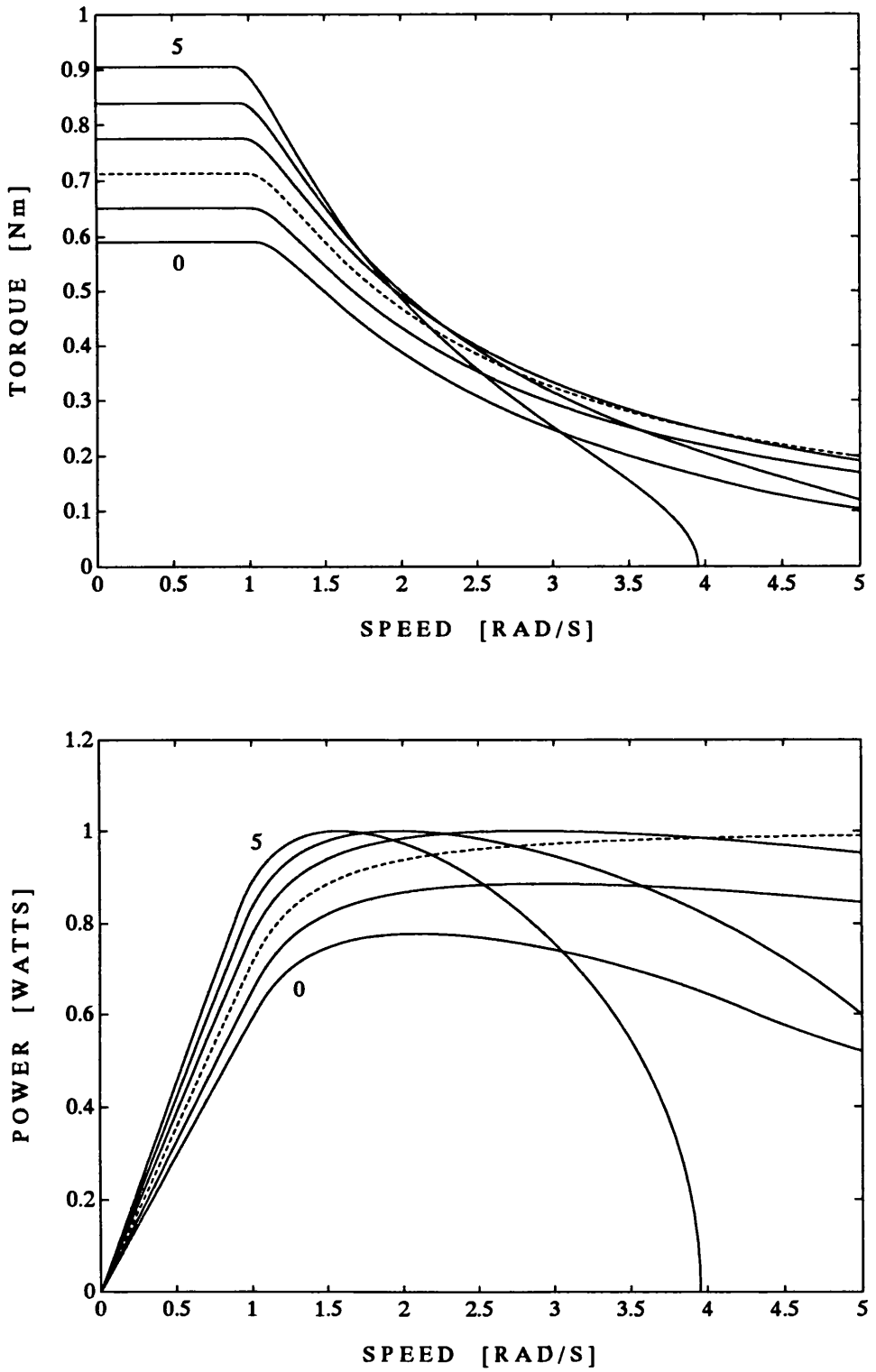

Figure 2.32: *Effect of adding magnet material to a* SYNCHREL *with* $\xi = 8$.

2.6 Theoretical Optimal Field-Weakening Designs

This chapter introduced the new concept of the IPM parameter plane. This represents a unified method for illustrating the effect of parameter changes on the field-weakening performance of the five drive classes. The analysis was based on obtaining the maximum torque from the motor drive within a given voltage and current rating. The IPM parameter plane has shown that the optimal field-weakening performance for brushless synchronous AC motor drives offers unity normalised output power up to infinite speeds but is limited to an inverter utilisation of about 0.7. There is an fundamental tradeoff between the field-weakening performance and the inverter utilisation. Unity inverter utilisation can only be achieved with drives with no field-weakening capability ($\Psi_{mn} = 1$).

The optimal field-weakening performance can be obtained from any drive design lying on the optimal field-weakening design line in the IPM parameter plane. These designs fall into three catagories :

- synchronous reluctance motor drives with infinite saliency.
- interior permanent magnet motor drives where $\Psi_m = L_d I_c$.
- surface permanent magnet motor drives with $\Psi_{mn} = 1/\sqrt{2}$.

Note that all these optimal designs share a common characteristic : the effective d-axis flux-linkage is zero when rated current is applied to the d-axis of the motor. For instance with an infinite saliency ratio synchronous reluctance motor drive $L_d = 0$ and so aligning the current phasor with the d-axis yields zero flux. With permanent magnet motor drives the optimum field-weakening criterion (2.1) means that the stator d-axis flux-linkage due to the finite saliency ratio is precisely cancelled by the permanent magnet flux. This results in a zero total d-axis flux-linkage which is equivalent to having $L_d = 0$. Thus the drive has effectively infinite saliency ratio and hence excellent field-weakening performance.

Clearly infinite saliency ratio synchronous reluctance motor drives are impossible however high-saliency designs may offer a sufficiently wide field-weakening performance.

The synchronous reluctance motor drive has the following advantages [7, 21] over permanent magnet motors :

- no magnets. This reduces the cost and eliminates problems of magnetisation and demagnetisation withstand.
- no open-circuit back-emf voltage. This eliminates the problem of uncontrollable fault currents and means that no demagnetising current is required at high speed.
- a thermally rugged rotor, capable of operating to extreme temperatures.
- no temperature sensitive parameters except the stator resistance.
- simpler control. Vector control of the synchronous reluctance motor drive is simpler than that for the induction motor due to its synchronous nature.

According to the idealised constant parameter analysis in Sec. 2.3.4, the constant-power speed range and inverter utilisation of synchronous reluctance motor drives is determined by the saliency ratio. A saliency ratio of 8 will ideally give a constant-power speed range of about 4:1 and an inverter utilisation of just over 0.6. If synchronous reluctance motor drives can achieve the required field-weakening performance then they will be preferred to permanent magnet motor drives, all other things being equal. If synchronous reluctance motor drives are unable to achieve the desired field-weakening performance then the next best option is to use a high-saliency optimal field-weakening IPM design. These offer the following advantages [7, 39] :

- low magnet requirements : and so low cost. The majority of the torque is generated from the reluctance nature of the motor.
- lower open-circuit voltages at high speeds : high magnet-induced open-circuit voltages can present a hazard if the controller was to trip out at high speed [11]. High-saliency optimal field-weakening IPM designs have a lower back-emf voltage (see Fig. 2.25). For instance with an optimal field-weakening SPM design the induced voltage at rated speed is approximately 70% of the rated voltage. Thus at five times rated speed, the open-circuit terminal voltage will be three and a

half times the rated voltage. For an optimal field-weakening IPM design with a saliency ratio of 7, the back-emf is about 20% of rated voltage at rated speed. Thus at five times rated speed, the open-circuit voltage will be only equal to the rated motor voltage.

- reduced sensitivity to magnet flux variations. This was shown by Figs. 2.31 and 2.32. This makes the performance less sensitive to changes in the magnet flux due to temperature or production variations.

- reduced no-load iron losses due to the lower magnet flux. This should give higher efficiency under high-speed, light-load conditions compared to surface permanent magnet motor drive designs.

- reduced copper losses due to the reduction in the "defluxing" current requirements under light load, high speed conditions. Under no-load operation, the optimal field-weakening SPM design would only be able to operate up to $1/0.7 = 1.4$ times rated speed before the open-circuit terminal voltage reaches the rated voltage. To operate at higher speeds some "defluxing" current would be required to keep the terminal voltage below its rated value. However an optimal field-weakening IPM design with a saliency ratio of 7 could operate up to $1/0.2 = 5$ times rated speed before rated terminal voltage is reached.

The effect of practical factors on the field-weakening performance will be investigated in the next chapter.

Chapter 3

Practical Limitations

This chapter examines the effect of practical factors such as stator resistance, iron losses, magnetic saturation, DQ cross-coupling, minimum magnet operating point and mechanical constraints on how closely the ideal field-weakening performance predicted in the previous chapter can be achieved.

First the location of existing and proposed motor drive designs in the IPM parameter plane is shown. The effect of practical factors on the low speed torque, inverter utilisation and constant-power speed range are analysed. The results are validated against experimental measurements for a surface permanent magnet and two synchronous reluctance motor drives. Finally conclusions are drawn about the best drive for field-weakening applications.

3.1 Achievable IPM Parameter Plane Designs

If this entire thesis had to be summarised in a single diagram, then Fig. 3.1 would be that diagram. It shows the location of practical brushless synchronous AC motor designs on a contour plot of the constant-power speed range in the IPM parameter plane. These designs can be grouped into five classes :

- surface permanent magnet,
- single-barrier synchronous reluctance,
- single-barrier interior permanent magnet,
- multiple-barrier synchronous reluctance,
- multiple-barrier interior permanent magnet.

Note that the more interesting designs are marked with the first four letters of their author's name and that crosses are used to represent multiple-barrier designs and discs used to represent single-barrier, spoke-type or surface permanent magnet designs.

The optimal field-weakening performance is obtained from designs which lie on the optimal IPM design line (solid line in Fig. 3.1). An infinite constant-power speed range can be obtained by designs lying in the zone on the left of the optimal IPM design line, but these designs show a lower inverter utilisation at rated speed and lower output power at high speeds than optimal designs (see Fig. 2.23 on pg. 97).

Surface permanent magnet motor drives (bottom right of Fig. 3.1) use either ferrite or rare-earth magnets. The low permeability of these magnets mean that the motors have no saliency. From examining commercial designs [40, 41, 42] it was found that ferrite SPM designs generally have values of Ψ_{mn} in the range 0.83 to 0.92 while rare-earth designs have values in the range 0.90 to 0.96. Rare-earth permanent magnet motor drives have a higher Ψ_{mn} as the magnets generate more flux (see Fig. 2.29 on pg. 102). In general surface permanent magnet motor drives have constant-power speed ranges below 3:1 and it is usually below 2:1.

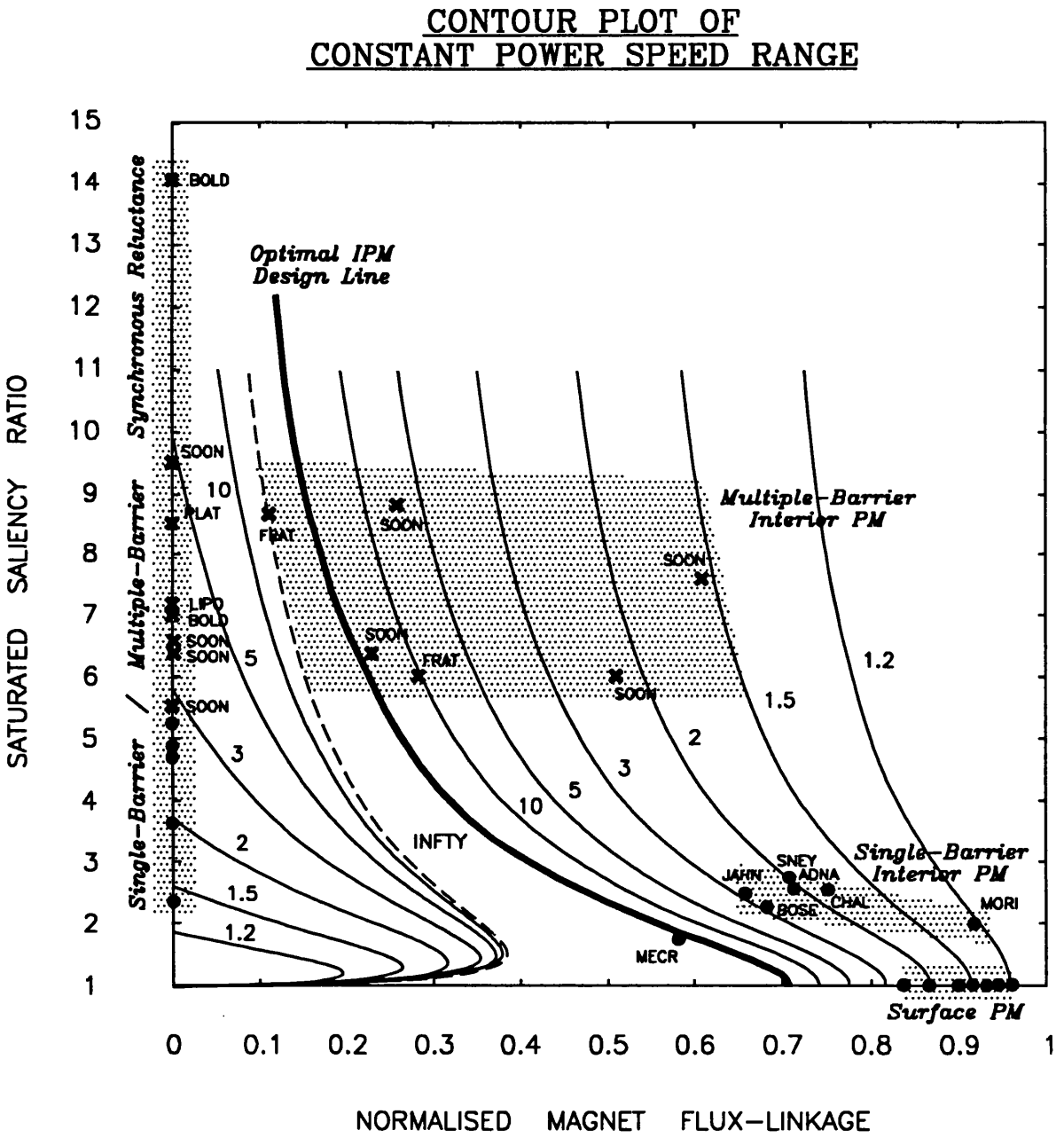

Figure 3.1: *Location of motor drive designs in the* IPM *parameter plane.*

Single-barrier synchronous reluctance motor drives achieve saliency ratios in the range 2 to 5 [21, 43, 44]. This type of motor was originally fitted with a cage to allow self-starting. It was popular for fibre-spinning applications in the late fifties and early sixties [7]. Note that the field-weakening range of these drives is small.

The simplest interior permanent magnet motors are of the single-barrier or spoke-type construction. These designs are usually finite maximum speed IPM drives with constant-power speed ranges between 1.5:1 and 3:1 [2, 5, 30, 38, 45, 46]. The design described by Mecrow et al. [47] is an unusually highly-rated drive which theoretically has a wide field-weakening performance. It uses a high electric loading and can only be operated intermittently or else requires substantial external forced cooling. The other single-barrier designs could also achieve comparable performance if they were similarly cooled. The main drawbacks of obtaining a wide field-weakening range with these motor drives is the requirement for external cooling, the high open-circuit back-emf voltage, the high magnet cost and the difficulty of ensuring sufficient demagnetisation withstand over the full temperature range.

Multiple-barrier or axially-laminated synchronous reluctance motor drives can achieve saturated saliency ratios in the range 5 to 14 [48, 49, 50, 51, 52, 53]. The highest saliency ratios are obtained with two-pole designs such as those built by Boldea et al. [48] which feature unsaturated saliencies of up to 20. These high saliency designs should theoretically offer a wide field-weakening range.

Adding permanent magnet material to these motors can produce drives with a potential for the optimum field-weakening performance [54]. The four designs marked "SOON" in the multiple-barrier IPM zone represent the calculated effect of adding ferrite and rare-earth magnets to two axially-laminated synchronous reluctance motor designs. Note that by adding a suitable quantity of magnet material it is possible to obtain an optimal field-weakening design. The design of these motor drives is discussed in detail in Part Two.

The design by Fratta et al. [54] (marked "FRAT") is a multiple-barrier (radially-laminated) motor using ferrite magnets and a fan-cooled stator. Two points are shown for this design. The one with the higher saliency corresponds to the unsaturated

parameters, while the lower saliency point corresponds to the saturated parameters. Heavy saturation has caused a unusually high maximum-torque-per-ampere current-angle. This in turn causes the saturated design to appear to be a finite maximum speed IPM drive even though it is actually a infinite maximum speed IPM drive. This shows a significant limitation with the IPM parameter plane in that it assumes the drive operates at the constant parameter maximum-torque-per-ampere current-angle. The actual operating current-angle can be substantially different to this due to saturation. Thus the IPM parameter plane is mainly useful to give a rough idea of the field-weakening performance.

3.2 Practical Factors

3.2.1 Copper Losses

Stator copper losses are present in all electrical machines. They are the sole source of loss at standstill for brushless AC synchronous motors and the ability of the motor to dissipate these losses generally determines the maximum continuous stator current and hence output torque. Stator resistance can be modelled by a resistance in series with the ideal motor as shown in Fig. 3.2. Note the definition of the *internal power-factor* $\cos\phi_i$, the *magnetising voltage* V_m and the *magnetising current* I_m. In this case $I_m = I$.

Due to scaling effects, the per-unit copper loss R_{sn} (the copper loss expressed as a fraction of the rated input kVA) to a first approximation is inversely proportional to the motor diameter [12]. Thus the smaller the motor, the higher the per-unit copper loss. For motors in the range 1 to 10kW it is typically about 0.05pu or less, while a typical 120W induction motor had a 0.2pu stator copper loss.

The effect of stator resistance is to reduce the magnetising voltage. Adding stator resistance does not alter the maximum-torque-per-ampere current-angle and thus $\cos\phi_i$ will be unaffected by it. From Fig. 3.2, if $V_n = 1$ and if $R_{sn} \ll 1$ then :

$$V_{mn} = \sqrt{1 + (I_n R_{sn}\cos\phi_i)^2 - (I_n R_{sn})^2} - I_n R_{sn}\cos\phi_i \approx 1 - I_n R_{sn}\cos\phi_i \qquad (3.1)$$

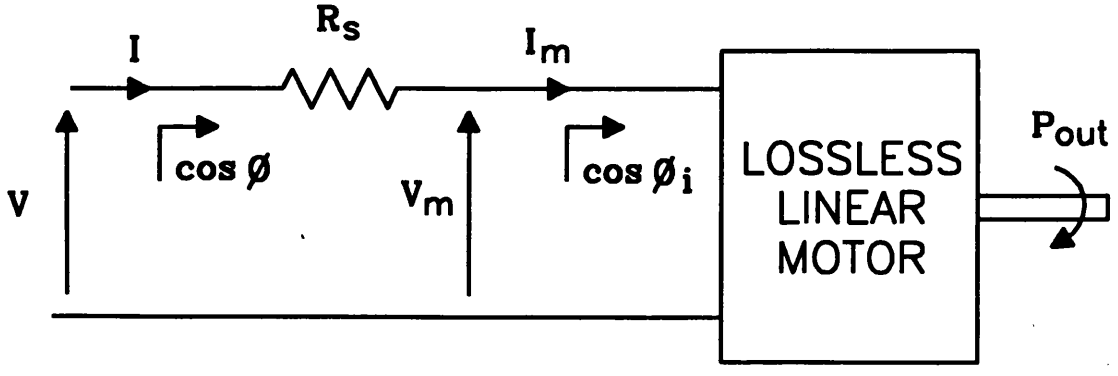

Figure 3.2: *Modelling stator resistance.*

The rated speed is proportional to V_m. Thus the rated speed $w_{k(new)}$ taking into account stator resistance with respect to the original rated speed $w_{k(old)}$ can be obtained from (3.1) with $I_n = 1$:

$$\frac{w_{k(new)}}{w_{k(old)}} = V_{mn} \approx 1 - R_{sn} \cos \phi_i \tag{3.2}$$

The inverter utilisation κ is the ratio of the rated output power to the input kVA rating. For a lossless drive it is equal to the internal power-factor. As stator resistance has no effect on the rated output torque, thus the reduction in the inverter utilisation is proportional to the reduction in the rated speed. The inverter utilisation κ_R taking into account stator resistance can be obtained from (3.2) as :

$$\kappa_R \approx [1 - R_{sn} \cos \phi_i] \cos \phi_i = [1 - R_{sn} \kappa] \kappa \tag{3.3}$$

Equation (3.2) shows that the internal power-factor $\cos \phi_i$ determines the "sensitivity" of the motor drive to stator resistance. The internal power-factor of a surface permanent magnet motor drive when delivering rated torque as a function of the constant-power speed range σ (from Table 2.1) is given by :

$$\cos \phi_i = \sqrt{\frac{1 + 1/\sigma}{2}} \tag{3.4}$$

and that for a synchronous reluctance motor drive (from Table 2.2) is :

$$\cos \phi_i = \frac{\xi - 1}{2\sqrt{\xi \sigma}} \qquad \text{where} \qquad \xi = \sigma + \sqrt{\sigma^2 - 1} \tag{3.5}$$

These equations are illustrated in Fig. 3.3. Note that surface permanent magnet motor drives have a higher power-factor than synchronous reluctance motor drives for the same constant-power speed range. However as the constant-power speed range approaches infinity, the power-factor of both drives under rated torque operation approaches $1/\sqrt{2}$.

As mentioned above, the normalised copper loss is typically less than 0.05pu for motor drives in the range 1 to 10kW. Thus the reduction in the rated speed and in the inverter utilisation due to stator resistance is generally less than 5%.

It can be shown that to a first approximation, stator resistance has no effect on the constant-power speed range of brushless synchronous AC motor drives. Consider an

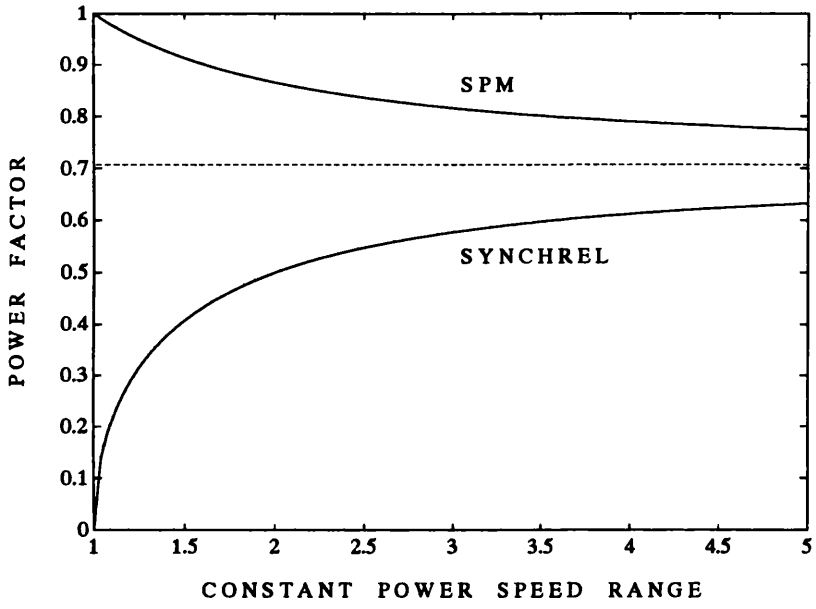

Figure 3.3: *Power-factor at rated torque as a function of CPSR.*

ideal, lossless, constant parameter drive (ie. $R_s = 0$) whose performance is shown by the solid line in Fig. 3.4. Note that the mechanical output power P_m is given by :

$$P_m = V_m I_m \cos\phi_i \tag{3.6}$$

The mechanical output power is equal at the limits of the constant-power speed range. During field-weakening, as $R_s = 0$ thus $V_m = V = 1$ and so $I_m \cos\phi_i$ at the rated speed ω_{k1} must be equal to $I_m \cos\phi_i$ at the constant-power speed ω_{p1}.

When resistance is added to the ideal motor, the terminal voltage at rated speed decreases as shown by (3.1). Fig. 3.4 illustrates this for an extremely large value of R_s (dashed line). During Mode II operation as the power-factor increases, the magnetising voltage decreases. As $I_m \cos\phi_i$ is equal at both ends of the constant-power speed range, thus from (3.1) V_m is also approximately equal at both ends. Thus as far as calculating the constant-power speed range is concerned, the motor drive is simply operating from a *constant* lower voltage. However as the constant-power speed range is independent of voltage, *thus to a first approximation* the constant-power speed range is independent of stator resistance for *all* drives.

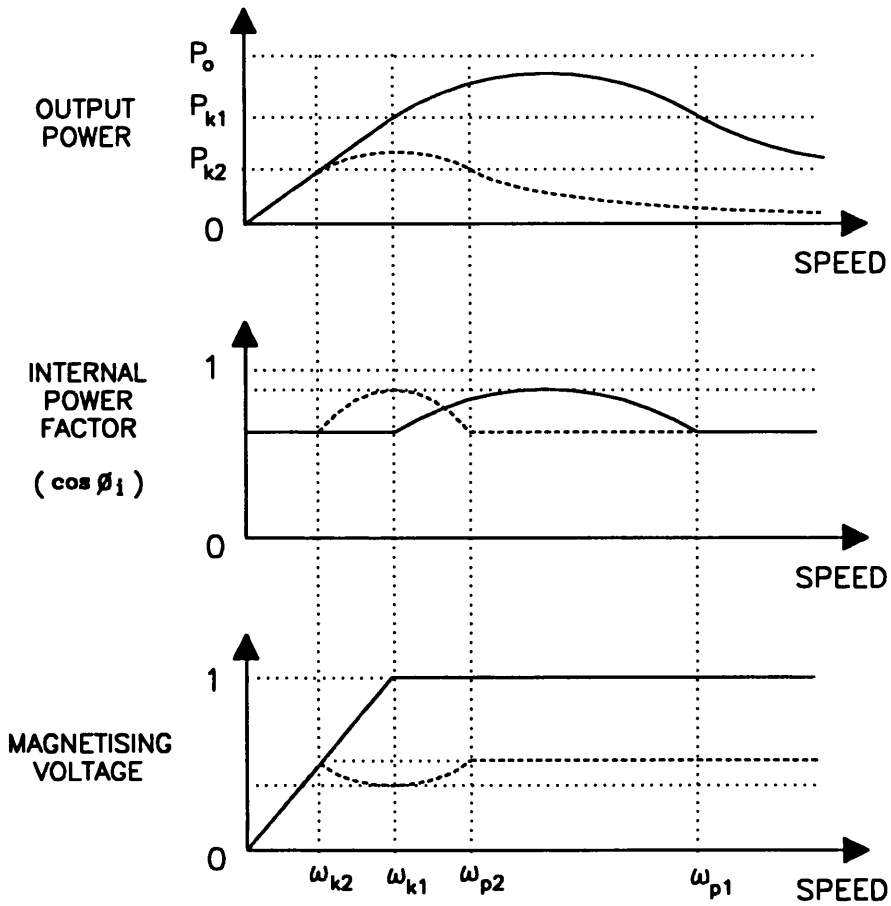

Figure 3.4: *Effect of stator resistance on the constant-power speed range.*

Drives with the constant-power speed range entirely within Mode II also have $I_m = 1$ during this period. From (3.1), V_m is thus *exactly* the same at w_k and w_p and hence the constant-power speed range is completely unaffected by stator resistance. This covers all drives classes except the infinite maximum speed IPM drive where the constant-power speed range is only unaffected to a first approximation. It is important to note that the above discussion assumes that the optimal field-weakening control strategy is unaffected by stator resistance. This is valid only for small values of R_s.

A final point from Fig. 3.4 is that the stator resistance reduces the terminal voltage during Mode II operation and hence reduces the ratio of the peak output power to the rated output power. This makes the constant-power speed range more sensitive to losses which increase with speed.

3.2.2 Saturation and Cross-Coupling

Up to this point it has been assumed that the d- and q-axis inductances are constant. In general this is far from the case and the inductances are actually functions of the currents in both axes. *Saturation* describes the effect of a current in an axis on the inductance in that axis, for instance I_d on L_d. It occurs to some extent in all well-designed reluctance machines.

Cross-coupling is used to describe the effect of a current in one axis on the inductance in the other axis, say I_q on L_d. It can be substantial in single-barrier [30, 43, 55, 56] and spoke-magnet designs [47, 57]. This is because the low saliency means that the d-axis (low-inductance axis) flux is significant and can cause partial saturation of the q-axis (high-inductance axis) flux paths and also that heavy saturation in the q-axis paths can also affect the d-axis inductance.

Cross-coupling can also be introduced in permanent magnet machines by the familiar armature reaction effect as found in DC motors [14]. Large q-axis currents causes saturation which reduces the total magnet flux Ψ_m and effectively makes L_d appear to increase as Ψ_m is normally *assumed* constant [57]. This has the opposite effect to that produced by saturation of the d-axis flux paths by I_q which causes L_d to decrease. The apparent change in L_d with I_q thus depends on which effect is predominant. This is determined by the actual motor design.

Multiple-barrier (axially-laminated) designs do not show significant cross-coupling as the high saliency ratio means that the d-axis flux is low and so does not saturate the q-axis flux paths. The d-axis flux path is also mainly air and so even heavy q-axis saturation will not cause much change in L_d. It was shown in the previous chapter that multiple-barrier designs are required to obtain the high saliency ratios required for good field-weakening performance and so the effect of cross-coupling can be neglected.

The effect of saturation however cannot be ignored. It is especially important in the high inductance q-axis. As the reluctance torque is proportional to $L_q - L_d$, saturation of L_q dramatically reduces the reluctance torque below that predicted by unsaturated parameters [38, 47]. The effect is similar to that shown in Fig. 2.30 on pg. 104. Halving

L_q in going from design B to design A nearly halves the output torque. Note that the high speed performance is relatively unaffected as it is mainly determined by L_d, Ψ_m and I_c.

In high-saliency interior permanent magnet and "unity" saliency surface permanent magnet motor drives, the d-axis inductance is low and shows little saturation as its magnetic path is mainly through air or low-permeability magnets. However due to the sensitivity of the field-weakening performance to this parameter even small changes can have significant effects. For instance some surface permanent magnet motor drive designs show significant saturation due to the magnet flux alone. In these designs, the d-axis inductance will increase significantly with increasing demagnetising current as the steel comes out of saturation (see Sec. 3.4.1).

The effect of saturation on the inverter utilisation is small in surface permanent magnet motor drives due to the small inductances involved, however it is significant for synchronous reluctance motor drives. For these drives saturation has two effects : firstly it reduces the saliency ratio from the unsaturated value ξ_u to the saturated value ξ_s and secondly it increases the maximum-torque-per-ampere current-angle γ_m above the ideal 45°. This is shown in Fig. 3.5. The inverter utilisation is simply the power-factor which from Table 2.2 is given by :

$$\kappa = \cos\phi_i = \frac{\xi_s - 1}{\sqrt{2}} \sqrt{\frac{\sin 2\gamma_m}{\tan\gamma_m + \xi_s^2 \cot\gamma_m}} \tag{3.7}$$

This is illustrated as a contour plot in Fig. 3.6. Saturation causes the saliency ratio to decrease, which decreases the inverter utilisation. It however also increases γ_m which initially increases the inverter utilisation but ultimately causes it to fall.

Fig. 3.6 is also useful for illustrating the effect of saturation on the constant-power speed range. Firstly note that the inverter utilisation during Mode II operation is equal to the normalised output power. Consider a *constant parameter* lossless synchronous reluctance motor drive with $\xi = 7$. At the maximum-torque-per-ampere current-angle $\gamma_m = 45°$, the rated output power P_k is about 0.6pu. During field-weakening the current-angle is increased. The output power rises and peaks at the maximum power-factor angle $\gamma_v = \arctan\sqrt{\xi} \approx 69°$. It then falls and at the constant-power angle

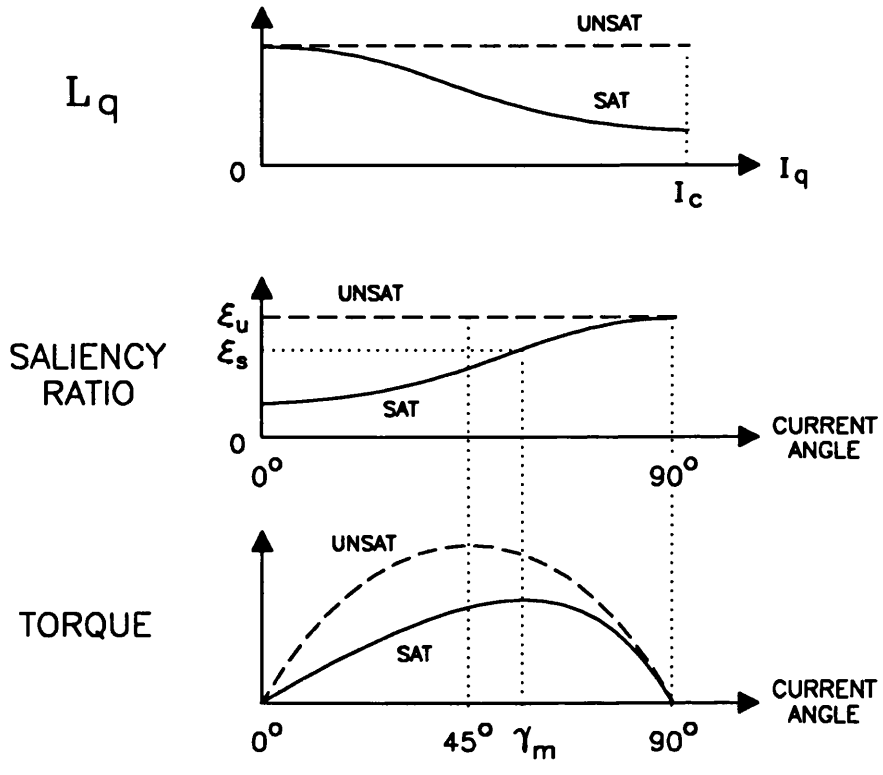

Figure 3.5: *Effect of saturation on the torque versus current-angle characteristic.*

$\gamma_p = \arctan \xi \approx 82°$ the output power is again equal to P_k. For a constant parameter synchronous reluctance motor drive this also corresponds to the Mode III transition current-angle γ_t (see Sec. 2.3.3).

Saturation critically affects the constant-power speed range of synchronous reluctance motor drives. Perhaps surprisingly the effect of the increase in the maximum-torque-per-ampere current-angle is just as significant as the reduction in saliency ratio. During field-weakening operation the current-angle is normally increased from $\gamma_m = 45°$ to γ_t. Saturation causes γ_m to increase beyond 45°. There is thus effectively less room to field-weaken the motor drive and so the constant-power speed range is reduced.

In order to calculate the effect of saturation on the constant-power speed range it is necessary to make some assumptions about the variation of L_q with I_q. Fig. 3.7 shows saturation characteristics for a range of axially-laminated motors. Design #1 is a 7.5kW interior permanent magnet design (see Chapter 5), design #2 is a 120W

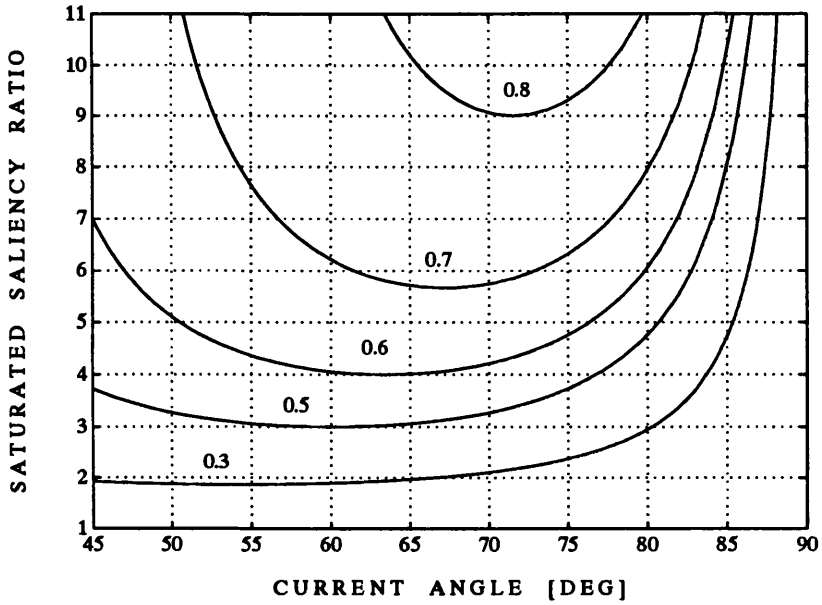

Figure 3.6: *Inverter utilisation as a function of current-angle and saturated saliency ratio.*

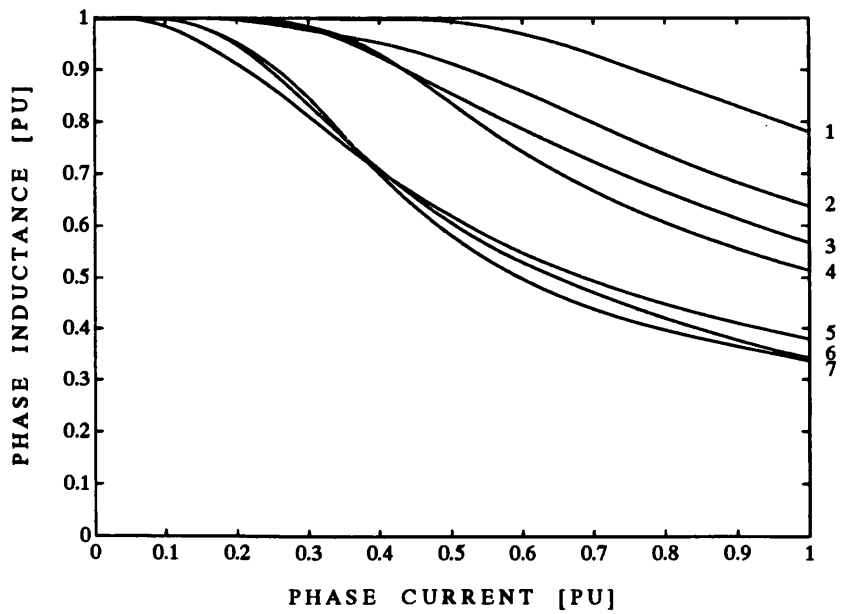

Figure 3.7: *Typical saturation characteristics.*

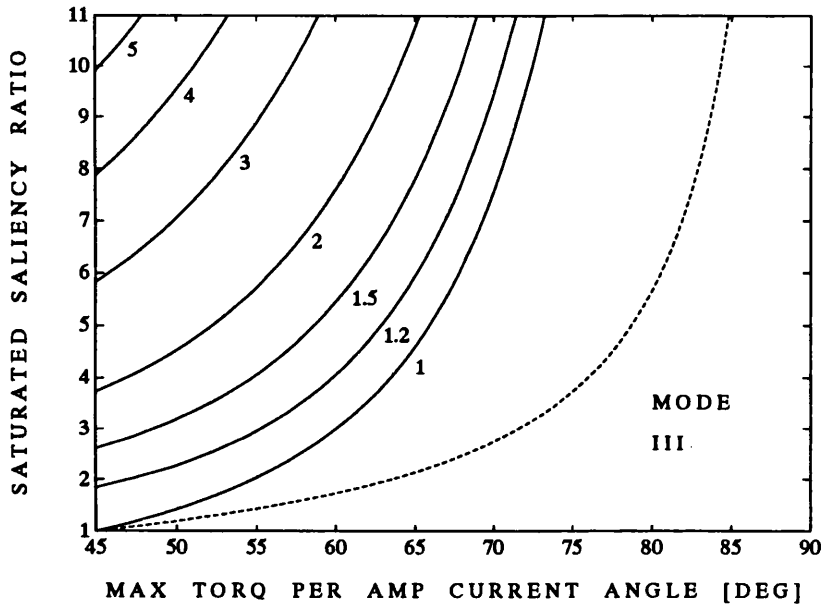

Figure 3.8: *Contour plot of the CPSR using a constant saturation model.*

synchronous reluctance design (see Sec. 3.4.1), design #3 is a 2kW design described by Platt [50], design #4 is a 7.5kW synchronous reluctance design (see Chapter 5), design #5 is 1kW synchronous reluctance design (see Sec. 3.4.1), design #6 is a two-pole 1.5kW synchronous reluctance design described by Boldea et al. [48] and design #7 is a 18kW interior permanent magnet design described by Fratta et al. [54].

The *constant saturation model* assumes that during field-weakening the inductances remain saturated. From γ_m and ξ_s, (3.7) can be used to calculate the constant-power speed range. The results are plotted in Fig. 3.8. Note that the unity constant-power speed range contour line corresponds to the maximum power-factor current-angle γ_v as the output power monotonically decreases beyond this point (assuming constant parameters).

It is however unrealistic to use a constant saturation model as it is clear that during field-weakening I_q approaches zero and hence L_q unsaturates. Better approximations to the actual saturation characteristics shown in Fig. 3.7 are the linear and quadratic saturation curves shown in Fig. 3.9. These can be defined in terms of a single parameter

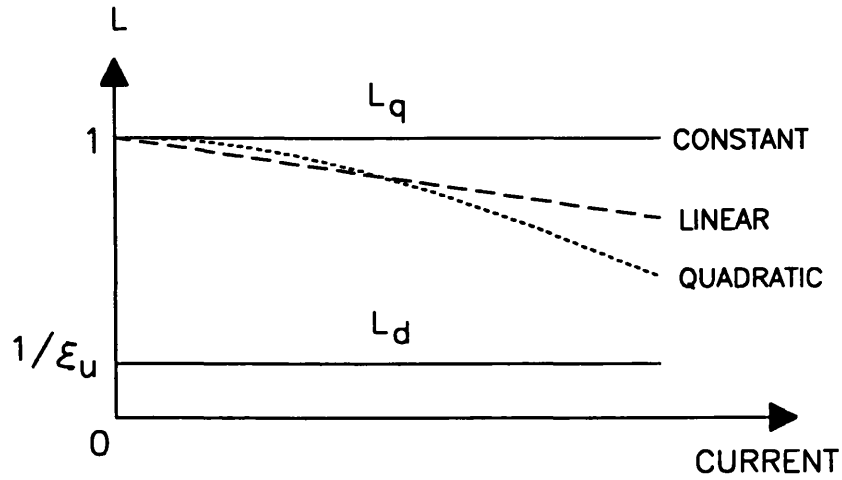

Figure 3.9: *Three saturation models.*

Table 3.1: *The saturation models*

Mode Type	L_q	L_d
constant	1	$1/\xi_u$
linear	$1-\alpha I_n$	$1/\xi_u$
quadratic	$1-\alpha I_n^2$	$1/\xi_u$

α as shown in Table 3.1. The saturation parameter α and the unsaturated saliency ratio ξ_u as functions of γ_m and ξ_s can be obtained for the general n-th order saturation characteristic $1-\alpha I_n^n$ by differentiating the torque expression and equating to zero :

$$\begin{aligned} \alpha &= \frac{\xi_s - 1}{\cos^n \gamma_m [\xi_s - 1 - (n\xi_s/2)\tan\gamma_m \tan 2\gamma_m]} \\ \xi_u &= \frac{\xi_s}{1-\alpha\cos^n\gamma_m} \end{aligned} \tag{3.8}$$

Using (3.8) the constant-power speed range can be calculated numerically using the equations given in Sec. 3.3. The results are plotted in Fig. 3.10 for n equals 1 (linear saturation) and 2 (quadratic saturation). The models predict the same constant-power speed range for unsaturated motors, however their predictions diverge as γ_m and hence the degree of saturation increases. The linear and quadratic models take into account

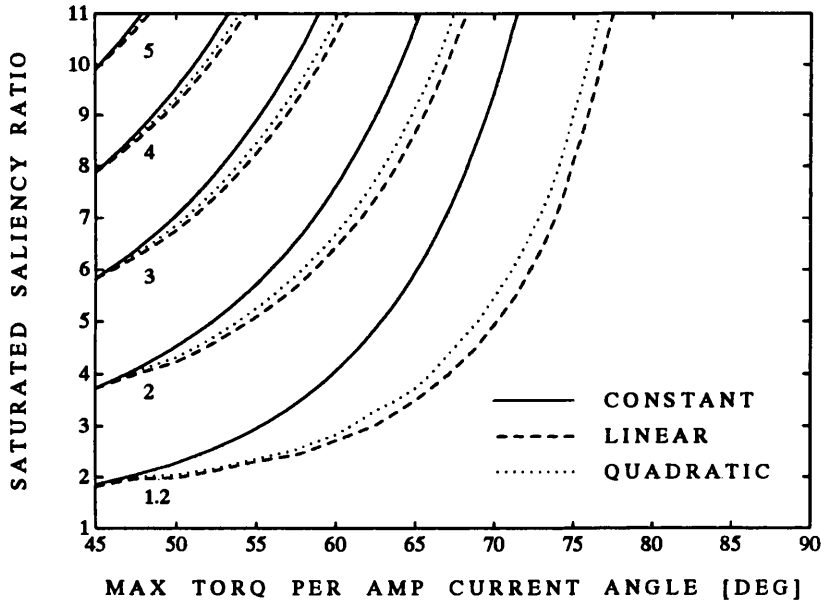

Figure 3.10: *Comparison of the CPSR predicted by the three saturation models.*

the lessening of saturation during field-weakening and hence show a greater constant-power speed range. The quadratic models predicts a slightly lower constant-power speed range than the linear model as it saturates less due to the steepness of quadratic saturation curve with increasing current. All three models predict a dramatic drop in the constant-power speed range with increasing saturation. The small difference between the results of the linear and quadratic saturation models indicate that using more refined models are unlikely to yield substantially different results. Note that typical designs show values of γ_m in the range 50° to 65°. The constant-power speed range of practical designs is discussed further in Sec. 3.4.3.

3.2.3 Iron Losses

In a synchronous machine, the two main types of iron losses are stator iron losses and rotor iron losses. The stator iron losses are caused by the rotation of the main flux distribution in the machine at synchronous speed. The flux is due to the stator currents and/or rotor magnets. The rotor iron losses are ideally zero in the steady-state as the

field distribution is stationary with respect to the rotor, however in practice pole-face losses and losses due to main flux variations can be significant.

Sources of Iron Loss

Iron losses can be split into two main components : *eddy-current* losses due to voltages induced in the laminations by the rate of change of flux and *hysteresis* losses due to flux reversals. To a first approximation the relationship between the total iron loss P_{fe}, the peak magnetic flux density $\hat{B}$ and the frequency f is given by [14] :

$$P_{fe} \approx \underbrace{K_e \hat{B}^2 f^2}_{\text{eddy-current}} + \underbrace{K_h \hat{B}^2 f}_{\text{hysteresis}} \tag{3.9}$$

where K_e and K_h are the eddy-current and hysteresis proportionality constants which depend on the lamination material used.

Consider the stator losses in an ideal field-weakening motor drive working in the constant-power operating region. In order to maintain the terminal voltage constant, the *fundamental* airgap flux must be inversely proportional to speed, that is $\hat{B} \propto 1/f$. From (3.9) the *fundamental* eddy-current losses would remain constant and the *fundamental* hysteresis losses would be approximately inversely proportional to frequency. The net result is that the fundamental iron losses will decrease with increasing speed.

Schiferl and Lipo [4] have shown that in permanent magnet machines, harmonic flux components can cause the harmonic iron losses to increase dramatically during field-weakening. In [56] they analysed a single-barrier interior permanent magnet motor drive and found that under low flux levels (ie. during field-weakening) the harmonic iron losses could be up to six times greater than the fundamental iron losses. The high harmonic iron losses were mainly caused by distortion of the airgap field due to the single-barrier construction. A multiple-barrier or axially-laminated construction should reduce the airgap flux distortion as well as require less magnet material and so reduce the harmonic flux levels.

Steady-state rotor iron losses in synchronous machines are due to pole-face losses and main flux variations. The pole-face losses are caused by rapid changes in the

local gap reluctance due to the interaction of the stator slotting and the rotor laminations. This loss occurs in all electrical machines but is especially important in axially-laminated motors. This is because the interleaved lamination and insulation layers cause the flux pulsations to spread through a substantial part of the rotor instead of being confined to the surface as in conventional machines [58, 59]. Marongui [59] shows that this can cause the rotor iron losses to be several times greater than the stator iron losses. Various techniques to reduce these losses have been proposed including : restricting the flux pulsations to the rotor surface by making the rotor segment pitch equal to, or a multiple of the stator tooth pitch [39]; increasing the rotor lamination thickness to decrease the peak flux density [7] and cutting radial slits in the the rotor to decrease the eddy-current losses [48].

Main flux variations are fluctuations in the total flux per pole Φ in reluctance machines caused by : non-sinusoidal stator winding distributions, having a non-integral number of slots per pole or by harmonics in the stator current. The latter effect is significant when using relatively low PWM frequencies.

Modelling the Iron Loss

To a first approximation, from (3.9), the fundamental iron loss can be conservatively modelled as :

$$P_{fe} \propto \hat{B}^2 f^2 \propto V_m^2 \tag{3.10}$$

This can be represented simply in the equivalent circuit as an iron loss resistance R_c as shown in Fig. 3.11.

Iron losses have two effects : they reduce the rated output power and increase γ_m [49]. The iron loss current $I_c = V_m/R_c$ decreases I_m but has little effect on V_m. If the iron losses are small, then from Fig. 3.11 the total inverter utilisation κ_T taking into account stator resistance and iron loss is :

$$\kappa_T \approx \kappa_R \left[1 - \frac{\kappa_R}{\kappa R_{cn}}\right] \tag{3.11}$$

The reduction in I_m will result in a small increase in the rated speed.

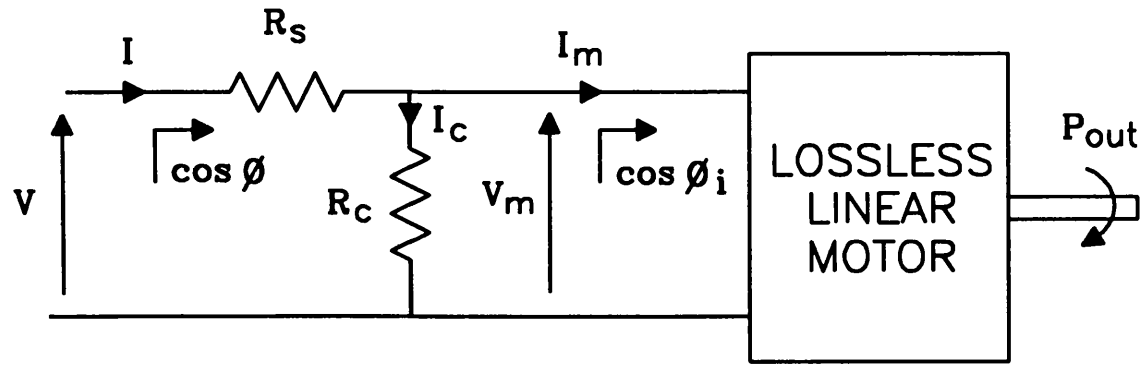

Figure 3.11: *Modelling the fundamental iron loss.*

The increase in γ_m with iron losses was investigated by Xu, Xu, Lipo and Novotny [49]. They showed that the increase is caused by a discrepancy between the *external* current-angle ($\tan\gamma = -I_d/I_q$) and the *internal* (or magnetising) current-angle ($\tan\gamma_i = -I_{dm}/I_{qm}$). The internal maximum-torque-per-ampere current-angle γ_{mi} is relatively unaffected by moderate levels of iron loss as it is mainly dependent on the saturation characteristics of the motor. In fact iron losses reduce the magnetising current I_m which reduces saturation. This causes γ_{mi} to reduce slightly when iron losses are modelled and also the saturated saliency ratio to increase slightly. Despite the slight reduction in γ_{mi} with iron losses, the external maximum-torque-per-ampere current-angle γ_m generally increases significantly due to I_c. This is analysed in greater detail in Sec. 3.3.2.

Using a similar argument as that used for stator resistance it can be shown that fundamental iron losses do not have a first order effect on the constant-power speed range (see Sec. 3.2.1). This is because at least for drives with a constant-power speed range in Mode II, the values of I_m and $\cos\phi_i$ and thus V_m are the same at w_k and w_p. Also, while iron loss increases γ_m, it does not cause substantial changes to γ_{mi} and it is γ_{mi} which mainly determines the constant-power speed range (at least for synchronous reluctance motor drives).

3.2.4 Other Factors

Two other factors which limit the achievable field-weakening range are the minimum magnet operating point and mechanical limitations.

Morimoto et al. [34] has shown that restrictions on the minimum magnet operating point to prevent permanent demagnetisation can drastically reduce the high-speed performance. Optimal field-weakening performance inherently requires that rated stator current in the d-axis be capable or reducing the effective d-axis flux-linkage to zero (see Sec. 2.1). Neglecting leakage, this means that the flux in the magnets must be reduced to zero (see Fig. 2.28). Magnet leakage flux and stator leakage inductance will however raise the minimum magnet operating point in practical designs. Demagnetisation withstand is thus an important consideration and some margin over the steady-state requirements is necessary to provide a measure of safety in coping with overload and transient conditions. This is examined using finite-element analysis in Sec. 5.3.3.

Finally mechanical strength limitations present the ultimate limitation to field-weakening performance. The design of high-speed switched-reluctance and induction motors [60] has been investigated, but that of synchronous reluctance motors is less well understood. A 24 000rpm, 1.3kW, salient-pole synchronous reluctance machine has been built by Chiba and Fukao [61], however the achieved saliency ratio of two to three is too low for good field-weakening performance. The mechanical limitations of axially-laminated designs is discussed in Sec. 5.2.2.

3.3 Practical Field-Weakening Control

This section shows how the field-weakening performance of interior permanent magnet motor drives incorporating stator resistance, magnetic saturation and fundamental iron loss can be calculated. It assumes that the optimal field-weakening control strategies calculated in Chapter 2 remain the same. This is valid as long as the resistance, saturation and iron loss are not substantial.

3.3.1 Lossless Linear Model

The control and performance of *normalised* lossless, linear interior permanent magnet motor drives was analysed in Sec. 2.4. This section uses the same models but derives equations in terms of *un-normalised* quantities. This is necessary to obtain the actual rather than the normalised torque versus speed curves.

A lossless linear interior permanent magnet motor drive can be characterised by seven parameters : the number of phases m, the number of pole-pairs p, the phase inductances L_q and L_d, the magnet flux Ψ_m and the inverter voltage V_c and current I_c ratings. Note that all the d- and q-axis voltages and currents are expressed as rms phase quantities. From (2.23) the DQ phase voltage equations are :

$$\left.\begin{array}{rcl} V_d &=& -w\xi L_d I_q \\ V_q &=& wL_d I_d + w\Psi_m \end{array}\right\} \quad \text{where} \quad \begin{array}{rcl} V &=& \sqrt{V_q^2 + V_d^2} \;\leq\; V_c \\ I &=& \sqrt{I_q^2 + I_d^2} \;\leq\; I_c \end{array} \tag{3.12}$$

where w is the electrical speed and $\xi = L_q/L_d$. Defining γ as the angle by which I leads the q-axis then $I_d = -I\sin\gamma$ and $I_q = I\cos\gamma$. Thus :

$$\left.\begin{array}{rcl} V_d &=& -w\xi L_d I\cos\gamma \\ V_q &=& -wL_d I\sin\gamma + w\Psi_m \end{array}\right\} \quad \text{where} \quad \begin{array}{rcl} V &=& \sqrt{V_q^2 + V_d^2} \;\leq\; V_c \\ I &=& \sqrt{I_q^2 + I_d^2} \;\leq\; I_c \end{array} \tag{3.13}$$

The electrical speed corresponding to a given phase voltage V, phase current I and current-angle γ can be found from (3.13) as :

$$\omega = \frac{V}{\sqrt{(\xi L_d I\cos\gamma)^2 + (-L_d I\sin\gamma + \Psi_m)^2}} \tag{3.14}$$

From (2.23) the output torque T is given by :

$$T = \Psi_m I_q - (\xi - 1) L_d I_q I_d \tag{3.15}$$

or in terms of γ, the torque is given as :

$$T = \Psi_m I \cos\gamma + \frac{1}{2}(\xi - 1) L_d I^2 \sin 2\gamma \tag{3.16}$$

The mechanical output torque T_m is given by :

$$T_m = mpT \tag{3.17}$$

The mechanical output speed ω_m is :

$$w_m = \frac{w}{p} \tag{3.18}$$

The mechanical output power P_m is :

$$P_m = T_m \omega_m \tag{3.19}$$

The electrical input power P_e is :

$$P_e = m\left[V_d I_d + V_q I_q\right] \tag{3.20}$$

The efficiency η is :

$$\eta = \frac{P_m}{P_e} \tag{3.21}$$

The power-factor $\cos\phi$ is given by :

$$\cos\phi = \frac{P_e}{mVI} \tag{3.22}$$

Mode I Operation

The maximum-torque-per-ampere current-angle γ_m is calculated by differentiating (3.16) with respect to γ with $I = I_c$:

$$\sin\gamma_m = \begin{cases} 0 & \xi = 1 \\ \dfrac{-\Psi_m + \sqrt{\Psi_m^2 + 8(\xi-1)^2 L_d^2 I_c^2}}{4(\xi - 1) L_d I_c} & \xi > 1 \end{cases} \tag{3.23}$$

The rated speed ω_k is obtained by substituting $\gamma = \gamma_m$, $V = V_c$ and $I = I_c$ into (3.14) to give :

$$\omega_k = \frac{V_c}{\sqrt{(\xi L_d I_c \cos\gamma_m)^2 + (-L_d I_c \sin\gamma_m + \Psi_m)^2}} \tag{3.24}$$

The rated torque T_k is obtained by substituting $\gamma = \gamma_m$ and $I = I_c$ into (3.16) to give :

$$T_k = \Psi_m I_c \cos\gamma_m + \frac{1}{2}(\xi - 1) L_d I_c^2 \sin 2\gamma_m \tag{3.25}$$

Mode II Operation

As the speed is increased, rated current is maintained in the motor and the current-angle is increased from γ_m to maintain rated voltage. For a given γ the Mode II speed and torque are given by substituting $V = V_c$ and $I = I_c$ into (3.14) and (3.16) giving :

$$\omega = \frac{V_c}{\sqrt{(\xi L_d I_c \cos\gamma)^2 + (-L_d I_c \sin\gamma + \Psi_m)^2}} \tag{3.26}$$

$$T = \Psi_m I_c \cos\gamma + \frac{1}{2}(\xi - 1) L_d I_c^2 \sin 2\gamma \tag{3.27}$$

Mode III Operation

Here the drive is purely voltage-limited and hence is operated at the maximum-torque-per-volt operating point [34]. Consider the operating point given by ΔI_d where :

$$I_d = -\Psi_m / L_d - \Delta I_d \tag{3.28}$$

Substituting this into (3.12) with $V = V_c$ gives :

$$I_q = \frac{\sqrt{(V_c/\omega)^2 - (L_d \Delta I_d)^2}}{\xi L_d} \tag{3.29}$$

Section 2.2 showed that $\Delta I_d = 0$ for surface permanent magnet motor drives during Mode III. Otherwise the value of ΔI_d which gives the maximum torque for a given voltage V_c and speed ω is obtained by substituting (3.28) and (3.29) into (3.15) and differentiating with respect to ΔI_d [34]. This gives :

$$\Delta I_d = \begin{cases} 0 & \xi = 1 \\ \dfrac{-\xi\Psi_m + \sqrt{(\xi\Psi_m)^2 + 8(\xi - 1)(V_c/\omega)^2}}{4(\xi - 1)L_d} & \xi \neq 1 \end{cases} \tag{3.30}$$

Thus for a given speed ω, the optimal value of I_d can be obtained from (3.28) and (3.30). The optimal I_q is obtained from (3.29) and the corresponding torque from (3.15). This assumes that the optimal control strategies derived for the lossless, constant parameter motor drive in Chapter 2 can also be applied to I_{qm} and I_{dm}. This is clearly only a first approximation, but should give reasonable results for small values of non-idealities.

3.3.2 Modelling Non-Idealities

Fig. 3.12 shows a steady-state equivalent circuit for a lossy interior permanent magnet motor drive. This is based on the equivalent circuit used by Betz [62]. The lossless equivalent circuit is shown to the right of the dashed line. Note that the d- and q-axis synchronous inductances have been split into a stator leakage inductance L_l and a magnetising inductance L_m. This allows the iron loss resistance R_c to appear across the airgap magnetising voltage V_m. The equivalent circuit shown allows different values of R_c in the two axes though in practice R_{qc} and R_{dc} are normally assumed to be equal [49, 62]. Due to the iron loss, the terminal current I is no longer equal to the magnetising current I_m. The phasor diagram corresponding to the equivalent circuit is given in Fig. 3.13.

Stator Resistance

From Fig. 3.12, adding stator resistance R_s to the linear lossless DQ voltage equations (3.12–3.13) yields :

$$\begin{aligned} V_d &= R_s I_d - w\xi L_d I_q \\ V_q &= R_s I_q + wL_d I_d + w\Psi_m \end{aligned} \tag{3.31}$$

and in terms of γ :

$$\begin{aligned} V_d &= R_s I_d - w\xi L_d I\cos\gamma \\ V_q &= R_s I_q - wL_d I\sin\gamma + w\Psi_m \end{aligned} \tag{3.32}$$

In order to calculate the motor drive operating characteristics in Mode II and III it is necessary to calculate the speed ω corresponding to a given value of I_d and I_q when

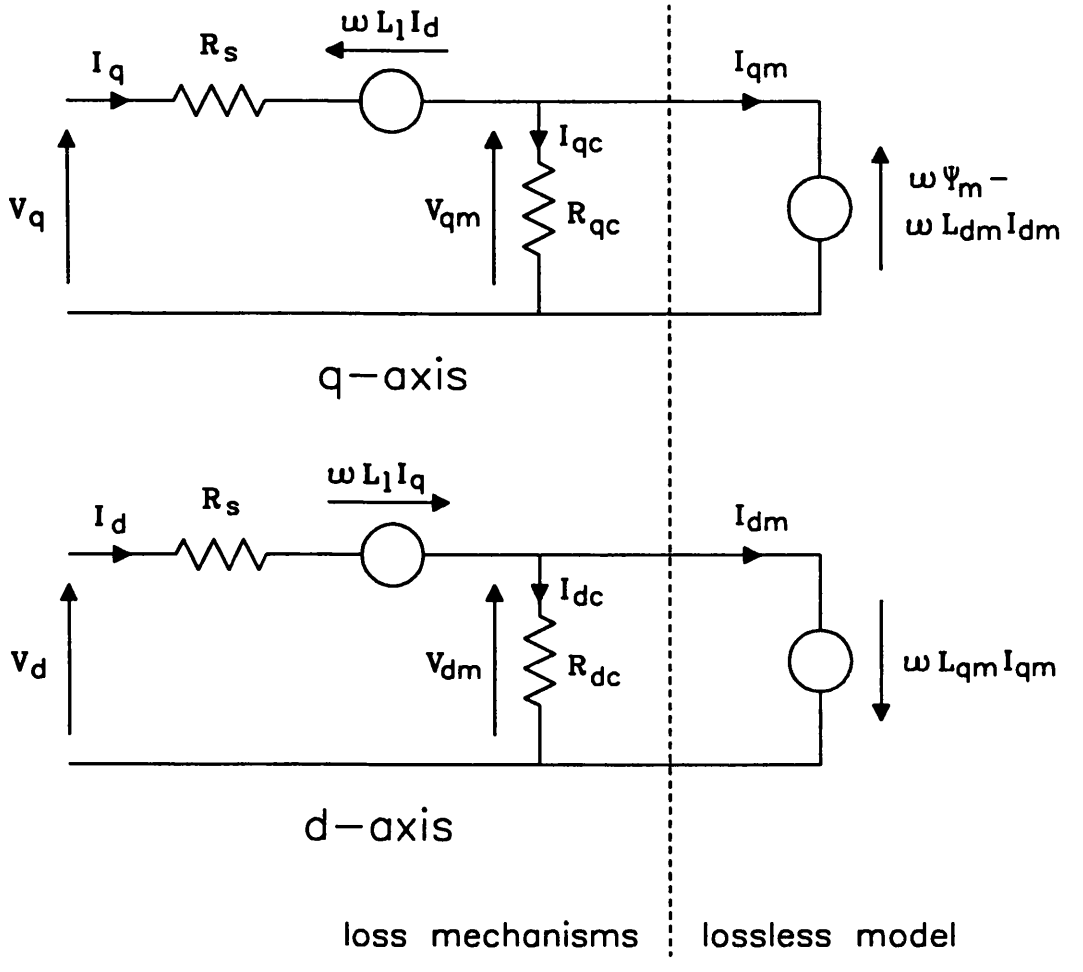

Figure 3.12: *Steady-state equivalent circuit for a lossy* IPM *motor drive.*

$V = V_c$. For simplicity it is convenient to rewrite (3.31) as :

$$\begin{aligned} V_d &= R_s I_d - \omega K_d \\ V_q &= R_s I_q + \omega K_q \end{aligned} \tag{3.33}$$

where K_d and K_q are two constants, defined as :

$$\begin{aligned} K_d &\equiv L_q I_q \\ K_q &\equiv L_d I_d + \Psi_m \end{aligned}$$

Applying $V_c^2 = V_d^2 + V_q^2$ gives :

$$\omega = \frac{-B \pm \sqrt{B^2 - 4AC}}{2A} \tag{3.34}$$

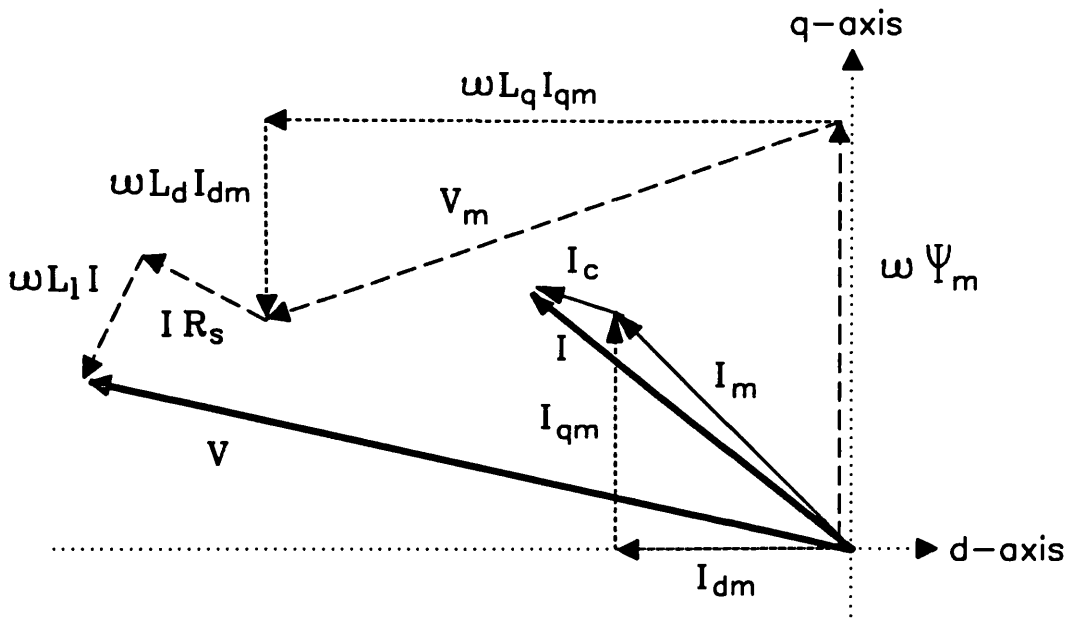

Figure 3.13: *Phasor diagram for a lossy interior permanent magnet motor drive.*

where :

$$\begin{aligned} A &= K_d^2 + K_q^2 \\ B &= 2R_s(-K_d I_d + K_q I_q) \\ C &= R_s^2(I_d^2 + I_q^2) - V_c^2 \end{aligned}$$

Magnetic Saturation

In general this can be taken into account by making L_d and L_q arbitrary functions of I_d and I_q respectively. The Mode I and II trajectories are still well defined, but the Mode III trajectory (3.28–3.30) generally requires some iteration.

Iron Losses

From inspection of the full equivalent circuit in Fig. 3.12 the following equations can be obtained :

$$\left.\begin{aligned} I_q &= I_{qm} + \frac{V_{qm}}{R_{qc}} \\ I_d &= I_{dm} + \frac{V_{dm}}{R_{dc}} \end{aligned}\right\} \tag{3.35}$$

$$\left.\begin{aligned} V_{qm} &= \omega\Psi_m + \omega L_{dm} I_{dm} \\ V_{dm} &= -\omega L_{qm} I_{qm} \end{aligned}\right\} \tag{3.36}$$

where ω is the electrical speed. Rearranging (3.35–3.36) for I_{qm} and I_{dm} in terms of I_q and I_d gives :

$$I_{qm} = \frac{R_{dc}(R_{qc} I_q - \omega\Psi_m - \omega L_{dm} I_d)}{R_{dc} R_{qc} + \omega^2 L_{dm} L_{qm}} \tag{3.37}$$

$$I_{dm} = \frac{R_{dc} R_{qc} I_d + \omega L_{qm} R_{qc} I_q - \omega^2 \Psi_m L_{qm}}{R_{dc} R_{qc} + \omega^2 L_{dm} L_{qm}} \tag{3.38}$$

Due to saturation $L_{dm} = f_1(I_{dm})$ and $L_{qm} = f_2(I_{qm})$ and so it is necessary to iteratively solve these equations. The initial estimate of L_{dm} and L_{qm} is obtained by assuming $I_{dm} = I_d$ and $I_{qm} = I_q$. Once I_{dm} and I_{qm} have been obtained, the output torque can be obtained from (3.15) as :

$$T = \Psi_m I_{qm} - (L_{qm} - L_{dm}) I_{qm} I_{dm} \tag{3.39}$$

The d- and q-axis voltage equations can be obtained from Fig. 3.12 as :

$$\begin{aligned} V_q &= I_q R_s + \omega(\Psi_m + L_l I_d + L_{dm} I_{dm}) \\ V_d &= I_d R_s - \omega(L_l I_q + L_{qm} I_{qm}) \end{aligned} \tag{3.40}$$

During Mode II and III, $V = V_c$ and (3.40) can be solved using (3.33–3.34) to give ω. The other performance parameters of the motor drive can then be found from (3.17–3.22).

The effect of iron loss on γ_m and on the synchronous reluctance motor drive torque versus angle characteristic at rated current and speed will now be examined and quantified. From (3.37–3.38), for a synchronous reluctance motor drive ($\Psi_m = 0$) with

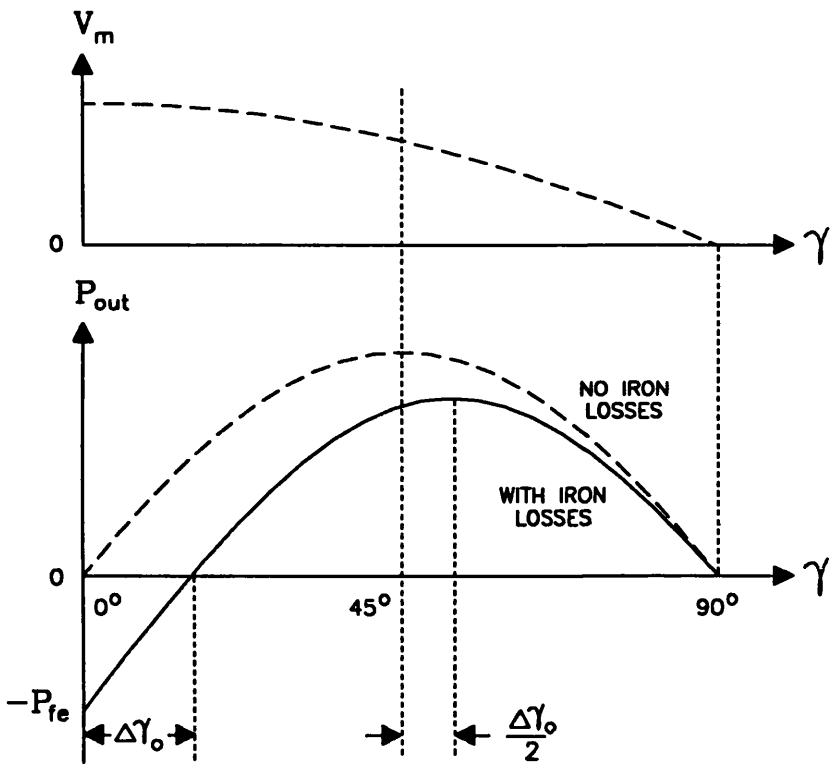

Figure 3.14: *Power and magnetising voltage versus current-angle for a synchronous reluctance motor drive operated at rated current and speed.*

high saliency ($L_{dm} \approx 0$), low iron loss, equal iron loss resistances ($R_{dc} = R_{qc} = R_c$), operating at rated current I_c then :

$$I_{qm} \approx I_c \cos\gamma \tag{3.41}$$

$$I_{dm} \approx -I_c \sin\gamma + \left(\frac{wL_{qm}I_c}{R_c}\right)\cos\gamma \tag{3.42}$$

As the saliency ratio is high, $V_{qm} \ll V_{dm}$ and so :

$$V_m \approx V_{dm} = -wL_{qm}I_c \cos\gamma \tag{3.43}$$

As iron losses are proportional to V_m^2, thus the losses will be largest at $\gamma = 0°$ and zero at $\gamma = 90°$. This is shown in Fig. 3.14.

Iron losses cause the internal current-angle γ_i to be less than the external current-angle γ. In fact when $\gamma = 0°$, $\gamma_i < 0°$ and so the torque is negative. Defining $\Delta\gamma$ as

the difference between the external and internal current-angles gives :

$$\Delta\gamma \equiv \gamma - \gamma_i \tag{3.44}$$

then from (3.42) the zero torque point occurs when $I_{dm} = 0$ and $\gamma = \Delta\gamma_o$:

$$\Delta\gamma_o \approx \arctan\left(\frac{wL_{qm}}{R_c}\right) \tag{3.45}$$

This is illustrated in Fig. 3.14. In order to determine R_c it is sometimes convenient to measure the (negative) output power at $\gamma = 0°$. With $\gamma = 0°$, using Fig. 3.12 the iron losses are $P_{fe} = V_m^2/R_c$ while the input electrical power is $P_e \approx V_{qm}I_{qm}$. From (3.43) it can be shown that $P_e/P_{fe} \approx 1/\xi_m$ where ξ_m is the *magnetising saliency ratio* L_{qm}/L_{dm}. Hence the mechanical output power $P_m = P_e - P_{fe}$ is given by :

$$P_m(\gamma = 0°) \approx -P_{fe}(\gamma = 0°)\left[1 - \frac{1}{\xi_m}\right] \tag{3.46}$$

Thus for moderate values of iron loss, the (negative) mechanical output power at $\gamma = 0°$ is equal to the iron loss if the saturated magnetising saliency ratio is high.

From Fig. 3.14, for an infinitely salient synchronous reluctance motor drive $\Delta\gamma$ is zero at 90° ($V_m = 0$) and approximately $\Delta\gamma_o$ at 0°. To a first approximation $\Delta\gamma$ decreases linearly from $\gamma = 0°$ to $\gamma = 90°$. Neglecting saturation the maximum-torque-per-ampere current-angle $\gamma_{mi} = 45°$ and thus γ_m will be shifted by about half of $\Delta\gamma_o$, that is $\gamma_m \approx \gamma_{mi} + \Delta\gamma_o/2$.

3.4 Validation of Results

This section validates the results of the earlier work in this chapter with experimental measurements. It consists of three parts. Firstly the torque versus current-angle characteristics of a surface permanent magnet and two synchronous reluctance motor drives are modelled. Next the calculated and measured field-weakening performance is compared. Finally the last section examines the constant-power speed range achieved by a selection of synchronous reluctance motor drive designs.

3.4.1 Torque versus Current-Angle Characteristics

This section models the performance of a 2kW surface permanent magnet motor drive and a 120W and a 2kW synchronous reluctance motor drive. The main parameters of the drives are given in Table 3.2. Note that the two 2kW motors were operated at about one quarter of rated voltage in order to keep the field-weakening characteristics within the 4000rpm dynamometer maximum speed restriction. Theoretically this should increase the per-unit copper losses four times and decrease the per-unit iron

Table 3.2: *Main parameters of the motor drives tested.*

	Synchronous Reluctance		Surface PM
	120W	2kW	2kW
nominal torque [Nm]	1	3	4
nominal rated speed [rpm]	1600	6000	6000
pole-pairs	2	2	2
rated voltage V_c [V_{ll} rms]	110	$380/\sqrt{2}$	$380/\sqrt{2}$
rated current I_c [A rms]	1.7	6	6
base voltage V_o [V_{ll} rms]	110	$100/\sqrt{2}$	$100/\sqrt{2}$
base current I_o [A rms]	1.7	6	6
R_{sn} [pu]	0.21	0.15	0.153
R_{cn} [pu]	12.6	8.8	44
CPSR	2	1.3	2

losses four times.

The 2kW surface permanent magnet motor drive is a commercial unit designed for servo applications and uses samarium-cobalt magnets. It shows little saturation, high copper losses, low iron losses and a constant-power speed range of about two. The 120W and 2kW synchronous reluctance motor drives are custom-built axially-laminated designs (see App. A). The 120W synchronous reluctance motor uses an induction motor stator and was operated at rated voltage. It shows moderate saturation, high copper losses, moderate iron losses and a constant-power speed range of about two. The 2kW synchronous reluctance motor uses the same stator as the surface permanent magnet motor and was also operated at reduced voltage. It shows heavy saturation, high copper losses, moderate iron losses and a low constant-power speed range of about 1.3.

The surface permanent magnet motor and synchronous reluctance motor saturation characteristics were obtained from instantaneous flux-linkage tests (see Sec. 4.4.2). Care is required in measuring the d-axis surface permanent magnet motor inductance as the promagnetising characteristic is substantially different from the demagnetising characteristic due to the magnet flux causing saturation (see Sec. 3.2.2). The measured flux-linkage results for the 2kW surface permanent magnet motor drive design are shown in Fig. 3.15. Note that the q-axis characteristic is relatively symmetrical while the d-axis curve is "offset" due to the magnet flux producing a "DC flux bias".

The torque versus current-angle characteristic is shown in Fig. 3.16 at rated current at 3000rpm. It compares the measured characteristic with the calculated characteristic using :

- a lossless constant unsaturated parameter model,
- a lossless saturating model,
- a saturating model taking into account iron losses.

It shows that for surface permanent magnet designs, saturation and iron losses have relatively little effect on the torque versus current-angle curve. However they need to

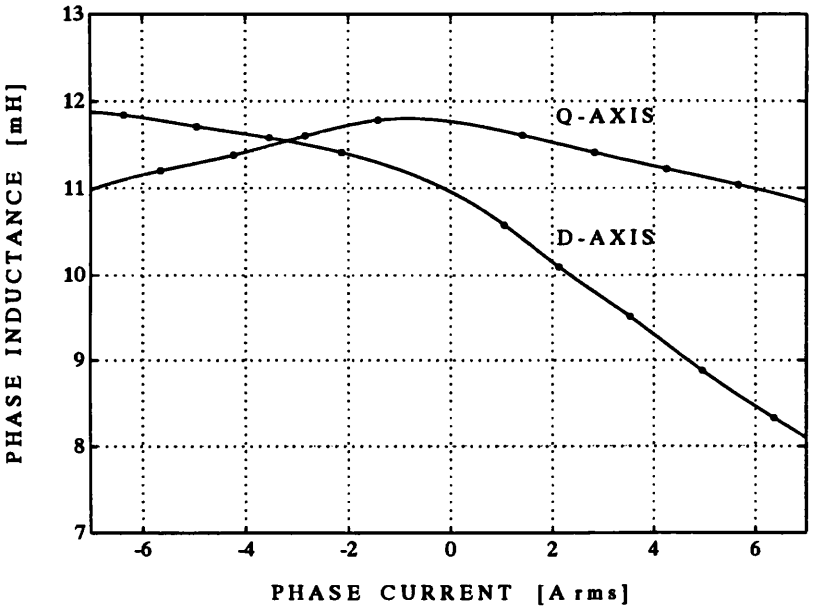

Figure 3.15: *Measured 2kW* SPM *flux-linkage test results.*

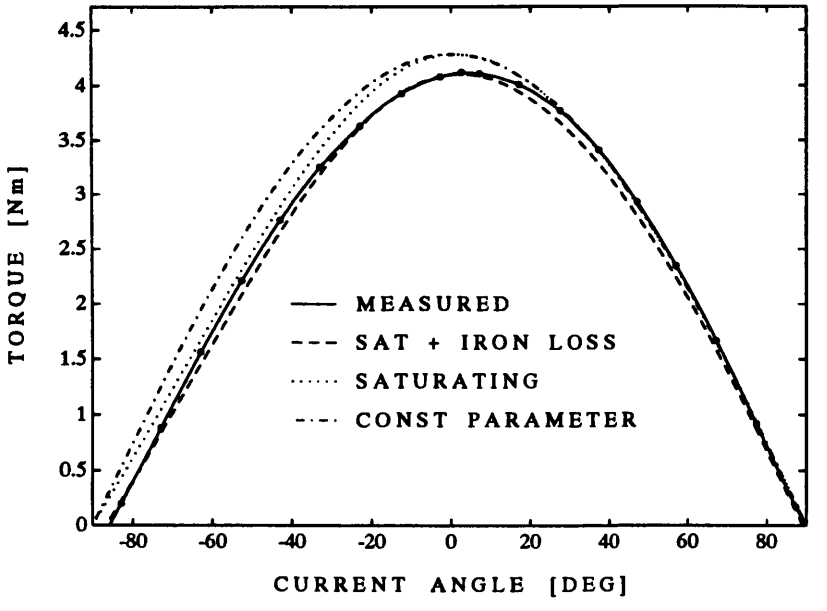

Figure 3.16: *2kW* SPM *torque versus current-angle results.*

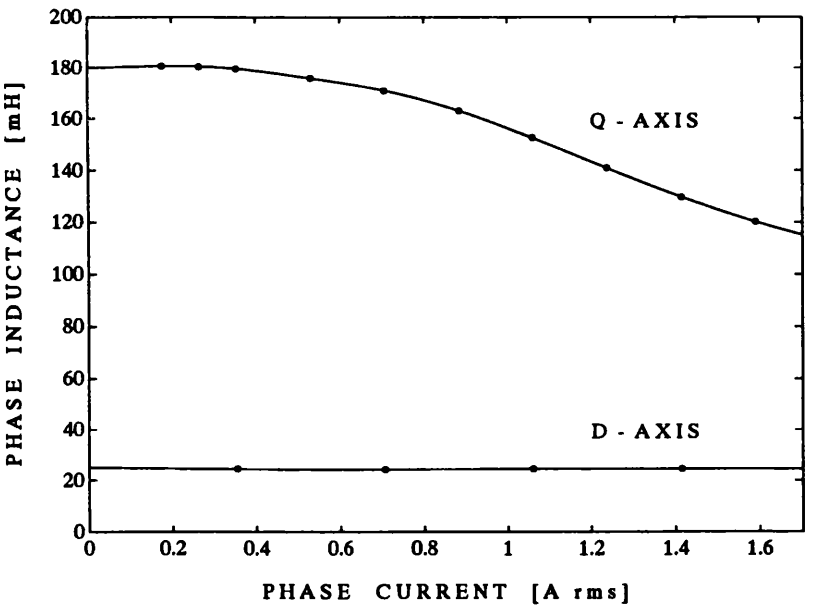

Figure 3.17: *Measured 120W* SYNCHREL *flux-linkage results.*

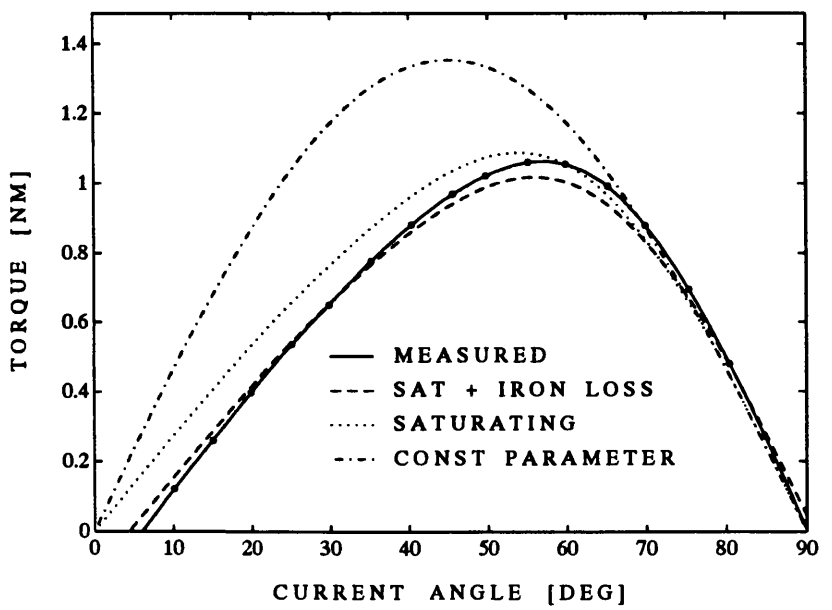

Figure 3.18: *120W* SYNCHREL *torque versus current-angle results.*

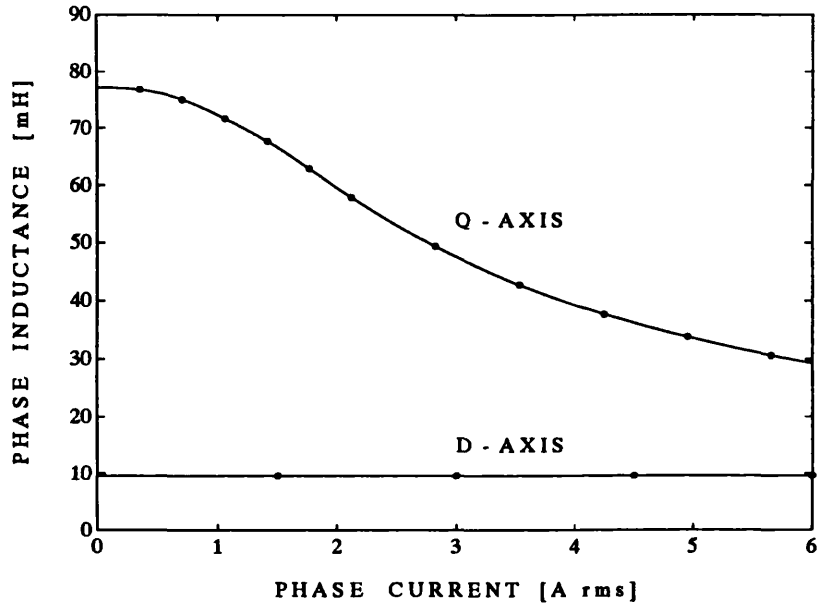

Figure 3.19: *Measured 2kW* SYNCHREL *flux-linkage test results.*

be taken into account to get the best match between theory and experiment. Note that iron losses cause the torque to become negative at $\gamma = -90°$.

Fig. 3.17 shows the measured flux-linkage versus current characteristics for the 120W synchronous reluctance motor drive. The shape of the curves is typical of synchronous reluctance motor drives, though perhaps showing somewhat less saturation than normal (see Fig. 3.7). The torque versus current-angle characteristics are shown in Fig. 3.18 at rated current at 1500rpm. A comparison of the calculated characteristics using constant unsaturated inductances against that taking into account saturation shows that saturation causes a substantial reduction in the maximum output torque and an increase in the maximum-torque-per-ampere current-angle beyond 45°. Adding iron losses further decreases the output torque and causes output power to become negative at $\gamma = 0°$. These results were predicted in Sec. 3.2. The full model provides a good match with the measured results.

Fig. 3.19 shows the measured flux-linkage characteristics for the 2kW synchronous reluctance motor drive. This shows considerably more saturation than the 120W design

due to the thin stator teeth and high electric loading in the surface permanent magnet motor stator used. In fact the excessive saturation causes the performance to be rather poor, however this is a useful characteristic when one is testing the accuracy of models as it turns second order effects into first order ones!

3.4.2 Modelling the Field-Weakening Characteristics

The field-weakening performance of the motors was measured using a custom-built 7.5kW, 5kHz IGBT inverter with a hysteresis current controller. This is described in Appendix A. The current magnitude and angle were varied manually to determine the maximum torque at a given speed within the motor's voltage and current-limit constraints. Table 3.3 shows a comparison between the measured, calculated and approximated performance of the two synchronous reluctance motor drive designs. The measured results are shown in bold on the top row for each motor drive and are compared against that predicted by the equivalent circuit model and that obtained from simple approximations. The inverter utilisation is estimated using (3.3) and (3.11). The constant-power speed range is estimated from the saliency and γ_{mi} using Fig. 3.10.

The first three rows represent three constant parameter models. The unsaturated ($\xi_u, \gamma_m = 45°$) and saturated ($\xi_s, \gamma_m = 45°$) lossless constant parameter models considerably overestimate the output torque and constant-power speed range. Adding stator resistance and iron loss to the constant parameter saturated model ($\xi_s + R_s + R_c$) shows that iron loss increases γ_m and that it causes a difference between γ_m and γ_{mi}. As predicted, γ_{mi} and the constant-power speed range only change slightly when iron losses are taken into account. Thus iron loss and stator resistance have little effect on the constant-power speed range of synchronous reluctance motors.

Modelling the saturation characteristics (ξ) considerably alters γ_{mi} and dramatically decreases the constant-power speed range. The estimates produced by the three saturation models (constant, linear and quadratic) give a fair estimate of the constant-power speed range. Note that as expected, the constant saturation model underestimates the calculated constant-power speed range obtained from the measured saturation charac-

Table 3.3: *Comparison of measured and calculated synchronous reluctance motor drive results. The arrows indicate the value at that location is the same as that pointed to.*

	Calculated From Equivalent Circuit Model							Approximations			
	ξ (sat)	γ_m	γ_{mi}	T_k Nm	w_k rpm	κ	CPSR	κ	CPSR cons	CPSR linear	CPSR quad
120W SYNCHREL											
measured		**56.5°**		**1.067**	**1580**	**0.545**	**2.13**				
$\xi_u, \gamma_m = 45°$	7.35	→	45°	1.348	1388	0.605	3.74		←	←	←
$\xi_s, \gamma_m = 45°$	6.37	→	45°	1.141	1596	0.589	3.26		←	←	←
$\xi_s + R_s + R_c$	6.37	48.3°	45.1°	1.048	1425	0.483	3.25	0.473	3.25	3.25	3.25
ξ	6.37	→	53.9°	1.088	1892	0.666	2.43		2.32	2.50	2.45
$\xi + R_s$	6.37	→	53.9°	↑	1604	0.564	↑	0.564	↑	↑	↑
$\xi + R_s + R_c$	6.44	55.9°	53.1°	1.012	1624	0.531	2.52	0.526	2.42	2.59	2.54
2kW SYNCHREL											
measured		**64.8°**		**3.28**	**1180**	**0.551**	**1.26**				
$\xi_u, \gamma_m = 45°$	8.46	→	45°	7.72	563	0.619	4.29		←	←	←
$\xi_s, \gamma_m = 45°$	5.26	→	45°	4.41	895	0.563	2.73		←	←	←
$\xi_s + R_s + R_c$	5.26	50.0°	45.2°	3.89	858	0.476	2.70	0.458	2.71	2.71	2.71
ξ	5.26	→	62.9°	3.58	1324	0.676	1.59		1.25	1.56	1.51
$\xi + R_s$	5.26	→	62.9°	↑	1179	0.602	↑	0.602	↑	↑	↑
$\xi + R_s + R_c$	5.40	66.2°	62.0°	3.26	1199	0.557	1.66	0.541	1.34	1.64	1.58

teristic, while the linear and quadratic saturation models give better estimates. The closeness of the match between the shape of the actual saturation characteristic and that of the model used determines the accuracy. For the 120W motor the saturation characteristic is closer to the quadratic saturation model while for the 1kW the linear model is closer. These are reflected in the accuracy of the predictions.

Adding stator resistance ($\xi + R_s$) and iron loss ($\xi + R_s + R_c$) to the model shows again that iron loss affects γ_m. Note that γ_{mi} decreases slightly and the saturated saliency ratio increases slightly with iron loss due to the reduced magnetising current. This was not seen with the ($\xi_s + R_s + R_c$) model as saturation was not modelled.

The full model ($\xi + R_s + R_c$) produces a more accurate estimate of the constant-

Table 3.4: *Comparison of measured and calculated* SPM *results.*

	Calculated From Equivalent Circuit Model							Approximations
	ξ (sat)	γ_m	γ_{mi}	T_k Nm	w_k rpm	κ	CPSR	κ
2kW SPM measured		**3.6°**		**4.13**	**1250**	**0.736**	**1.98**	
ξ_{unsat}	1.08	→	2.6°	4.29	1435	0.876	1.87	
ξ	1.02	→	0.7°	4.28	1436	0.876	2.01	
$\xi + R_s$	1.02	→	0.7°	↑	1236	0.754	2.01	0.758
$\xi + R_s + R_c$	1.02	1.3°	0.8°	4.21	1238	0.743	1.95	0.744

power speed range than the constant parameter models but still overestimates the actual constant-power speed range by about 20 to 30%. This is probably due to harmonic iron losses making the total iron loss increase more rapidly with speed than predicted by the fundamental equivalent circuit. This is exacerbated by the relatively low peak output power compared to the rated output power due to the high stator resistance (see Sec. 3.2.1).

With regard to the inverter utilisation κ, the full models show a good match with the measured characteristics. Note that κ shows only small variations with the different models as changes in the rated output torque T_k are partially compensated by opposite changes in the rated speed ω_k. The approximate formula (3.11) shows a reasonable match with the full model.

The surface permanent magnet motor drive characteristics in Table 3.4 show similar results. Using an unsaturated constant parameter, lossless model the constant-power speed range is underestimated as L_d is underestimated (see Fig. 3.15). Once the full saturation characteristic is modelled (ξ) the constant-power speed range is closely predicted. As with synchronous reluctance motor drives, modelling iron losses increases γ_m while not significantly affecting γ_{mi}.

Unlike synchronous reluctance motor drives, the constant-power speed range of surface permanent magnet motor drives appears to be sensitive to iron losses. The constant-power speed range of the 2kW drive showed a small decrease (3%) with adding

a small iron loss (R_{cn} = 44pu). Using a more reasonable (full voltage) iron loss resistance of R_{cn} = 15pu gave a significant 10% reduction in the constant-power speed range compared to that with no iron losses. Note that this is still a small reduction compared to what substantial drop caused by saturation in synchronous reluctance motor drives.

The torque and power versus speed test results for the 2kW surface permanent magnet and 120W synchronous reluctance motor drive are shown in Figs. 3.20 and 3.21. Both drives showed operation in Mode I and II. The synchronous reluctance motor drive reached Mode III operation at about 4100rpm. The effect of using a fixed current-angle γ_m (ie. no field-weakening) was also measured.

The solid lines show the measured characteristics. With no field-weakening the output torque above rated speed falls sharply while with field-weakening a constant-power speed range of about two is achieved with both drives.

The dash-dot curves show the calculated characteristics with an unsaturated constant parameter lossless model ($\xi_u, \gamma_m = 45^o$). Comparing it with the measured surface permanent magnet characteristic shows the effect of stator resistance in reducing the magnetising voltage and hence the power in the field-weakening region. Saturation substantially alters both the low speed and field-weakening characteristics of synchronous reluctance motor drives, while in surface permanent magnet motor drives it tends to affect only the field-weakening characteristics.

The dotted curves are the calculated characteristics including saturation and stator resistance ($\xi + R_s$). These yield a better match to the measured characteristics.

Finally the dashed curves show the effect of including iron loss ($\xi + R_s + R_c$) into the previous model. Note the good correspondence between the calculated and the actual control characteristics. The small residual difference between the calculated and measured power characteristics could be due to the harmonic iron loss, d-q cross-coupling or friction and windage losses.

A summary of the effects of the stator resistance, magnetic saturation and iron loss on field-weakening performance of the 2kW surface permanent magnet and 120W

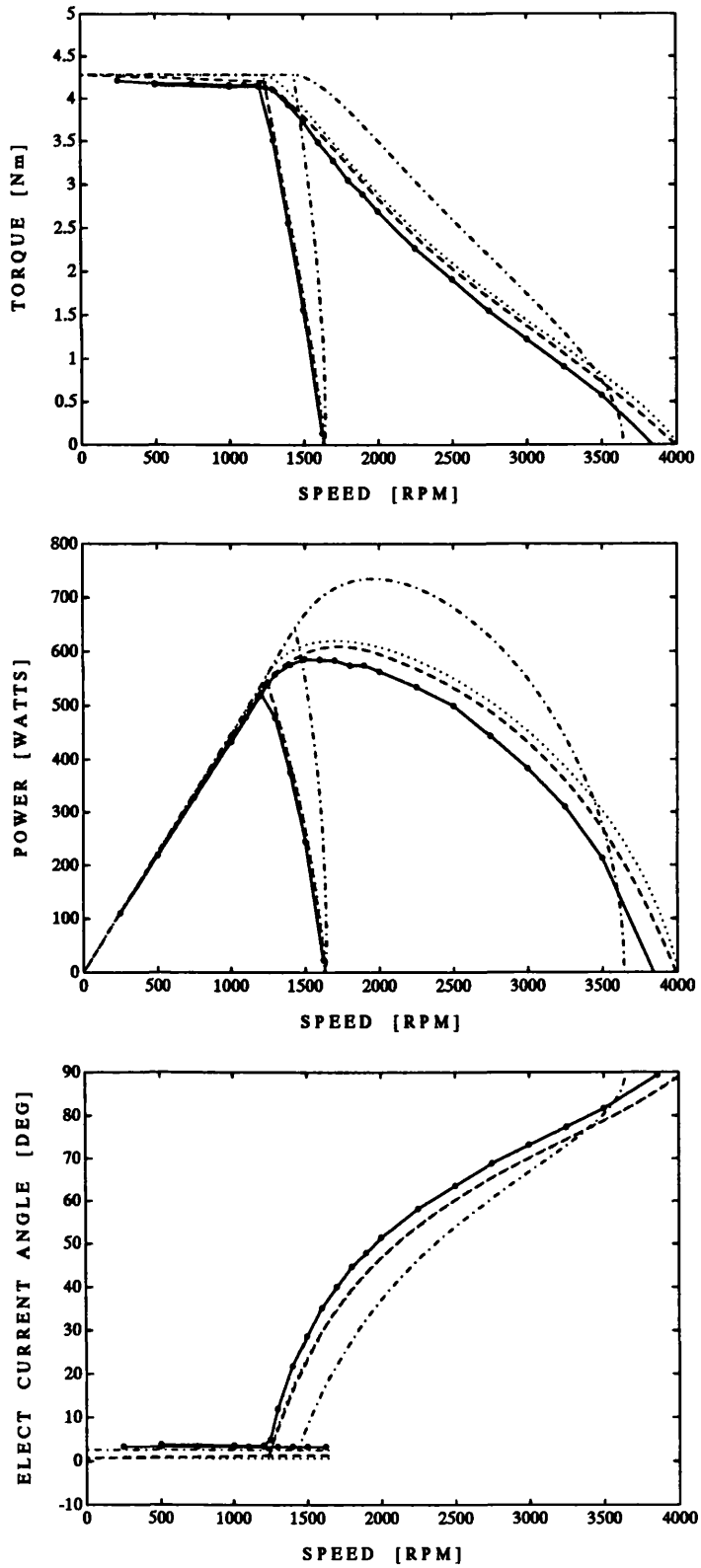

Figure 3.20: *2kW SPM performance with and without field-weakening. Measured results (solid line), lossless linear unsaturated model (dash-dot line), model including saturation and stator resistance (dotted line) and full model (dashed line)*

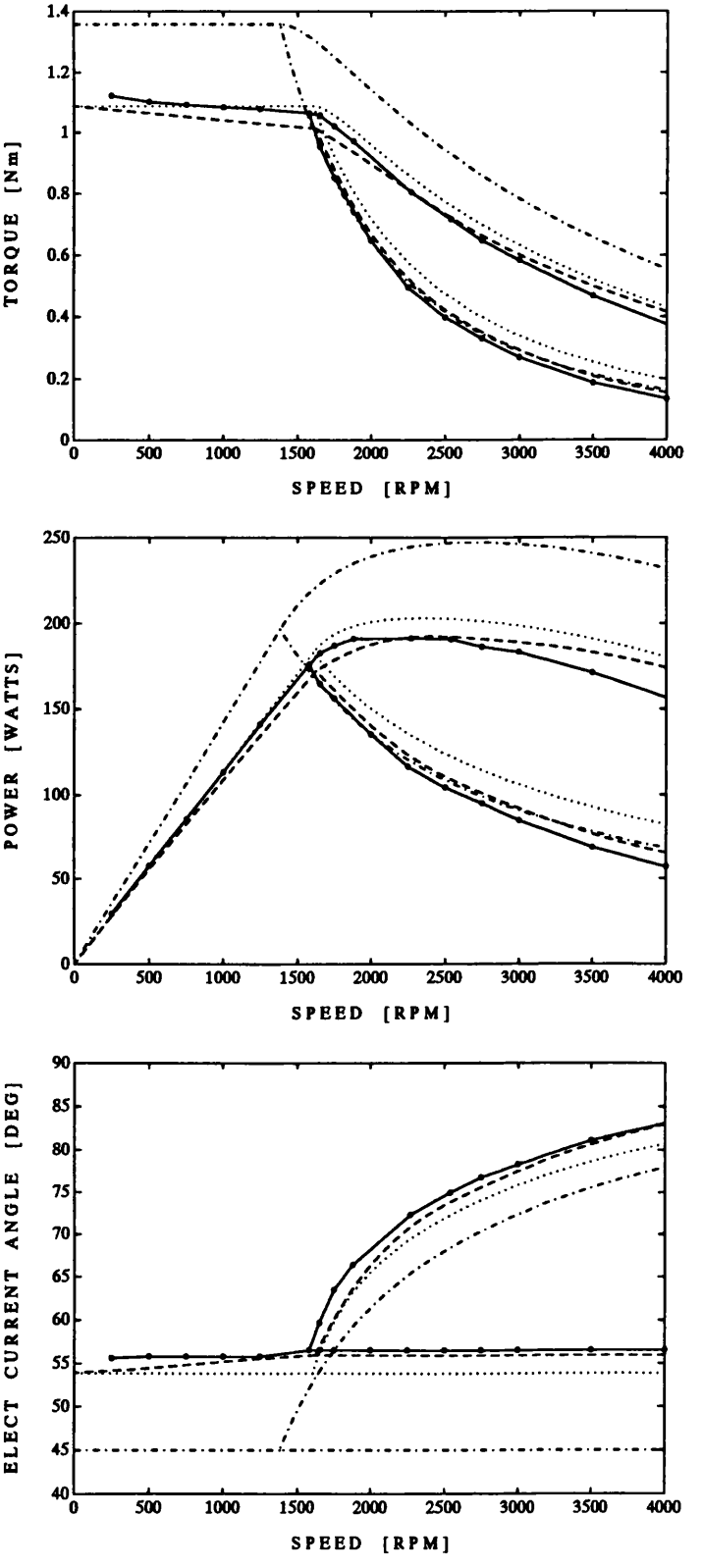

Figure 3.21: *120W* SYNCHREL *performance with and without field-weakening. Measured results (solid line), lossless linear unsaturated model (dash-dot line), model including saturation and stator resistance (dotted line) and full model (dashed line).*

Table 3.5: *Summary of effects of practical factors.*

	1kW SPM			120W Synchrel		
	T_k	κ	CPSR	T_k	κ	CPSR
Copper Loss	0%	-14%	0%	0%	-15%	0%
Saturation	-0.2%	0%	+8%	-20%	+22%	-35%
Iron Loss	-1.6%	-1.5%	-3%	-7%	-6%	+4%

synchronous reluctance motors is shown in Table 3.5. This clearly shows the sensitivity of synchronous reluctance designs to saturation.

3.4.3 Achievable CPSR of Synchronous Reluctance Drives

Section 3.2.2 discussed a technique for estimating the reduction in the constant-power speed range in synchronous reluctance motor drives due to γ_{mi} being greater than 45° due to saturation. This section examines how this affects practical designs.

Table 3.6 shows the measured or calculated constant-power speed range for seven synchronous reluctance motor designs. The first four were built in the department and consist of three axially-laminated designs and one single-barrier design. Design #5 is calculated from the measured inductance characteristics of an axially-laminated interior permanent magnet motor drive (see Chapter 6). Designs #6 and #7 are from published experimental inductance characteristics for two axially-laminated designs [48, 50].

The designs are illustrated in Fig. 3.22. Note that most designs have constant-power speed ranges of 2 to 3:1.

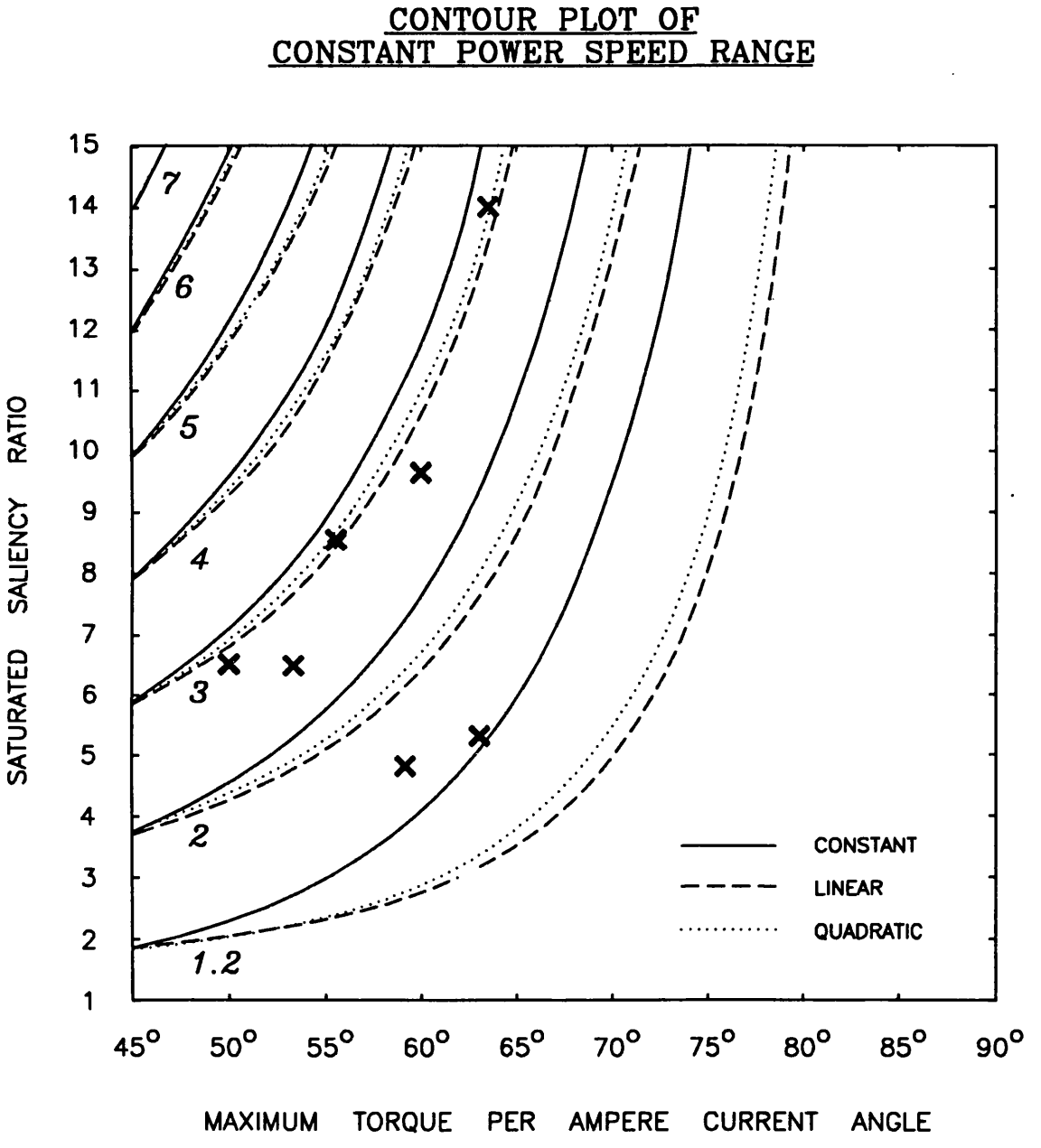

Figure 3.22: *Location of practical* SYNCHREL *designs on* CPSR *contour plot.*

Table 3.6: *Effect of saturation on the measured* CPSR *of* SYNCHRELs. *(* = calculated* CPSR*).*

No.	Power	Pole-Pairs	ξ_u	ξ_s	γ_{mi}	CPSR
1	120W	2	7.35	6.37	53.9°	2.1
2	1kW	2	8.46	5.26	62.9°	1.3
3	7.5kW	2	11.5	9.6	60°	2.5
4	7.5kW	2	6.5	4.8	59°	2
5	7.5kW	2	6.7	6.4	50.2°	2.75 (*)
6	1.5kW	1	21.1	14	63.8°	3.1 (*)
7	120W	2	10.5	8.5	55.6°	2.95 (*)

3.5 Practical Optimal Field-Weakening Designs

The effect of stator resistance, magnetic saturation and iron losses on the field-weakening performance of surface permanent magnet and synchronous reluctance motors was examined. The effects were analysed and the results obtained validated by experimental tests.

Stator resistance and iron losses do not have much effect on the constant-power speed range of surface permanent magnet and synchronous reluctance motor drives, however they do reduce the inverter utilisation. With moderate values of iron loss, the two synchronous reluctance motor drives showed no significant change in constant-power speed range while the surface permanent magnet motor drive showed a small (10%) reduction.

Saturation has little effect on the field-weakening performance of surface permanent magnet motor drives due to the low inductances involved. However it was found that the performance of synchronous reluctance motor drives was substantially affected. This is because the increase in the maximum-torque-per-ampere current-angle due to saturation reduces the field-weakening range dramatically. For instance a design with a unsaturated saliency ratio of 21 and a saturated saliency ratio of 14 has a theoretical constant-power speed range of about 7:1 but in practice it is only about 3:1. Examining a number of designs spanning 120W to 7.5kW showed that a constant-power speed range of 2 to 3:1 is typical. Careful optimisation may improve this somewhat but it would be difficult to improve this substantially.

In conclusion the field-weakening performance of synchronous reluctance motor drives is generally limited by saturation to a constant-power speed range of about two to three. Hence from the results of Sec. 2.6, high-saliency axially-laminated interior permanent magnet motor drives offer the best option for a wide field-weakening performance. The design, modelling and testing of such motor drives are examined in the second part of this thesis.

Part II

Design of Axially-Laminated Motor Drives for Field-Weakening Applications

Chapter 4

Modelling Axially-Laminated Motors

In Chapter 3 it was concluded that the optimum practical field-weakening performance would be achieved by high-saliency axially-laminated interior permanent magnet motor designs. The remainder of this thesis examines the modelling, design, construction and testing of such motors.

This chapter examines the modelling of axially-laminated synchronous reluctance motors. This is because an optimal field-weakening, high-saliency interior permanent magnet motor drive generates the majority of its output torque from its reluctance nature. An understanding of the modelling of the reluctance nature is necessary before attempting the optimisation of the motor geometry.

Firstly the history of the synchronous reluctance motor is reviewed and the importance of the d- and q-axis inductances shown. Their definition is discussed and the calculation of the inductances using analytical, finite-element and lumped-circuit analysis is examined. Means for measuring the inductances are described and the results are validated using experimental tests on a 120W axially-laminated motor.

The work in this chapter forms the basis for an axially-laminated design program (see App. D) and a general-purpose lumped-circuit solver (see App. E).

4.1 Introduction

4.1.1 Historical Development

The three main classes of synchronous reluctance motor are illustrated in Fig. 4.1. The earliest types were of a salient-pole construction [20]. These were line-start motors and used a starting cage (not shown). Salient-pole designs are generally not used for inverter-driven variable-speed applications due to their low saliency. An exception to this is extremely high speed applications which require their mechanical robustness. Chiba and Fukao [61] have built a 24 000 rpm, 1.3kW salient-pole spindle motor and achieved saliency ratios in the range of 2 to 3.

The single-barrier construction uses an internal cut-out (flux-barrier) to produce the desired saliency. It was also used in line-start motors. A useful benefit is that it allows the optional insertion of magnets into the cut-outs to improve its performance [63]. Saturated saliency ratios in the range 2 to 5 are common [43, 44].

The multiple-barrier design uses multiple internal flux-barriers to yield an improved saliency ratio. The optimum performance is obtained by using as many barriers as possible in order to most closely approximate the ideal magnetically anisotropic rotor [21]. However using many barriers makes the motor difficult to construct. Conventional

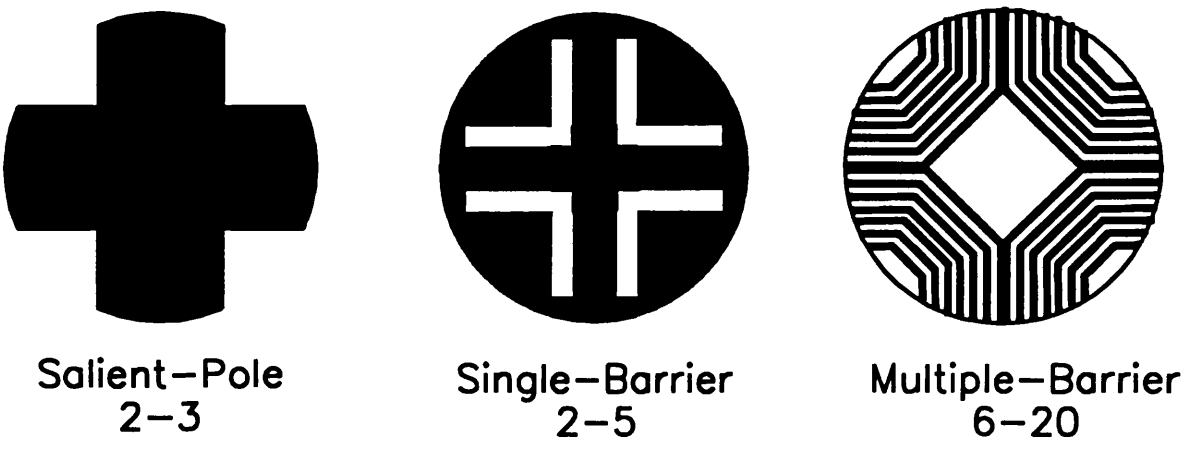

Figure 4.1: *Four-pole rotor designs with approximate saliency ratios.*

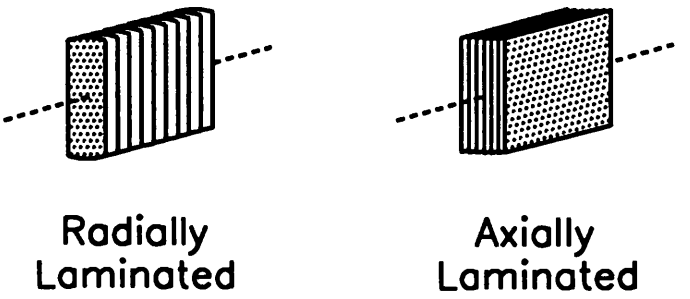

Figure 4.2: *Radially-laminated and axially-laminated construction.*

motors are made by punching laminations with the rotor design and then stacking these on the shaft in a similar way to washers on a pipe. This *radially-laminated* form of construction is illustrated in Fig. 4.2. However with many internal barriers, the laminations begin to resemble paper doilies and are flimsy [63]. The *axially-laminated* construction is more complex but is more practical when there is a high numbers of barriers. It uses interleaved layers of lamination and non-magnetic material stacked *parallel* to the rotor axis as shown in Fig. 4.2 for a two-pole design. In a four-pole design the lamination and insulation layers are bent into trough shapes as shown in Fig. 4.1. In Sec. 3.1 it was shown that saliency ratios in the range 6 to 20 can be achieved with axially-laminated motors.

As well as being required for good field-weakening performance, the axially-laminated form of construction has been shown to be necessary to obtain the high output torque and saliency ratio required to make synchronous reluctance motors competitive with induction motors [7, 21, 64, 65].

4.1.2 Definition of Inductances

Synchronous reluctance motors can be characterised by their d-axis (low inductance axis) inductance L_d and q-axis (high inductance axis) inductance L_q. The torque per ampere is proportional to $(L_q - L_d)$ while the saliency ratio ($\xi = L_q/L_d$) determines many of the motor's operating characteristics such as field-weakening range, power-factor and sensitivity to parameter variations (see Sec. 2.3.4).

The interior permanent magnet motor drive equivalent circuit was shown in Fig. 3.12 on pg. 135. The synchronous reluctance motor drive equivalent circuit is identical to this except the magnet flux-linkage Ψ_m is zero. The d- and q-axis synchronous inductances are given by :

$$\left.\begin{aligned} L_d &= L_{dm} + L_l \\ L_q &= L_{qm} + L_l \end{aligned}\right\} \tag{4.1}$$

where L_l is the stator leakage inductance and L_{dm} and L_{qm} are the magnetising inductances. The stator leakage inductance consists of the stator slot-leakage inductance L_{slt} and end-winding inductance L_{end}. Saturation is taken into account by making the magnetising inductances functions of the currents in their respective axes. Cross-coupling is neglected for the reasons described in Sec. 3.2.2.

A general assumption in the analysis of synchronous reluctance motors has been the use of sinusoidally-distributed windings [66]. This results in the following expressions for the phase self-inductance L and mutual inductance M as a function of the rotor angle θ.

$$\left.\begin{aligned} L &= L_l + L_0 + L_2 \sin 2\theta \\ M &= M_0 + M_2 \sin(2\theta \pm \tfrac{2\pi}{3}) \end{aligned}\right\} \tag{4.2}$$

Each inductance consists of a constant 'magnetising' term and a second harmonic component. With the sinusoidally-distributed winding assumption it can be shown that :

$$M_0 = -L_0/2 \qquad L_2 = M_2 \tag{4.3}$$

From this the d- and q-axis inductances can be shown [67] to be :

$$\left.\begin{aligned} L_q &= \tfrac{3}{2}(L_0 + L_2) + L_l \\ L_d &= \tfrac{3}{2}(L_0 - L_2) + L_l \end{aligned}\right\} \tag{4.4}$$

Chiba and Fukao [68] showed that space harmonics mean that the relationships in (4.3) no longer hold. They showed that a more general definition of L_d and L_q is :

$$\left.\begin{aligned} L_q &= (L_0 - M_0) + (L_2/2 + M_2) + L_l \\ L_d &= (L_0 - M_0) - (L_2/2 + M_2) + L_l \end{aligned}\right\} \tag{4.5}$$

Note that this simplifies to (4.4) when (4.3) holds.

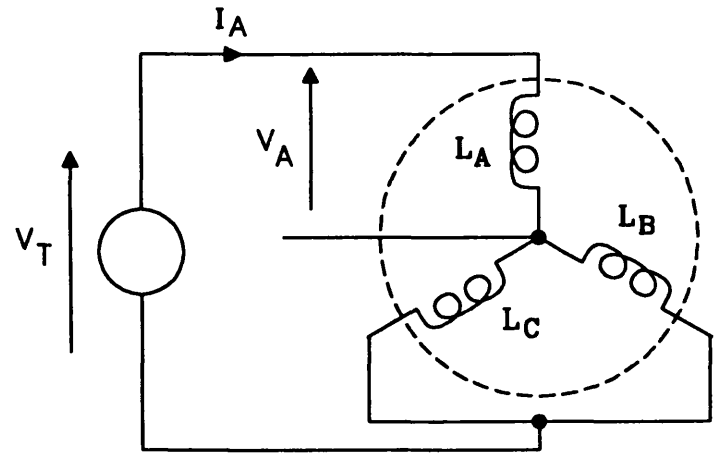

Figure 4.3: *Circuit for measurement and calculation of the phase inductances.*

For axially-laminated motors the error in using the sinusoidally-distributed winding assumption is not as substantial as with the salient-pole motor analysed by Chiba and Fukao. Despite this it is still important in defining the inductances. In finite-element, lumped-circuit and experimental measurements it is convenient to calculate L_d and L_q by aligning the rotor with the magnetic axis of phase A (see Fig. 4.3) and measuring or calculating the flux-linkage ψ as a function of current. Note that the voltage V is equal to the product of the flux-linkage and the supply frequency w. Two different inductances can be calculated from the circuit. The *actual* phase inductance is defined from V_A and I_A as :

$$L_{dq} \equiv \frac{\psi_A}{I_A} = \frac{V_A}{wI_A} \tag{4.6}$$

Note that this requires access to the star point[1] if it is to be measured experimentally.

The *weighted-average* phase inductance is defined as 2/3 of the inductance calculated from the total motor flux-linkage (V_T and I_A).

$$L_{dq} \equiv \frac{2}{3}\frac{\psi_T}{I_A} = \frac{2}{3}\frac{V_T}{wI_A} \tag{4.7}$$

Using the definitions of L_d and L_q given in (4.4) it can be shown that for a machine with

[1]Synchronous reluctance motors are generally star-connected. A delta-connected motor can have large circulating third harmonic currents which increase the torque ripple and the iron and copper losses [7].

sinusoidally-distributed windings, the actual and the weighted-average inductances are equal. However in real machines with non-sinusoidal inductances, the two techniques yield different values. The 'real' values of L_d and L_q could be obtained by measuring L and M as a function of θ using the procedure described by Chiba and Fukao, calculating L_0, L_2, M_0 and M_2 and then applying (4.5). Note that it is difficult to take saturation into account with this technique.

In practice the weighted-average inductances were used as some of the motors tested did not give access to the star point. Although this was found to give reasonable agreement with the measured results [69], further investigation is desirable.

4.1.3 Obtaining the Inductances

Fig. 3.7 on pg. 123 showed the measured q-axis inductance characteristics of a number of axially-laminated motors. Note that all the motors show some degree of saturation in the q-axis. On the other hand, the d-axis inductance usually shows no significant saturation in axially-laminated designs as the d-axis flux path is mostly through air.

Fig. 4.4 shows the variety of methods available for determining the inductance characteristics of synchronous reluctance motors. The methods which are underlined are discussed in detail. Analytical techniques are described in Sec. 4.2, numerical techniques are described in Sec. 4.3, experimental techniques are discussed in Sec. 4.4 and the results are validated in Sec. 4.5.

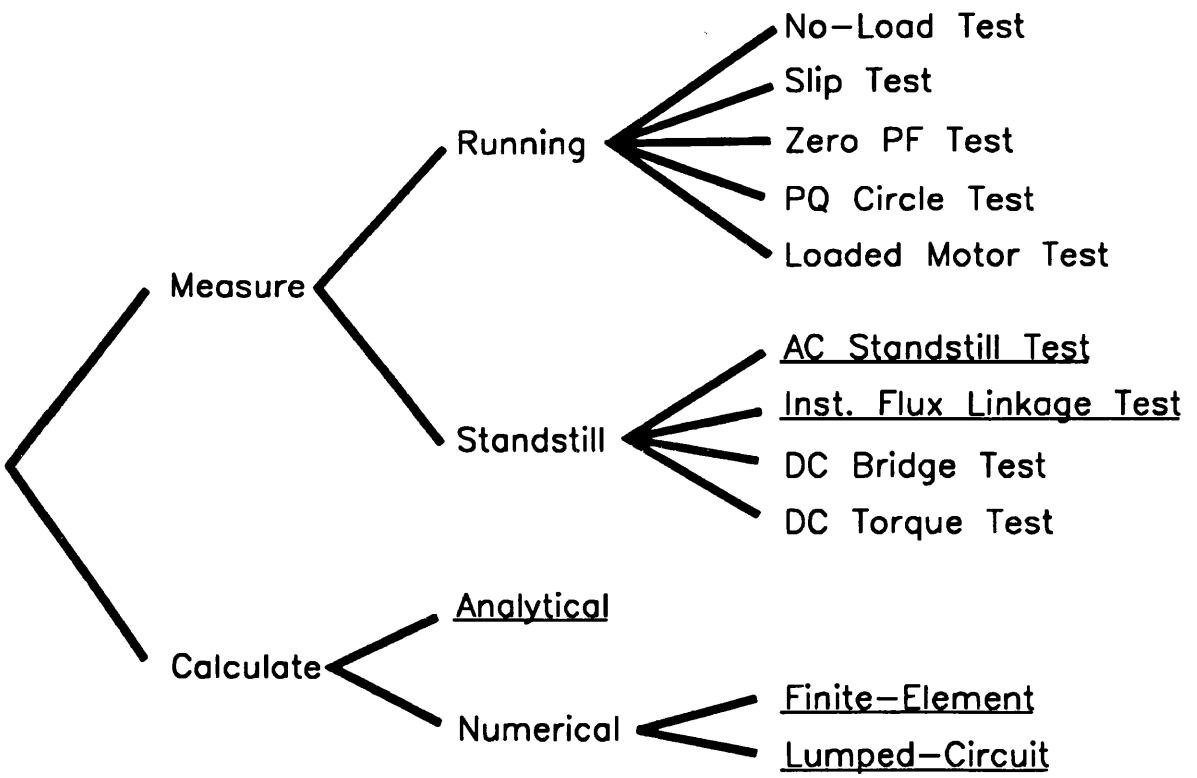

Figure 4.4: *Obtaining the inductance characteristics.*

4.2 Analytical Calculation

This can be used for predicting the unsaturated L_q. It can also be used for estimating L_d but this is more difficult as a significant part of L_d is formed by leakage inductances. It is difficult to accurately take into account saturation analytically.

First analytical techniques for calculating the q-axis and d-axis inductance are reviewed. A novel technique for calculating L_d based on the inductance of an ideal non-magnetic rotor is described. It is validated by experimental results from five axially-laminated designs.

The formulas described in this section are implemented in an axially-laminated motor design program (PC-AXL) which is described in App. D.

4.2.1 Winding Factors

The following equations on the winding factors are based on the analysis by Miller [12].

In order to calculate the inductances it is necessary to first calculate the effective number of sine-distributed series turns per phase N_s. This is given by :

$$N_s = \frac{4}{\pi} k_{w1} N_{ph} \tag{4.8}$$

where N_{ph} is the actual number of series turns per phase and k_{w1} is the conventional fundamental winding factor. The fundamental winding factor is given by :

$$k_{w1} = k_{d1} k_{p1} k_{s1} \tag{4.9}$$

where k_{d1}, k_{p1} and k_{s1} are respectively the fundamental distribution factor, chord factor and skew factor of the winding. The distribution factor takes into account the fact that the winding is distributed over a number of slots and not concentrated in a single one. For a winding with a slot-pitch of γ electrical degrees and q slots per pole per phase, the fundamental distribution factor k_{d1} is given by :

$$k_{d1} = \frac{\sin(q\gamma/2)}{q \sin(\gamma/2)} \tag{4.10}$$

The chording factor takes into account windings with a pitch less than the ideal 180° electrical. This causes a first order reduction in the stator resistance and hence copper losses. If the winding is short-pitched by ε electrical degrees, then the fundamental chording factor k_{p1} is given by :

$$k_{p1} = \cos\frac{\varepsilon}{2} \tag{4.11}$$

Skew is often used to reduce torque ripple in motors. If a winding is skewed by 2σ electrical radians, then the fundamental skew factor k_{s1} is given by :

$$k_{s1} = \frac{\sin\sigma}{\sigma} \tag{4.12}$$

4.2.2 Effective Airgap

The effective airgap g'' of the motor is larger than the mechanical airgap g due to the rotor and stator slotting. The effective airgap is given by :

$$g'' = g k_{cr} k_{cs} \tag{4.13}$$

where k_{cr} and k_{cs} are the Carter's coefficients taking into account rotor and stator slotting respectively. The Carter's coefficient is given by [70] :

$$k_c = \frac{w_t + w_s}{w_t + (1-\sigma)w_s} \tag{4.14}$$

where w_t is the width of the tooth, w_s is the width of the slot opening and σ is a function of w_s and g. For open slots σ is [70] :

$$\sigma_o = \frac{2}{\pi}\left[\arctan\frac{w_s}{2g} - \frac{g}{w_s}\ln\left(1+\left(\frac{w_s}{2g}\right)^2\right)\right] \tag{4.15}$$

For semi-closed slots this is modified to [70] :

$$\sigma_{sc} = \sigma_o + 0.0364\left(\frac{w_s}{g}\right)^{2/3} \tag{4.16}$$

These equations are illustrated in Fig. 4.5

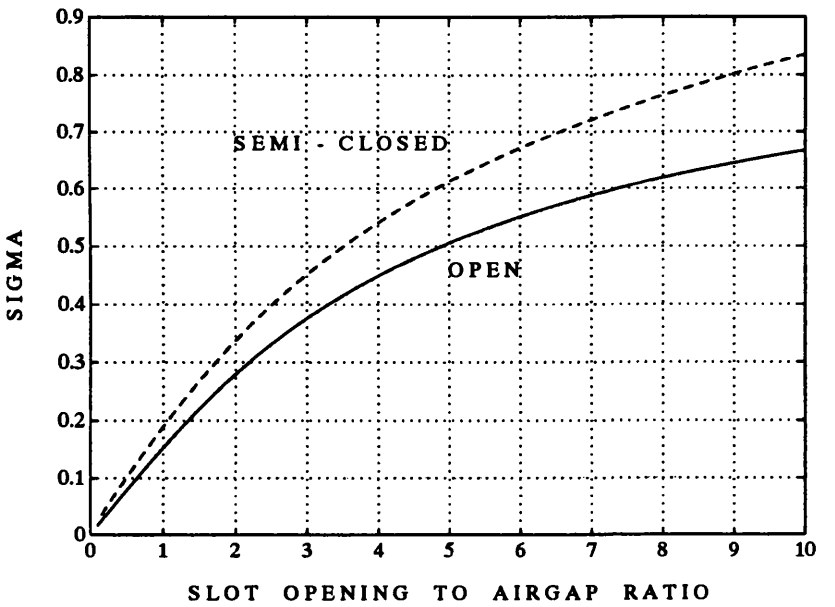

Figure 4.5: *Carter's coefficient for open and semi-closed slots.*

4.2.3 Q-Axis Inductance

The q-axis magnetising inductance L_{qm} is much greater than the stator leakage inductance L_l and hence :

$$L_q = L_{qm} + L_l \approx L_{qm} \tag{4.17}$$

The magnetising inductance L_m of a round rotor machine is [12] :

$$L_m = \frac{3\pi\mu_o N_s^2 l r_1}{8p^2 g''} \tag{4.18}$$

where N_s and g'' are given by (4.8) and (4.13), l is the stack-length, r_1 is the airgap radius and p is the number of pole-pairs.

If the pole-arc was 180° then $L_{qm} = L_m$, however practical axially-laminated motors have a finite pole arc. The ratio of the q-axis magnetising inductance to L_m for a motor with a pole arc of α electrical radians is given by [71] :

$$\frac{L_{qm}}{L_m} = \frac{\int_{(\pi-\alpha)/2}^{(\pi+\alpha)/2} \sin^2\theta d\theta}{\int_0^{\pi} \sin^2\theta d\theta} = \frac{\alpha + \sin\alpha}{\pi} \tag{4.19}$$

4.2.4 D-Axis Inductance and Saliency Ratio

Various formulas have been proposed in the literature for estimating the d-axis magnetising inductance and saliency ratio. One technique is to use (4.18) with a large airgap. Miller et al. [63] roughly approximates the effective d-axis airgap for a four-pole machine as $(ar_1 + g)$. This gives a saliency ratio of :

$$\xi = \frac{ar_1}{g} + 1 \tag{4.20}$$

where the *rotor insulation ratio* a is given by :

$$a \equiv \frac{w_{ins}}{w_{ins} + w_{lam}} \tag{4.21}$$

where w_{lam} is the thickness of the lamination material and w_{ins} is the thickness of the non-magnetic insulation material.

Boldea and Nasar [64] approximate the airgap permeance as a function of angular position and Vagati et al. [72] perform a lumped-circuit analysis. They both show that :

$$\xi \propto \frac{r_1}{pg} \tag{4.22}$$

Platt [50] derives an approximate analytical solution as :

$$L_{dm} = \frac{3\pi^3(p-1)\mu_o N_s^2 l r_1}{64p^2 a r_1 + 8\pi^2 p^2 (p-1)g} \tag{4.23}$$

A new technique is to consider the *intrinsic d-axis inductance* L_{di}. This is the inductance of a cylindrical stator with a sine-distributed airgap winding and an ideal non-magnetic rotor. It is shown in [73] that the radial B_r and tangential B_θ magnetic field components inside such a stator at a position defined by (r, θ) is given by :

$$\left.\begin{matrix} B_r \\ B_\theta \end{matrix}\right\} = \frac{\mu_o N_s I}{2r_1}\left(\frac{r}{r_1}\right)^{p-1} \left.\begin{matrix} \cos \\ -\sin \end{matrix}\right\} p\theta \tag{4.24}$$

Thus the magnitude of the flux density $|B|$ is given by :

$$|B| = \sqrt{B_r^2 + B_\theta^2} = \frac{\mu_o N_s I}{2r_1}\left(\frac{r}{r_1}\right)^{p-1} \tag{4.25}$$

From this it can be shown that the inductance is :

$$L_{di} = \frac{3\pi\mu_o N_s^2 l}{8p} \tag{4.26}$$

which is independent of the rotor diameter. This is similar to Eqn. 4.23 as generally $ar_1 \gg (p-1)g$.

Now if a large number of thin laminations separated by layers of insulation are placed in the inside the stator in such a way that the layers are always perpendicular to the flux lines, then the field distribution would be unchanged [63]. It would however cause the inductance to increase inversely proportional to the rotor insulation ratio. This increased inductance is termed the *intrinsic magnetising d-axis inductance* L_{dmi} :

$$L_{dmi} = \frac{3\pi\mu_o N_s^2 l}{8pa} \tag{4.27}$$

The *intrinsic saliency ratio*, ξ_i is the maximum possible saliency ratio for a given motor geometry. It is the ratio of the inductance with a solid rotor to the inductance with no rotor. From (4.18) and (4.26) it is defined as :

$$\xi_i \equiv \frac{L_m}{L_{di}} = \frac{r_1}{pg} \tag{4.28}$$

The *intrinsic magnetising saliency ratio* ξ_{mi} takes into account the iron content in the rotor. It is defined as :

$$\xi_{mi} \equiv \frac{L_m}{L_{dmi}} = \frac{ar_1}{pg} \tag{4.29}$$

This is a similar result to that obtained by other authors as given in (4.20) and (4.22). It sets an upper limit to the saliency ratio achievable with a given motor geometry.

The *actual magnetising saliency ratio* $\xi_m = L_{qm}/L_{dm}$ is lower than ξ_{mi} due to the finite rotor pole arc, Carter's coefficient and the distortion of the d-axis field distribution due to the rotor laminations (see Sec. 4.3.2). The *unsaturated saliency ratio* ξ_u, is lower than ξ_m due to the swamping effect of the stator leakage inductance. This consists of the slot-leakage and end-winding inductances and can be estimated using the same techniques as for induction machines (see Secs. 4.2.5 and 4.2.6).

Table 4.1 compares the intrinsic magnetising saliency ratio with the measured saliency ratio for five axially-laminated synchronous reluctance motors. The first three

Table 4.1: *Dimensions and saliency ratio of five axially-laminated designs.*

	#1	#2	#3	#4	#5
P_m [kW]	0.12	1.0	7.5	0.55	1.5
p	2	2	2	1	1
l [mm]	32	76	202	60	80
$2r_1$ [mm]	57	59	127	60	80
g [mm]	0.26	0.21	0.50	0.25	0.30
w_{lam} [mm]	0.30	0.30	0.50	0.50	0.50
w_{ins} [mm]	0.30	0.30	0.50	0.30	0.30
a	0.50	0.50	0.50	0.38	0.38
ξ_i	55	70	64	120	133
ξ_{mi}	27	35	32	45	50
ξ_u	7.4	8.2	11.5	10.8	21
ξ_u/ξ_{mi}	0.27	0.23	0.36	0.24	0.42

were built in the SPEED Laboratory (see App. A) and the other two were described by Boldea [48, 74]. Note that for the five designs the ratio ξ_u/ξ_{mi} lies between 0.2 and 0.4 with the ratio increasing with the size of the motor. This could be due to a reduction in the stator leakage inductance relative to the d-axis magnetising inductance. This relationship has not been described before and gives a simple means for roughly estimating the expected unsaturated saliency ratio from the motor dimensions. It is also useful in estimating the effects of changing the motor parameters (see Chapter 5).

4.2.5 Slot-Leakage Inductance

Stator slot-leakage inductance forms a significant proportion of the total d-axis inductance of axially-laminated motors. The slot-leakage per phase L_{slt} is given by [75] :

$$L_{slt} = \frac{4N_{ph}^2 m \mu_o l}{S_1} P_s \tag{4.30}$$

where m is the number of stator phases, S_1 is the number of stator slots and P_s is the total slot permeance ratio. This is the sum of the slot permeances for each of the three

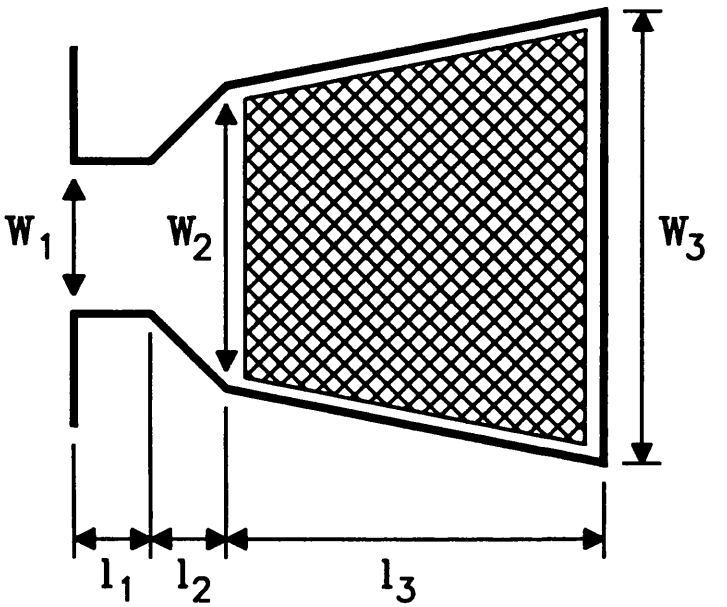

Figure 4.6: *Trapezoidal slot dimensions.*

sections shown in Fig. 4.6. These can be calculated if the simplifying approximation that the flux in the slot is everywhere parallel to the bottom of the slot is used.

Neglecting fringing into the airgap, the permeance of the slot section closest to the airgap is :

$$P_{s1} = \frac{l_1}{w_1} \tag{4.31}$$

If $l_1 \ll w_1$ then fringing into the airgap can be significant. An approximation can be obtained by assuming the flux lines outside the slot forms concentric semi-circles with their centre at the middle of the slot opening. The permeance is obtained by integrating over the face of the slot using the method described by Staton [76] :

$$P_{s1} = \frac{l_1}{w_1} + \frac{1}{\pi} \ln \frac{r_b}{r_a} \tag{4.32}$$

where r_a is half the slot opening and r_b is the slot pitch minus r_a.

The permeance ratio of the inside of the tang can be calculated as :

$$P_{s2} = \frac{l_2}{w_2 - w_1} \ln \frac{w_2}{w_1} \tag{4.33}$$

The calculation of the permeance ratio of the main body of the slot takes into

account the distributed nature of the slot conductors. For parallel-sided slots $w_2 = w_3$:

$$P_{s3} = \frac{l_3}{3w_3} \tag{4.34}$$

For trapezoidal slots P_{s3} can be approximated [77] as :

$$P_{s3} = \frac{l_3}{w_3} \frac{4\beta^2 - \beta^4 - 4\ln\beta - 3}{4(1-\beta)(1-\beta^2)^2} \quad \text{where} \quad \beta = \frac{w_2}{w_3} \tag{4.35}$$

Note that because of the distributed nature of the conductors, the slot permeance is particularly sensitive to the slot dimensions near the airgap and relatively insensitive to the shape of the bottom of the slot. Thus the error in approximating a trapezoidal slot by a parallel-sided slot of width w_2 is small. It also means that the error in approximating round-bottom slots by trapezoidal ones is also small.

4.2.6 End-Winding Leakage Inductance

The end-winding inductance is the inductance of the coil end turns outside the rotor stack. It is extremely difficult to calculate analytically as it depends on the winding type and how the winding is wound [75]. The most accurate method for estimating this is to use 3-D finite-element techniques [78].

4.3 Finite-Element and Lumped-Circuit Analysis

Finite-element modelling can be used to predict the q-axis saturation characteristic as well as to calculate the d-axis inductance. It involves partitioning the motor geometry into a large number (thousands) of triangular elements, applying the required currents and boundary conditions, then solving Maxwell's equations to obtain the complete electromagnetic field solution [79]. This can then be processed to yield the desired flux-linkages and inductances. Two-dimensional finite-element analysis can be used to calculate the magnetising and slot-leakage inductances but cannot give the end-winding inductance. This requires three-dimensional analysis.

Lumped-circuit analysis can also be used to calculate the q-axis saturation characteristic. Basically the geometry is partitioned into a small number (tens) of parts and an equivalent magnetic circuit is formed. This non-linear circuit can then solved numerically in the same way as electrical circuits. It is much faster than finite-element analysis as the number of elements is small. However it is sensitive to how well the system is partitioned and how the effective dimensions of each part is calculated.

4.3.1 BH Characteristics

The accuracy of finite-element and lumped-circuit analysis results depend critically on the accuracy of the magnetic (BH) characteristics used. These characteristics show the magnetic flux density B obtained with a given magnetic field strength H, or vice versa. For lamination and magnet materials the BH characteristics can be obtained from the manufacturer's curves or from test results.

Lamination materials show a substantial fall in the permeability at low flux levels. This is termed the "Rayleigh" region [79]. It is normally not modelled as : it generally has little effect on the motor performance; it makes the unsaturated inductance more difficult to determine; and because faster numerical convergence is obtained if the BH curve is monotonic.

Permanent magnet materials can be modelled by defining a BH characteristic where

the value of B is non-zero when H is zero. In the finite-element package used (Vector Field's PE2D), it was only possible to model the first and second-quadrant magnet characteristic. This is normally all that is required.

A useful technique in order to introduce quasi three-dimensional effects into two-dimensional models is to "dilute" the BH characteristic [80]. For instance this can be used in order to represent regions which do not extend through the full cross-section of the motor. Thus the effect of bolt-holes through the rotor can be modelled by reducing the effective thickness of the rotor in this region by dividing the B values by a fixed factor.

Conventional motor steel lamination material is *non-oriented* and has the same magnetic properties in all transverse directions. Grain-oriented lamination materials show superior magnetic properties (see Sec. 6.1.2) along their preferred transverse axis but poor magnetic properties orthogonal to this. It can only be used in applications such as the rotors of axially-laminated motors where the flux passes in one transverse direction.

It is generally not possible to take into account the anisotropic nature of grain-oriented steel or permanent material in two-dimensional finite-element analysis. This does not present a problem when modelling grain-oriented axially-laminated rotors as the flux densities in the transverse direction are low and are limited by the non-magnetic insulation material and not by saturation in the rotor steel.

4.3.2 Finite-Element Analysis

A two-dimensional motor model is generally used. For a four-pole motor it is normally only necessary to model one eighth of the cross-section in order to obtain the d- and q-axis inductances (see Fig. 4.7 on pg. 175). This assumes that the stator winding is symmetrical enough to allow this. For instance with a four-pole fractional slot-pitch winding it was necessary to model half the motor.

The motor geometry can be input interactively or via a "script" file. This is a program written in the modelling language used by the finite-element package. In

the analysis of axially-laminated motors, extensive use was made of script files due to both the complexity of the rotor geometry and its simple, repetitive structure. In conjunction with Dr. Dave Staton, I wrote a general axially-laminated motor script file (a listing is given in App. C). This creates a finite-element model from the standard stator geometry parameters (number of slots, tooth angle, slot depth etc.) and the rotor parameters (number of layers, thickness of layers etc.). This greatly reduced the time and effort required to model new motor designs. This technique was used to obtain all the finite-element models in this thesis.

Fig. 4.7 shows the finite-element model used for calculating the q-axis saturation characteristic of a 120W axially-laminated motor. This is design #1 in Table 4.1 on pg. 169. Care is required in modelling axially-laminated rotors due to the extremely fine structure at the rotor surface. In fact the axially-laminated motor has one of the most magnetically complex rotor geometries of all the motor types. To calculate the unsaturated q-axis inductance accurately requires a large number of elements in the airgap to model the fringing around each lamination. All finite-element packages have a limit on the maximum number of elements which can be modelled. This may restrict the modelling of large motors with many laminations, or motors with unusual windings where symmetry cannot be used effectively. At high currents, saturation of the iron paths mean that the modelling of the airgap region is less critical.

Figs. 4.9–4.12 show the q- and d-axis flux density distribution and airgap flux graphs for a 1A rms phase current (rated current = 1.7A). The airgap flux graphs shows the magnitude of the magnetic flux density in Tesla at the centre of the airgap as a function of the radial position. The airgap flux density is modulated by the stator slotting and also features a high frequency ripple due to the rotor laminations. The limited accuracy at which the field near the rotor surface can be modelled can be clearly seen from the irregularities in the high frequency ripple. This is despite using a large number of elements (approximately 6500) in the model. The package used (PE2D) is limited to a maximum of 10000 elements.

The d-axis flux distribution (Fig. 4.11) shows that the non-ideal lamination geometry and the stator slotting lead to a distorted rotor flux distribution. This has been

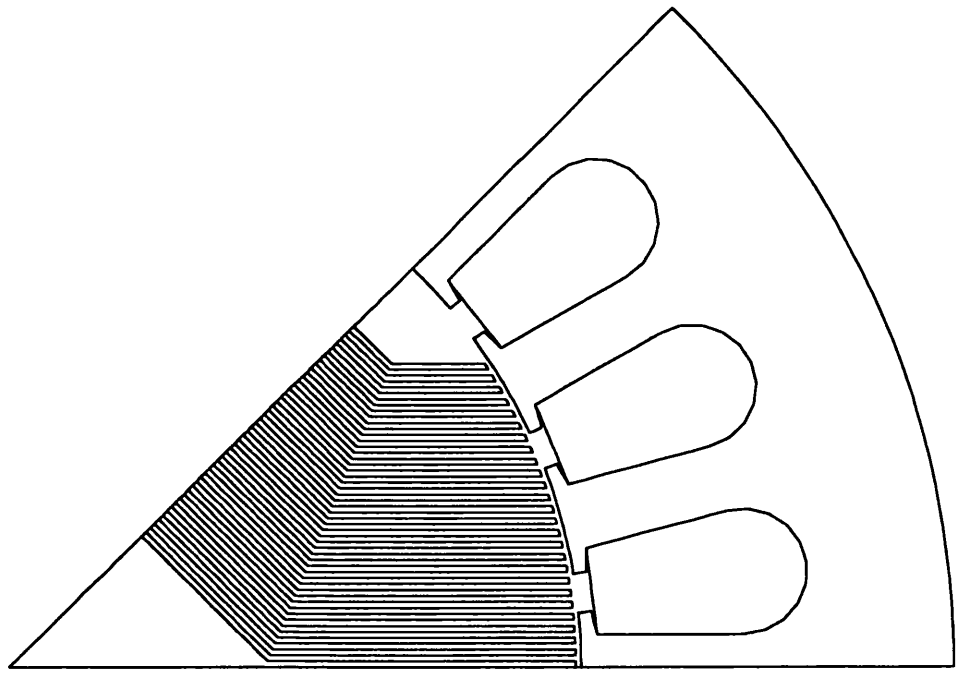

Figure 4.7: *120W motor geometry.*

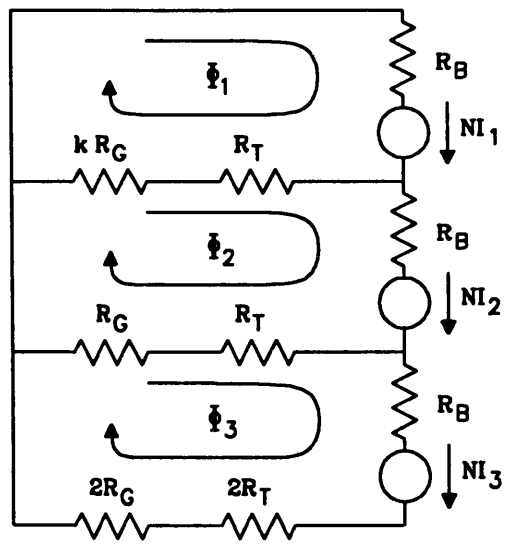

Figure 4.8: *120W q-axis lumped-circuit model.*

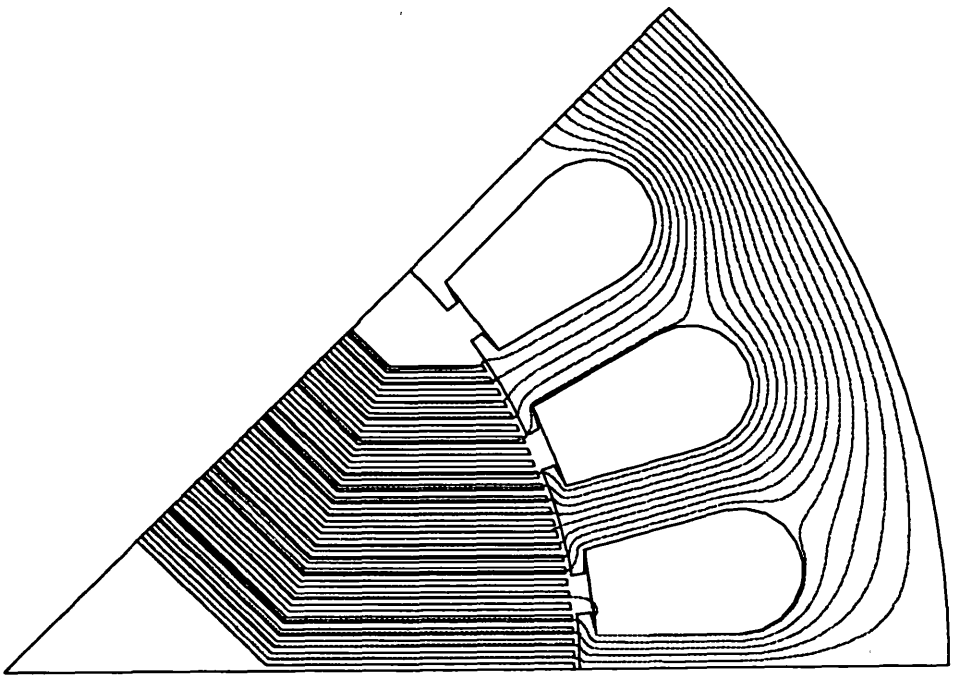

Figure 4.9: *120W q-axis flux distribution.*

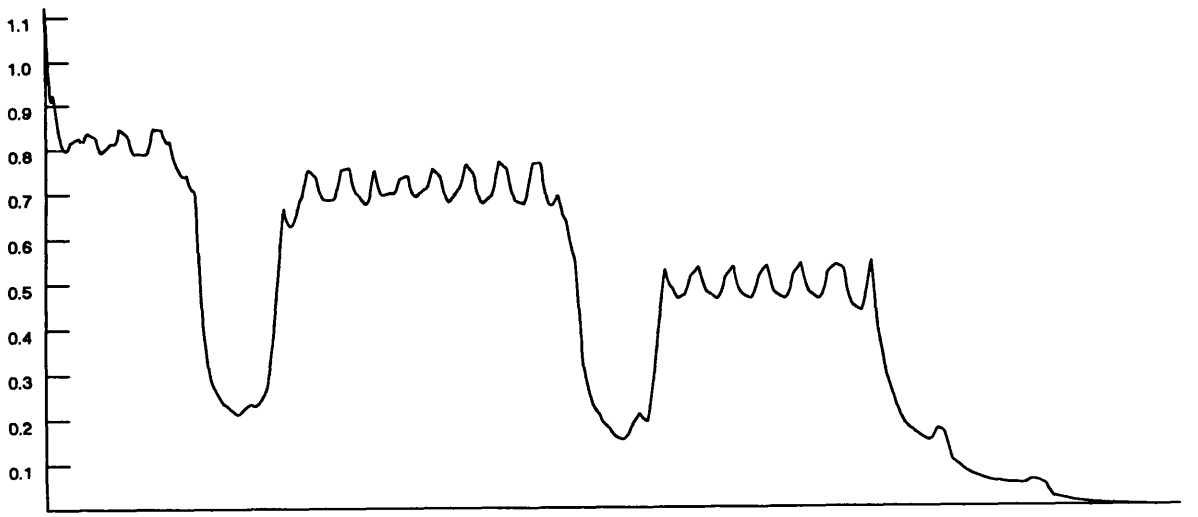

Figure 4.10: *120W q-axis airgap flux graph [T].*

explored by Staton, Miller and Wood [81]. The distorted flux distribution will cause the d-axis magnetising inductance to be greater than predicted by (4.27). Note that the airgap flux density in the d-axis case (Fig. 4.12) is much lower than in the q-axis case. Close inspection of Fig. 4.11 shows that there are flux reversals in the the radial airgap flux direction. This is not seen in the airgap flux plot as this shows only the magnitude.

4.3.3 Lumped-Circuit Analysis

The first step in performing a lumped-circuit analysis is to produce an equivalent magnetic circuit. Consider the q-axis case for the 120W motor shown in Fig. 4.9. This can be modelled using the simple three mesh circuit shown in Fig. 4.8 if the rotor is assumed to be infinitely permeable.

The airgap reluctances R_G were calculated using the effective airgap g'' (4.13) to take into account rotor and stator slotting. The tooth reluctances R_T were taken to be that of the straight section of the tooth. Finally the back-iron reluctances R_B consisted of a width given by the minimum back-iron depth plus one third of the slot bottom fillet radius and a length equal to the slot pitch measured midway in the thinnest section of the back-iron. Note that the above choice of dimensions is somewhat arbitrary.

The next step is to apply the currents, calculate the resulting magneto-motive forces (MMFs) and solve for the three fluxes Φ_1, Φ_2 and Φ_3. In order to do this a general-purpose non-linear lumped-circuit solver was written using Matlab [37]. A full description of the solver is given in App. E. The lump-circuit solver solves the equivalent circuit with known MMF sources NI_n for the flux Φ_n in each of the n circuit meshes :

$$\begin{bmatrix} NI_1 \\ \vdots \\ NI_n \end{bmatrix} = \begin{bmatrix} \mathcal{R}_{11} & \cdots & \mathcal{R}_{1n} \\ \vdots & & \vdots \\ \mathcal{R}_{n1} & \cdots & \mathcal{R}_{nn} \end{bmatrix} \begin{bmatrix} \Phi_1 \\ \vdots \\ \Phi_n \end{bmatrix} \tag{4.36}$$

where the n^2 mesh reluctances $\mathcal{R}_{nn}$ represent the reluctance between nodes. Each mesh

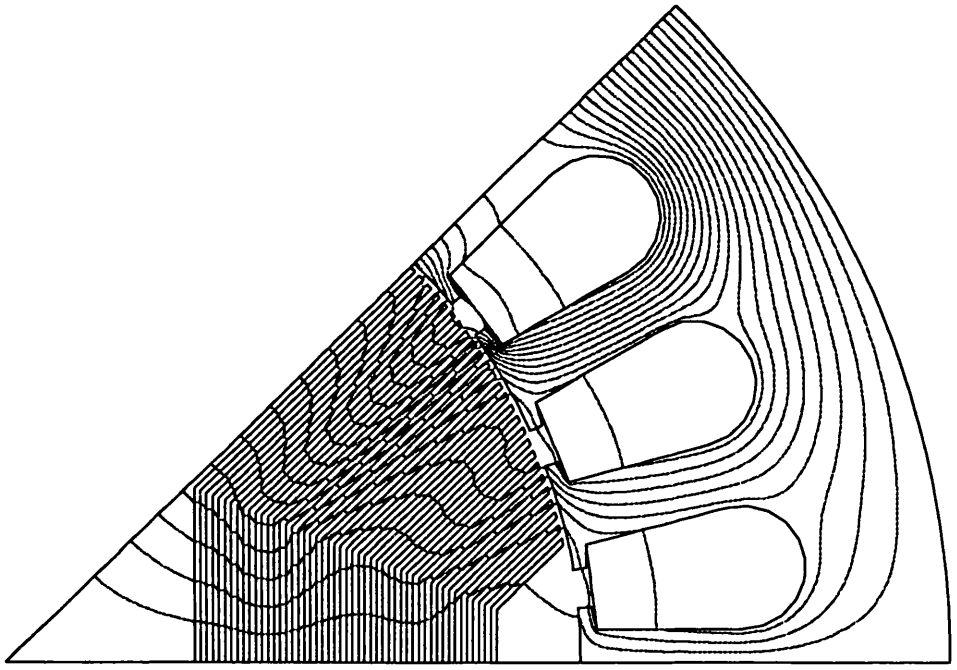

Figure 4.11: *120W d-axis flux distribution.*

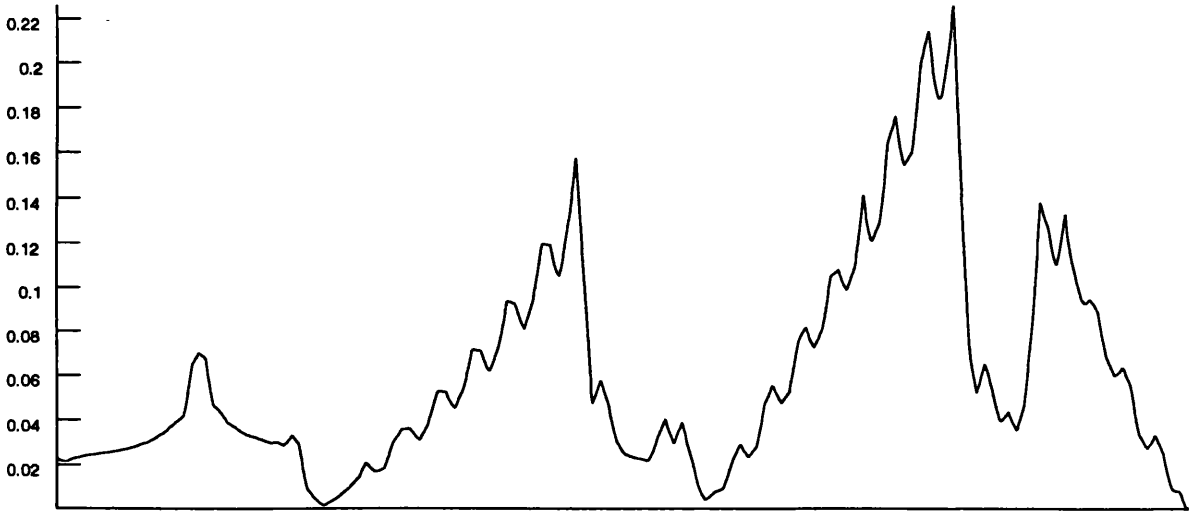

Figure 4.12: *120W d-axis airgap flux graph [T].*

reluctance consists of a linear combination of the circuit reluctances $\mathcal{R}_m$:

$$\begin{bmatrix} \mathcal{R}_{11} \\ \vdots \\ \mathcal{R}_{1n} \\ \mathcal{R}_{21} \\ \vdots \\ \vdots \\ \mathcal{R}_{nn} \end{bmatrix} = \begin{bmatrix} \mathcal{C}_{111} & \cdots & \mathcal{C}_{11m} \\ \vdots & & \vdots \\ \mathcal{C}_{1n1} & \cdots & \mathcal{C}_{1nm} \\ \mathcal{C}_{211} & \cdots & \mathcal{C}_{21m} \\ \vdots & & \vdots \\ \vdots & & \vdots \\ \mathcal{C}_{nn1} & \cdots & \mathcal{C}_{nnm} \end{bmatrix} \begin{bmatrix} \mathcal{R}_1 \\ \mathcal{R}_2 \\ \vdots \\ \mathcal{R}_m \end{bmatrix} \tag{4.37}$$

where $\mathcal{C}_{nnm}$ is a connection factor representing the circuit geometry and can be -1, 0 or $+1$. The value of each of the m circuit reluctances $\mathcal{R}_m$ is a function of the flux Φ_{Rm} in the reluctance which in turn is a linear combination of the mesh fluxes Φ_n :

$$\begin{bmatrix} \Phi_{R1} \\ \vdots \\ \Phi_{Rm} \end{bmatrix} = \begin{bmatrix} \mathcal{F}_{11} & \cdots & \mathcal{F}_{1n} \\ \vdots & & \vdots \\ \mathcal{F}_{m1} & \cdots & \mathcal{F}_{mn} \end{bmatrix} \begin{bmatrix} \Phi_1 \\ \vdots \\ \Phi_n \end{bmatrix} \tag{4.38}$$

where $\mathcal{F}_{ab}$ can be -1, 0 or $+1$.

The reluctance of each lumped circuit element $\mathcal{R}_m$ is related to the flux Φ_{Rm} in it by its physical dimensions and magnetic characteristics. Initially the linear values of reluctance are used. An interative numerical technique is used to solve the circuit for the loop fluxes. Once these are obtained, the inductances can be calculated from the winding distribution.

4.4 Measurement of Inductance

The d- and q-axis inductances of synchronous reluctance machines can be determined experimentally by a variety of tests. These can be divided into *running* and *standstill* tests (see Fig. 4.4 on pg. 163).

The running tests were mainly developed for testing line-start motors with a squirrel-cage. The tests are usually performed from a fixed-voltage fixed-frequency supply. The main types are described by Klingshirn [82]. These include the no-load test, the slip test, the zero power-factor test, the PQ circle diagram test and the loaded motor test. The no-load or light-running test can be used to obtain L_q as a function of current. The slip test involves driving the motor at a speed slightly different than synchronous speed. The stator current is then modulated by the slip frequency and the inductances can be calculated from the maximum and minimum current. The zero power-factor test calculates the inductances based on the terminal voltage and current with two current-angles where the input power-factor is zero. The PQ circle diagram test calculates the inductances based on the variation of the operating point in the real/reactive power plane on changing from motoring to generating. Finally the loaded motor test calculates L_d from the voltages, current and input power variations as the motor is loaded (knowing L_q using the no-load test).

Standstill tests are generally easier to perform than running tests on axially-laminated motors designed for inverter operation. Standstill tests also have the advantage that they can usually be applied to machines containing permanent magnets. The tests are similar to those used to measure the magnetisation characteristics of switched-reluctance motors [83, 84]. The four main types are the AC standstill test, the DC bridge test, the instantaneous flux-linkage test and the standstill torque test.

The AC standstill test is the standstill equivalent of the no-load test except that it can be used to obtain L_d as well as L_q. It is simple, gives accurate results when the iron loss is low and is widely used [48, 50].

The DC bridge test calculates the inductance by measuring the change in flux-linkage when the stator current is increased from zero to a fixed value. It is described

by Miller [55]. The flux-linkage is measured by integrating the voltage across the stator winding with a ballistic galvanometer. The effect of stator resistance is eliminated by using a Wheatstone bridge configuration. The main advantage of this test is that it can be applied to motors with a squirrel-cage as it is unaffected by eddy-currents.

The instantaneous flux-linkage test is similar in principle to the DC bridge test. However instead of measuring the change in flux-linkage for a given change in current, it measures the *instantaneous* flux-linkage as the stator current is ramped from zero to its rated value. It allows simple, accurate compensation for stator resistance and produces the entire saturation curve in one test.

The DC standstill torque test is based on the same principles as the loaded motor test. It was developed for line-start synchronous reluctance motors to calculate L_d knowing L_q from the no-load test. DC currents are applied to the motor and the resulting torque is measured. It calculates L_d based on the fact that the torque is proportional to $L_q - L_d$.

Out of the above tests, the AC standstill test and the instantaneous flux-linkage test are the easiest to perform and the most widely applicable to inverter-driven axially-laminated motors.

4.4.1 AC Standstill Test

This involves aligning the d- or q-axis of the rotor with the magnetic axis of phase A and applying a variable-voltage 50Hz supply across the motor terminals as shown in Fig. 4.3. The inductance can be obtained from the terminal voltage and current if the stator resistance is known. A more accurate method is to also measure the input power to allow the stator resistance to be calculated as well.

The AC standstill test gives accurate results if the inductances show little saturation and if there are low iron losses. The effect of saturation is underestimated due to the "averaging" nature of the test. Thus it is mainly useful for measuring the unsaturated inductances. The q-axis test gives unusually high iron losses as the rotor flux oscillates at 50Hz. Note that under normal steady-state operating conditions it would be constant

due to the synchronous nature of the machine. Neglecting iron losses in the equivalent circuit causes the value of AC stator resistance to appear to be much higher than the DC value. The error produced by this was less than 1% with a 120W motor but was substantial with a 7.5kW motor. In fact with the 7.5kW motor the losses were so large that it was not possible to obtain useful results for L_q even when modelling an iron loss resistance in the equivalent circuit as shown in Fig. 3.12.

4.4.2 Instantaneous Flux-Linkage Test

This involves measuring the instantaneous flux-linkage $\lambda(t)$:

$$\lambda(t) = \int [v(t) - i(t)R]\, dt \tag{4.39}$$

as the current is ramped up from zero up to its rated value. The saturation characteristic can then be obtained by dividing the flux-linkage by the instantaneous current. This allows the entire saturation curve can then be obtained from one test [85].

This method was found to give accurate results even in the case of a high degree of saturation and high iron losses. Saturation is calculated correctly as the instantaneous flux-linkage is used. This was particularly important in the case of the d-axis inductance of permanent magnet motors where the saturation characteristic is not symmetrical about the origin (see Fig. 3.15). An AC standstill test could not be used in this case.

The effect of iron losses is reduced compared to the AC standstill test as the flux-linkage is varied more slowly. In the AC standstill test the rotor flux reverses every half mains cycle (10ms). In the instantaneous flux-linkage test the current can be ramped up over a much longer period of time (say one second). This nearly eliminates the eddy-current losses as these are proportional to the square of the rate of change of flux (see Sec. 3.2.3). Note that the hysteresis loss per cycle is unaffected.

Equation (4.39) shows that the flux-linkage can be obtained from the stator terminal voltage if the stator resistance is known. Lovatt and Stephenson [83] found difficulties with this technique due to the variation of the stator resistance with temperature. A solution to this was described by Cossar and Miller [85]. This involves recording the

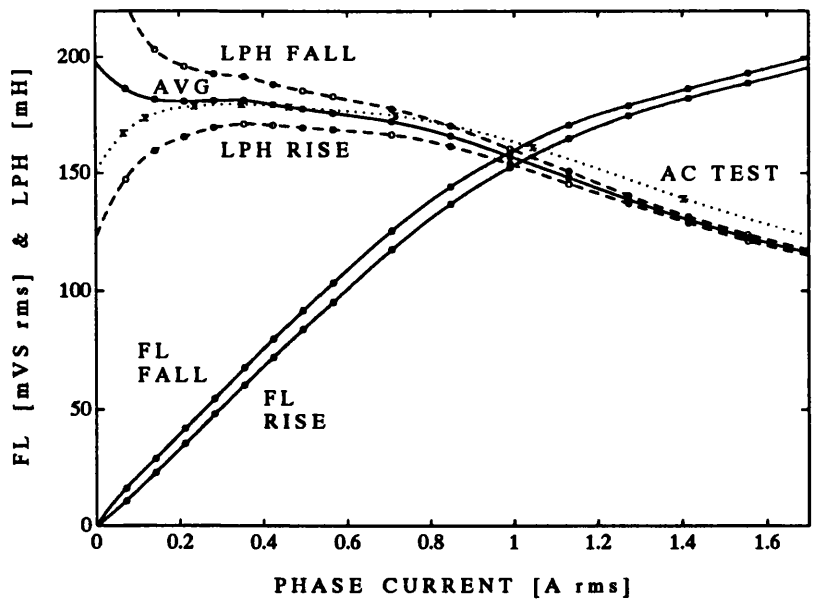

Figure 4.13: *Experimental results from AC and flux-linkage tests.*

stator voltage and current waveforms with a digital sampling oscilloscope as the current is ramped up to its rated value and then back down to zero. The correct value of stator resistance is obtained by finding the value which returns the flux-linkage to zero when the current is ramped back down to zero.

Hysteresis iron losses mean that the rising and falling flux-linkage (FL) curves form a "hysteresis" loop. This is shown in Fig. 4.13 along with the calculated inductance characteristics. The average inductance curve (AVG) is calculated by averaging the two flux-linkage curves. It corresponds well with the unsaturated inductance calculated with the AC standstill test (dotted line). Note the tendency mentioned earlier of the AC standstill test to overestimate the saturated inductance.

At low currents the inductance falls due to the low permeability of the stator and rotor iron at low flux levels. This is shown by the AC standstill test results in Fig. 4.13. The errors in the inductance calculated from the flux-linkage method are large at low currents and it is assumed for simplicity that the unsaturated inductance is a constant value. This has no significant effect on the predicted characteristics.

4.5 Experimental Tests

A four-pole, 120W axially-laminated motor (design #1 in Table 4.1) was modelled. This uses a standard 24 slot induction motor stator with a single-layer, equi-turn consequent pole, concentric winding. Only one eighth of the motor needed to be modelled in the finite-element and lumped-circuit analysis due to symmetry in the rotor and in the stator winding (see Fig. 4.7). Each rotor pole consists of 26 lamination and 25 insulation layers and is clamped to the square cross-section shaft by a brass pole-piece and three non-magnetic stainless-steel bolts. Grain-oriented material was used for the rotor laminations for its high saturation flux density and low iron losses (see Sec. 6.1.2).

4.5.1 Inductance Characteristics

Finite-element results showing the effect of replacing the rotor or stator steel with infinitely permeable magnetic material are shown in Fig. 4.14. From the small change in the results when using real or ideal rotor steel it is clear that the majority of the saturation in the motor occurs in the stator. This is because of the use of grain-oriented steel in the rotor and also due to the greater iron cross-sectional area in the rotor per stator slot pitch compared to the stator tooth area. The latter point is partly offset by the area of the rotor laminations taken up by the bolts. This is discussed further in Sec. 5.2.3. Fig. 4.14 also shows the saturation curve predicted using the lumped-circuit model described in Sec. 4.3. Given the simplicity of the calculations, the results show a reasonable match with the finite-element results.

Table 4.2 compares the measured unsaturated inductances with that calculated using finite-element, analytical and lumped-circuit techniques. The unsaturated inductances were measured using the AC standstill test.

Finite-element analysis using a smooth stator, a sine-distributed airgap winding and a non-magnetic rotor was used to obtain a value for L_{di}. This corresponded well with the analytical prediction given by (4.26). Next a slotted stator and the actual winding was modelled to introduce slot-leakage L_{slt}. The difference between these values and

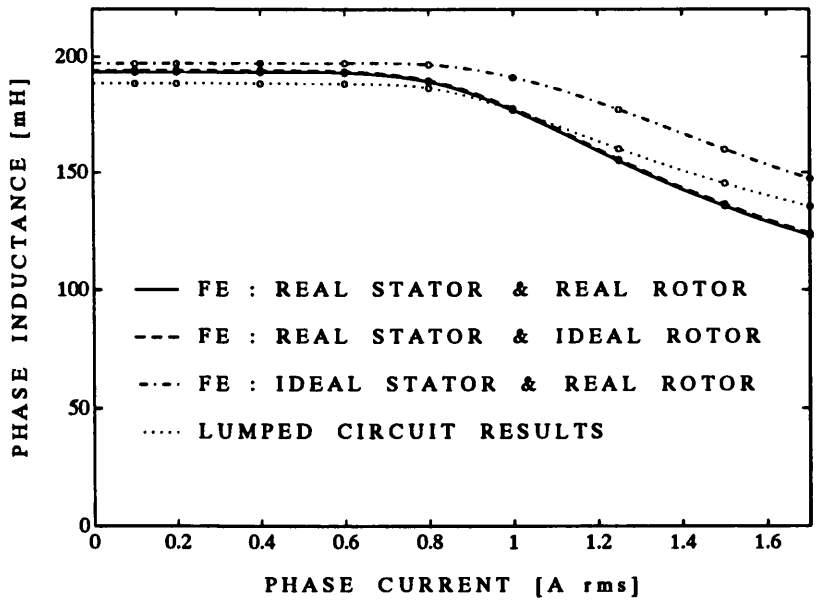

Figure 4.14: *Effect of using ideal stator and rotor steel.*

that measured for the stator without a rotor is mainly due to end-winding inductance L_{end} which is relatively large in this motor due to the short stack length (see Table 4.1 on pg. 169).

The measured d-axis inductance with the rotor inserted corresponds well with the value from finite-element analysis which has been corrected for the end-winding inductance. According to (4.27), inserting the rotor should increase L_d by an amount equal to L_{di} (4.8mH) if the lamination and insulation thicknesses are equal. However the measured results show that the actual increase (8.4mH) is nearly double this. This could be due to the rotor laminations distorting the ideal field distribution or else due to end-effects with the short stack length. Nevertheless the analytical prediction using (4.27) and corrected for end-winding inductance is only about 14% low compared to the measured result. This is reasonable considering its simplicity.

Table 4.2 and Fig. 4.15 compare the calculated and measured unsaturated q-axis inductance and the saturation characteristics. The finite-element, analytical and lumped-circuit results are consistent and predict the general shape of the characteristic well

Table 4.2: *Comparison of unsaturated inductances for 120W motor. The * indicates the values have been corrected for the endwinding inductance.*

Inductance mH	Measured	Finite Elment	Lumped Circuit	Analytical
L_{di}	—	4.82	—	4.85
$L_{di} + L_{slt}$	—	9.2	—	9.8
$L_{di} + L_{slt} + L_{end}$	**16.0**	—	—	—
L_{end} (from above)	—	6.8	—	6.2
$L_{dmi} + L_{slt}$	—	17.5	—	14.7
$L_d = L_{dmi} + L_{slt} + L_{end}$	**24.4**	24.3*	—	20.9*
L_q (unsat)	**181**	200*	195*	197*

however they significantly overestimate the measured inductance (by about 10%). They also appear to underestimate the amount of saturation in the motor. The descrepancy with the unsaturated inductance could be due to the difficulty in measuring the small airgap (0.265mm) accurately. The descrepancy in the saturation may be due to neglecting the effect of the bolt holes (see Sec. 5.2.3).

4.5.2 Comparison of Measured Characteristics

Figs. 4.16–4.17 show comparisons between the calculated and measured steady-state operating characteristics for the 120W axially-laminated motor at rated speed (1500 rpm) and rated phase current (1.7A). The calculated curves were obtained using the equations derived in Sec. 3.3. The two iron loss resistances were assumed to be equal and of constant value and the leakage inductance was combined into the magnetising inductances. The iron loss resistance was obtained from tests with $\gamma = 0°$.

Figs. 4.16–4.17 show that the measured performance characteristics are accurately predicted by the calculated characteristics using the instantaneous flux-linkage test results. The calculated performance from the finite-element and lumped-circuit results show a reasonable match with the torque, voltage and saliency characteristics. Note that the power-factor and efficiency curves appear to be relatively insensitive to errors

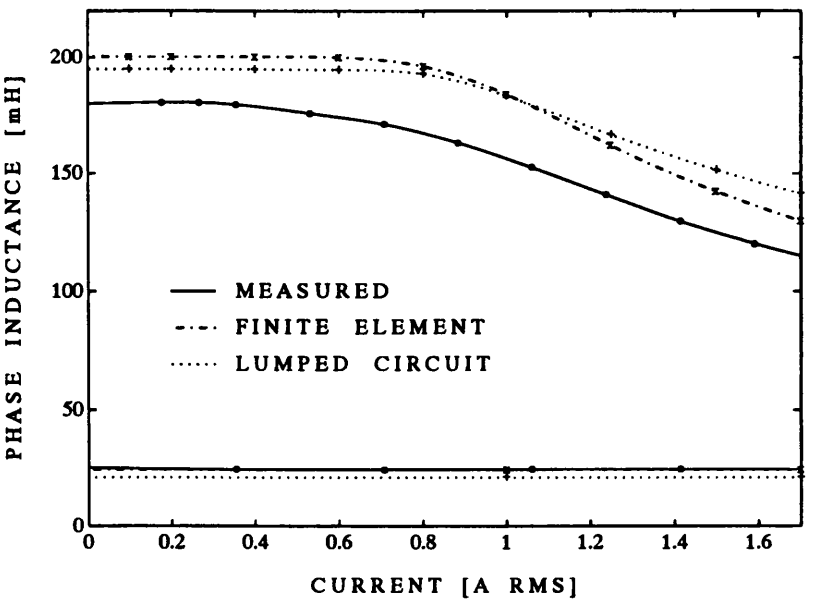

Figure 4.15: *Calculated and measured 120W saturation results (corrected for endwinding inductance).*

in the flux-linkage characteristics. The efficiency is low due to the relatively high copper losses in the small (120W) motor.

Table 4.3 compares the manufacturer's catalogue ratings for the induction motor against the measured performance of the synchronous reluctance motor. The synchronous reluctance motor shows a significant improvement in both the efficiency and power-factor over the induction motor. It should however be noted that induction motors are relatively inefficient in small sizes. Thus it would be fairer to compare two large motors (a comparison of a 7.5kW induction motor and synchronous reluctance motor is given in Chapter 6). Also the synchronous reluctance motor uses a slightly smaller airgap (13% less). To a first approximation the rated torque is proportional to L_q which from (4.18) is inversely proportional to the airgap. The rated torque for the synchronous reluctance motor at rated current is 27% greater than that for the induction motor. Thus it is clear that even for the same airgap that the synchronous reluctance motor would still generate significantly more torque than the induction motor for this

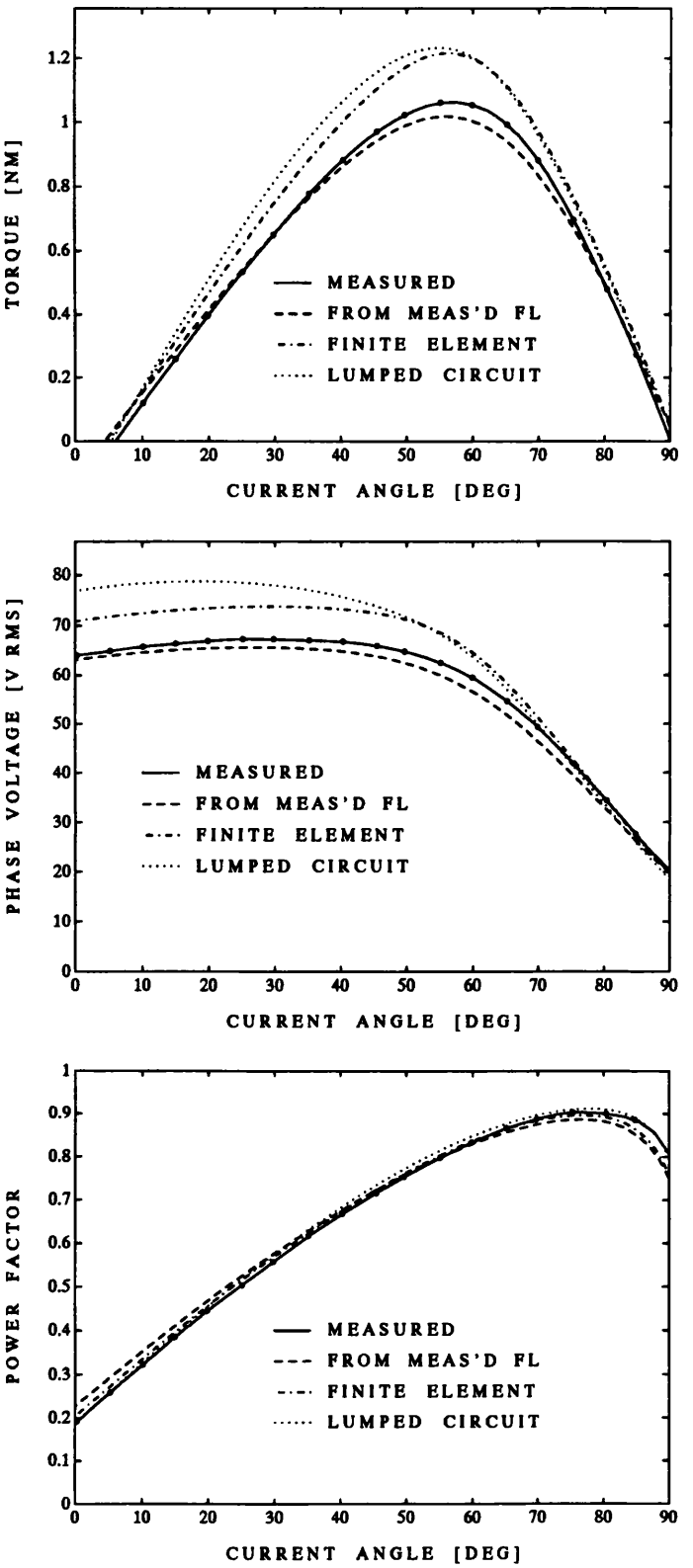

Figure 4.16: *Comparison between the 120W calculated and measured characteristics for the torque, voltage and power-factor versus current-angle.*

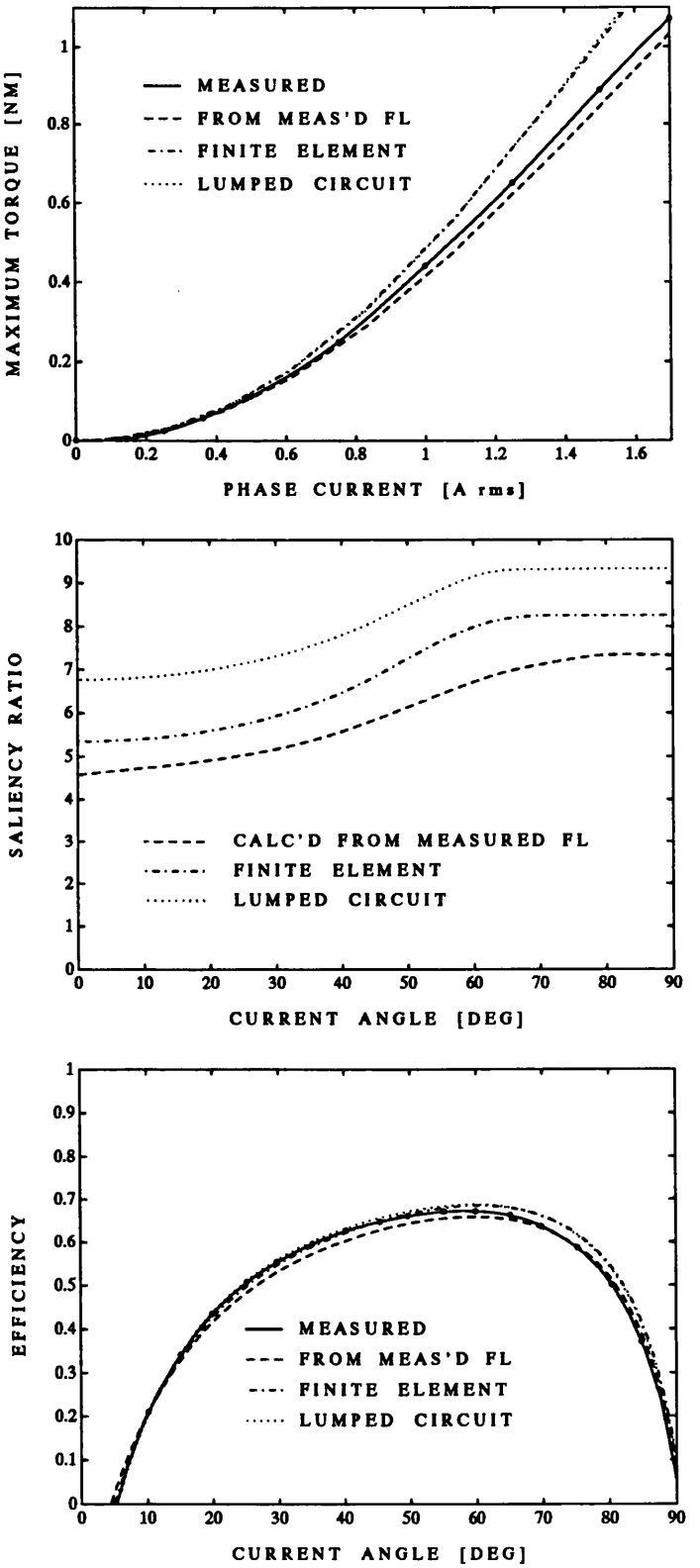

Figure 4.17: *Comparison between the 120W calculated and measured characteristics for the torque versus current, saliency versus current-angle and power-factor versus current-angle.*

Table 4.3: *Comparison between the 120W induction motor and* SYNCHREL *in the same stator.*

Parameter	IM	Synchrel
Mean Airgap (mm)	0.305	0.265
Rated Line Voltage (Vrms)	110	110
Rated Phase Current (Arms)	1.7	1.7
Rated Speed (rpm)	1360	1580
Output Torque (Nm)	0.84	1.07
Power Output (W)	120	165
Efficiency (%)	61	66
Power Factor	0.62	0.82
Apparent Efficiency	0.38	0.54

frame size.

4.6 Conclusions

This section examined the definition of the d- and q-axis inductances and discussed their calculation using analytical, finite-element and lumped-circuit techniques. The concept of the intrinsic magnetising saliency ratio $\xi_{mi} = ar_1/pg$ was introduced. This is the maximum saliency ratio theoretically possible with a given motor geometry. Practical motors generally achieve unsaturated saliency ratios of between 20–40% of this.

Finite-element methods should provide the most accurate results however the complex axially-laminated motor geometry pushes the software packages to their limits. Lumped-circuit models are faster to solve but generally require validation against finite-element models.

Means for measuring the inductance characteristics were discussed. The AC stand-still test is the simplest to perform but the instantaneous flux-linkage test provides the most accurate results for the saturation characteristics.

Experimental validation was performed with a 120W motor. The performance characteristics predicted using the results of the instantaneous flux-linkage test showed an excellent correspondence with the measured motor performance. The finite-element and lumped-circuit results predicted the shape of the curves well, however slightly overestimated the output torque. This could be due to difficulties in measuring the airgap accurately and the effect of bolt holes in the rotor.

Chapter 5

Design of Axially-Laminated Motors

This chapter describes the design and optimisation of axially-laminated brushless synchronous AC motor drives for a wide field-weakening range. A 7.5kW synchronous reluctance design and a 7.5kW interior permanent magnet design are examined. The effect of pole-number, mechanical constraints, pole-piece material, airgap size, rotor insulation ratio, magnet material and demagnetisation-withstand are considered. The construction and testing of the motor drives is described in the next chapter.

5.1 Introduction

It is only recently that the design of brushless synchronous AC motor drives for a wide field-weakening range has been considered. The majority of the previous work has concentrated on examining the performance of existing designs [2, 33, 46]. There is also a surprising lack of published test results showing the constant-power speed range achieved.

Two commercial interior permanent magnet spindle drives are presently available. Mannesmann Rexroth offer motors in the 2 to 10kW range with constant-power speed ranges from 1.8:1 up to 3:1 [86]. GEC Alsthom offer motors in the 6 to 18kW range with a constant-power speed range of 4:1 [23, 87]. Little information is available about the design of these motors due to their proprietary nature. However from the constant-power speed range figures given it is likely that the Mannesman Rexroth design uses a single-barrier construction with ferrite magnets (see Fig. 3.1). The GEC Alsthom design with its better field-weakening performance probably uses several internal flux-barriers. Both designs probably use a conventional radially-laminated geometry due to the low number of flux-barriers.

Jack, Mecrow and Mitcham [88] describe the design of a 20kW spoke-type permanent magnet machine for vehicle traction drives. It uses samarium-cobalt (SmCo) magnets and has a design constant-power speed range of 5:1. Such a design features high torque per volume and power per weight ratios. It uses a high stator current density and requires water-cooling for continuous operation. The high stator currents allow a wide field-weakening range despite the use of a single-barrier construction with rare-earth magnets (see Fig. 3.1). The design is more of a surface permanent magnet design as the high saturation nearly completely removes the saliency. This type of optimal field-weakening design has the disadvantage of having a high back-emf voltage (see Sec. 2.6).

The optimisation of the output torque and power-factor (via the saliency ratio) of the axially-laminated synchronous reluctance geometry has been investigated by Boldea [64, 74], Lipo [89] and Staton, Miller and Wood [21, 81]. This chapter seeks to

optimise the field-weakening performance and particularly the constant-power speed range. It was shown in Sec. 3.2.2 that this is heavily dependent on the saturated saliency ratio and the maximum-torque-per-ampere current-angle. Extensive use is made of the analytical and finite-element modelling techniques described in Chapter 4.

The modelling and design of multiple-barrier interior permanent magnet motor drives was investigated by Fratta, Vagati, Villata and Marongiu. They found problems with high iron losses in axially-laminated designs due to rotor flux pulsations [59] (see Sec. 3.2.3). Due to this they concentrated on the radially-laminated geometry with a low number of barriers. They investigated the design and optimisation of this type of rotor in detail [72]. Their design analysis uses analytical and lumped-circuit models and does not take into account the effect of saturation. A prototype machine incorporating ferrite magnets was described [39] however no field-weakening results were presented.

Despite the reported high iron losses the axially-laminated geometry was chosen because it offers the potential for the highest saliency ratio and hence best field-weakening performance. An existing D132 frame size[1] induction motor stator was used for the design. Though this will not be optimised for axially-laminated reluctance designs it should give a reasonable performance, is readily available and allows useful comparison with the induction motor performance.

Lipo [7] suggested that an axially-laminated interior permanent magnet motor could be constructed by sandwiching bar magnets between the laminations. The new design uses this idea with rubber-bonded magnet sheet. In axially-laminated motors the magnet requirement is low enough to allow the use of rubber-bonded ferrite magnets. This is a flexible, isotropic, low-cost material available in thin sheets (0.4 to 1mm) and is normally used in applications such as magnetic "L" plates for cars and refrigerator door seals. In the motor design, the flexibility is important as the magnets are sandwiched between magnetic laminations which have sharp bends in a four-pole motor. Compared even with sintered ferrite magnets, its magnetic properties are poor but prove to be all that it required for this application.

[1]This indicates that the centre of the shaft is 132mm above the mounting surface.

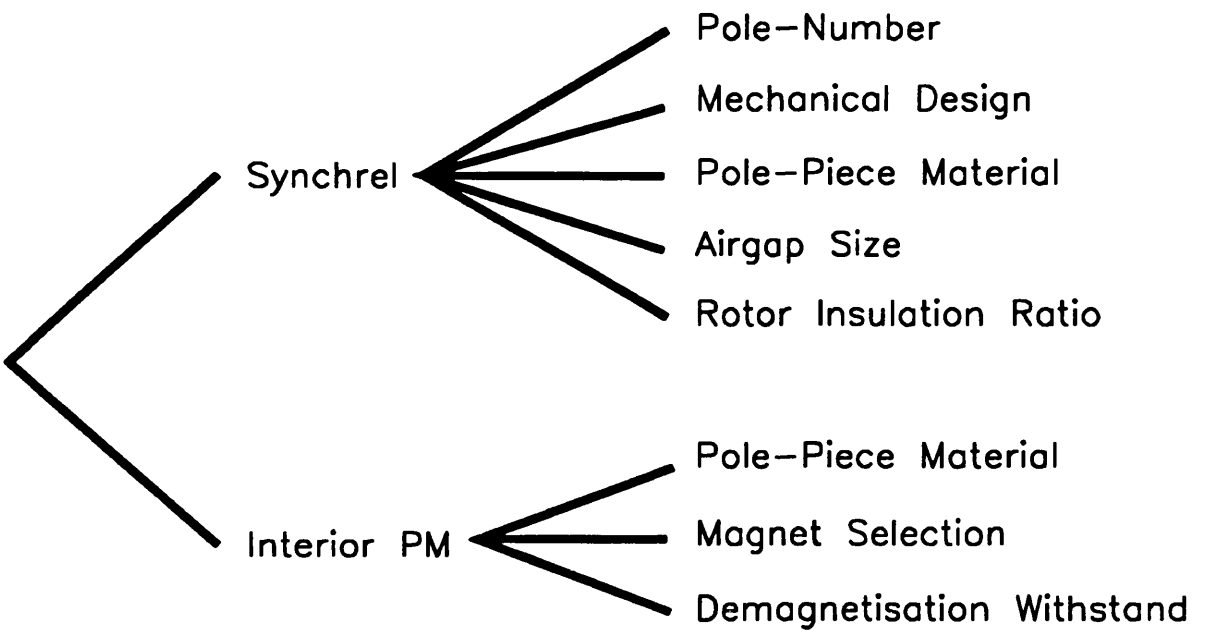

Figure 5.1: *Design procedure for axially-laminated motors.*

Due to the time constraints it was necessary to finalise the design of the motors before all the analysis described in this section was completed. Thus though the prototype synchronous reluctance design gives reasonable performance, the analysis shows that the parameters chosen were not always optimum. This section investigates how the prototype machine could be optimised for future designs and how much improvement is possible.

Fig. 5.1 shows the design approach used in this chapter. Sec. 5.2 considers the design of a 7.5kW axially-laminated synchronous reluctance motor. It makes extensive use of finite-element modelling to investigate the effect of changing the design parameters on the field-weakening performance. Sec. 5.3 examines the tradeoffs in the reluctance performance involved in adding magnets into the rotor, the selection of the magnet material and the demagnetisation-withstand constraints.

5.2 Optimal Synchronous Reluctance Design

Axially-laminated interior permanent magnet motors designed for good field-weakening performance are predominantly reluctance machines. Thus firstly the optimisation of the performance of the axially-laminated synchronous reluctance motor drive is examined. The major design parameters are : pole number, mechanical design, pole-piece material, airgap size and lamination to barrier ratio. Each of these will now be examined in turn.

5.2.1 Pole Number

The intrinsic magnetising saliency ratio equation (4.29) showed that the unsaturated magnetising saliency ratio is inversely proportional to the number of poles. Most axially-laminated designs have four poles [49, 50, 71, 81, 90] although Boldea has built two-pole designs [48] and El-Antably et al. [91] and Rao [92] have built six-pole designs (see Fig. 5.2). The two-pole designs offer the highest saliency (21 has been achieved) and the simplest rotor design as no bending is required. The main drawback is that unlike the higher pole number designs, there is no room for a shaft to run through the rotor. In [48] this was overcome for two small motors (0.55kW and 1.5kW) by glueing endplates to the rotor stack. This is however impractical for larger motors.

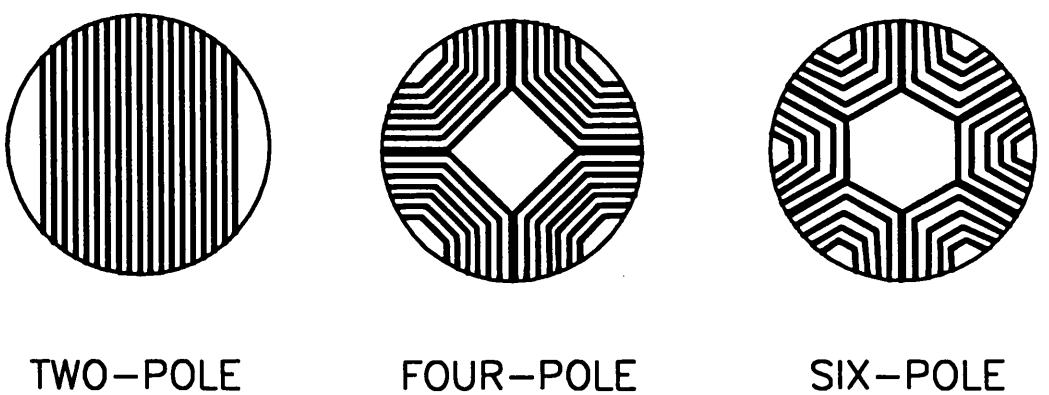

Figure 5.2: *Two, four and six-pole rotors*

Six-pole designs can be built but are more complex and have a saliency ratio which is theoretically two thirds of that for the four-pole design. However it was shown in Fig. 3.22 that the improvement in the constant-power speed range due to increasing the saturated saliency ratio can be substantially offset by the associated increase in saturation (and hence the maximum-torque-per-ampere current-angle). Thus in large motors (say greater than 15kW), six or eight-pole designs may yield better performance because the shorter flux paths reduces the saturation. This decreases the maximum-torque-per-ampere current-angle which improves the constant-power speed range.

Using the approximation described in Sec. 4.2.4, a 7.5kW synchronous reluctance motor would have an unsaturated saliency ratio of approximately $0.4\xi_{mi}$. From this a four-pole design using the same airgap as the equivalent induction motor would have a saliency ratio of about 13. A six-pole 7.5kW motor design would thus yield too low a saliency ratio (about 8) for good performance. Thus a four-pole 7.5kW design was used.

5.2.2 Mechanical Design

A commercial four-pole 7.5kW induction motor stator was used for the prototype. Its main dimensional information is listed in Table 5.1. An induction motor based on this stator is actually capable of 11kW at rated speed, but is derated to 7.5kW for a 10:1 constant torque speed range with a shaft-mounted fan [93, 94]. This is due to the reduced cooling effect of the fan at low speeds restricting the torque in this region.

Fig. 5.3 shows the finite-element model of the rotor and stator of the 7.5kW motor. A comparison with the model of the 120W motor shown in Fig. 4.7 on pg. 175 shows the effects of scale on the relative proportions. The most striking effects are the decrease in the relative slot volume and the increase in the relative back-iron thickness in the larger motor.

The rotor consists of a square cross-section shaft to which the four rotor poles are bolted (see Figs. 5.4 and 5.5). Each pole consists of a stack of interleaved lamination and insulation layers. The laminations are bent and the insulation material scored

Table 5.1: *Four-pole 7.5kW stator information.*

Rated Output Power	7.5kW
Rated Voltage	$415V_{ll}$ rms
Rated Current	15 A rms
Winding Connection	star
Phase Resistance (hot)	0.75Ω
Poles	4
Slots	36
Stack Length	202.4mm
Stator Inner Diameter	127.08mm

prior to assembly. The poles are held in place by pole-pieces which are secured by bolts which run through the pole and into the shaft. Note that non-magnetic bolts are necessary to avoid magnetically short-circuiting the rotor.

The edge length l_s of the square cross-section shaft is generally chosen so that the two lines formed by the bends in the laminations in each pole intersect roughly at the outside of the rotor (see Fig. 5.4). From geometry this occurs when :

$$l_s = \frac{2\tan 22.5^o}{1+\tan 22.5^o} r_1 \approx 0.6 r_1 \tag{5.1}$$

This choice gives well-shaped pole-pieces, maximises the pole-arc and gives a reasonably stiff shaft.

A reasonable amount of pole-piece material is desirable in order to give the pole-pieces sufficient strength. A pole-arc of 120^o electrical was found acceptable.

There is a tradeoff on the size of the bolts. The axial length of the rotor lost due to the bolts is proportional to their diameter, while their strength is proportional to the square of the diameter. Thus for a given total bolt strength, the larger the bolts, the less rotor magnetic cross-section lost. However a reasonable number of bolts should be used in order to distribute the forces more evenly over the rotor length.

The bolts carry the centrifugal forces which attempt to lift the poles from the shaft. In order to calculate the forces involved, the following conservative simplifying assumptions are used : the shaft is circular with a radius r_s equal to half its edge

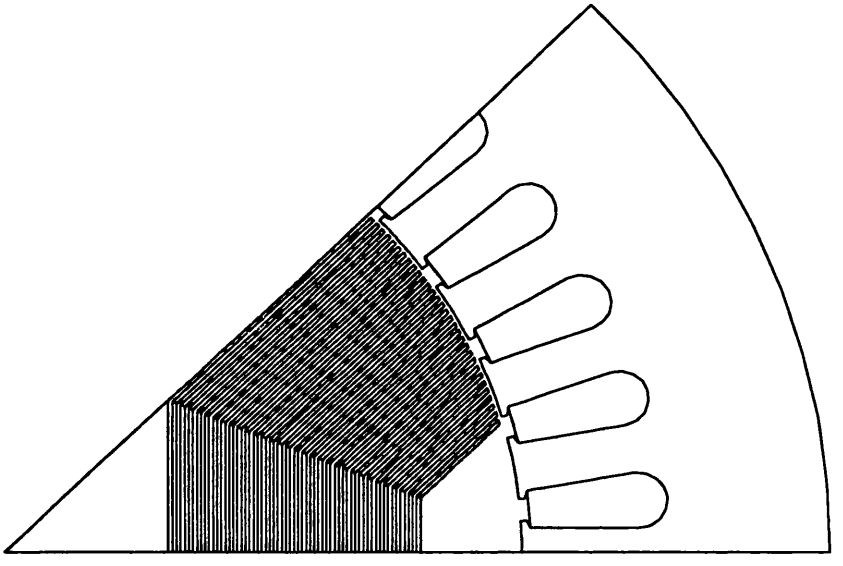

Figure 5.3: *Cross-section of 7.5kW synchronous reluctance motor.*

length; the density of the rotor is that of iron; and finally that only forces parallel to the bolt axis contribute to tensile forces in it. From these assumptions it can be shown that the force on each bolt, F_b is given by :

$$F_b = \frac{\sqrt{2}}{3N_b}\rho_l\omega^2(r_1^3 - r_s^3) \tag{5.2}$$

where N_b is the number of bolts per pole, ρ_l is the density of the laminations and ω is the mechanical speed. The density of steel is approximately 7800kgm^{-3} [95].

The maximum force which each bolt can carry is determined by the minimum force required to cause it to fail. There are three failure mechanisms each with its own maximum allowable force [96] :

1. Tensile failure of bolt :

$$F_1 = (\pi/4)D_{minor}^2\sigma_{yb} \tag{5.3}$$

2. Shear failure of bolt threads :

$$F_2 = (\pi/4)D_{minor}l_{bs}\sigma_{yb} \tag{5.4}$$

3. Shear failure of shaft threads :

$$F_3 = (\pi/4)D_{major}l_{bs}\sigma_{ys} \tag{5.5}$$

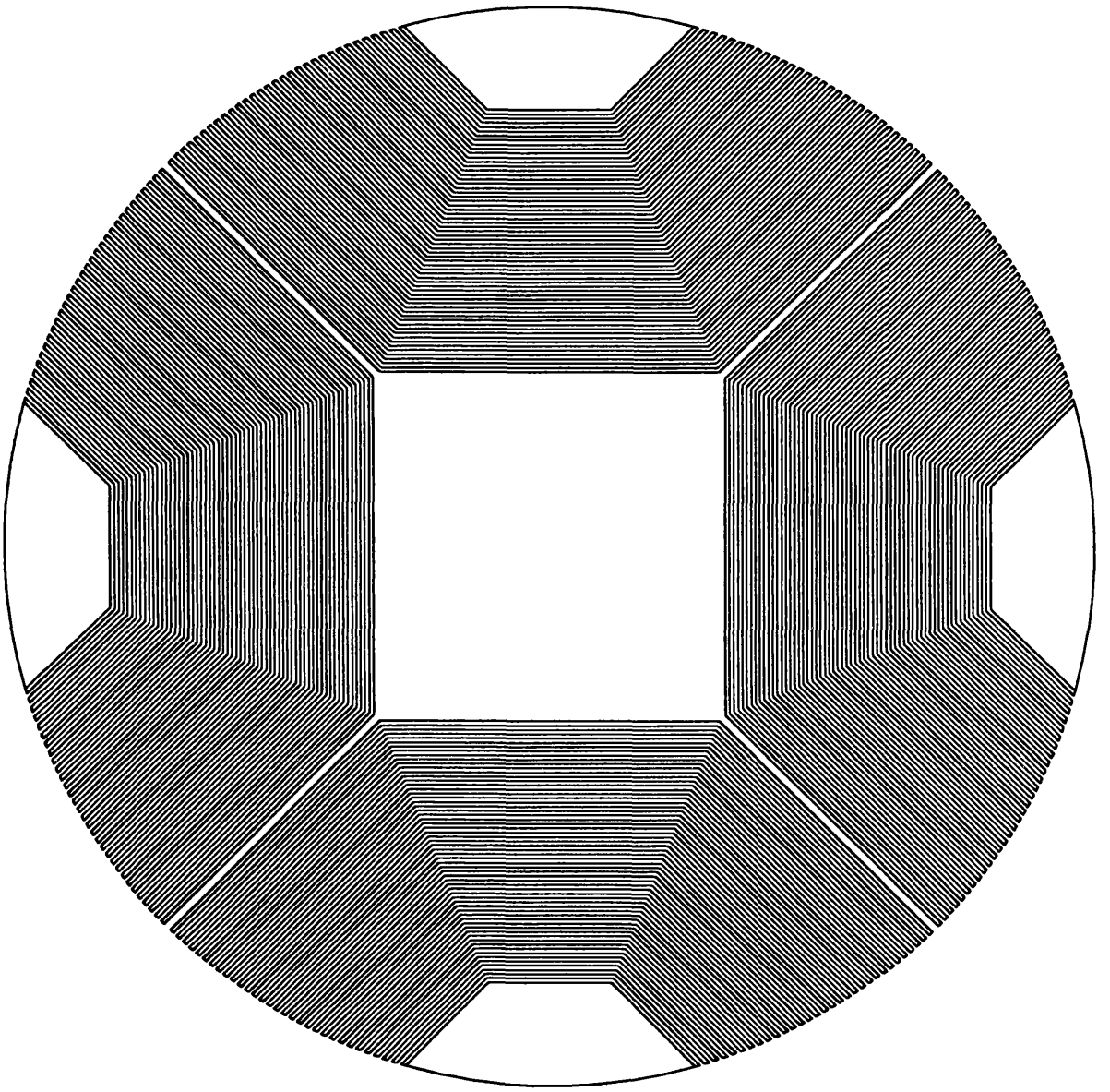

Figure 5.4: *7.5kW axially-laminated rotor cross-sectional view.*

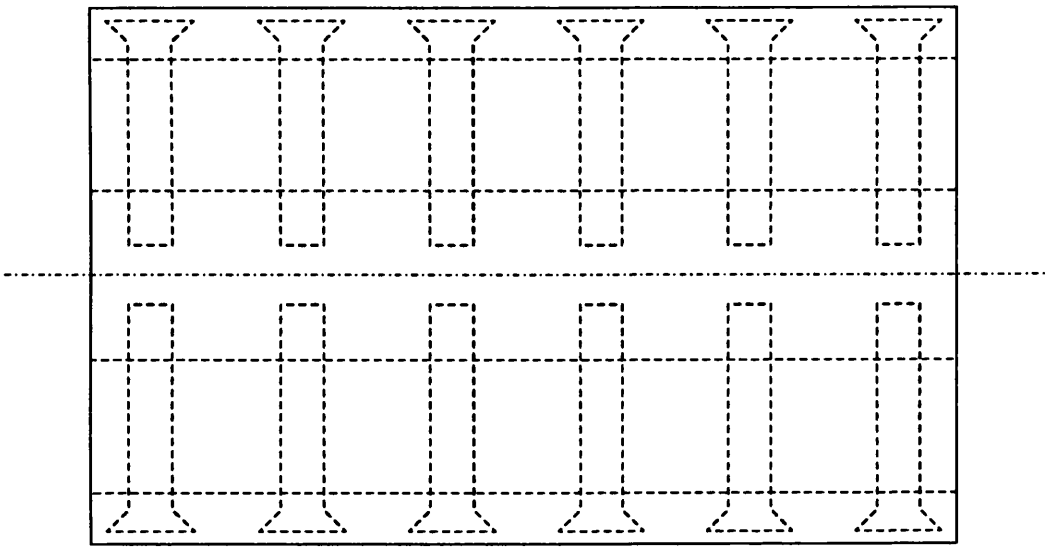

Figure 5.5: *7.5kW axially-laminated rotor axial view.*

where D_{major} is the bolt major diameter[2], D_{minor} is the bolt minor diameter[3], l_{bs} is length of the bolt which is embedded in the shaft, σ_{yb} is the yield stress of the bolt and σ_{ys} is the yield stress of shaft. The yield stress of stainless steel is about 230MPa and of mild steel is about 300MPa [95].

The more bolts used in the design, the less iron cross-section is available to carry flux. For 10mm diameter non-magnetic stainless steel bolts the failure forces F_1, F_2 and F_3 are 12kN, 19kN and 31kN respectively. Thus the bolts will clearly fail in tension first. Six bolts per pole gives a failure speed of 6000rpm for the 7.5kW design. Allowing a factor of four safety margin with respect to the bolt stress gives a maximum safe operating speed of 3000rpm.

In order for a wide field-weakening range to be useful, the rotor should be mechanically capable of operating up to a sufficiently high speed. The rated speed of the drive with rated voltage should be comparable to the induction motor, that is about 1500rpm. A 3000rpm maximum speed limitation will thus limit the drive to a constant-power speed range of about 2:1. In order to demonstrate the wide field-

[2]The major diameter is the diameter of the bolt measured at the top of the screw threads.

[3]The minor diameter is the diameter of the bolt measured at the bottom of the screw threads.

Table 5.2: *Effect of pole-pieces and bolts.*

Property	Magnetic Pole-Pieces	Prototype	No Bolts
Pole-Pieces	magnetic	non-magnetic	non-magnetic
Bolt Holes	present	present	absent
Torque [Nm]	59.2	54.6	62.3
ξ_u	10.7	12.3	12.2
ξ_s	9.2	10.7	10.8
CPSR	2.38	2.44	3.43
γ_m	61.2°	62.9°	56.6°

weakening range this can be overcome by simply operating the motor at a lower voltage in order to reduce the rated speed. However it is clear that for a commercial motor drive it will be necessary to examine alternative means for holding the rotor together.

The effect of the six bolt holes per pole is to locally reduce the effective rotor magnetic cross-section by $6 \times 10mm = 60mm$ or 30%. This increases the saturation in the rotor.

5.2.3 Pole-Piece Material and Bolt Holes

The next choice is the type of pole-pieces used. Either magnetic (steel) or non-magnetic (brass) pole-pieces can be used. Magnetic pole-pieces increase the effective pole-arc to 180° electrical and hence increase the q-axis inductance (4.19) and thus the output torque. However they also increases the d-axis inductance which reduces the saliency ratio. The prototype used non-magnetic pole-pieces to obtain the highest saliency ratio. The d- and q-axis flux plots are shown in Fig. 5.6. Note the similarities with the 120W flux plots shown in Figs. 4.9 and 4.11 in Sec. 4.3.2.

Fig. 5.7 and Table 5.2 show the finite-element results of the effect of using magnetic pole-pieces and also of removing the bolt holes, on the saturation characteristics and

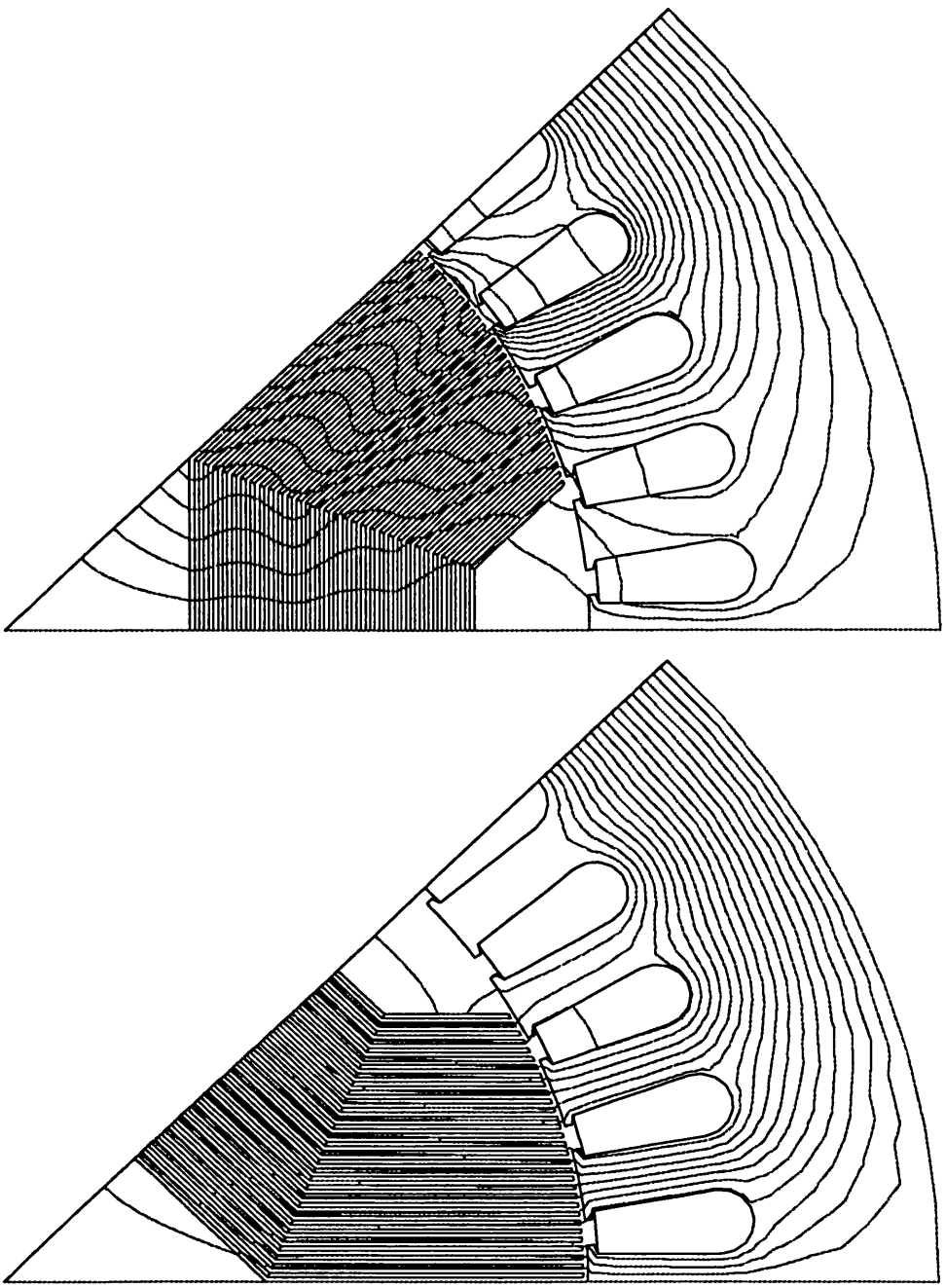

Figure 5.6: *7.5kW* SYNCHREL *d-axis (top) and q-axis (bottom) flux plots.*

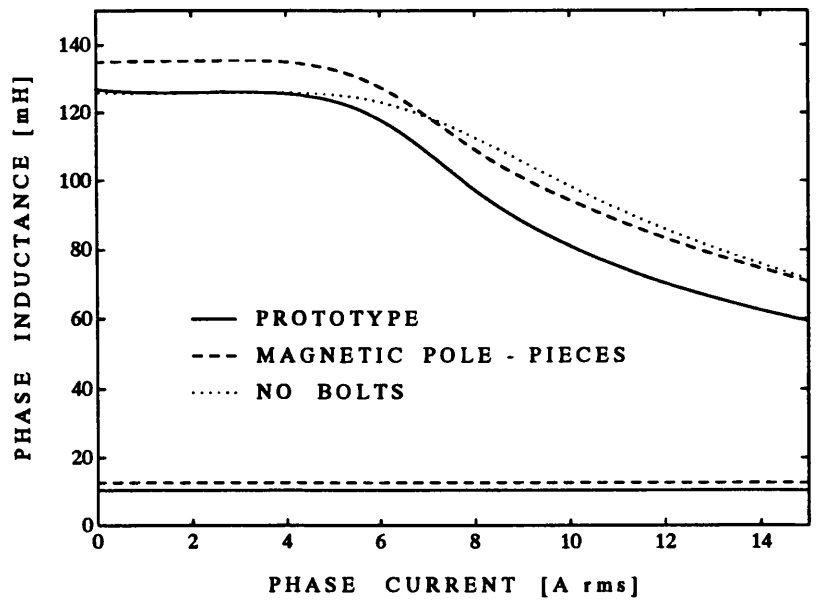

Figure 5.7: *Calculated inductance characteristics for the 7.5kW* SYNCHREL.

the field-weakening performance. The bolt holes are modelled using the pseudo 3-D technique described in Sec. 4.3.1. Magnetic pole-pieces increase the output torque by 9%, decrease the saturated saliency ratio by 15% and reduce the constant-power speed range by 2.5%. The bolt holes reduce the output torque by 14% and the constant-power speed range (CPSR) by 40%. Note that L_d is unaffected by the bolt holes. Despite the lower saturation when the bolt holes are absent, the saturated saliency ratio is similar to that of the prototype due to the lower γ_m. This highlights the sensitivity of the constant-power speed range to γ_m.

The above results show that for this particular design that magnetic pole-pieces would have given more torque with no significant reduction in the constant-power speed range. This however cannot be generalised to all axially-laminated motors as it is dependent on the degree of saturation in the rotor. The results also show that removing the bolts and hence increasing the effective rotor cross-section yields substantial performance improvements. This could be achieved by either increasing the length of the rotor beyond that of the stator or else by finding some means for reducing the

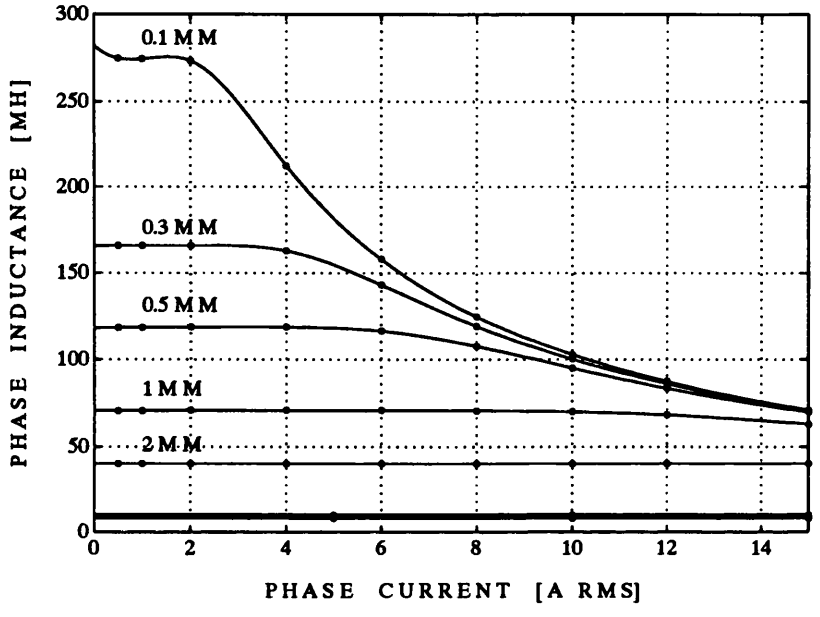

Figure 5.8: *Calculated flux-linkage characteristics with different airgaps.*

number of bolts without compromising the mechanical strength.

5.2.4 Airgap Size

The intrinsic magnetising saliency ratio equation (4.29) shows that the unsaturated magnetising saliency ratio is inversely proportional to the airgap size. In practice as the airgap is decreased, magnetic saturation will cause the saturated saliency ratio to be limited. Thus decreasing the airgap beyond a certain point will not significantly improve the field-weakening performance and may even make it worse.

Fig. 5.8 shows the calculated finite-element flux-linkage characteristics for the 7.5kW synchronous reluctance motor with a range of airgaps from 0.1mm to 2mm. Note that the induction motor uses an airgap of about 0.5mm. The unsaturated q-axis inductance is not quite inversely proportional to the airgap due to Carter's coefficient (see Sec. 4.2.2). For airgaps of 2mm and 1mm the inductance characteristics show little saturation. However as the airgap is decreased below 1mm, saturation occurs firstly

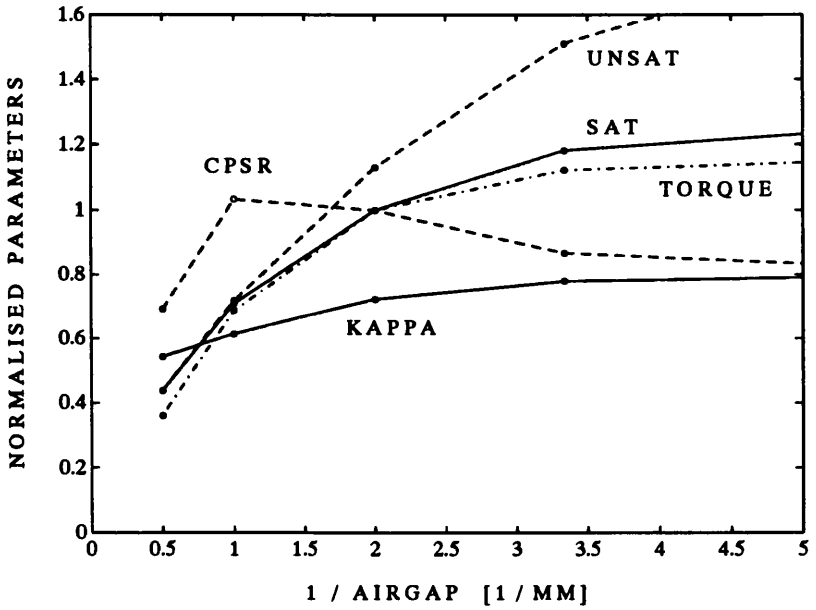

Figure 5.9: *Effect of airgap size on the calculated performance characteristics.*

at high currents and then at progressively lower currents. For a given value of current, once the airgap is small enough to cause the inductance to saturate, then decreasing the airgap further has little effect. With regards to the d-axis inductance, decreasing the airgap produces slightly more leakage flux and hence produces a second-order increase in the d-axis inductance.

The operating characteristics of the designs were calculated from the inductance characteristics and the normalised results are shown in Fig. 5.9 as a function of the *inverse airgap* ($1/g$). The unsaturated saliency ratio (UNSAT) and the saturated saliency ratio (SAT) are normalised against the saturated saliency ratio at the nominal airgap (0.5mm). The torque and constant-power speed range are also normalised against their respective values at this value of airgap. The inverter utilisation κ (KAPPA) is the ratio of the rated output power of the motor to the inverter VA rating (see Sec. 1.1).

All the characteristics except the constant-power speed range improve monotonically with increasing $1/g$. Note that as the airgap becomes very small, all the parameters except the unsaturated saliency ratio asymptote towards constant values.

Thus decreasing the airgap below about 0.25mm will not yield a significant change in performance. With zero airgap the output torque is about 15% greater and the constant-power speed range about 15% less than what is obtained with a 0.5mm airgap.

The constant-power speed range differs from the other characteristics in that it peaks at about $g = 1$mm. This is associated with the increase of both the saturated saliency ratio and the maximum-torque-per-ampere current-angle with decreasing airgap size. The first effect causes the constant-power speed range to increase while the second causes it to decrease. It is not worthwhile using the maximum constant-power speed range airgap size as the peak constant-power speed range is only a few percent larger than that obtained with a 0.5mm airgap and the torque falls rapidly with increasing airgap.

5.2.5 Rotor Insulation Ratio

The intrinsic magnetising saliency ratio equation (4.29) shows that the unsaturated magnetising saliency ratio is proportional to the rotor insulation ratio a. This is the proportion of air in the rotor (4.21). Increasing the rotor insulation ratio increases the unsaturated saliency ratio but may decrease the output torque due to saturation. The prototype used equal lamination and insulation thicknesses ($a = 0.5$).

Boldea and Nasar [64], Lipo [89] and Staton, Miller and Wood [21] have investigated the effect of the rotor insulation ratio on the saliency ratio and the output torque. Boldea and Nasar recommend using values of a in the range 0.33 to 0.40 with the upper limit due to rotor saturation. Lipo suggests a value of about 1/3 in order to maximise the output torque and also to reduce rotor iron losses. Staton et al. found a value of 0.5 gave optimum results.

Finite-element analysis was used to calculate the saturation characteristics of the 7.5kW motor with different values of rotor insulation ratio. The results are shown in Fig. 5.10. Consider first the d-axis inductance. This is composed of the leakage inductance L_l which is relatively constant and the magnetising inductance L_{dm} which

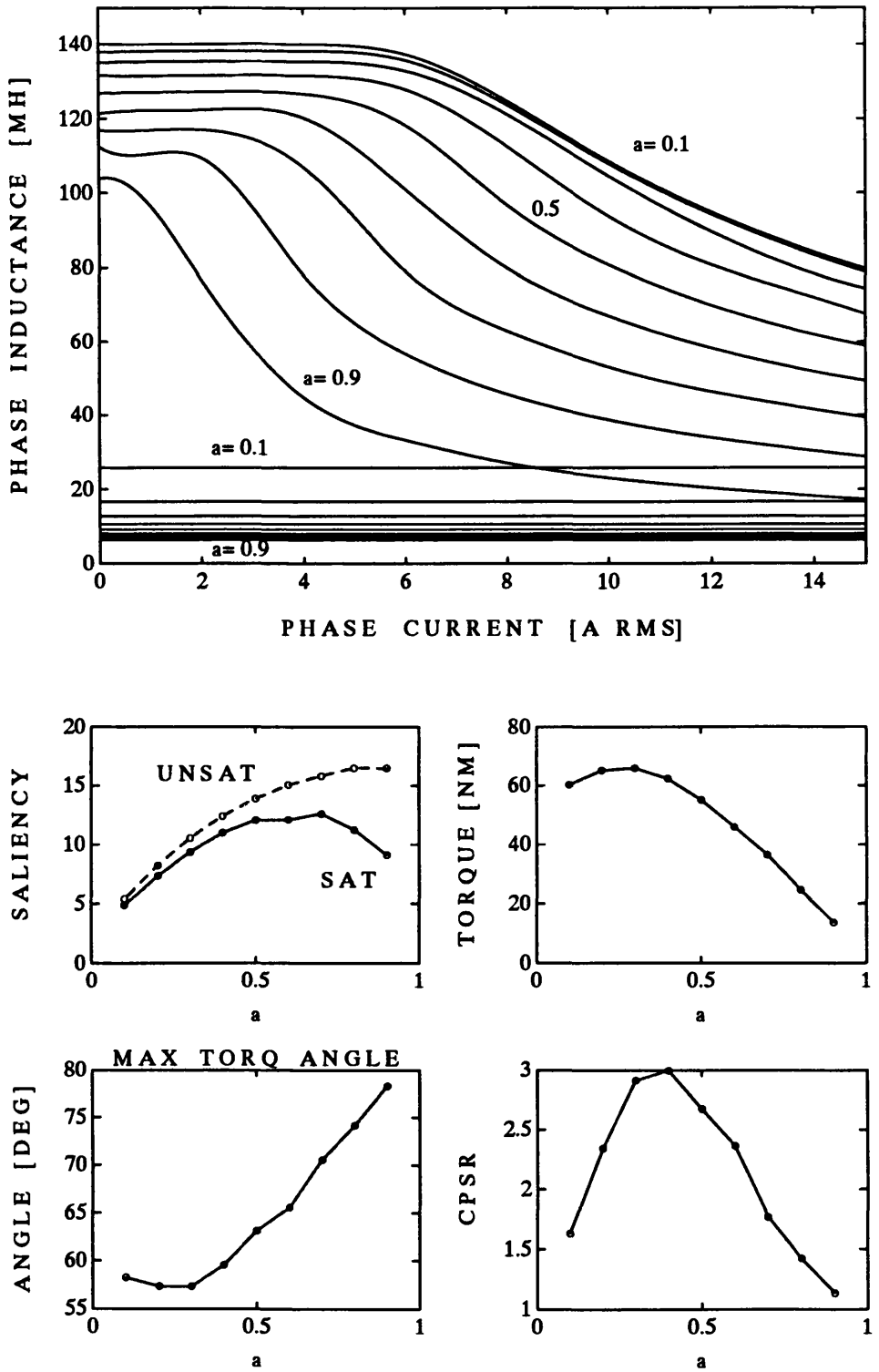

Figure 5.10: *Effect of the rotor insulation ratio on the calculated performance characteristics. Top : flux-linkage characteristics. Bottom : calculated performance.*

is ideally inversely proportional to a (4.27). Note that for small values of a, L_{dm} and hence L_d becomes large as there is little non-magnetic material in the rotor.

Decreasing a increases the unsaturated q-axis inductance due to the reduction in Carter's coefficient (see Sec. 4.2.2). The amount of saturation decreases with decreasing a as the volume of iron in the rotor increases. Note that there is only a small change in the characteristic from going from $a = 0.2$ to $a = 0.1$ which indicates for these values of a there is little saturation in the rotor.

From (4.29) the saliency ratio should be proportional to a. This is true for low values of a, however for larger values, Carter's coefficient reduces the unsaturated saliency ratio and heavy saturation brings down the saturated saliency ratio. This is reflected in the maximum-torque-per-ampere current-angle plot. The torque peaks at about $a = 0.3$ and the constant-power speed range (CPSR) peaks at about $a = 0.4$. Note that these results are sensitive to how much of the rotor cross-section is lost due to the bolt holes. The value of $a = 0.5$ used in the prototype is not optimal, but gives reasonable performance.

5.3 Optimal IPM Design

A major problem with synchronous reluctance motor drives with regard to field-weakening performance is the limited achievable constant-power speed range. The prototype 7.5kW design described in the previous section had a calculated saturated saliency ratio of about 11 (see Table 5.2). Ideally it would have a constant-power speed range of about half this, that is about 5:1, however due to saturation its calculated constant-power speed range is only about 2.4:1. This dramatic reduction is seen in all synchronous reluctance designs as shown in Fig. 3.22 on pg. 152. The previous section has shown that the prototype synchronous reluctance design is not optimally dimensioned. However it was also shown that it would be difficult to achieve a constant-power speed range substantially above about 3:1, even with an optimally dimensioned design.

The limited field-weakening performance can be overcome by adding the correct amount of permanent magnet material to the motor. This produces an optimal field-weakening axially-laminated interior permanent magnet motor drive. The theoretical field-weakening performance of such drives was investigated in Chapter 2.

A larger airgap (0.92mm instead of 0.5mm) was used in the interior permanent magnet motor design. This reduced the output torque so that it was comparable to the synchronous reluctance motor drive and did not exceed the dynamometer capacity (see App. A). This also allowed the investigation of the effect of increasing the airgap on the inductance characteristics.

The design of the axially-laminated interior permanent magnet motor drive is based on the prototype synchronous reluctance motor. The main design decisions are : pole-piece material, magnet type and demagnetisation-withstand. Each of these will now be examined.

5.3.1 Pole-Piece Material

Finite-element analysis was used to investigate the effect of using magnetic and non-magnetic pole-pieces on the motor back-emf waveform. Figs. 5.11 and 5.12 show

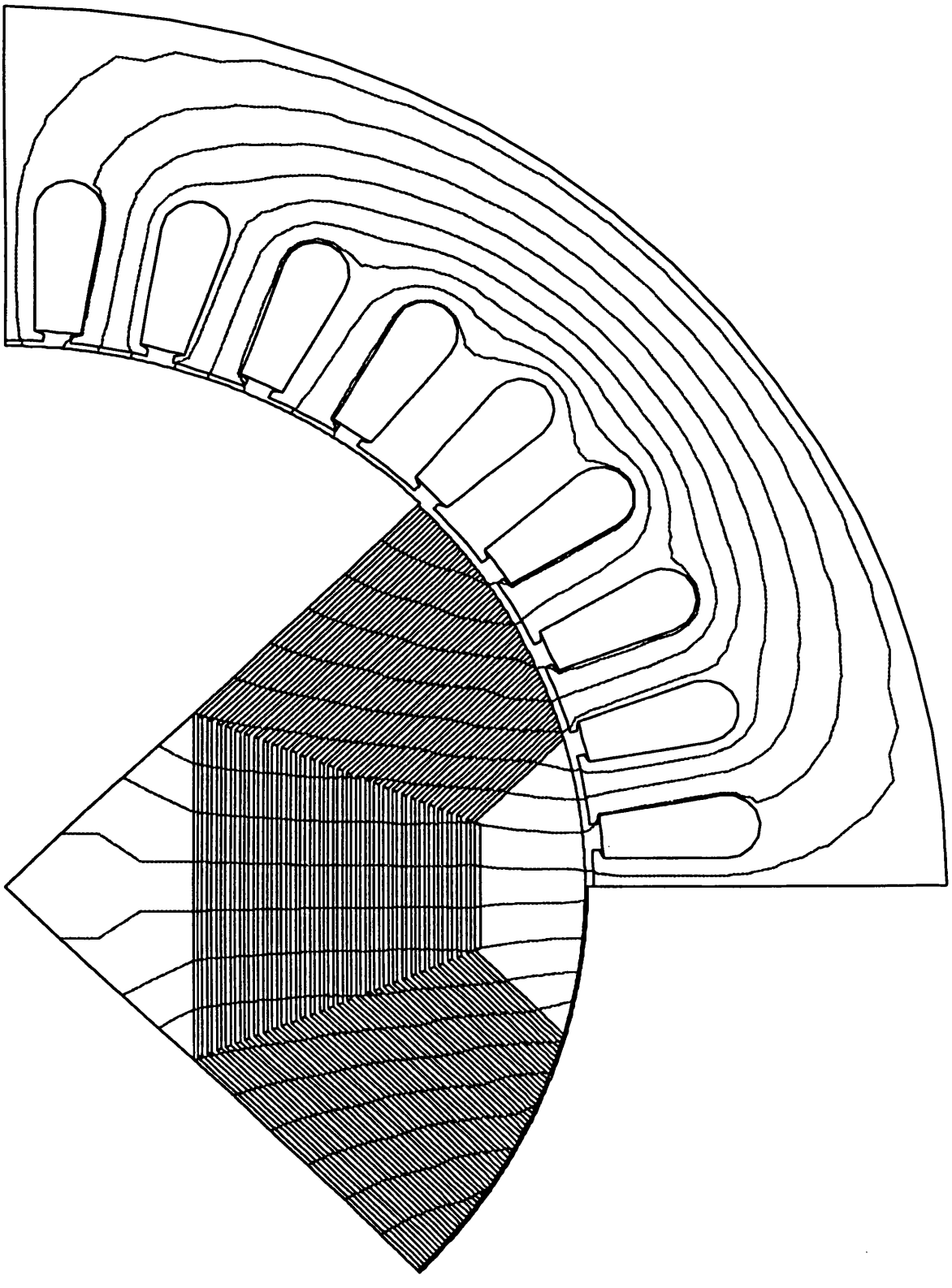

Figure 5.11: IPM *motor drive flux plot with magnetic pole-pieces.*

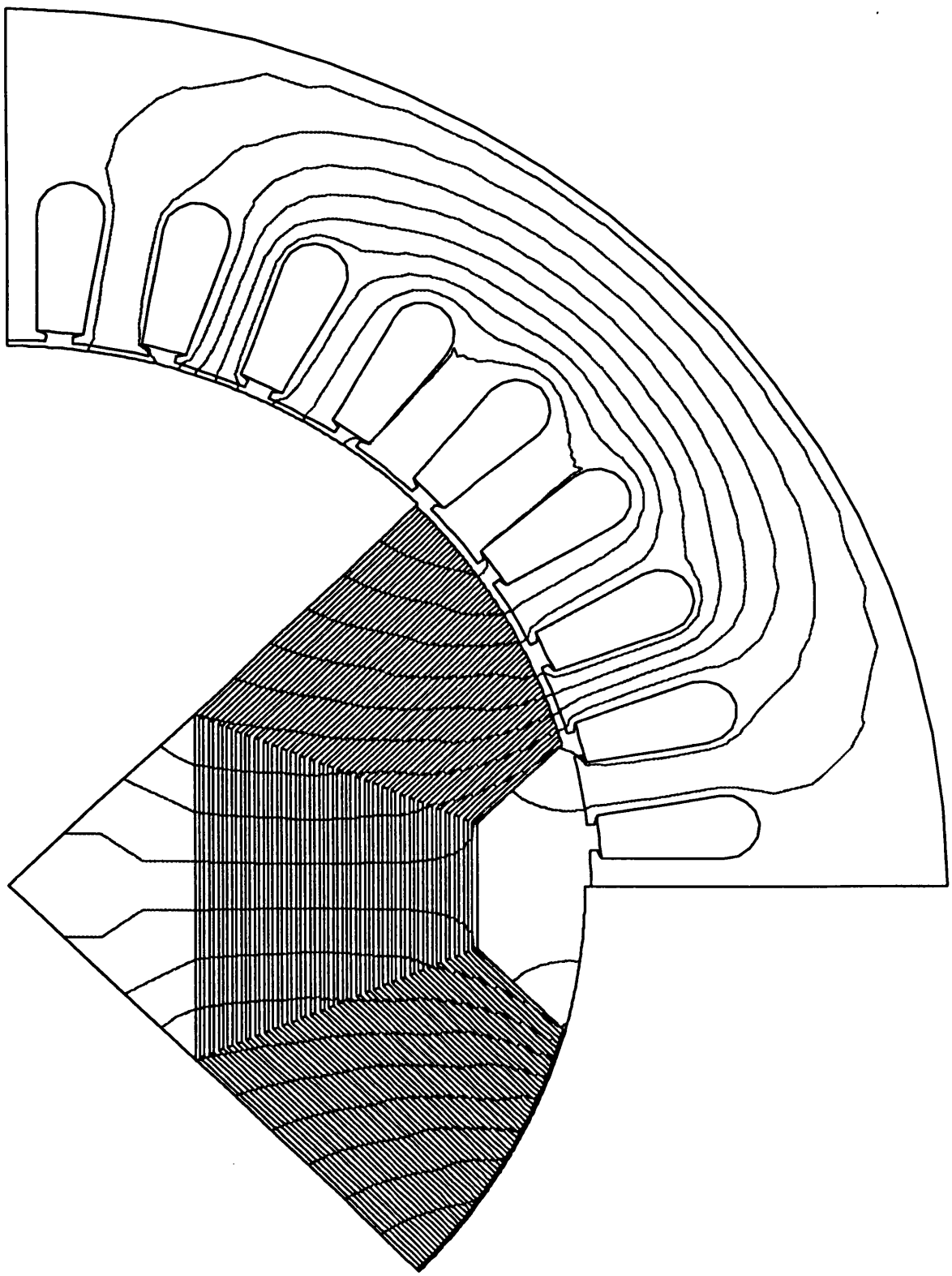

Figure 5.12: IPM *motor drive flux plot with non-magnetic pole-pieces.*

magnet flux plots for the two cases. Note that there is no stator current. The associated magnet airgap flux distribution is shown in Fig. 5.13. Note the distortion to the ideal sinusoidal distribution when using non-magnetic pole-pieces.

The line-to-line back-emf voltage can be calculated (see Fig. 5.13) using the procedure described by Miller et al. [97]. The flux in each stator tooth at a given rotor position can be calculated from the airgap flux distribution. This is repeated as the rotor is stepped through ten mechanical 1^o steps. From this information the flux in each tooth at any integral degree rotor position can be calculated from symmetry. Based on this and a knowledge of the winding distribution, the back-emf voltage can be calculated.

Magnetic pole-pieces increase the fundamental back-emf voltage by 13% and result in a far more sinusoidal airgap flux density distribution and hence back-emf waveform. This is important in order to reduce harmonic iron losses, especially in the field-weakening region [4]. Thus magnetic pole-pieces were used despite the small loss in the saliency ratio shown in Sec. 5.2.3.

The calculated inductance characteristics are shown in Fig. 5.14. The unsaturated q-axis inductance is substantially lower than that for the synchronous reluctance design (see Fig. 5.7) due to the larger airgap. As predicted in Sec. 5.2.4 the flux-linkage characteristics show much less saturation.

5.3.2 Magnet Selection

Table 5.3 [12] shows the remanence of common magnet types. Ferrite magnets are low-cost and are widely used for general-purpose applications. For higher performance, more expensive rare-earth magnets such as neodynium-iron-boron (NdFeB) and samarium-cobalt (SmCo) are used. Sintered magnets are the most common. These are moulded by heating the magnet powder to high temperatures. Rubber-bonded magnets consist of a plastic binder and the magnet powder. These are flexible but have remanences of about half that of the sintered materials.

The 7.5kW axially-laminated interior permanent magnet motor design requires

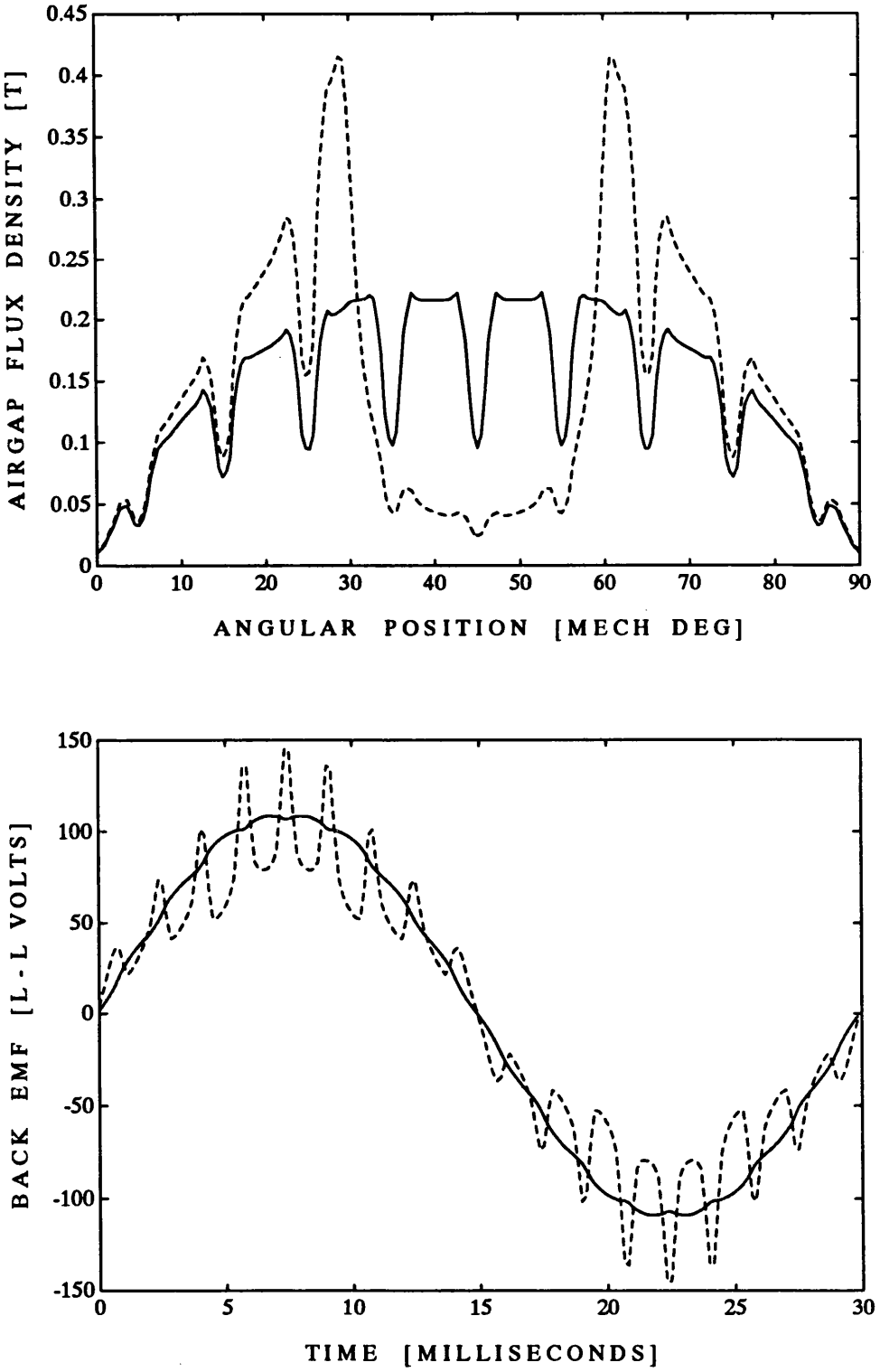

Figure 5.13: *Calculated airgap flux distribution (top) and line-to-line back-emf waveforms at 1000rpm (bottom) with magnetic (solid line) and non-magnetic (dashed line) pole-pieces.*

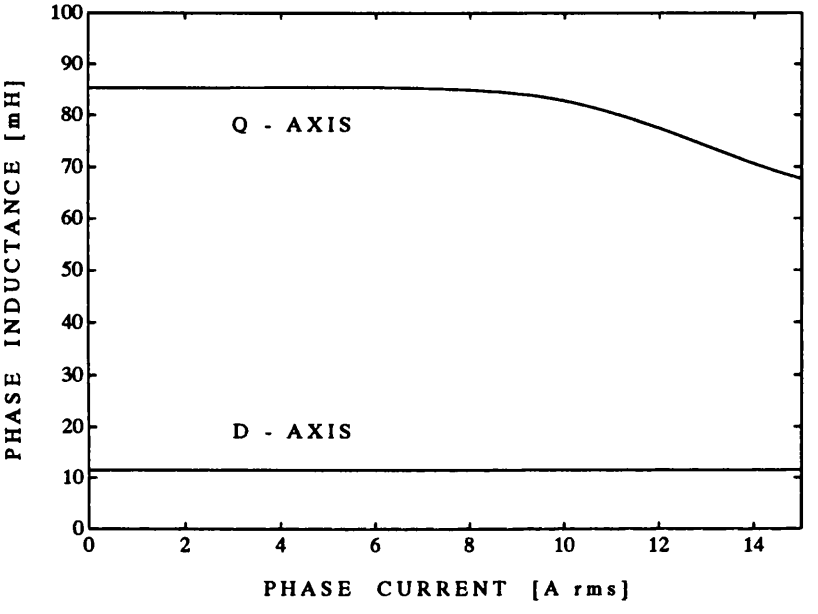

Figure 5.14: *7.5kW axially-laminated* IPM *flux-linkage characteristics.*

magnets with the following properties : available in thin sheets ($\leq$0.5mm), flexible enough to be bent through 45° in a radius of a few millimetres, high coercivity, high maximum operating temperature and low cost. The only flexible magnet sheet presently commercially available in quantity is rubber-bonded ferrite, though flexible neodymium-iron-boron (NdFeB) magnet sheet is under development. Typical properties of these two materials are summarised in Table 5.4.

The optimum field-weakening criteria $\Psi_m = L_d I_c$ (2.1) gives the optimum value of magnet flux-linkage. Finite-element calculations corrected for end-winding inductance gives $L_d = 11.5$mH. Thus the optimum magnet flux-linkage Ψ_m is :

$$\Psi_m = L_d I_c = 11.5\text{mH} \times 15\text{Arms} = 0.173\text{Vs} \tag{5.6}$$

The finite-element flux plots in Fig. 5.11 were calculated with rubber-bonded ferrite magnets. From Fig. 5.13, flexible ferrite magnets give $\Psi_m = 0.214$Vs which is slightly more than the optimal magnet flux-density.

Figs. 5.15 and 5.16 show the effect on the calculated field-weakening characteristics of adding magnet material to the motor drive. The performance of a pure synchronous

Table 5.3: *Typical magnet properties.*

Magnet Type	Remanence
Rubber-bonded Ferrite	0.17 T
Sintered Ferrite	0.4 T
Rubber-bonded NdFeB	0.45 T
Sintered SmCo	1.0 T
Sintered NdFeB	1.1 T

Table 5.4: *Typical flexible magnetic sheet properties. Courtesy of Anchor Magnets, Lucas AEC and Cookson Technology.*

Property	Ferrite	NdFeB
Remanent Flux Density B_r [T]	0.165	0.4–0.5
Coercivity H_c [kA/m]	110	
Intrinsic Coercivity H_{ci} [kA/m]	180	700–1000
Recoil Permeability μ_{rec}	1.10	1.06
Density ρ [kg/m^3]	3600	5000
Max. Continuous Temp. [°C]	80	60–100
Max. Intermittent Temp. [°C]	110	
Temp. Coeff. of B_r [%/°C]	-0.2	-0.1
Temp. Coeff. of H_{ci} [%/°C]	0.4	-0.6
Magnet Thickness [mm]	≥ 0.4	≥ 0.4

reluctance motor with a 0.92mm airgap (point A in the contour plot) is compared against that with the optimal magnet flux (point B), rubber-bonded ferrite magnets (point C) and rubber-bonded NdFeB magnets (point D). Note that point B should ideally lie exactly on the right-hand side of infinite constant-power speed range band as it is an optimal field-weakening design. It does not because the contour plot is calculated for a constant parameter model while the motor shows some saturation.

From Fig. 5.16 the synchronous reluctance motor drive shows a constant-power speed range of 3.2. Adding the optimal magnet flux increases the rated torque and produces a motor drive with the optimal field-weakening performance, that is, full output power up to infinite speeds. The motor drive using rubber-bonded ferrite mag-

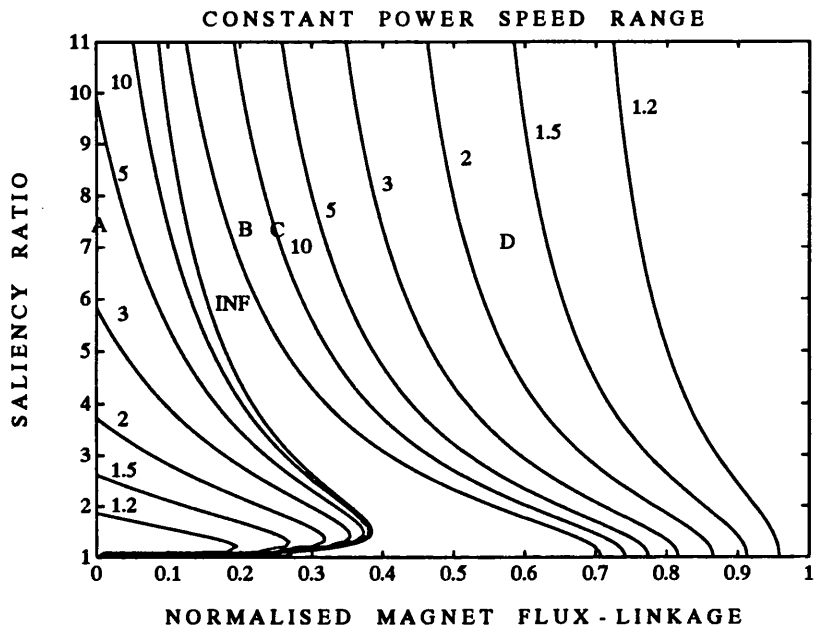

Figure 5.15: *Location of the designs on the* IPM *parameter plane.*

net sheet has a slight excess of flux. This gives it slightly more torque at low speed than the optimal design but reduces the constant-power speed range from infinity to 13. Using NdFeB magnets substantially enhances the low speed torque at the price of a poor field-weakening performance. Note that this assumes that all the insulation layers are replaced with rubber-bonded NdFeB sheet. If only a fraction of the layers are replaced then the magnet flux can be reduced to the optimum amount. Alternatively the proportion of magnet material in the rubber could be decreased in order to reduce the remanence. Both these techniques would give the benefit of the far better demagnetisation-withstand capability of NdFeB magnets.

Rubber-bonded ferrite magnet sheet was used in the prototype due to its ready availability.

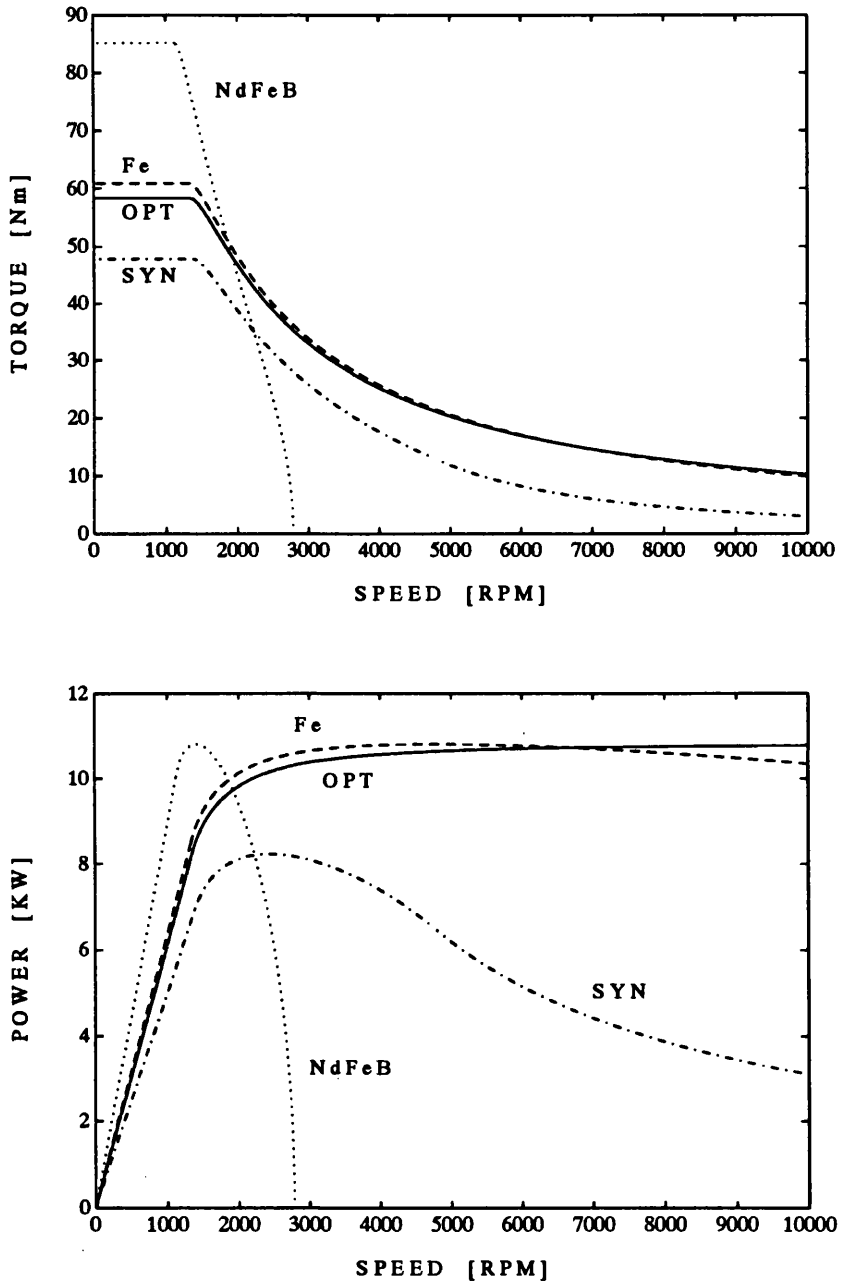

Figure 5.16: *Calculated field-weakening performance curves for a purely synchronous reluctance design (SYN), an optimal design (OPT), a design using rubber-bonded ferrite magnets (Fe) and a design using rubber-bonded NdFeB magnets (NdFeB).*

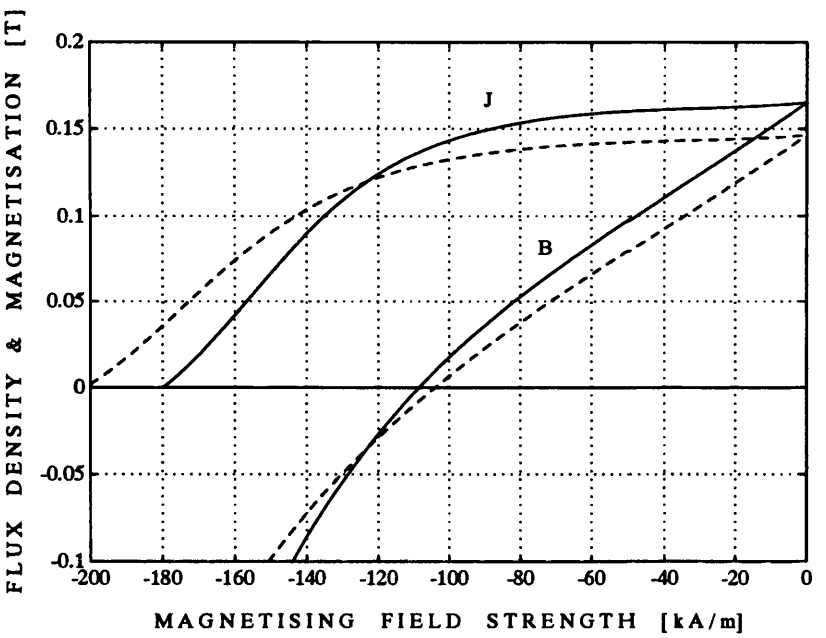

Figure 5.17: *Magnetic properties of rubber-bonded ferrite sheet. The solid line is the measured characteristic (courtesy of Lucas AEC) at 20°C and the dashed line is the calculated characteristic at 80°C.*

5.3.3 Demagnetisation-Withstand

An important design consideration is demagnetisation-withstand. This is because in an optimal field-weakening design the total effective flux in the magnet axis is reduced to zero by rated stator current in that axis. Note that does not actually require the flux in the magnets to be reduced to zero because a substantial proportion of L_d (about 40% in the 7.5kW design) consists of slot-leakage and end-winding inductance which does not produce airgap flux. Nevertheless the magnet operating point is low under these conditions.

The measured demagnetisation curve of the flexible ferrite magnet sheet is shown in Fig. 5.17. Due to the "softness" of the characteristic, care is required to prevent irreversible demagnetisation of the magnets. Fig. 5.18 shows a finite-element flux plot of the worst case demagnetisation condition : rated current in the least inductive axis. It should be compared with Fig. 5.11 where there is no demagnetising current. Note

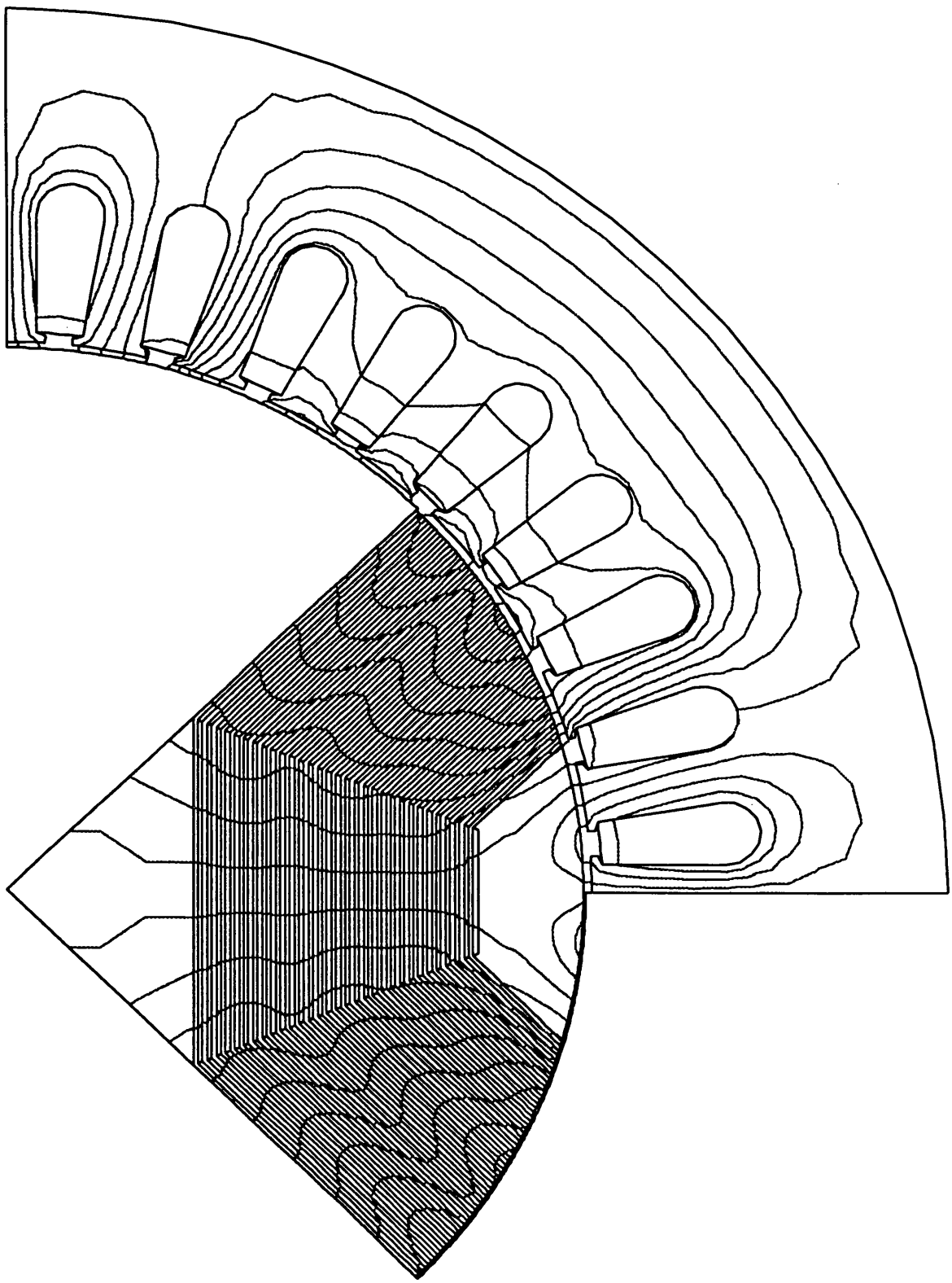

Figure 5.18: *Worst case demagnetisation flux plot.*

that a substantial proportion of the stator flux is forced into leakage paths. Under these conditions the magnetic field in the magnets decreases to about 0.04 to 0.08T. This will not cause irreversible demagnetisation as it is above the knee in the characteristic. Thus there is no danger of demagnetisation as long as the rated stator current is not exceeded.

5.4 Summary of Designs

The prototype axially-laminated synchronous reluctance motor had four poles, non-magnetic pole-pieces, a 0.5mm airgap and a rotor insulation ratio of 0.5. The calculated constant-power speed range was about 2.4. The analysis showed that using magnetic pole-pieces and a smaller value of rotor insulation ratio would yield a significantly higher output torque and a constant-power speed range of about three.

Adding permanent magnets to the motor drive improves its field-weakening performance dramatically. The prototype interior permanent magnet motor used a 0.92mm airgap to give it a comparable output torque to the synchronous reluctance design and also to prevent it overloading the dynamometer. Magnetic pole-pieces were necessary to produce a sinusoidal back-emf waveform and so reduce iron losses during field-weakening. Rubber-bonded ferrite magnets were used as they gave nearly the optimum magnet flux-linkage. They showed sufficient demagnetisation-withstand capability as long as the rated stator current was not exceeded.

Chapter 6

Construction and Test of 7.5kW Motors

This chapter examines the construction and testing of the 7.5kW axially-laminated synchronous reluctance and interior permanent magnet motors. A comprehensive set of test results are presented showing both the performance in the constant torque and in the field-weakening operating regions.

6.1 Construction

6.1.1 Magnetisation of Ferrite Magnet Sheet

The rubber-bonded ferrite magnet sheet is normally supplied magnetised in a multi-pole fashion on one surface. Thus it was necessary to remagnetise it through the thickness. This was performed by passing it between the poles of a large electromagnet. The electromagnet used had 4 inch diameter flat circular pole-pieces with an adjustable airgap. It had provision for watercooling however this was not used. The magnetic flux density in the airgap as a function of the excitation current for two different airgaps is shown in Fig. 6.1. This was measured using a search coil and a ballistic galvanometer. In order to fully magnetise the ferrite magnet sheet a field of about five times the intrinsic coercivity is required [76]. From Fig. 5.17 this implies H=900kA/m or equivalently B=1.1T. This can easily be reached with the electromagnet used.

The magnet sheet was magnetised before assembly. The problem with this proce-

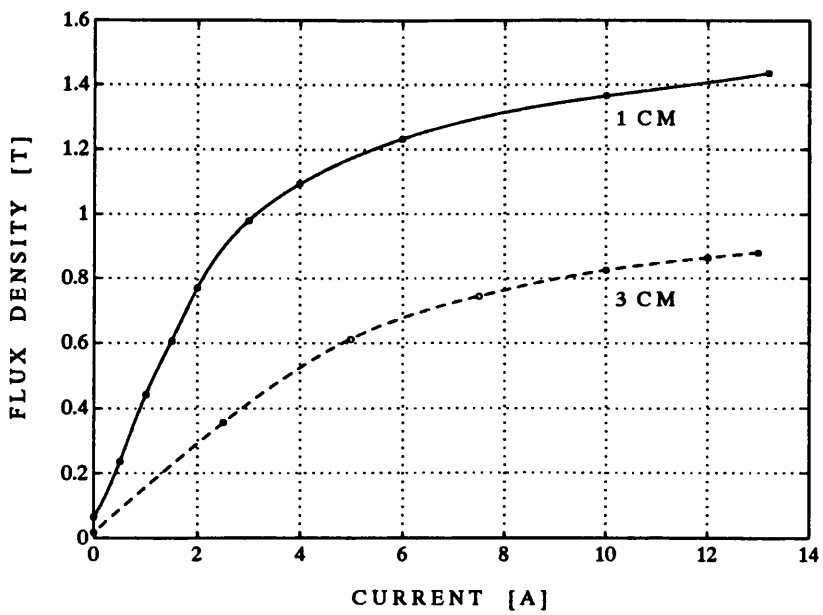

Figure 6.1: *Electromagnet characteristics with different airgaps.*

dure is that the operating point of the sheet magnet material in free air was so low that partial demagnetisation occurred immediately on withdrawal from the magnetising field. Tests on samples revealed a remanence of only about 0.14T instead of the 0.165T obtained by Lucas (see Fig. 5.17) with a sample of a similar but not identical material. Thus the lower remanance may also be partly due to variations in the properties of the material. The 15% lower flux density obtained is allowable as Sec. 5.3.2 showed that the ferrite magnet material produced about 20% excess flux. Thus the actual flux density achieved would now be closer to the optimal amount. An excessive magnet flux density could have been reduced by replacing some of the magnet material with normal insulation material, however this is no longer necessary. Note that the magnets could probably be magnetised *in situ* if desired due to the relatively low magnetising field requirement.

The maximum continuous operating temperature of both the ferrite and NdFeB flexible sheet magnets is limited by the binders used. Present materials are limited to 60–100°C. This is not however an intrinsic limit and if there is a sufficiently large market, alternative binders could be found.

6.1.2 Construction Process

The two 7.5kW axially-laminated rotors were built by the departmental mechanical workshop.

The design of the shaft is similar to that for the original induction motor except the centre section has a square cross-section (see Fig. 6.2). This is drilled and tapped to accept the six 10mm stainless steel bolts per pole. A balancing disk is fitted in order to correct for inevitable small asymmetries in the construction.

Each rotor pole consists of a stack of lamination and insulation layers. Grain-oriented lamination material (Unisil 50M7) was used as this has several times lower iron losses and has better magnetic properties compared to conventional non-oriented steel. Normally grain-oriented steel is only available in thickness of up to 0.35mm, however a 0.5mm variety has recently been introduced by Orb Electrical Steels and

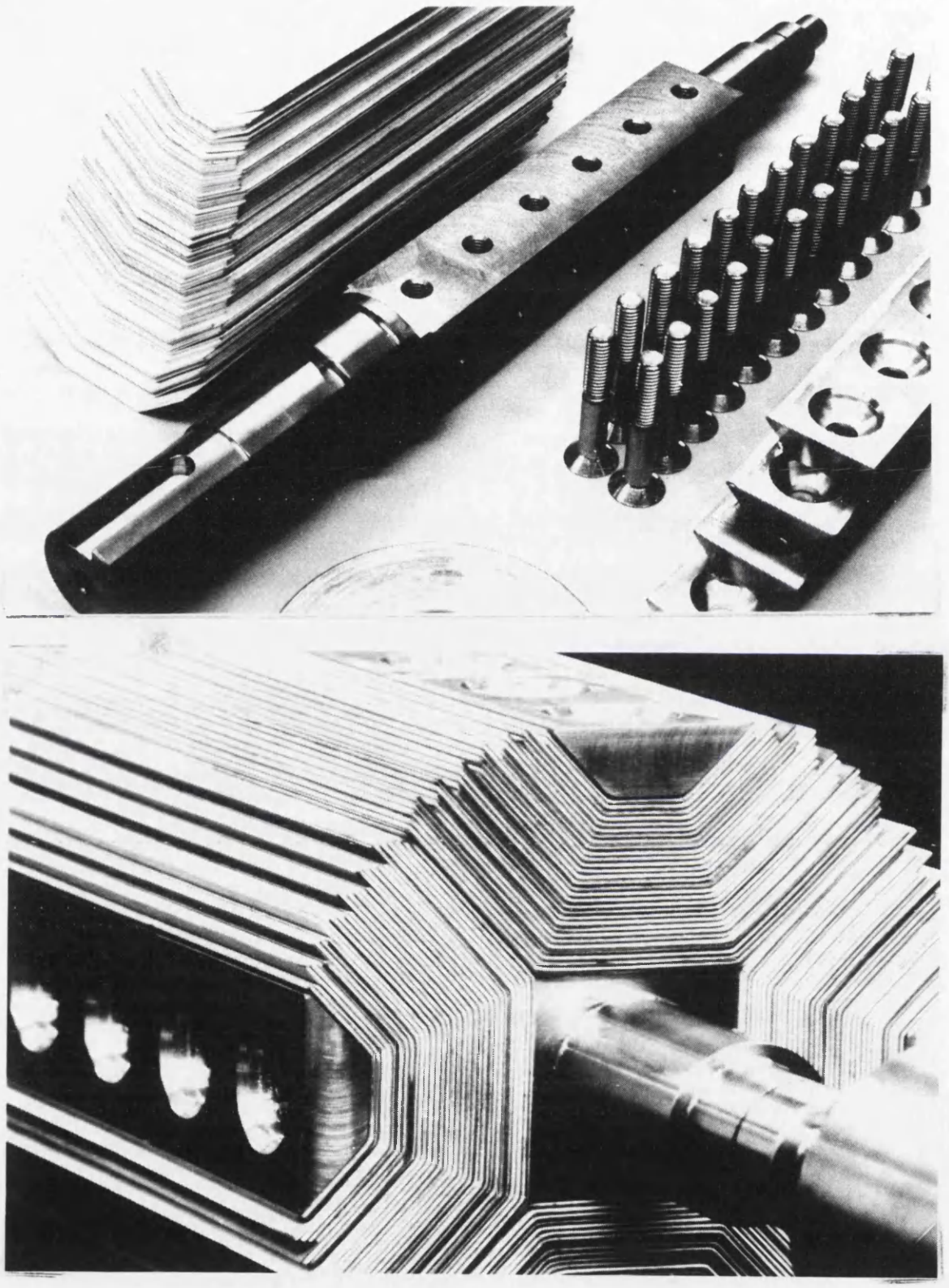

Figure 6.2: *Top : 7.5kW rotor components before assembly. Bottom : Assembled 7.5kW axially-laminated rotor before turning and grinding operations.*

this was used in the prototypes. Each motor contains about two square metres of lamination material. The laminations are cut slightly oversize and are individually bent to give the correct shape. Nomex slot insulation material is used in the synchronous reluctance motor. This is a stiff, high temperature (Class F) plastic material available in thicknesses up to 0.5mm. It is scored prior to assembly. The rubber-magnet material is flexible enough such that it is not necessary to score it.

The pole-pieces are made of brass for the synchronous reluctance motor and mild steel for the interior permanent magnet motor. They are made slightly oversize and then are milled to fit snugly into the poles. The lamination and insulation layers are stacked together and the pole-pieces fitted on top. The entire pole is then clamped and drilled. Next the rotor is assembled by bolting the four poles onto the shaft (see Fig. 6.2). It is then turned roughly down to size. The final diameter required is obtained by grinding. This is calculated from the stator inside diameter and the required airgap. Care is required in measuring the stator inside diameter as it is often irregular and coated with a layer of varnish. A number of measurements should be taken at various positions and the results averaged. The finished rotor is shown in Fig. 6.3.

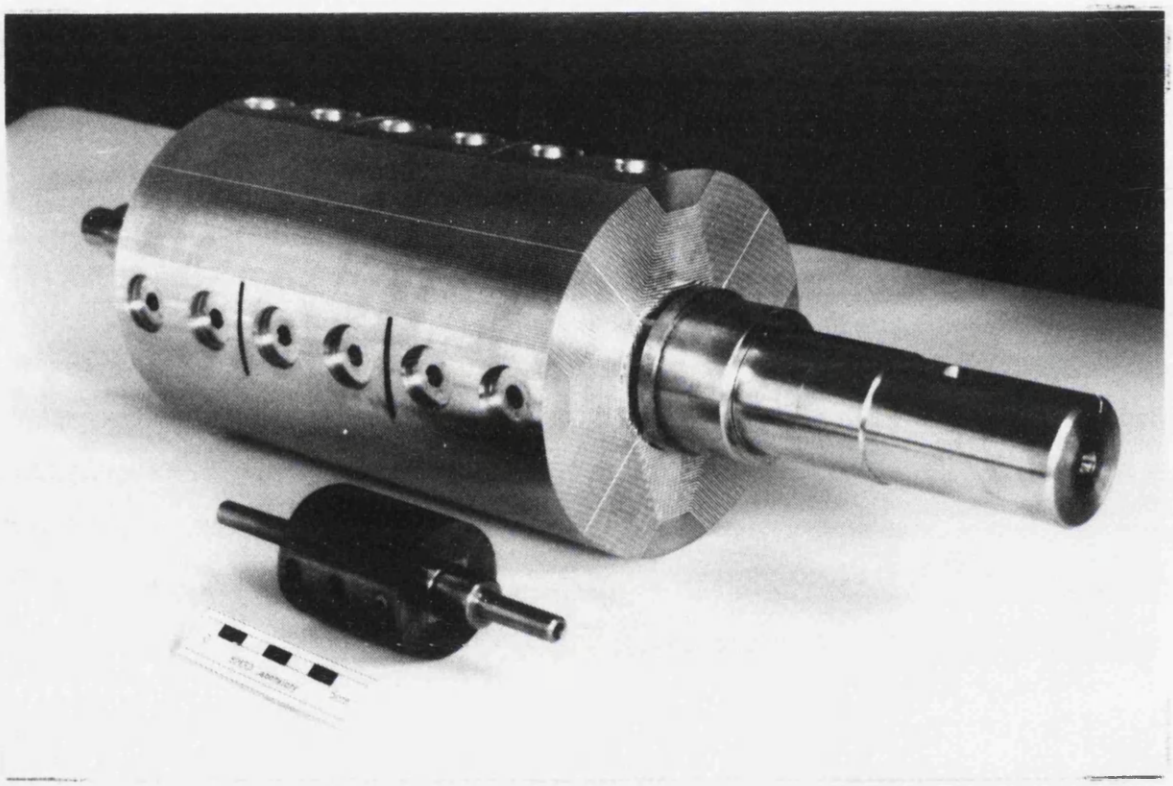

Figure 6.3: *Experimental 7.5kW axially-laminated rotor with 50W prototype in foreground. The scale in the front is 5cm long.*

6.2 Experimental Results

The 7.5kW axially-laminated interior permanent magnet and synchronous reluctance motor design parameters are summarised in Table 6.1.

6.2.1 Inductance Characteristics

The inductance characteristics of the two motors (see Fig. 6.4) were measured using the instantaneous flux-linkage method described in Sec. 4.4. AC standstill tests were found to give poor results due to the large iron losses produced by the flux oscillations in the rotor. Note that under normal field-oriented control, the flux in the rotor is substantially constant and so these losses will not appear.

The measured inductance characteristics correspond well with the finite-element predictions. The interior permanent magnet motor shows much less saturation than the synchronous reluctance motor due to the larger airgap. This can be clearly seen from Table 6.2 where the interior permanent magnet motor's unsaturated saliency ratio ξ_u is 6.7 and the saturated value ξ_s is 6.3. The use of iron pole-pieces causes the d-axis (low inductance axis) inductance of the interior permanent magnet motor to be significantly greater than that of the synchronous reluctance motor.

Table 6.1: *Motor design parameters.*

Parameter	IM	SYNCHREL	IPM
Airgap [mm]	0.48	0.517	0.917
Stator Inner Dia. [mm]	127	127	127
Stack Length [mm]	202	202	202
Poles	4	4	4
Lamination Thick. [mm]		0.50	0.50
Ins./Magnet Thick. [mm]		0.50	0.50
Rotor Layers		62	62
Pole Arc [elec deg]		131	131
Pole Pieces		brass	iron

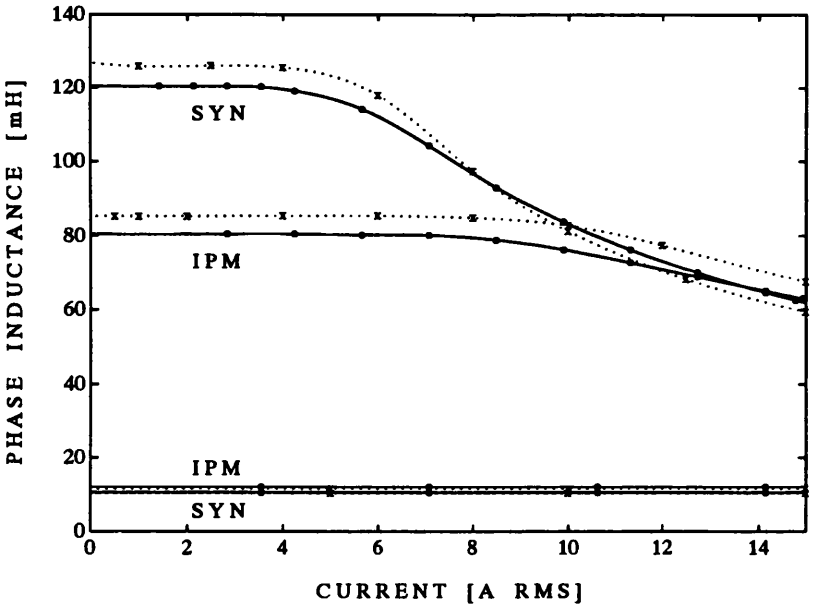

Figure 6.4: *Comparison of measured inductance characteristics (solid) and finite-element results (dotted).*

Table 6.2: *Measured inductance characteristics.*

Parameter	SYNCHREL	IPM
L_d [mH]	10.5	12.0
ξ_u	11.5	6.7
ξ_s	9.6	6.3

6.2.2 Back-Emf Voltage

A comparison of the measured and calculated back-emf waveforms for the interior permanent magnet motor are given in Fig. 6.5. This shows that the waveform shape is accurately predicted. The measured magnet flux-linkage is 0.174Vs which is about 20% lower than the calculated value. This is due to the difficulty in fully magnetising the magnets described in Sec. 6.1.1. The maximum stator d-axis flux-linkage is $L_d I_c =$ 180mVs which is close to the magnet flux-linkage. Thus this design is a near optimum field-weakening design.

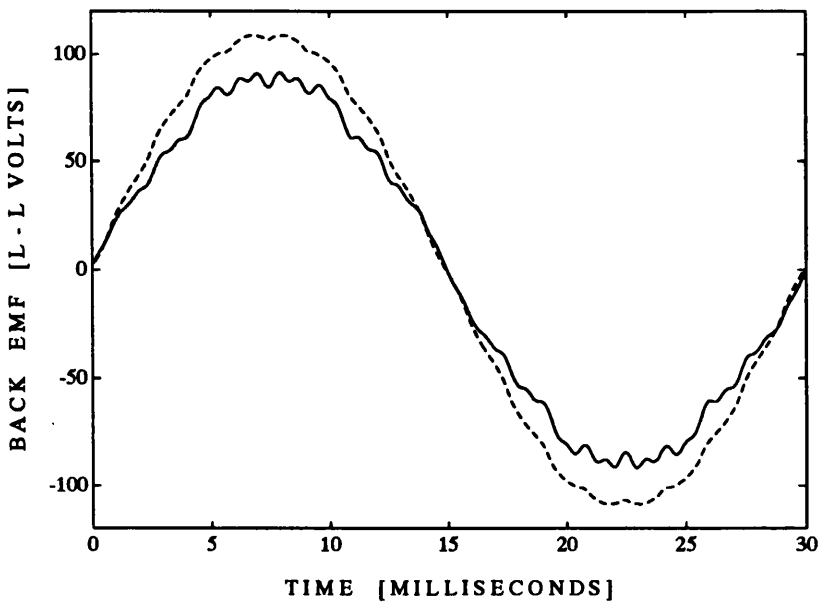

Figure 6.5: *Comparison of measured (solid) and calculated (dashed) line-to-line back-emf voltage at 1000rpm.*

6.2.3 Constant Speed Tests

The constant speed tests were performed on a fully-instrumented 50Nm dynamometer using a vector-controlled induction motor as a load. A 7.5kW, 5kHz IGBT inverter and an analog hysteresis current controller was built to control the test motor. The current controller allows full control over the current magnitude and current-angle. App. A describes the dynamometer, inverter and controller in more detail.

The current is measured using a three-phase power analyser and the torque is obtained from an inline torque transducer. The fundamental phase voltage is obtained by filtering the line-to-line voltage waveforms with a second-order Butterworth filter (see App. A).

Fig. 6.6 shows the effect of varying the current-angle for operation at rated current at 500rpm. The finite-element inductance predictions (with the measured magnet flux-linkage) give a good approximation to the performance though the calculated

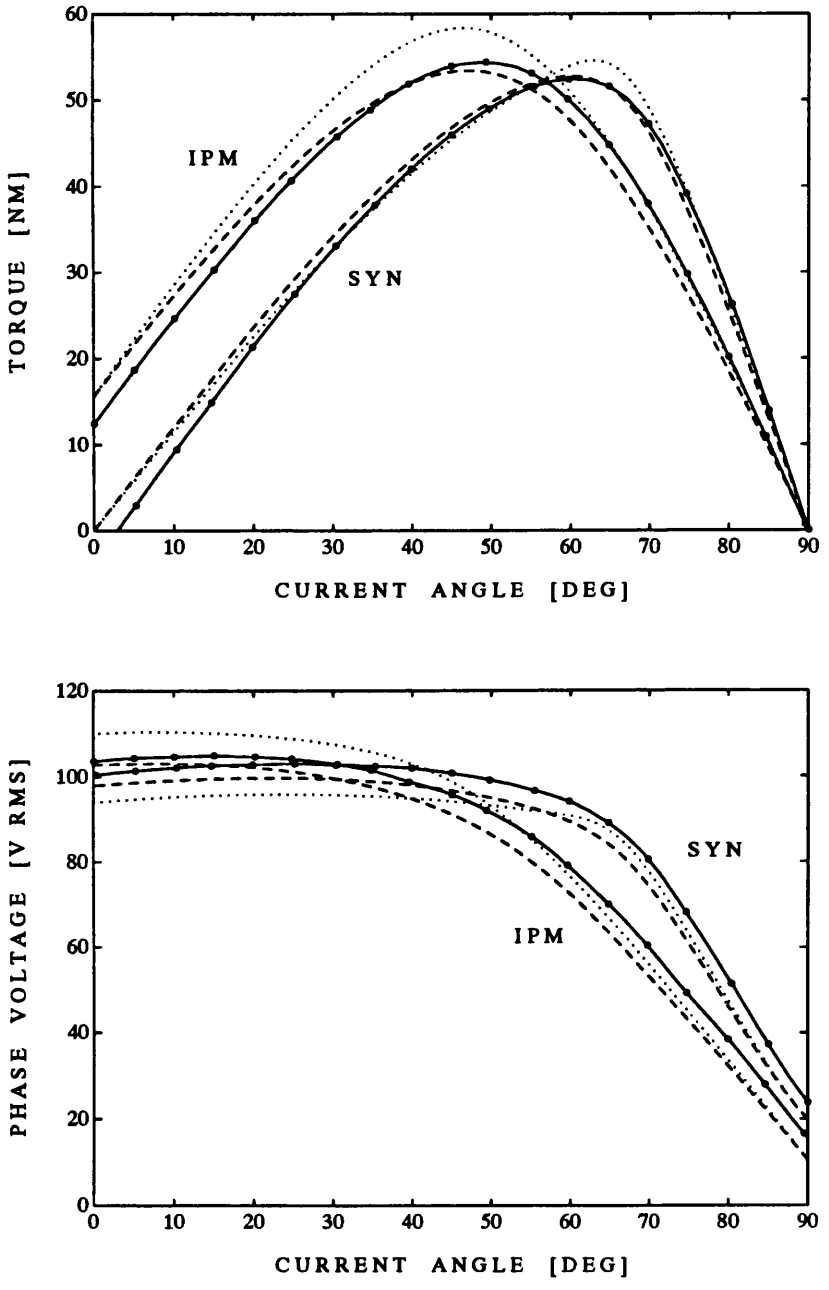

Figure 6.6: *Torque and fundamental voltage characteristics of the 7.5kW synchronous reluctance (SYN) and interior permanent magnet motor (IPM). The torque and voltage characteristics are measured at 500rpm and 15A. Measured results (solid), calculated from the measured inductance characteristics (dashed) and finite-element predictions (dotted).*

characteristics from the measured inductance results are generally better as would be expected. Note the reduction in the terminal voltage as the current-angle is increased towards 90°. This is the key to the field-weakening operation.

6.2.4 Field-Weakening Tests

A comparison between the calculated and measured field-weakening characteristics at rated current and one third of rated voltage are shown in Fig. 6.7. The reduced voltage was used to allow the field-weakening region to be characterised without overstressing the rotor mechanically (see Sec. 5.2.2). Note that to a first approximation, the constant-power speed range is independent of the supply voltage.

Ideally the induction motor drive has a constant-power speed range of about 2.5. This is the ratio of the breakdown torque to the rated torque (see Sec. 1.2). Note that this is a standard general-purpose induction motor and it is not designed for a wide constant-power speed range. Typical induction motor main spindle drives have constant-power speed ranges of 3 to 5:1.

The synchronous reluctance motor drive has a measured constant-power speed range of also about 2.5. As predicted by the model, the interior permanent magnet motor drive shows an excellent field-weakening characteristic. The rated speed is about 420rpm at which the output power is about 2.4kW. The highest measured speed was 3160rpm, constrained by mechanical limitations in the prototype motor. This corresponds to a 7.5:1 constant-power speed range, and at the highest speed the output power was still over 2.8kW. Thus the actual constant-power speed range is probably greater than 10:1 and may even reach 15:1.

The calculated characteristics were based on the measured inductance and magnet flux-linkage and did not take into account iron losses or friction and windage losses. This causes the descrepancy between the measured and calculated power output curves.

The required control characteristics are predicted accurately as shown by the current-angle versus speed graph in Fig. 6.7. The synchronous reluctance motor drive enters the purely voltage-limited or inverse power region (Mode III) at about 1500rpm. Note

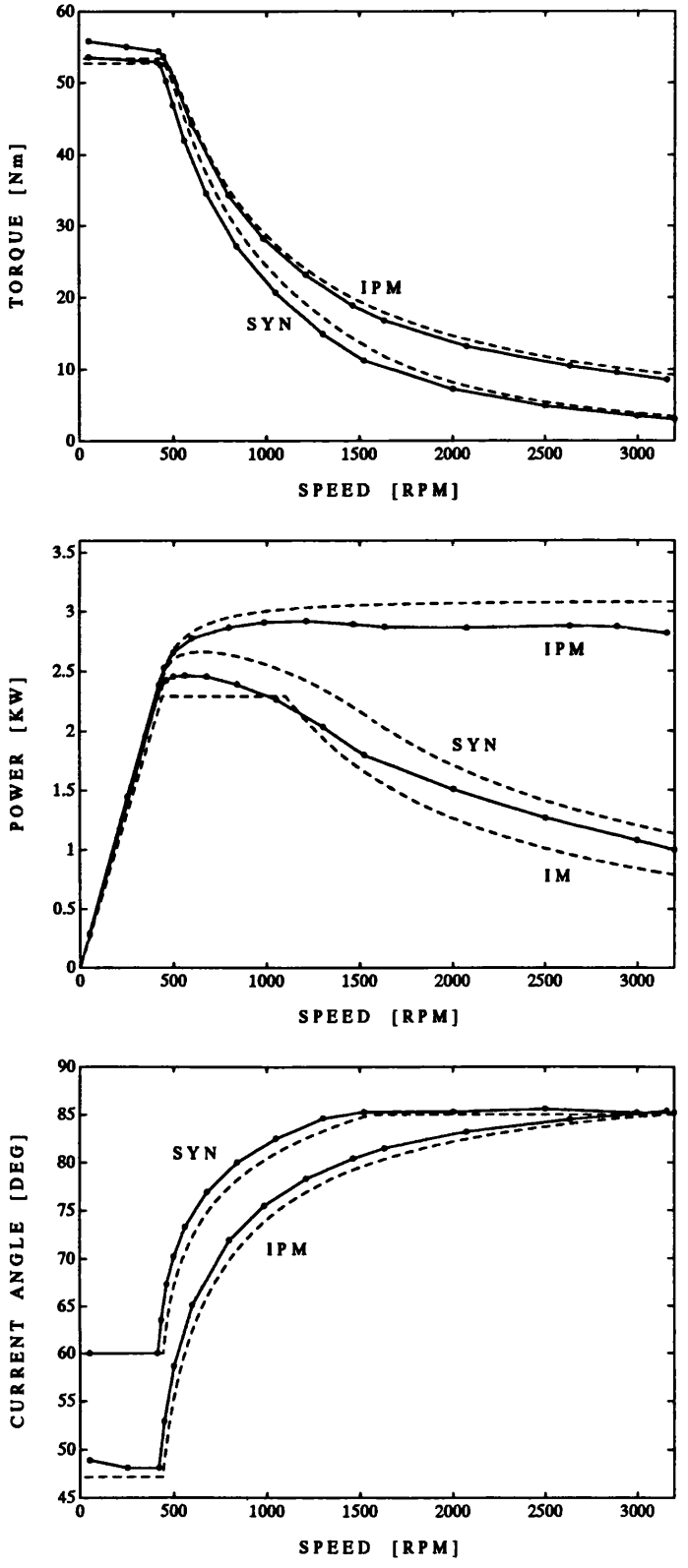

Figure 6.7: *Field-weakening characteristics at rated current and one third of rated voltage. Measured results (solid lines) and calculated results (dashed lines). The calculated characteristic of the induction motor drive is given for comparison.*

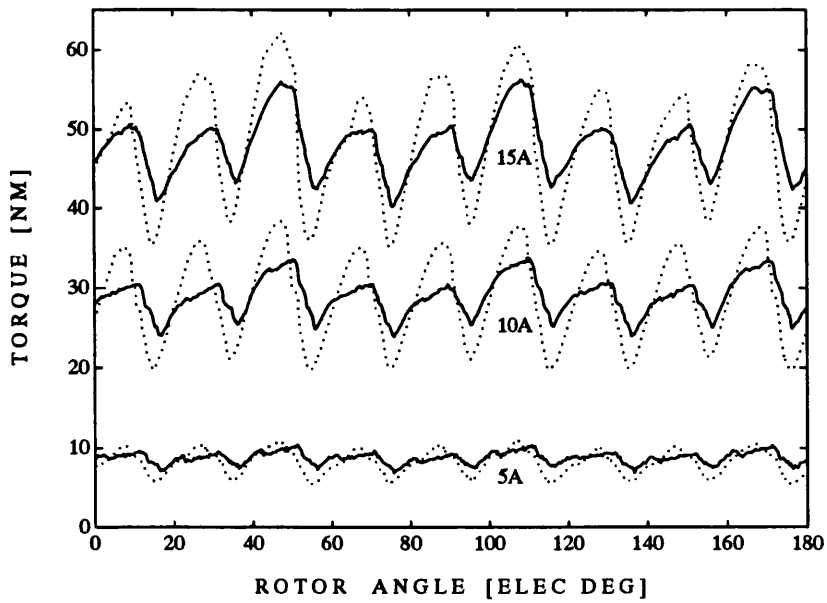

Figure 6.8: *Measured torque-ripple for the 7.5kW axially-laminated (solid line) and single-barrier (dotted line) synchronous reluctance motor at three levels of current ($\gamma = 45°$).*

that after this point the current-angle remains relatively constant and the current magnitude is decreased. The interior permanent magnet motor remains in the voltage-and-current-limited region (Mode II) throughout the field-weakening range. Note the sensitivity of the performance to the current-angle at high speeds. In an actual drive, voltage control rather than current control may be preferred due to the lower sensitivity to errors in the angle [7].

6.2.5 Torque Ripple Tests

A comparison of the measured torque-ripple performance of the 7.5kW axially-laminated synchronous reluctance motor drive against that of a 7.5kW single-barrier synchronous reluctance design [69] is given in Fig. 6.8. Note the axially-laminated design has approximately half the torque-ripple of the single-barrier design. The torque-ripple at full load is approximately 20%. The large torque-ripple even with the axially-laminated

Table 6.3: *Measured full-load test results. The induction motor power-factor is low as the motor is actually capable of 11kW, but is derated to 7.5kW for a 10:1 constant torque speed range with a shaft-mounted fan. The induction motor test results are courtesy of Brook Crompton.*

Parameter	IM	SYNCHREL	IPM
Rated Line Voltage V_c [V]	415	415	415
Rated Current I_c [A]	15	15	15
Magnet Flux [Vs rms]	0	0	0.174
γ_m [deg]		64.1	48.1
Rated Speed w_k [rpm]	1460	1442	1396
Rated Torque T_k [Nm]	50	49.6	53.1
Rated Output Power P_k [kW]	7.5	7.48	7.76
Efficiency η [%]	87.5	85.5	89.5
Power Factor $\cos\phi$	0.72	0.813	0.804
Inverter Utilisation $\kappa = \eta\cos\phi$	0.63	0.696	0.720
CPSR	2.5	2.5	$\gg 7.5$

rotor construction is due to the lack of skew and the simple single-layer stator winding.

6.2.6 Full Load Tests

A comparison of the measured performance of the motor drives with rated voltage and current operating at rated torque and speed is shown in Table 6.3 (see Sec. 1.1 for definitions of these terms). The output torque of the synchronous reluctance and induction motor drives are similar. Despite having almost double the airgap, the interior permanent magnet motor drive still produces slightly more torque than the other two motors. With the same airgap it would be expected to produce about 15 to 20% more torque at the rated speed.

The synchronous reluctance motor drive shows a slightly lower efficiency than the induction motor drive but a much higher power-factor. The axially-laminated interior permanent magnet motor drive shows an improved efficiency and power-factor over the induction motor drive. The power-factor of the interior permanent magnet motor drive

is lower than the synchronous reluctance motor drive due to the larger airgap.

Chapter 7

Conclusions

This thesis examines and validates the reputation of the interior permanent magnet motor drive for having a wide constant-power speed range[1] (or field-weakening range) when operated from an inverter with a given volt-ampere (VA) rating. It consists of two parts. In the first part the theoretical and practical limitations to the field-weakening performance are analysed and drive designs featuring the optimal field-weakening performance are identified. The second part examines the design, modelling and testing of an optimally designed field-weakening motor drive.

The vector-controlled induction motor drive is commonly used in applications requiring a wide field-weakening range. It offers constant-power speed ranges of up to 4:1. Higher values can only be obtained by oversizing the drive or by using a mechanical winding changeover switch (see Sec. 1.2). Interior permanent magnet motor drives offer the following advantages over induction motor drives :

- an inherently wider constant-power speed range. Induction motors only offer constant-power speed ranges up to about 4:1 [25, 26] and it would be difficult to improve this substantially.
- better utilisation of the inverter as oversizing is not needed to achieve a wide constant-power speed range.

[1]This is the speed range over which a drive can deliver rated output power. For a more precise definition see Sec. 1.1.

- simpler control and faster low-speed dynamics due to the synchronous nature.
- higher efficiencies and lower losses due to the elimination of rotor copper losses (especially at low speeds).
- simpler implementation of sensorless control [98].

It is only recently that commercial interior permanent magnet motor drives designed for field-weakening applications have become available. These offer constant-power speed ranges of up to 4:1. This thesis examines how much improvement is possible and what tradeoffs are involved.

Part One : Theoretical and Practical Limitations

This part examines the theoretical and practical limitations to the field-weakening performance of the three types of brushless synchronous AC motor drive : the surface permanent magnet, the synchronous reluctance and the interior permanent magnet motor drive.

The theoretical limitations are examined using a lossless, constant parameter model. The circle diagram is used to show the optimal field-weakening control strategies. The new concept of the interior permanent magnet parameter plane is introduced to graphically illustrate the effect of changes in the motor drive parameters on the field-weakening performance. It was used to show that brushless synchronous AC motor drives can have a theoretical infinite constant-power speed range but that the inverter utilisation cannot exceed about 0.7 for such drives. The optimal field-weakening performance consists of an infinite constant-power speed range and an inverter utilisation of about 0.7.

The interior permanent magnet parameter plane also shows that theoretically three types of motor drives can achieve the optimal field-weakening performance described above :

- synchronous reluctance motors with an infinite saliency ratio.

- interior permanent magnet motors where the fundamental flux along the magnet axis can be reduced to zero by rated stator current in that axis.

- surface permanent magnet motors with an unusually high value of synchronous inductance.

Synchronous reluctance motors are preferred as they do not contain magnets. This reduces the cost, eliminates demagnetisation-withstand problems, gives the rotor a wider operating temperature range and means that there is no problem of excessive back-emf voltages at high speeds.

It is clearly impossible to build an infinite saliency ratio synchronous reluctance motor drive; however high saliency designs may offer a sufficiently good performance. Synchronous reluctance motors are characterised by their saliency ratio ξ. The highest saliency ratios are achieved with axially-laminated designs for which saliencies in the range 6 to 20 are common. The ideal constant-power speed range is about half the saliency ratio. It is shown that this is not significantly affected by iron losses or stator resistance, but is dramatically reduced by saturation. Saturation reduces the saliency ratio but more significantly increases the maximum-torque-per-ampere current-angle. The effect of saturation on the constant-power speed range was analysed. It was found that most synchronous reluctance designs have constant-power speed ranges between 2 to 3:1 and that it would be difficult to improve this substantially.

Due to this practical limitation to the field-weakening performance of synchronous reluctance motors, an optimal field-weakening interior permanent magnet motor drive design was developed. A high saliency ratio design is used as it :

- reduces the magnet requirements and hence cost. Thus ferrite magnets can be used instead of expensive rare-earth magnets.

- reduces the induced voltage at high speed. For an optimal interior permanent magnet design with a saliency ratio of 7, the back-emf is about 20% of rated voltage at rated speed instead of 70% for an optimal surface permanent magnet design. For a 5:1 constant-power speed range the open-circuit back-emf will thus

only be equal to the rated voltage at the maximum speed instead of three and a half times it with the surface permanent magnet design.

- reduces the required demagnetising current under light load, high speed operating conditions and hence improves the efficiency. This is important for traction applications as the drive spends a large proportion of its time with this operating point.

Part Two : Design of an Optimal Field-Weakening Axially-Laminated Interior Permanent Magnet Motor Drive

The highest saliency ratios are obtained with an axially-laminated form of construction. Thus this part of the thesis examines the modelling, design and testing of an optimal field-weakening, axially-laminated interior permanent magnet motor drive.

A useful design equation for axially-laminated motors is the *intrinsic magnetising saliency ratio* $\xi_{mi} = ar_1/pg$, where a is the proportion of the rotor which is insulation[2], r_1 is the airgap radius, p is the number of pole-pairs and g is the radial airgap. This is the maximum possible saliency ratio for a given motor geometry. The actual unsaturated saliency ratio is considerably lower than this due to practical factors such as Carter's coefficient, the finite pole-arc and the stator leakage inductance. The measured unsaturated saliency ratio is typically in the range $0.2\xi_{mi} < \xi < 0.4\xi_{mi}$ with the larger values associated with larger motors. For example for a 7.5kW design with a 0.5mm airgap, $\xi_{mi} = 32$ and the measured unsaturated saliency ratio is $\xi_u = 11.5 = 0.36\xi_{mi}$.

The inductance saturation characteristics can be calculated or measured. It can be calculated using analytical, finite-element or lumped-circuit approaches. A design program PC-AXL, was written to estimate the unsaturated performance of axially-laminated motors using analytical formulas. A general-purpose lumped-circuit solver was also written. This allows the estimation of the motor's saturation characteristics. The finite-element method gives the most accurate results though the complex rotor geometry requires a large number of elements in the airgap to model the fringing

[2]Unity means a non-magnetic rotor, zero means a solid iron rotor.

accurately.

With regard to measurement (see Sec. 4.4) the instantaneous flux-linkage method gives the most accurate results. The AC standstill test is simpler to perform but can only be applied to motors which show low saturation and iron losses.

Axially-laminated interior permanent magnet motors designed for a wide field-weakening range are predominantly reluctance machines as can be seen by the low back-emf voltage at rated speed (see Fig. 2.25). Thus the optimisation of axially-laminated synchronous reluctance machines are considered first. Finite-element analysis was used to investigate the the effect of changing the number of poles, the pole-piece material type, the number of bolts, the airgap size and the rotor insulation ratio on the machine's performance.

A 7.5kW axially-laminated synchronous reluctance motor was built and tested. It has four poles, non-magnetic pole-pieces and a rotor insulation ratio of 0.5. The motor has a comparable torque to the induction motor, an unsaturated saliency of 11.5, a saturated saliency ratio of 9.6, a maximum-torque-per-ampere current-angle of 60° and a constant-power speed range of 2.5.

The design of axially-laminated interior permanent magnet motors is similar except that magnetic pole-pieces should be used to obtain a smooth sinusoidal back-emf waveform and that care is required to ensure suitable demagnetisation limits on the magnet material. The saliency ratio of the interior permanent magnet motor was sufficiently high to allow the use of rubber-bonded ferrite magnet sheet. This is a flexible, low-cost material used in applications such as refrigerator door seals. It has a remanence of about 0.16T. Finite-element analysis was used to show that rated stator current would not demagnetise the motor. In the future rubber-bonded NdFeB magnets could be used for their superior demagnetisation-withstand capability.

A 7.5kW axially-laminated interior permanent magnet motor designed for optimum field-weakening performance was built. It was based on alternating layers of grain-oriented lamination material and flexible ferrite magnet sheet. It used a larger airgap (0.9mm compared with 0.5mm for the synchronous reluctance motor and the induction

motor) in order not to exceed the torque capacity of the dynamometer and also to investigate the effect of using a larger airgap on the inductance characteristics.

The experimental results validated the theoretical predictions and showed that the motor has an extremely wide constant-power speed range which exceeds 7.5:1. This is in contrast to the measured constant-power speed range of 2.5:1 for the synchronous reluctance motor and the calculated value of 2.5:1 for the induction motor. Compared to the induction motor, the output torque was 6% greater, the efficiency was 2% higher (89.5% compared to 87.5%) and the power-factor was 0.80 compared to 0.72.

The exceptionally wide constant-power speed range combined with the fast low-speed dynamics makes the this new type of motor a serious contender for applications such as machine tool main spindle drives and traction.

General Conclusions

This thesis shows that brushless synchronous AC motor drives can have a theoretical infinite constant-power speed range but that the inverter utilisation cannot exceed about 0.7 for such drives. The optimal field-weakening performance consists of an infinite constant-power speed range and an inverter utilisation of about 0.7. This optimal field-weakening performance could theoretically be obtained with a variety of motor designs; however it was shown that when practical factors are taken into account that the axially-laminated interior permanent magnet motor drive offers the most feasible solution. An optimally designed axially-laminated 7.5kW motor drive using rubber-bonded ferrite magnets was built and a constant-power speed range exceeding 7.5:1 was demonstrated.

Future Work

This thesis has shown that a correctly designed, high-saliency interior PM motor drive offers an extremely wide field-weakening range. However considerably more work is required before such motor drives become commercially practical. Firstly the mechanical aspects of the design such as the maximum operating speed and construction need to

be improved and secondly the dynamic performance and control needs to be analysed.

The 7.5kW interior permanent magnet motor rotor is mechanically limited to about 3000rpm by the strength of the retaining bolts. With a rated speed of about 1500rpm this limits the constant-power speed range to about 2:1. This is despite the fact that it is "electrically" capable of a constant-power speed range exceeding 7.5:1. A desirable maximum mechanical speed is thus above 10000rpm and alternative rotor constructions need to be investigated in order to achieve this. One possibility is to use a carbon-fibre binding around the rotor.

The rotor complexity is a serious commercial drawback with the prototype motors. The axially-laminated construction gives the highest saliency ratios (about 11.5 for the 7.5kW design) however a conventional radially-laminated design with say 3 to 4 barriers has been shown by Fratta et al. [54] to yield a reasonable unsaturated saliency ratio of about 8. Thus it would be worthwhile investigating the tradeoffs in the field-weakening performance in using fewer barriers in order to obtain a simpler mechanical construction.

The analysis in this thesis was only concerned with steady-state limitations and the next step would be to analyse the dynamic performance of the interior permanent magnet motor drive. This would show how closely the steady-state limitations could be approached in a real system with practical control algorithms.

An aspect which requires further investigation is that the dynamic performance of the interior permanent magnet motor drive and in particular the rate of change of torque is slower than the corresponding synchronous reluctance motor drive. This is because the magnets mean that in order to reverse the output torque of the machine, it is necessary to reverse the current in the most inductive axis of the motor [64].

Finally the dynamic control of the interior permanent magnet motor drive in the field-weakening region needs to be analysed. This is complicated by the non-linearities produced by the transition between six-step and linear operation [46].

Appendix A

Experimental Test Equipment

This appendix describes the dynamometers, inverter and controller used to obtain the steady-state test results described in the main text.

A.1 Introduction

The work described in this thesis forms one part of a comprehensive research program at the Scottish Power Electronics and Electric Drives (SPEED) Laboratory at Glasgow University into synchronous reluctance motor drives. Fig. A.1 shows an overview of the group's activities and how they relate to one another. The heart of the experimental equipment is a set of three dynamometers (top right) with ratings of 2Nm, 5Nm and 50Nm. These were designed by Dr. Dave Staton (a research assistant in the group) [99] and built by Mr. Jimmy Kelly of the department's mechanical workshop. The dynamometers are fitted with four-quadrant vector-controlled load motors. Their capabilities are summarised in Table A.1. The torque rating of the dynamometers is usually limited by the rating of the inline torque transducer used, except in the case of the 5Nm dynamometer where it is limited by the rating of the load motor.

The three dynamometers allow a wide range of motors to be tested. To date a total of six axially-laminated rotors have been built. The majority of these have been designed for existing commercial induction motor stators. Dave first designed a

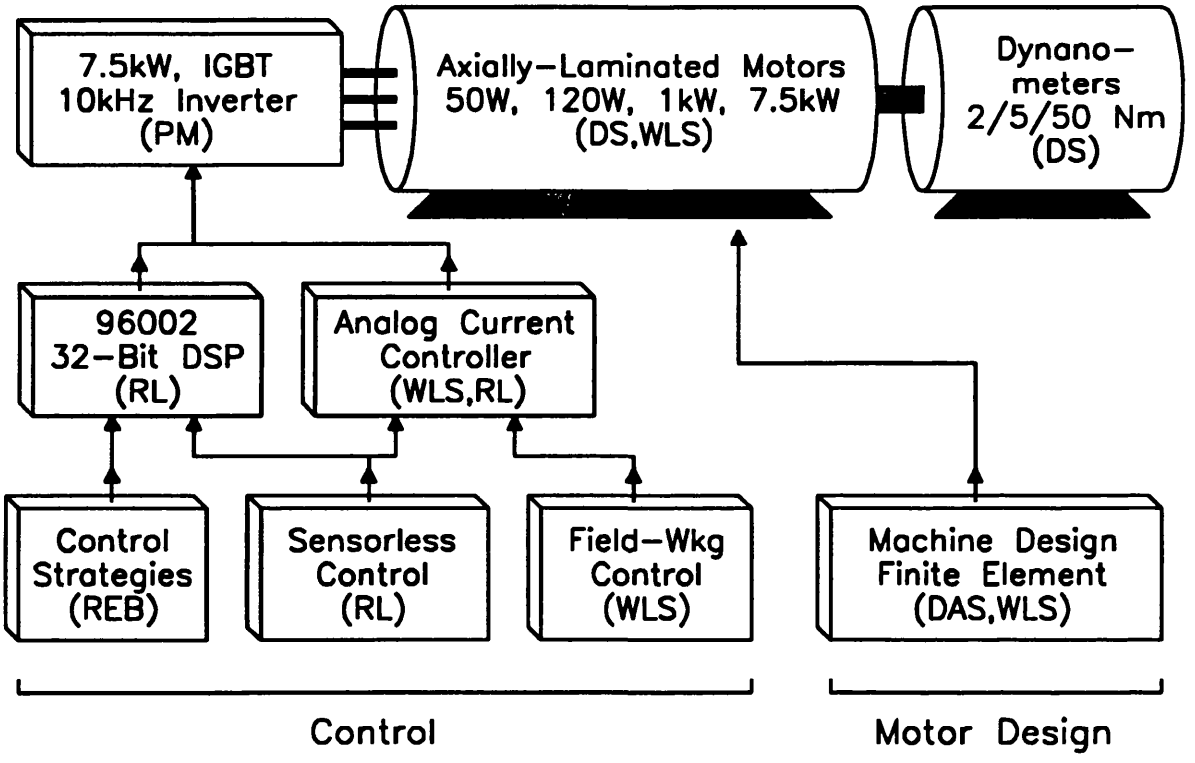

Figure A.1: *Overview of the SPEED Laboratory's synchronous reluctance program.*

Table A.1: *Summary of dynamometer capabilities.*

Parameter	Dynamometer		
	2Nm	5Nm	50Nm
Load Motor	brushless PM		induction
Controller	four quadrant vector-controlled		
Operating Modes	torque or speed control		
Rated Torque	2Nm	3.4Nm	50Nm
Peak Torque Capability	4Nm	10Nm	100Nm
Dynamometer Power Rating	800W	1.5kW	7.5kW
Base Speed	4000rpm		1500rpm
Max. Speed at Constant Power	4000rpm		3000rpm
Maximum Operating Speed	4000rpm		6000rpm

50W motor and later two 120W motors. He also carried out a comprehensive finite-element analysis on the design of multiple-barrier and axially-laminated motors [21]. Subsequently I designed the 1kW axially-laminated motor and two 7.5kW motors (see Chapter 5).

The motors were operated from a 7.5kW three-phase inverter which was designed and built by Mr. Peter Miller who is an electronics technician with the group. It is a general-purpose three-phase voltage-source inverter which accepts switching signals via three optical inputs. It is described in more detail in Sec. A.2.

The inverter can be controlled either by a digital signal processor (DSP) based system or by an analog current controller. The DSP system was built by a fellow PhD student, Mr. Rolf Lagerquist and is described in more detail in [100]. It is based on a 33MHz Motorola 96002 digital signal processor. The philosophy was to create a fully digital controller which can easily be adapted to control *any* type of brushless motor with only software changes. In the early part of Rolf's project he worked closely with Dr. Robert Betz, a visiting fellow from Newcastle University in Australia. Dr. Betz has made important contributions to the control of synchronous reluctance motor drives [6, 62].

The analog current controller was jointly built by Rolf and myself. This controller allows steady-state tests to be performed on brushless synchronous AC motors with full control over the current magnitude and angle. This is particularly important in measuring the field-weakening performance (see Chapter 2).

A.2 7.5kW Inverter

This section describes the 7.5kW three-phase general purpose inverter. A summary of its specifications is given in Table A.2.

The output power of an inverter is by convention specified as the rated mechanical output power of the motor it is designed to drive. Thus an inverter designed to drive motors with an output rating P_k of 7.5kW requires a minimum output volt-ampere (VA) rating of :

$$VA = \frac{P_k}{\eta \cos \phi} \tag{A.1}$$

where η and $\cos \phi$ are the full-load motor efficiency and power-factor respectively. Typically full-load values for a standard 7.5kW totally-enclosed fan-ventilated (TEFV) induction motor are $\eta = 0.87$ and $\cos \phi = 0.83$ [94]. This implies a minimum inverter output rating of 10.4kVA which corresponds to a line current of 14.5Arms at 415V. Some allowance must be made for transient capability and typical commercial 7.5kW inverters have output ratings in the range 11–14kVA [93]. The rated peak output current of the inverter is $14.5\sqrt{2} = 20.5A$. Toshiba MG50Q2YS91 insulated-gate bipolar transistor (IGBT) phase-legs rated at 1200V and 50A [101] were used to provide a substantial safety margin.

Table A.2: *7.5kW general-purpose inverter specification.*

Parameter	
Motor Output Power	7.5 kW
Rated Inverter kVA	11 kVA
Rated Input Voltage	415 V_{ll}
Rated Output Current	15 A_{rms}
Peak Phase Current	50 A
Maximum DC Link Voltage	770 V
Maximum Switching Frequency	5 kHz
Internal Regeneration Capacity	
continuous	100 W
peak	5 kW

Fig. A.2 gives a block diagram of the inverter. The nominal 415V three-phase supply is rectified and then filtered to form a nominal DC link voltage of [102] :

$$V_{DC} = 415V\sqrt{2} = 590V. \tag{A.2}$$

The DC link voltage is smoothed by six electrolytic capacitors which are connected in a parallel and series combination. This forms a total DC bus capacitance of 2250μF with a maximum voltage rating of 770V. The initial capacitor charging current is limited to a safe value by a 'soft-start' resistor which is later shorted out by a thyristor in parallel with it. An external three-phase auto-transformer can be used to alter the input voltage and so adjust the DC link voltage. This allows low-voltage motors to be driven.

The output section of the inverter consists of three phase-legs, each of which consists of two transistors and two freewheeling diodes. Each transistor is driven by a base drive module which has its own isolated power supply. The base drive modules are controlled by a commutation-and-inhibit-control card. This card accepts the three optical control signals from an external controller. A main control card implements DC link over-voltage, motor over-current and DC link over-current protection. It also contains the logic to control soft-starting, emergency stops and fault-handling.

Four 50A, high-bandwidth, flux-nulling Hall-effect transducers are used to monitor the three output phase currents and the DC link current. The number of turns in the phase current transducers can be altered to allow the inverter to control motors from its rated 7.5kW down to 120W.

Optical fibre links were used for the inverter digital inputs and outputs to eliminate noise problems. These are shown by the dashed lines in Fig. A.2. The inverter accepts three digital signals which control the output voltage of each phase-leg, and an active high enable input. It generates an active low fault output to the controller. The inverter transmits the three output phase currents, the DC link voltage, the DC link current and the resistive neutral voltage as 50Ω analog current-loops to the controller. This method provides the greatest noise immunity.

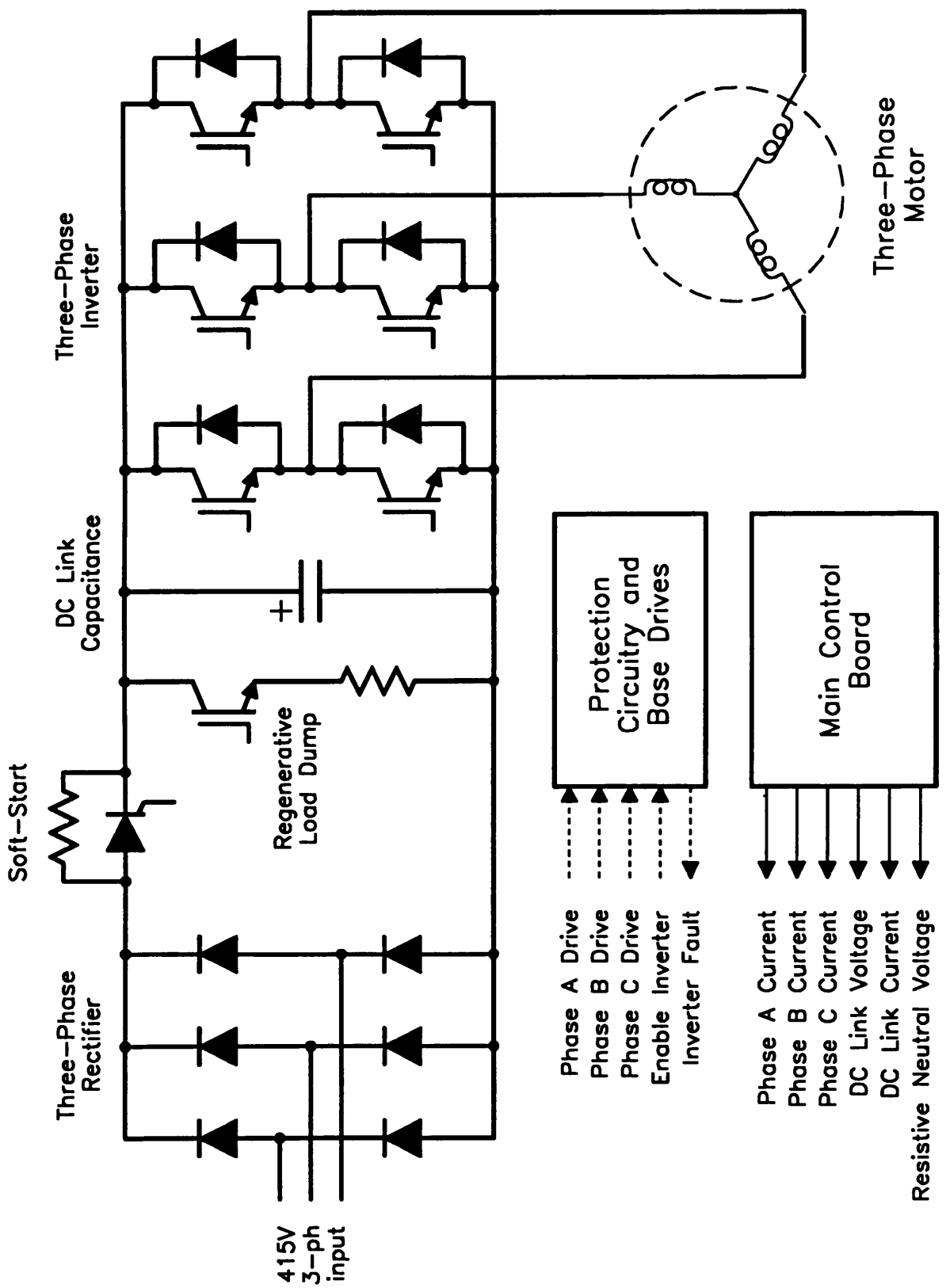

Figure A.2: *Block diagram of the 7.5kW inverter.*

A.3 Analog Current Controller

This is based on the design described by Pillay [19] and is basically a pulse-width-modulated (PWM) current controller. It allows the use of either current magnitude and current-angle references or d- and q-axis current components. The specifications are summarised in Table A.3. Two common types of current regulators used to drive synchronous motors [19] are :

Hysteresis Control : this is based on the principle of comparing the error in output current with upper and lower trip points. The smaller the error or hysteresis band, the more closely the output currents follow the reference currents; however the higher the required switching frequency. The switching frequency is uncontrolled. Thus an appropriate size of the hysteresis band must be calculated or determined experimentally in order to not exceed the maximum switching frequency of the inverter. A variant of the hysteresis controller involves sampling the output of the comparator at a fixed frequency in order to limit the maximum switching frequency.

Ramp Comparison Control : in this type of controller, the error between the reference and the actual current is compared to a sawtooth triangular wave and the resultant signal is used to switch the output transistors. This method gives a fixed switching frequency at the cost of introducing an average delay equal to half the switching frequency. This does not significantly affect the drive performance if the lag is less than one tenth of the machine's stator time constant.

The controller consists of a power supply, four main circuit boards and a connection board mounted in a 3U high, 19" rack. A block diagram of the controller is shown in Fig. A.3 and full circuit diagrams are shown in Figs. A.4–A.7.

Board I : Resolver Interface : This connects to the resolver and generates an 11bit digital output proportional to the mechanical angle of the shaft with respect to the A-phase motor magnetic axis. A function generator was used to generate the

Table A.3: *Analog current controller specifications.*

- interfaces directly to 7.5kW inverter :
  - gives access to all inverter analog outputs $I_a, I_b, I_c, V_{DC}, I_{DC}, V_n$.
  - controls 2, 4, 6 and 8 pole synchronous motors.
- flexible angle control :
  - digital offset for resolver for simple alignment.
  - LED display of mechanical rotor angle.
  - digital panel meter display of electrical current-angle.
- performs $|I|, \gamma$ or I_d, I_q current control :
  - γ can be either analog or digital (11-bits), with a resolution of 0.3° for 4-pole motors.
  - four-quadrant I_d and I_q control.
  - choice of front panel or external control.
- hysteresis or ramp-comparison current control with :
  - adjustable hysteresis bands.
  - adjustable frequency limit for hysteresis control.
  - adjustable frequency and amplitude of ramp comparison control
- uses a modular design for :
  - ease of testing : each board can be tested independently.
  - ease of future expansion : the main control signals are available on the system back-plane.

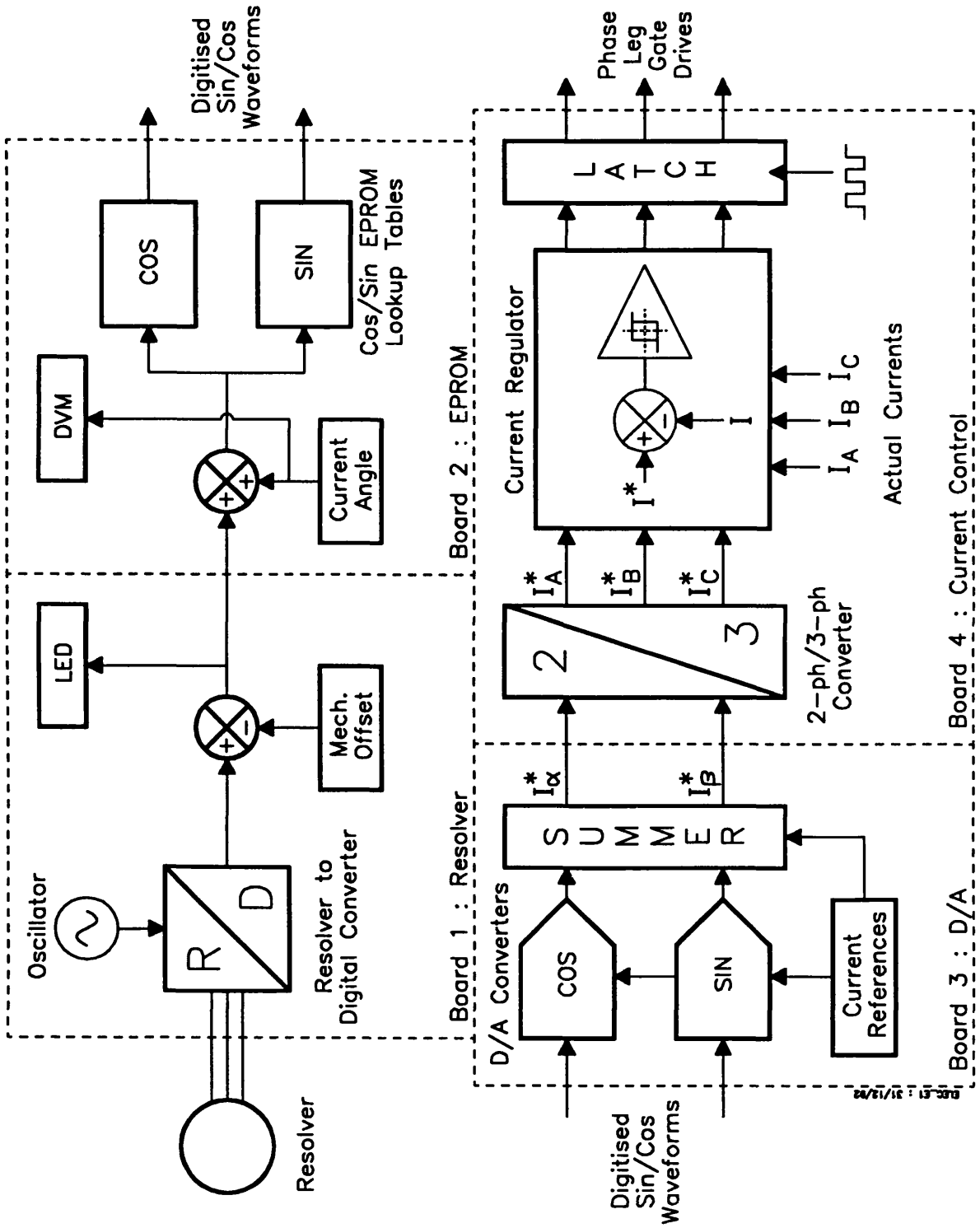

Figure A.3: *Block diagram of analog current controller.*

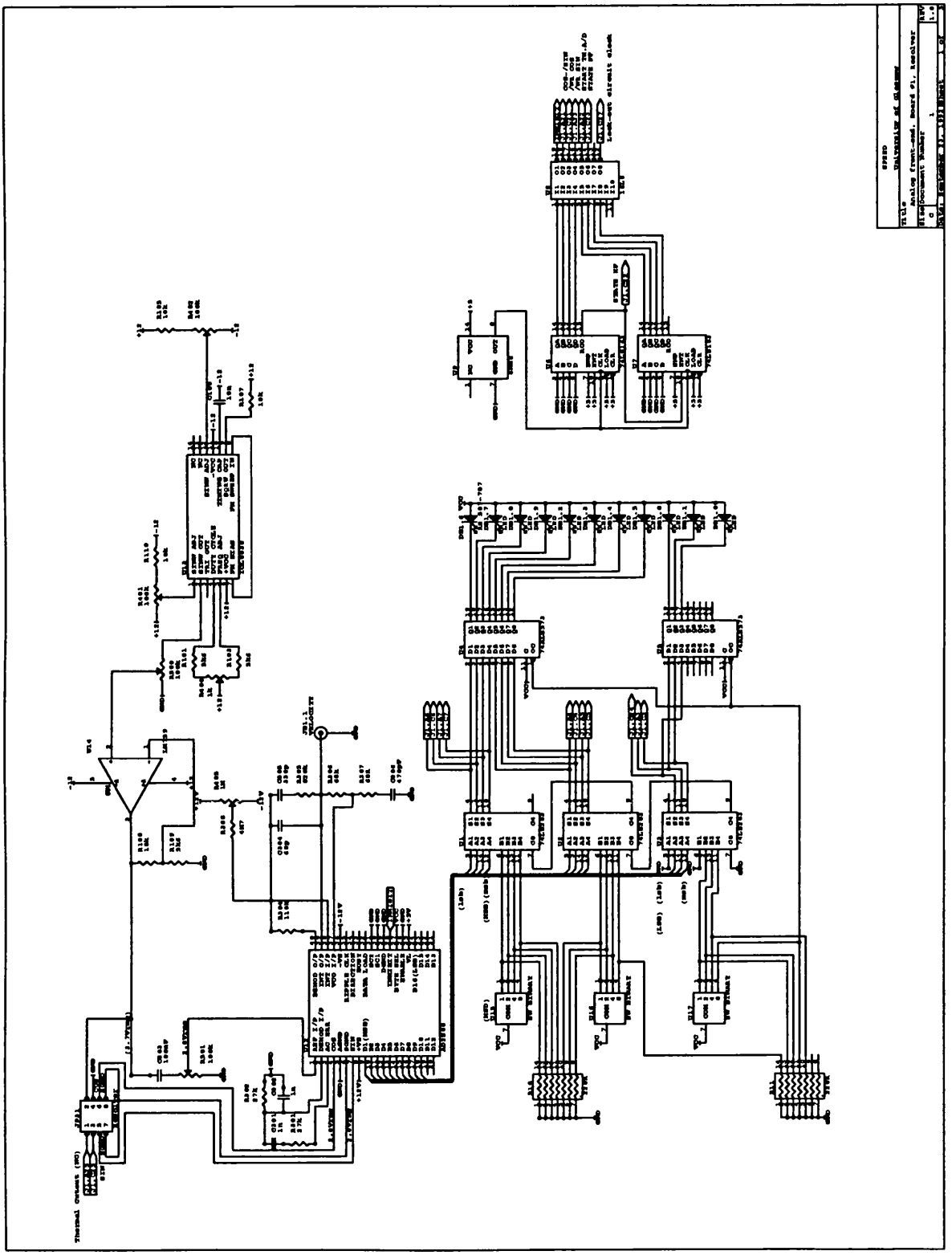

Figure A.4: *Resolver board circuit diagram.*

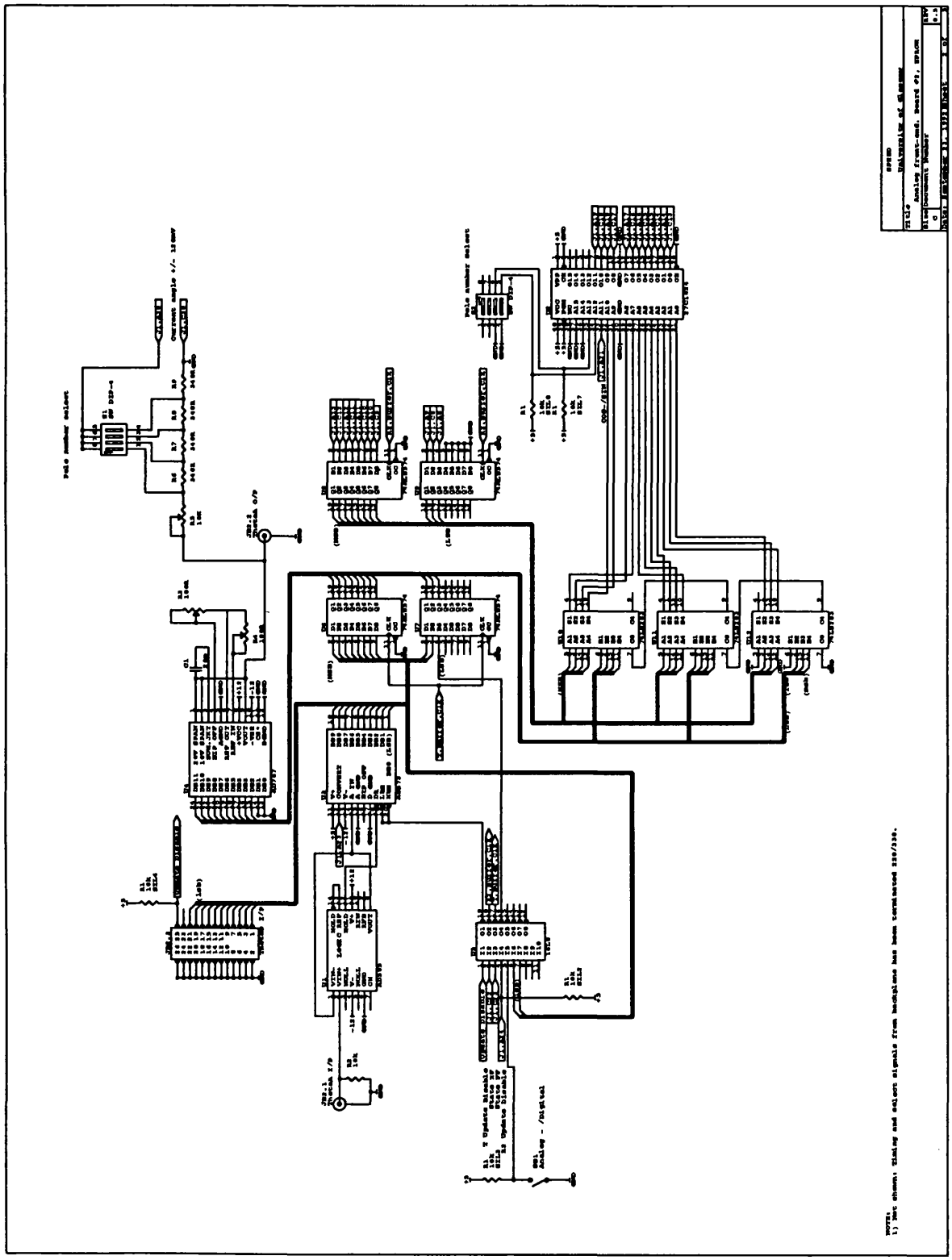

Figure A.5: *EPROM board circuit diagram.*

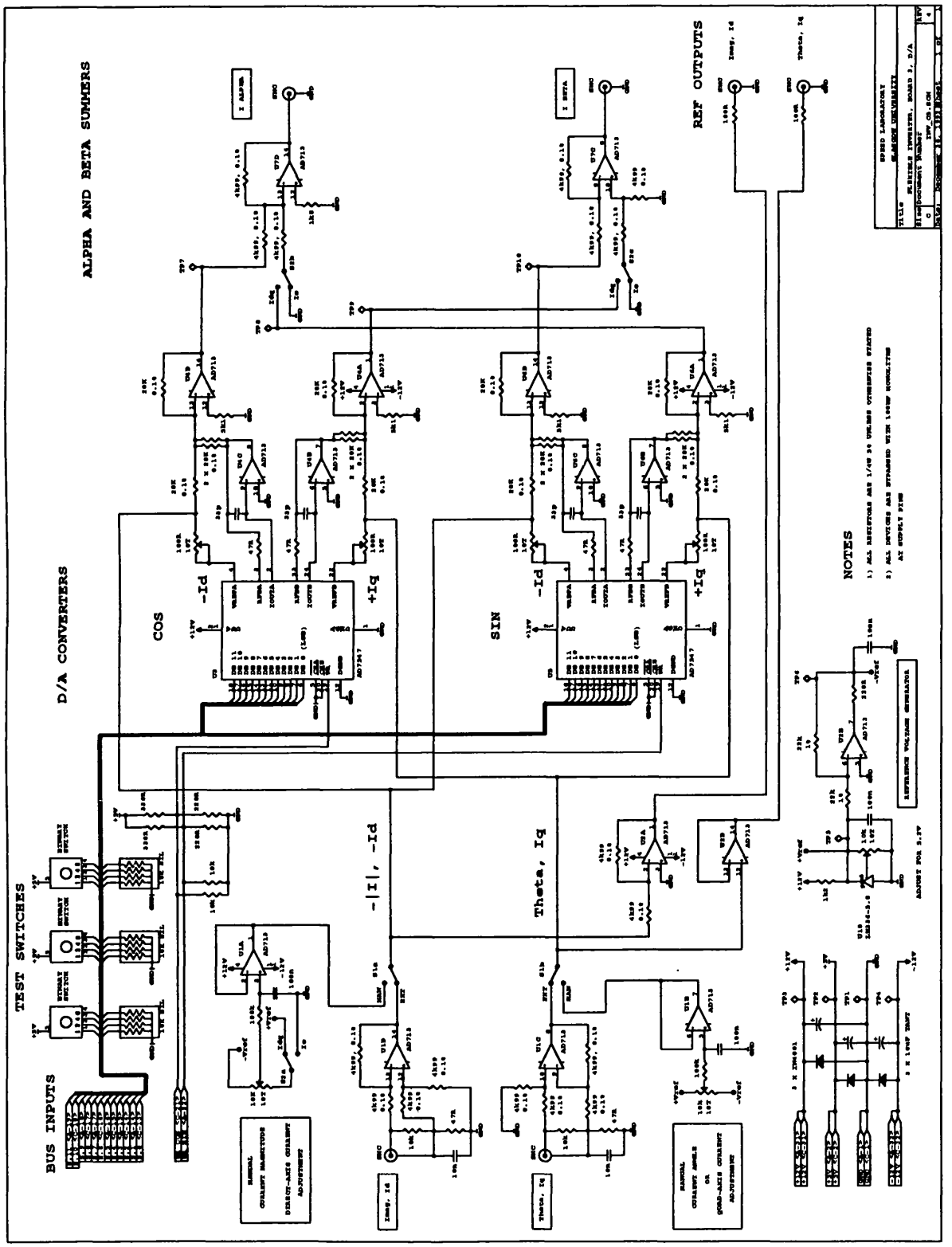

Figure A.6: *Digital-to-analog board circuit diagram.*

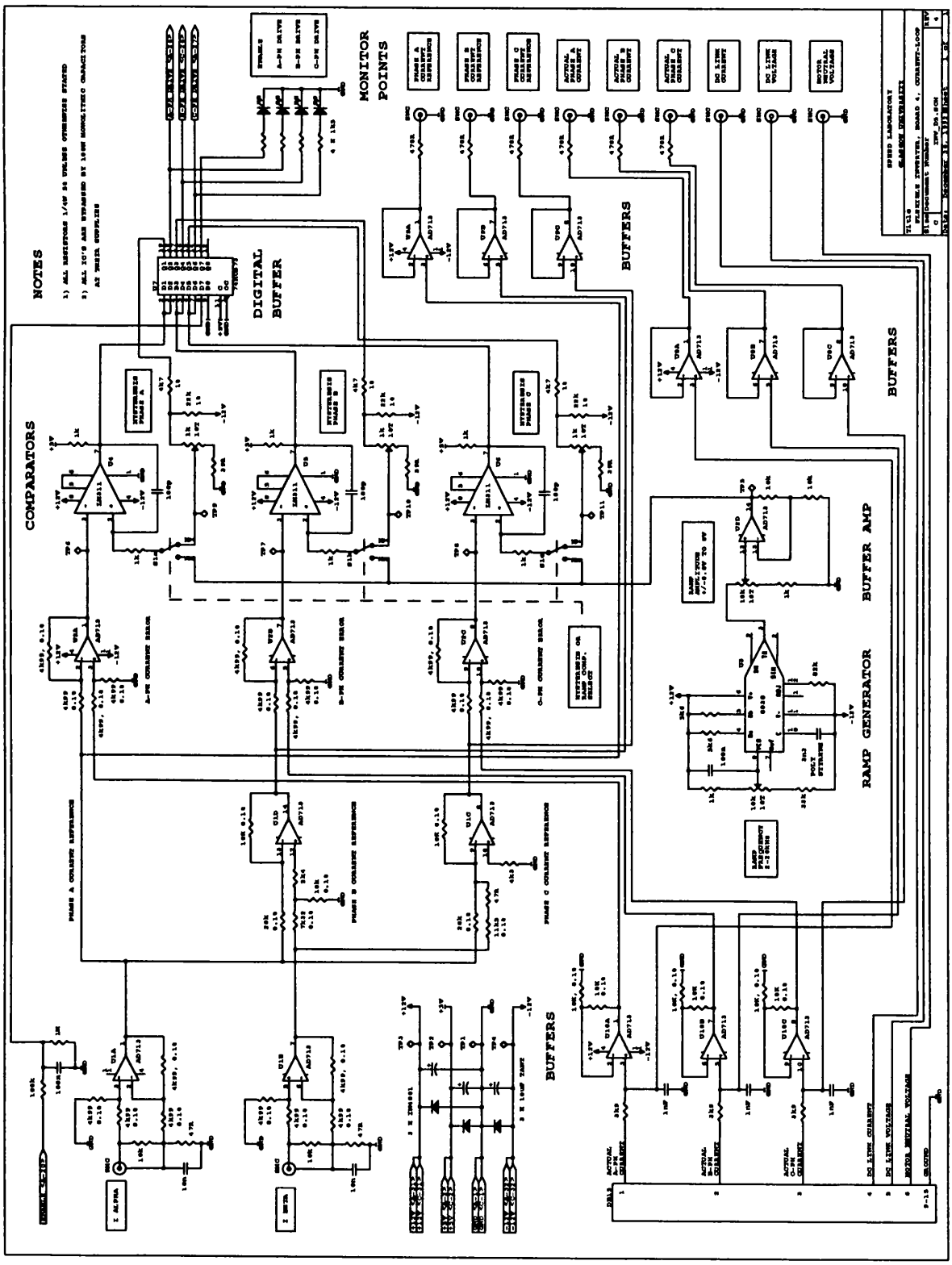

Figure A.7: *Current loop board circuit diagram.*

10kHz sinusoidal drive for the two-pole resolver. The sine and cosine outputs of the resolver are decoded by an AD2S80 resolver-to-digital converter (RDC). The number of digital output bits can be selected from 10 to 16 but there is a tradeoff between the maximum tracking rate and the output resolution. An output of 11 bits was used given a resolution of 0.35^o (electrical) for a four-pole motor.

Three 4-bit adders are used to add an adjustable digital offset to the mechanical rotor angle. This allows the reference axis to be set to the magnetic axis of phase A without adjusting the position of the resolver. Light-emitting diodes (LEDs) are used to indicate the actual rotor angle.

Board 2 : EPROM : This board digitally adds the required current-angle to the mechanical rotor angle produced by the resolver. The result is fed into a sine/cosine look-up table stored in an 1Mbit erasable-programmable-read-only-memory (EPROM). The output is two twelve bit words.

Board 3 : Digital-to-Analog Converter : Here the digital sine/cosine words are converted into a two-phase analog output I_α^*, I_β^* by digital-to-analog converters (DACs). The required current magnitude $|I|$, or I_d and I_q, are used to modulate the output magnitude.

Board 4 : Current Control : The two-phase reference is converted into a three-phase reference and then compared against the actual currents. A hysteresis or ramp-comparison current controller can be used. A latch at the output of the current regulator allows the limiting of the switching frequency of the hysteresis controller. It is disabled in the ramp-comparison mode.

A.4 System Performance

A.4.1 Troubleshooting

The inverter was only designed for 7.5kW motors however it was used for driving motors as small as 120W. For small motors the number of turns on the current sensors was increased in order to monitor and control the much smaller currents involved. However a serious limitation was found in driving high voltage (415V), low power (120W) motors. This was due to stray capacitances coupled with the high switching frequency producing a ripple current whose rms value was a third of the motor full-load current. A solution was to rewind to motor for a lower voltage (110V). The lower voltage reduced the capacitive currents and also increased the motor's rated current.

Another problem was high-frequency current ringing on the DC bus between the main DC link capacitors and the output transistors. These oscillations induced substantial noise in the control circuitry. The ringing was solved by placing a 'bus damper' in the DC link. This consists of a small ferrite transformer whose output is loaded by a damper resistor. Transitions in the DC link current induce a voltage across the damper resistor which absorbs energy and prevents ringing. The optimal value of coupling between the windings and the value of the damping resistor were determined empirically. This solution caused a moderate voltage overshoot of 190V across the output transistors under rated output conditions. This was not a problem in this circuit as the transistors were rated at 1200V.

The models in Chapters 2 and 3 are based on fundamental quantities only. Though the current waveform is a good approximation to the fundamental, the voltage waveform contains substantial harmonics. An analog filter was used to filter the voltage signal and allow accurate measurement of the fundamental voltage magnitude. The required specification was for less than 2% reduction in the fundamental output voltage at the maximum operating speed of 4000rpm, yet a hundred times reduction in the output ripple at the 5kHz switching frequency. A 2nd order Butterworth filter was chosen and this was designed using the standard procedure described in [103].

A.4.2 Conclusions

This section described the design and construction of a flexible inverter and controller which was used to test brushless synchronous AC motors varying in rating from 120W to 7.5kW. It allows the steady-state performance of motors to be tested both below the rated speed and in the field-weakening region. This controller could be extended to induction motors by simply generating the current-angle from a digital counter.

Appendix B

Published Papers

This appendix contains preprints of four conference papers which summarise the major points in the thesis.

B.1 Theoretical Limitations Paper

This paper entitled "Theoretical Limitations to the Field-Weakening Performance of the Five Classes of Brushless Synchronous AC Motor Drive" was presented at the Electrical Machines and Drives conference in Oxford in September 1993 (pages 127–132).

THEORETICAL LIMITATIONS TO THE FIELD-WEAKENING PERFORMANCE OF THE FIVE CLASSES OF BRUSHLESS SYNCHRONOUS AC MOTOR DRIVE

W L Soong and T J E Miller

SPEED Laboratory, Glasgow University, United Kingdom

ABSTRACT

A new "parameter plane" approach graphically illustrates the effect of the drive parameters on the shape of the optimal field-weakening characteristic of brushless synchronous AC motor drives with a limited inverter kVA rating. It unifies previous approaches to this problem and allows fundamental performance limitations of these drives to be identified.

Contour plots of important characteristics such as power at base speed and constant power speed range are illustrated in the parameter plane. These characteristics are calculated using a circle diagram approach to obtain the optimal torque control strategy for each of the five main classes of brushless synchronous AC motor drive.

1 : INTRODUCTION

Brushless synchronous AC motors are sinusoidal current driven machines which use a standard quasi-sinusoidally distributed AC stator winding and inverter. The three main types are shown in Fig. 1, where the dotted areas represent steel and the solid areas represent permanent magnets.

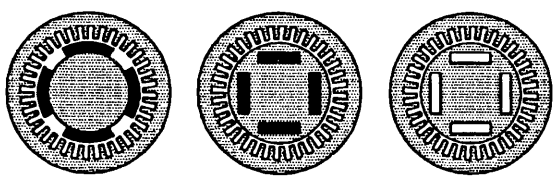

Figure 1: *Motor cross-sections.*

As the permeability of ferrite and rare-earth magnets is close to air, the surface permanent magnet motor (SPM) is non-salient and operates on magnet alignment torque while the synchronous reluctance motor (SYNCHREL) operates on reluctance torque. In terms of torque production the interior permanent magnet motor (IPM) is a hybrid of the SPM and SYNCHREL [1].

A *motor drive* consists of a motor and its inverter/controller. Rated torque is the maximum torque which can be obtained with rated current. The base speed ω_o is the speed at which the drive delivers rated torque with rated voltage and current. Above the base speed is the field-weakening region where a constant power characteristic is often desired. The maximum speed at which constant power can be maintained is ω_p and the constant power speed range (CPSR) equals ω_p/ω_o. A CPSR in the range 2–10 is required in applications such as traction and spindle drives [2,3].

The torque-speed characteristic of an IPM is ideally determined by seven parameters : the number of phases m, the number of pole-pairs p, the inverter voltage rating V_o, the inverter current rating I_o, the d-axis inductance L_d, the q-axis inductance L_q and the magnet flux-linkage Ψ_m. Only the latter four affect its shape. As the cost of the inverter is typically three to five times that of the motor [4], the ability of a motor drive to utilise a given inverter voltage and current rating is important.

Five main classes of brushless synchronous AC motor drive can be defined based on whether there is a *theoretical* finite maximum speed limit due to *voltage-limit* constraints. These are :

1. the finite maximum speed SPM drive.
2. the infinite maximum speed SPM drive.
3. the infinite maximum speed SYNCHREL drive.
4. the finite maximum speed IPM drive.
5. the infinite maximum speed IPM drive.

Note that *all* SYNCHREL drives have no theoretical speed limitation.

1.1 : Literature Review

Early work in the field-weakening of IPMs dealt with the analysis and control of existing machines [1,5,6]. It is only recently that the selection and effect of the drive parameters on the field-weakening performance of IPMs has started to be explored.

Sebastian [7] showed that inset permanent magnet motor designs offered more torque, a better field-weakening range but a lower base speed compared to conventional SPM designs.

Schiferl [8] used a per-unit system to reduce the seven IPM parameters to three independent ones. He also showed the motor drive design criterion for optimum field-weakening performance.

Morimoto [9] analysed the infinite maximum speed SPM and IPM using the circle diagram and described the optimal torque control strategy for these drives. He showed that the infinite maximum speed SPM has a true constant power characteristic in the high speed region and also investigated demagnetisation limitations.

Normalisation of the DQ equations to unity base speed further reduces the number of independent drive parameters by one [10,11,12]. Adnanes [2,13] normalised the SPM and investigated the field-weakening performance of the finite maximum speed SPM drive. Betz [14] used a

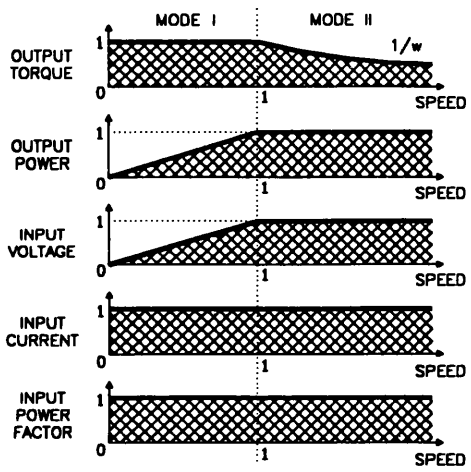

Figure 2: *Ideal field-weakening drive characteristics.*

normalised model to analyse the field-weakening performance of the SYNCHREL.

The above papers present a fragmented view of the effect of the drive parameters on the field-weakening performance of the five drive classes. They each only analyse a few of the drive classes and have difficulty in showing general results as the normalised IPM has two independent parameters rather the one parameter for the SPM and SYNCHREL.

This paper has two aims. Firstly to use the circle diagram to analyse the maximum torque operation of *all* five classes of brushless synchronous AC motor drive and hence show their similarities. Second, it describes a new graphical "parameter plane" approach which clearly illustrates the influence of drive parameters on the shape of the optimal torque-speed characteristic.

2 : THE CIRCLE DIAGRAM

2.1 : The Ideal Field-Weakening Motor Drive

The inverter utilisation at a given speed is the ratio of the motor output power to the inverter kVA capability. The ideal field-weakening motor drive is lossless and has unity inverter utilisation from base speed to infinite speeds (see Fig. 2). Note the importance of power-factor in determining inverter utilisation.

The nearest drive to this ideal is the separately-excited DC motor drive. This has direct control of the motor flux and it can therefore theoretically satisfy the power-factor requirements. Permanent magnet and reluctance machines have a *fixed* (or zero) excitation which will be shown to inherently limit their field-weakening capability.

It is useful to normalise the field-weakening performance of motor drives against the ideal characteristic. The inverter ratings are chosen for base voltage and base current. Base power is chosen to correspond to motor operation at rated VA and unity power-factor [8]. Finally the definition of base speed given above is used.

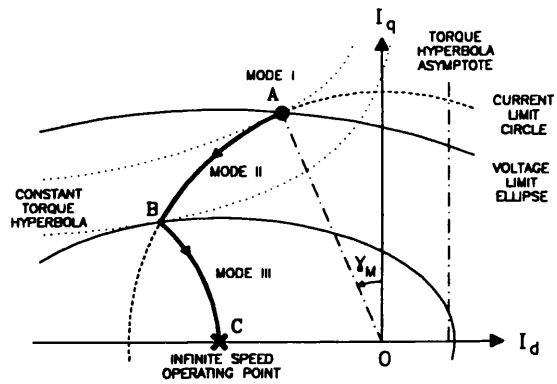

Figure 3: *The circle diagram for infinite maximum speed IPMs*

2.2 : The Circle Diagram

The following analysis uses a normalised DQ model with the magnet flux in the d-axis and the q-axis being the most inductive axis. With the saliency ratio, $\xi = L_q/L_d$:

$$V_{dn} = -w_n \xi L_{dn} I_{qn} \quad (1)$$

$$V_{qn} = w_n L_{dn} I_{dn} + w_n \Psi_{mn} \quad (2)$$

$$T_n = \Psi_{mn} I_{qn} - (\xi - 1) L_{dn} I_{dn} I_{qn} \quad (3)$$

Note the use of the subscript "n" to indicate normalised parameters. The current angle γ, is defined as the angle by which the stator current (or MMF) leads the q-axis.

$$V_{dn} = -w_n \xi L_{dn} I_n \cos\gamma \quad (4)$$

$$V_{qn} = -w_n L_{dn} I_n \sin\gamma + w_n \Psi_{mn} \quad (5)$$

$$T_n = \Psi_{mn} I_n \cos\gamma + \frac{1}{2}(\xi - 1) L_{dn} I_n^2 \sin 2\gamma \quad (6)$$

The motors are normally current-controlled and so a given operating point can be represented by its location in the (I_d, I_q) plane. The circle diagram is a graphical representation of the drive's voltage and current-limit constraints in this plane. It provides a useful means for visualising how these constraints restrict the steady-state operating point (see Fig. 3) [11].

The current-limit constraint, $I_n = \sqrt{I_{dn}^2 + I_{qn}^2} \leq 1$ defines a circle. Applying the voltage-limit constraint, $V_n = \sqrt{V_{dn}^2 + V_{qn}^2} \leq 1$ to Eqns. 1 and 2 yields :

$$\left(I_{dn} + \frac{\Psi_{mn}}{L_{dn}}\right)^2 + \xi^2 I_{qn}^2 \leq \left(\frac{1}{\omega_n L_{dn}}\right)^2 \quad (7)$$

which is the equation of an ellipse centred at $(-\Psi_{mn}/L_{dn}, 0)$, with an ellipticity of ξ and whose size is inversely proportional to speed [6,11]. The centre of the voltage-limit ellipse is termed the *infinite speed operating point* as the operating point must converge towards this at high speed.

Lines of constant torque are obtained from Eqn. 3 as hyperbolae whose asymptotes are the lines $I_{qn} = 0$ and $I_{dn} = \Psi_{mn}/(\xi - 1)L_{dn}$ [1].

Brushless synchronous AC motor drives have three operating modes as illustrated in Figs. 3 and 4 for an infinite maximum speed IPM drive. Using the notation described by Morimoto [9] these are :

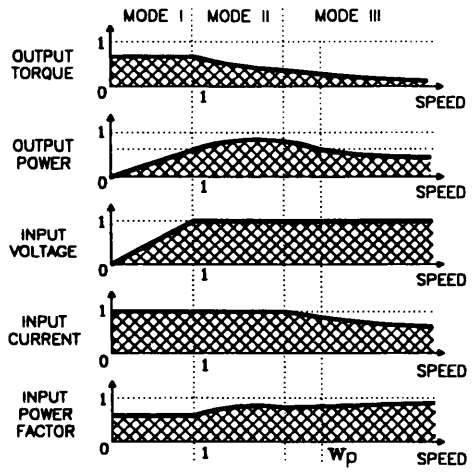

Figure 4: *Normalised field-weakening characteristics showing the three operating modes.*

- Mode I : current-limited region (constant torque). This is the region from zero speed to the base speed where maximum torque is obtained by operating at rated current with the optimal torque per ampere current angle γ_m. This corresponds to the point at which the torque hyperbolae are tangent to the current-limit circle (point A in Fig. 3).
- Mode II : current-and-voltage-limited region. Here the motor is operated at rated current with the minimum current angle required to give rated terminal voltage. That is, at the intersection of the voltage and current-limit loci (line AB).
- Mode III : voltage-limited region. Here the drive operates at the point where the torque hyperbolae are tangent to the voltage-limit ellipse (line BC).

Fig. 5 shows the optimal control strategies for the five classes of brushless synchronous AC motor drive. The dot shows the maximum torque per ampere operating point (Mode I). Above base speed the operating point moves along the intersection of the voltage-limit ellipse and current-limit circle (Mode II). For finite maximum speed drives the infinite speed operating point (the "x") lies outside the current-limit circle. For infinite maximum speed drives it lies within the current-limit circle and the operating point converges on this at high speed in the voltage-limit region (Mode III). Note that the SPM and SYNCHREL are simply special cases of the IPM.

Normalisation means the *shape* of the torque versus speed characteristic of the SPM [2] and the SYNCHREL [14] can each be characterised by one parameter. The choice of the parameter used is arbitrary, but a useful choice is the normalised magnet flux-linkage Ψ_{mn} for the SPM and the saliency ratio ξ for the SYNCHREL. Torque and power versus speed characteristics are shown in Fig. 6 for SPM and SYNCHREL drives.

A SPM with Ψ_{mn} equal to unity has zero inductance [2] and hence has no field-weakening capability. As the inductance increases and Ψ_{mn} decreases, the output power at base speed decreases slightly but the field-weakening range improves considerably. Optimum field-weakening

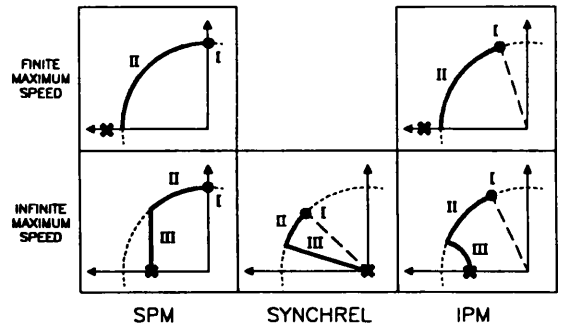

Figure 5: *Optimal control characteristics for the five drive classes.*

performance is obtained with $\Psi_{mn} = 1/\sqrt{2}$ in which case the output power approaches unity at high speed [2]. Decreasing Ψ_{mn} below this, decreases the high speed output power but introduces Mode III operation, which for the SPM is a true constant power region [9] with $P_n = \Psi_{mn}/\sqrt{1-\Psi_{mn}^2}$.

Fig. 6 shows that the performance of SYNCHRELs improves monotonically with increasing saliency ratio. The CPSR is approximately given by $\xi/2$ [14]. The optimal field-weakening performance is achieved with a SYNCHREL with an infinite saliency ratio and is *identical* to that obtained with the SPM with $\Psi_{mn} = 1/\sqrt{2}$:

$$T_n = \frac{1}{\omega_n}\sqrt{1-\frac{1}{2\omega_n^2}} \qquad \omega_n \geq 1 \tag{8}$$

This shows a *duality* between the SPM and SYNCHREL.

3 : IPM PARAMETER PLANE

The basis of the IPM parameter plane is that the *shape* of the torque versus speed characteristic of an IPM is determined by two independent parameters. Due to the IPM's "hybrid" construction, it is reasonable to select one parameter, Ψ_{mn} to represent its SPM nature and the other, ξ to represent its SYNCHREL nature.

Figs. 7 and 8 illustrate the IPM parameter plane, and show how it can represent all five drive classes. All pure SPM designs have $\xi = 1$ and lie on the x-axis while pure SYNCHREL designs have $\Psi_{mn} = 0$ and lie on the y-axis. The parameter plane extends to infinite saliency ratios, however the plots only cover $\xi \leq 11$ as most motor designs have saliencies in this range.

The third IPM parameter L_{dn} is a function of ξ and Ψ_{mn} [2]. L_{dn} is obtained by solving a quadratic for L_{dn}^2. The quadratic is the result of solving $V_n = 1$ using Eqns. 4 and 5 with $\omega_n = 1$ and $I_n = 1$ at $\gamma = \gamma_m$. γ_m is obtained by differentiating Eqn. 6 [9].

The normalised power at base speed P_{bn} can be obtained from Eqn. 6 and the normalised maximum operating speed is given by $\omega_{xn} = 1/(\Psi_{mn} - L_{dn})$ [2]. The normalised asymptotic output power at high speed $P_{an} = \Psi_{mn}/L_{dn}$ when $\Psi_{mn} \leq L_{dn}$ and is zero otherwise.

The CPSR is calculated separately for finite and infinite maximum speed drives. For finite maximum speed drives, the constant power speed ω_p occurs in Mode II.

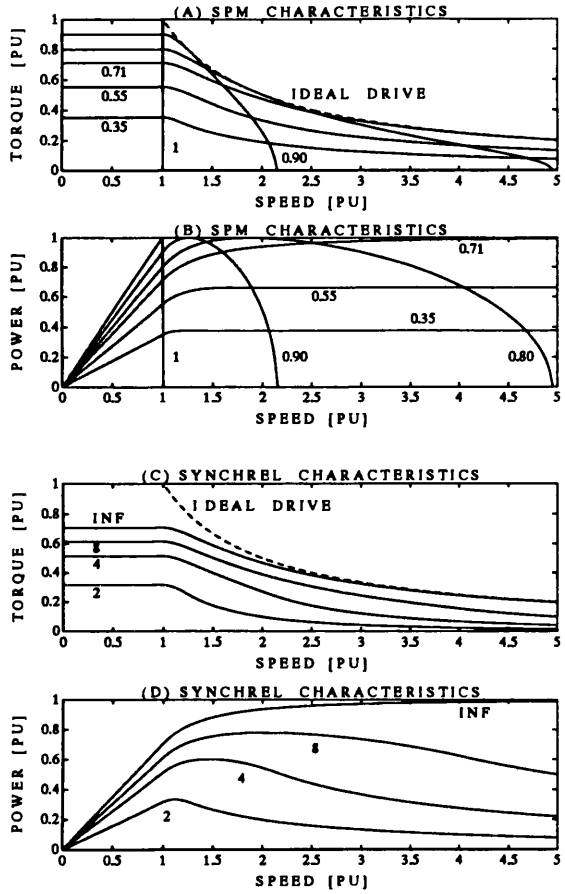

Figure 6: *Torque and power versus speed characteristics as a function of normalised magnet flux-linkage for the SPM and saliency ratio for the SYNCHREL.*

It is obtained by solving a quartic for $\sin \gamma_p$, the sine of the current angle corresponding to ω_p. For infinite maximum speed drives ω_p occurs in Mode III (see Fig. 4). The optimal Mode III trajectory is described in [9] and from this the CPSR can be obtained by solving a quartic for $1/\omega_{pn}^2$.

3.1 : Discussion

Figs. 9–12 show that *finite* maximum speed IPMs with the same maximum operating speed will have *similarly shaped, but not identical,* torque versus speed characteristics [2]. Note that designs with $P_{an} \geq P_{bn}$ have an infinite CPSR.

The parameter plane shows there is a fundamental trade-off between the power at base speed and the field-weakening range. The boundary between finite and infinite maximum speed drives is the *optimal* IPM *design line* (see Figs. 8 and 10). Optimum IPM designs have unity output power at infinite speed (see Fig. 11) [8], and have *similar, but not identical,* characteristics to the optimal SPM and SYNCHREL designs. Figs. 6 and 9 show that *all* optimal designs have a normalised output power at base speed of about 0.7pu. Thus, *when a maximum*

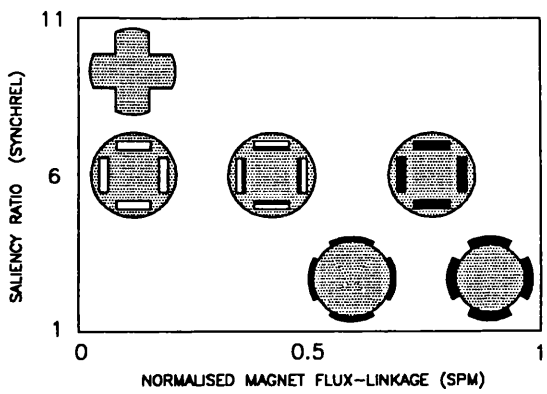

Figure 7: *The IPM parameter plane.*

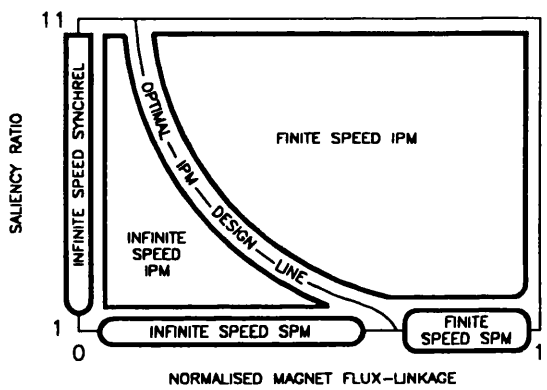

Figure 8: *The five drive classes.*

torque strategy is used, it is impossible for any brushless synchronous AC motor drive, even with infinite saliency, to achieve the ideal field-weakening characteristic shown in Fig. 2.

Fig. 10 also shows the location of practical motor drive designs (as "x" s) on the parameter plane. SPM designs usually have values of Ψ_{mn} in the range 0.85–0.95, though this can be decreased by adding external inductance in series with the motor [7]. Single-barrier SYNCHREL and IPM designs have saliencies in the range 2–5 while axially-laminated designs have saliency ratios in the range 7–10 [15] and thus theoretically have a reasonable field-weakening range (see Fig. 12).

The parameter plane is useful for visualising the effect of parameter changes on the field-weakening performance. The "shape" of the torque-speed characteristic of a linear, lossless IPM is affected by four parameters : I_o, Ψ_m, L_d and L_q. Varying I_o or Ψ_m does not alter the saliency ratio and hence moves the design parallel to the Ψ_{mn} axis (see dotted lines in Fig. 13). Increasing I_o or decreasing Ψ_m decreases Ψ_{mn}.

Varying L_q causes the design to move along the direction of the solid lines which roughly follow lines of constant ω_{zn} and P_{an}. Varying L_d causes the design to move along the direction of the (practically vertical) dashed lines. Note that for high saliency designs (ie. $\xi > 2$), $L_d \ll L_q$ and so L_d has little effect on ω_o and hence on

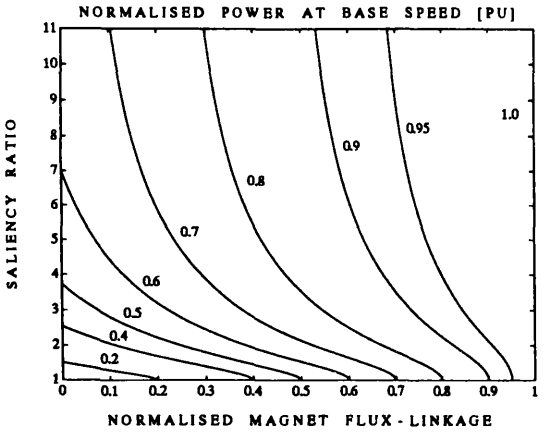

Figure 9: *Normalised power at base speed (P_{bn}).*

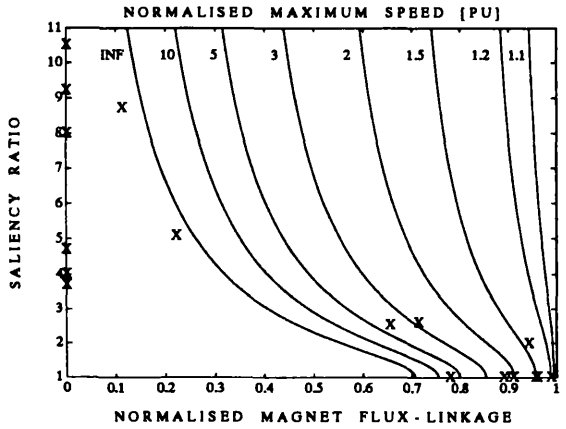

Figure 10: *Normalised maximum operating speed (ω_{xn}) and the location of actual drive designs ("x").*

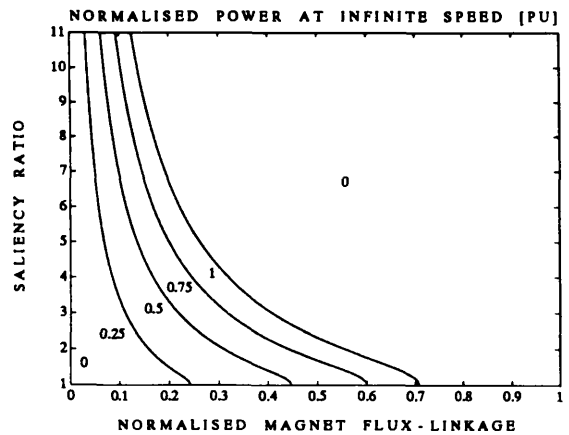

Figure 11: *Normalised asymptotic high speed output power (P_{an}).*

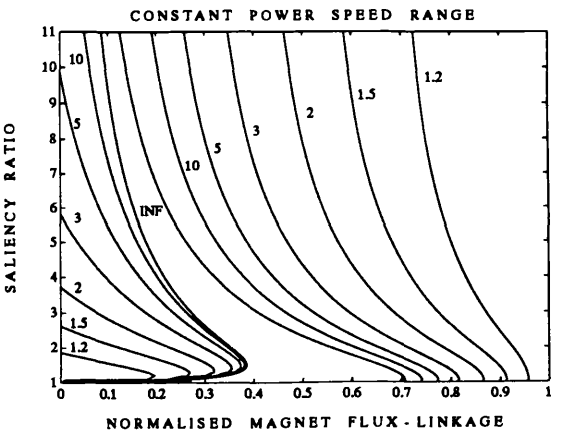

Figure 12: *Constant power speed range (CPSR).*

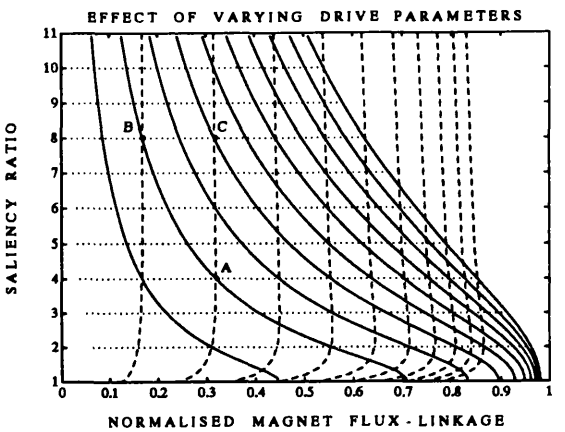

Figure 13: *Effect of varying L_q (solid), L_d (dashed), Ψ_m and I_o (dotted).*

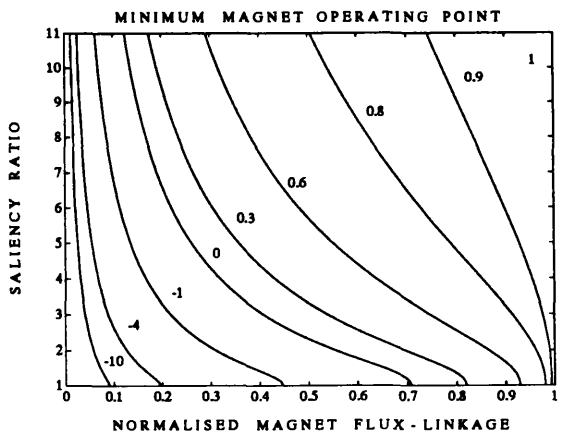

Figure 14: *Demagnetisation constraints.*

Ψ_{mn}. The spacing between the solid lines and also that between the dashed lines correspond to equal increments in the *actual* magnet flux-linkage Ψ_m.

Consider a motor drive design corresponding to point A in Fig. 13 : doubling L_q moves it to point B, doubling Ψ_m moves it to point C and doubling L_d returns it to point A. The new design has exactly the same torque-speed characteristic *shape* as the original one, but has twice the rated torque and half the base speed.

3.2 : Practical Factors

The effect of stator resistance and q-axis saturation is usually small in the field-weakening region, however high iron losses can drastically reduce the field-weakening range [16]. DQ cross-coupling is significant in low-saliency single-barrier designs [5,17] but not in axially-laminated designs due to their high saliency.

Demagnetisation limits are critical for permanent magnet motors. Assuming zero airgap and no leakage for simplicity, then Fig. 14 shows the minimum magnet operating point in the field-weakening region. Unity represents operation at remanence and zero corresponds to zero flux in the magnet. The minimum magnet operating point is inversely related to the field-weakening range and in optimal IPM designs is equal to zero. Thus for good field-weakening performance it is necessary to use magnets with a linear 2nd quadrant demagnetisation curve [9].

All designs on the optimal IPM design line have excellent field-weakening characteristics. However, the axially-laminated IPM [15] has useful characteristics such as low magnet requirements (due to the high saliency) and also a lower back-emf at high speeds. The latter point is important as damage may occur to the inverter if it trips out when field-weakening [1].

4 : CONCLUSIONS

This paper analysed the field-weakening performance of the five main classes of brushless synchronous AC motor drive when operated with a limited inverter kVA rating. It used the circle diagram to illustrate the optimal control strategy to obtain maximum output power at any speed and showed that the surface permanent magnet and synchronous reluctance motors are special cases of the interior permanent magnet motor.

The new concept of the parameter plane was introduced as a means for visualising the effect of parameter changes on the drive's field-weakening performance. It showed the fundamental tradeoff between the inverter utilisation at base speed and the field-weakening performance. Drives with the same maximum operating speed have similar torque-speed characteristics. Optimum field-weakening performance is obtained from designs at the boundary between finite and infinite theoretical maximum speed drives. These optimum designs all have an inverter utilisation of about 0.7 at base speed and hence the ideal motor drive field-weakening characteristic cannot be achieved *when using maximum torque control.*

The practical application of the parameter plane for designing brushless synchronous AC motor drives for a wide field-weakening range will be discussed in a later paper.

ACKNOWLEDGEMENTS

The support of the Commonwealth Scholarship Commission of the United Kingdom and the Glasgow University SPEED Consortium is gratefully acknowledged.

References

[1] T. M. Jahns, G. B. Kliman, and T. W. Neumann, "Interior PM synchronous motors for adjustable-speed drives," *IEEE Trans. Ind. Appl.*, vol. 22, pp. 738–747, Jul./Aug. 1986.

[2] A. K. Adnanes, "Torque analysis of permanent magnet synchronous motors," in *Power Electronics Specialists Conference*, pp. 695–701, 1991.

[3] B. V. Murty and L. J. Jacovides, "A critical evaluation of AC motor drives for traction," in *Proceedings of the Intersociety Energy Conversion Engineering Conference*, pp. 1.729–1.737, Aug. 1985.

[4] D. A. Staton, T. J. E. Miller, and S. E. Wood, "Optimisation of the synchronous reluctance motor," in *Electrical Machines and Drives Conference*, pp. 156–160, Sep. 1991.

[5] B. Sneyers, D. W. Novotny, and T. A. Lipo, "Field-weakening in buried permanent magnet AC motor drives," *IEEE Trans. Ind. Appl.*, vol. 21, pp. 398–407, Mar./Apr. 1985.

[6] T. M. Jahns, "Flux-weakening regime operation of an interior permanent magnet synchronous motor drive," *IEEE Trans. Ind. Appl.*, vol. 23, pp. 681–689, Jul./Aug. 1987.

[7] T. Sebastian and G. R. Slemon, "Operating limits of inverter-driven permanent magnet motor drives," *IEEE Trans. Ind. Appl.*, vol. 23, pp. 327–333, Mar./Apr. 1987.

[8] R. F. Schiferl and T. A. Lipo, "Power capability of salient pole permanent magnet synchronous motor in variable speed drive applications," *IEEE Trans. Ind. Appl.*, vol. 26, pp. 115–123, Jan./Feb. 1990.

[9] S. Morimoto, Y. Takeda, T. Hirasa, and K. Taniguchi, "Expansion of operating limits for permanent magnet motor by current vector control considering inverter capacity," *IEEE Trans. Ind. Appl.*, vol. 26, pp. 866–871, Sep./Oct. 1990.

[10] M. R. Harris, P. J. Lawrenson, and J. M. Stephenson, *Per-Unit Systems.* Cambridge University Press, 1970.

[11] T. J. E. Miller, *Brushless Permanent Magnet and Reluctance Motor Drives.* Oxford University Press, 1989.

[12] W. Leonhard, *Control of Electrical Drives.* Springer-Verlag, 1990.

[13] A. K. Adnanes and T. M. Undeland, "Optimum torque performance in PMSM drives above rated speed," in *Ind. Appl. Society Annual Meeting*, pp. 169–175, Oct. 1991.

[14] R. E. Betz, "Control of synchronous reluctance machines," in *Ind. Appl. Society Annual Meeting*, pp. 456–462, Sep. 1991.

[15] T. A. Lipo, A. Vagati, L. Malesani, and T. Fukao, eds., *Synchronous Reluctance Machines – A Viable Alternative for AC Drives*, Ind. Appl. Society Annual Meeting Tutorial, Oct. 1992.

[16] R. E. Betz, M. Jovanovic, R. Lagerquist, and T. J. E. Miller, "Aspects of the control of synchronous reluctance machines including saturation and iron losses," in *Ind. Appl. Society Annual Meeting*, pp. 456–463, Oct. 1992.

[17] B. C. Mecrow and A. G. Jack, "Operation of highly-rated permanent magnet synchronous machines," in *Electrical Machines and Drives Conference*, pp. 26–30, Sep. 1991.

B.2 Practical Limitations Paper

This paper entitled "Practical Field-Weakening Performance of the Five Classes of Brushless Synchronous AC Motor Drive" was presented at the European Power Electronics conference in Brighton in September 1993 (volume 5, pages 303–310).

PRACTICAL FIELD-WEAKENING PERFORMANCE OF THE FIVE CLASSES OF BRUSHLESS SYNCHRONOUS AC MOTOR DRIVE

W L Soong and T J E Miller

SPEED Laboratory, Glasgow University, United Kingdom

Abstract. The effect of stator resistance, magnetic saturation and iron losses on the field-weakening performance of synchronous reluctance and surface permanent magnet motors is examined. It is shown that the constant power speed range is relatively unaffected by stator resistance and iron losses but is strongly influenced by saturation. Methods for estimating the reduction in constant power speed range are described. The results are validated by comparisons with experimental measurements for a surface permanent magnet motor and two axially-laminated synchronous reluctance motors.

Keywords. Field-weakening, constant power speed range, synchronous motors, saturation, iron losses.

1 : INTRODUCTION

Brushless synchronous AC motors are sinusoidal current driven machines which use a standard quasi-sinusoidally distributed AC stator winding and inverter. The three main types are the surface permanent magnet motor (SPM), the synchronous reluctance motor (SYNCHREL) and the interior permanent magnet motor (IPM).

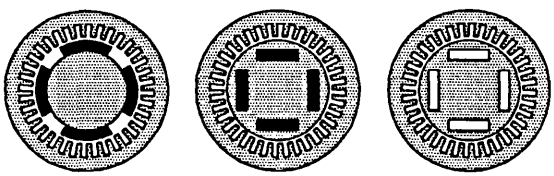

Figure 1: *Motor cross-sections.*

A *motor drive* consists of a motor and an inverter/controller. It was shown in an earlier paper [1] that five classes of brushless synchronous AC motor drive can be defined based on whether there is a *theoretical* finite maximum speed limit due to *voltage-limit* constraints. These are :

1. the finite maximum speed SPM drive.
2. the infinite maximum speed SPM drive.
3. the infinite maximum speed SYNCHREL drive.
4. the finite maximum speed IPM drive.
5. the infinite maximum speed IPM drive.

Note that *all* SYNCHREL drives have no theoretical speed limitation.

The earlier paper followed previous workers [2,3,4,5,6] in using lossless linear models to examine the effect of the motor drive parameters on the field-weakening performance. This was necessary in order to obtain general results and allow fundamental theoretical limitations to be identified. However the field-weakening performance can be substantially affected by practical factors such as stator resistance, magnetic saturation, iron losses and DQ cross-coupling.

Sneyers, Novotny and Lipo [7], and Mecrow and Jack [8] showed that DQ cross-coupling is significant in low-saliency single-barrier and radial-spoke IPM designs.

Xu, Xu, Lipo and Novotny [9] investigated the effect of stator resistance, saturation and iron losses on SYNCHREL performance below the knee-speed. They showed that saturation and iron losses increase the maximum torque per ampere angle beyond the theoretical 45° and that iron losses mean that there is a difference between the external and internal current angles.

Betz, Jovanovic, Lagerquist and Miller [10] derive expressions for the performance of the SYNCHREL including the effect of saturation and iron losses.

Chalmers [11] examined the effect of saturation on the field-weakening performance of IPMs. He showed the importance of modelling saturation for calculating the low speed characteristics.

The above papers have not presented a clear view of the effect of practical factors on the field-weakening performance. This paper aims to present general results showing the effect of stator resistance, saturation and iron losses on the field-weakening performance of SPM and SYNCHREL drives. It will describe simple techniques for calculating their effects and validate the results by comparisons with the measured performance. DQ cross-coupling has been neglected as the effect is small for the drives considered.

Though IPM drives are not directly examined, the field-weakening performance of finite maximum speed IPMs is similar to that of SPMs, and that of infinite maximum speed IPMs is similar to that of SYNCHRELs [1].

1.1 : Definitions and Terms

This paper assumes the use of a *maximum torque* control strategy [1] within a limited inverter (or motor) voltage

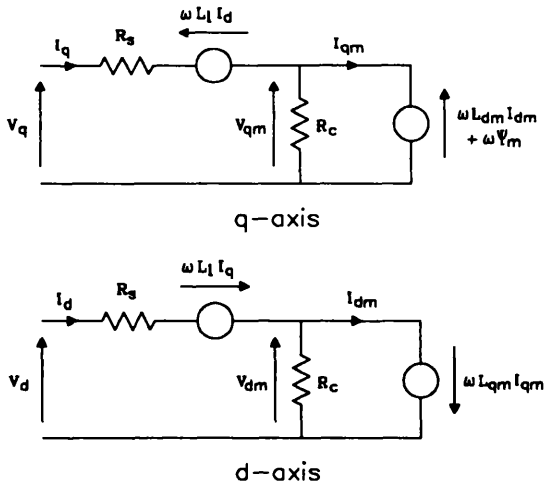

Figure 2: IPM *steady-state DQ equivalent circuit.*

and current rating.

Brushless synchronous motors are generally current-controlled and hence their operating point can be defined by the d- and q-axis current components (I_d, I_q). Alternatively it can be specified by the current magnitude I and the *current angle* γ. This is the angle between the current phasor and the q-axis. The IPM convention of having the q-axis being the most inductive axis and the magnet flux Ψ_m (if any) being in the d-axis is used.

At low speeds, the drive is operated with rated current I_o at the *maximum torque per ampere current angle* γ_m giving *rated torque* T_k. This can be maintained until the *knee-speed* ω_k is reached, at which point the required terminal voltage equals the drive's voltage rating V_o. This corresponds to *rated mechanical output power* P_k. In the field-weakening region (ie. above ω_k) the drive can maintain rated output power up to the *maximum constant power speed* ω_p.

In this paper, two parameters will be used to characterise the field-weakening performance of a motor drive. The *inverter utilisation* κ is the ratio of the P_k to the inverter kVA capability [1] and the *constant power speed range* (CPSR= $\sigma = \omega_p/\omega_k$) is the speed range over which the drive can maintain rated output power.

An IPM *steady-state* equivalent circuit incorporating leakage inductance L_l, stator resistance R_s and iron loss R_c is shown in Fig. 2 [9]. Saturation is modelled by making the magnetising inductances (L_{dm} and L_{qm}) functions of the corresponding magnetising currents (I_{dm} and I_{qm}). The magnetising saliency ratio is defined as $\xi_m = L_{qm}/L_{dm}$ and the saliency ratio is $\xi = L_q/L_d$ where $L_q = L_{qm} + L_l$ and $L_d = L_{dm} + L_l$.

1.2 : Circuit Equations

Solving for I_{dm} and I_{qm} in terms of I_d and I_q in Fig. 2 yields :

$$I_{qm} = \frac{R_c(R_c I_q - \omega\Psi_m - \omega L_{dm} I_d)}{R_c^2 + \omega^2 L_{dm} L_{qm}} \qquad (1)$$

$$I_{dm} = \frac{R_c^2 I_d + \omega L_{qm} R_c I_q - \omega^2 \Psi_m L_{qm}}{R_c^2 + \omega^2 L_{dm} L_{qm}} \qquad (2)$$

Due to saturation it is necessary to solve these equations iteratively.

The terminal voltage taking into account stator resistance R_s and leakage inductance L_l is :

$$V_q = I_q R_s + \omega L_l I_d + \omega L_{dm} I_{dm} + \omega\Psi_m \qquad (3)$$

$$V_d = I_d R_s - \omega L_l I_q - \omega L_{qm} I_{qm} \qquad (4)$$

Finally the inverter voltage-limit V_o and current-limit I_o constraints must be applied to the terminal voltage V and current I :

$$\begin{aligned} V_q^2 + V_d^2 &= V^2 \le V_o^2 \\ I_q^2 + I_d^2 &= I^2 \le I_o^2 \end{aligned} \qquad (5)$$

It was shown in [1] that the maximum torque versus speed characteristic has three operating modes. Mode I is the current-limited or "constant torque" region below the knee-speed where $I = I_o$ and $V \le V_o$. Mode II is the current-and-voltage-limited region where $V = V_o$ and $I = I_o$. Mode III is the voltage-limited region where $V = V_o$ and $I \le I_o$.

2 : INVERTER UTILISATION

In a lossless linear brushless synchronous AC motor drive, the inverter utilisation κ equals the power-factor in Mode II. From the equivalent circuit shown in Fig. 2 it can be shown that for an SPM drive with a CPSR= σ :

$$\kappa = \sqrt{\frac{1 + 1/\sigma}{2}} \qquad (6)$$

For a SYNCHREL drive :

$$\kappa = \frac{\xi - 1}{2\sqrt{\xi\sigma}} \quad \text{where} \quad \xi = \sigma + \sqrt{\sigma^2 - 1} \qquad (7)$$

Fig. 3 illustrates these equations. Finite maximum speed IPMs have a similar characteristic to SPMs and infinite maximum speed IPM drives have a similar characteristic to SYNCHRELs [1].

In general SPM drives have a higher power-factor than SYNCHREL drives for the same CPSR however both curves asymptote towards $\kappa = 1/\sqrt{2}$ as the CPSR approaches infinity.

2.1 : Stator Resistance

Stator resistance effectively reduces the available voltage, the knee-speed and hence the inverter utilisation. The inverter utilisation taking into account stator resistance is κ_R. It is a function of the power-factor $\cos\phi = \kappa$ and the normalised stator resistance R_{sn} (see [1]) and can be obtained from the equivalent circuit shown in Fig. 5 :

$$\kappa_R = \kappa\left[\sqrt{1 + (R_{sn}\kappa)^2 - R_{sn}^2} - R_{sn}\kappa\right] \approx \kappa[1 - R_{sn}\kappa] \qquad (8)$$

Note that SPM drives have a high power-factor at the knee-speed and hence are more sensitive to stator resistance than a SYNCHREL drive with the same CPSR.

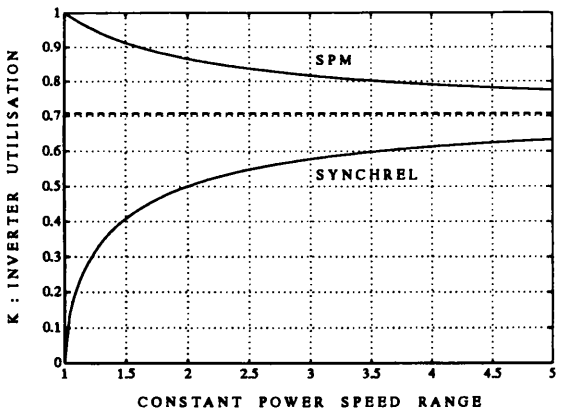

Figure 3: *Inverter utilisation (κ) for* SPM *and* SYNCHREL *drives as a function of* CPSR.

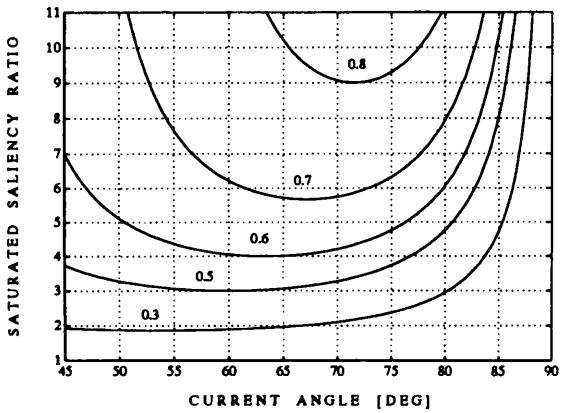

Figure 4: SYNCHREL *Mode II inverter utilisation κ.*

2.2 : Magnetic Saturation

Saturation is generally small in SPM drive designs due to the large effective airgap and so has little effect on the inverter utilisation. It is however significant in SYNCHREL designs where it causes the saliency ratio ξ to fall and the maximum torque per ampere current angle γ_m to exceed 45° [9].

For a SYNCHREL κ as a function of the saturated saliency ratio and γ for Mode II operation is given by [6] :

$$\kappa = \cos\phi = \frac{\xi - 1}{\sqrt{2}} \sqrt{\frac{\sin 2\gamma}{\tan\gamma + \xi^2 \cot\gamma}} \qquad (9)$$

This is illustrated as a contour plot in Fig. 4. Saturation causes the saliency ratio to decrease which decreases the inverter utilisation. It however also increases γ_m which initially increases the inverter utilisation but ultimately also causes it to fall. In general, the higher the saliency ratio, the less sensitive is the inverter utilisation to saturation. This is because as saturation decreases the output torque, it also increases the knee-speed.

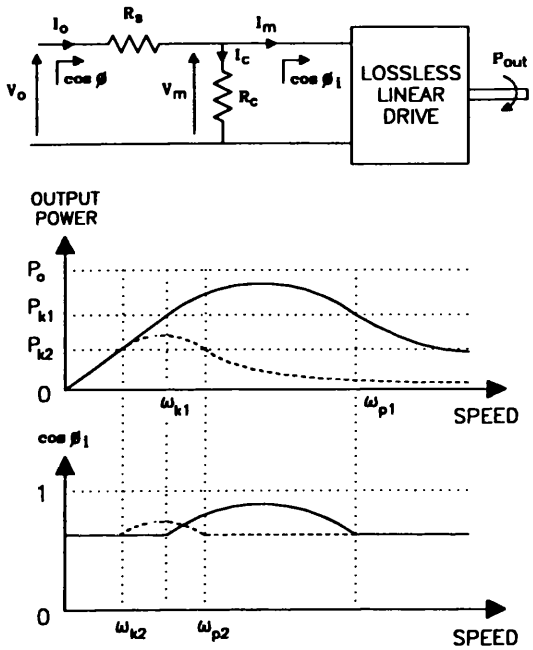

Figure 5: *Stator resistance decreases the knee-speed but does not alter the* CPSR.

2.3 : Iron Losses

Iron losses reduce the inverter utilisation. If the iron loss is small, then from Fig. 5 the total inverter utilisation κ_T taking into account stator resistance and iron loss is :

$$\kappa_T \approx \kappa_R \left[1 - \frac{\kappa_R}{\kappa R_{cn}}\right] \qquad (10)$$

where R_{cn} is the normalised iron loss resistance.

3 : CONSTANT POWER SPEED RANGE

3.1 : Stator Resistance

The CPSR of SPM and SYNCHREL motor drives is unaffected by stator resistance. This will be shown for a SYNCHREL drive using Fig. 5. Note that the mechanical output power $P_m = V_m I_m \cos\phi_i$.

During the constant power speed range, rated voltage and current are applied to the motor (Mode II operation). Under these circumstances the normalised output power of a lossless linear motor (ie. $R_s = 0$, $R_c = \infty$) equals the *internal* power-factor $\cos\phi_i$. Thus the internal power-factor is equal at the limits of the constant power speed range. This is shown by the solid line in Fig. 5 where the power-factor at the knee-speed ω_{k1} equals the power-factor at ω_{p1}.

If $R_s \neq 0$ then the drive has the characteristics shown by the dashed line where $\omega_{k2} < \omega_{k1}$ as the magnetising voltage V_m is reduced. The stator resistance means that V_m is determined by the internal power-factor. At some speed ω_{p2} the internal power-factor will equal that at the base speed ω_{k2}. V_m is thus the same and hence the output power must be the same. Thus ω_{k2} and ω_{p2}

correspond to the constant power speed range limits of a lossless linear drive with a reduced supply voltage (actually $\kappa_R V_o/\kappa$) compared to V_o. As the CPSR of a lossless linear drive is unaffected by the rated voltage, thus the CPSR is unaffected by stator resistance.

The same argument can also be applied to any drive in which the constant power speed range occurs entirely in Mode II. This includes finite maximum speed SPM and IPM drives.

3.2 : Magnetic Saturation

Though saturation is generally small in SPM designs, the field-weakening characteristic is sensitive to L_d and so the saturated values should be used.

For SYNCHRELs, saturation critically affects the CPSR obtained and so must be taken into account.

Fig. 4 shows the variation in output power of a SYNCHREL in Mode II. Consider a lossless linear motor with $\xi = 7$. As the motor is linear $\gamma_m = 45°$ and from Fig. 4 the output power P_k at the knee-speed is ≈ 0.6pu. During field-weakening the current angle is increased. The output power rises and peaks at the *maximum power-factor angle* $\gamma_{pf} = \arctan\sqrt{\xi}$ [6]. It then falls and at the *constant power angle* γ_p the output power is equal again to P_k. For a linear motor this also corresponds to the *Mode III transition angle* $\gamma_t = \arctan\xi$ (for $\xi = 7$, $\gamma_t \approx 82°$).

Saturation causes γ_m to exceed 45°. A *constant saturation* model assumes that the level of saturation is unchanged throughout the field-weakening region. Fig. 4 shows that $\gamma_m > 45°$ will cause γ_p to reduce and hence the CPSR will be reduced. In fact if $\gamma_m \geq \gamma_{pf}$ the CPSR is unity (for a constant saturation model).

Using a constant saturation model, the reduced CPSR can be calculated from Fig. 4 and is shown as a contour plot in Fig. 6. The dashed line corresponds to γ_t and operation to the right of this line corresponds to Mode III operation. Note that the Mode II output power shown in Fig. 4 for this region does not represent the maximum possible because Mode II operation does not give the maximum torque here (see [1]).

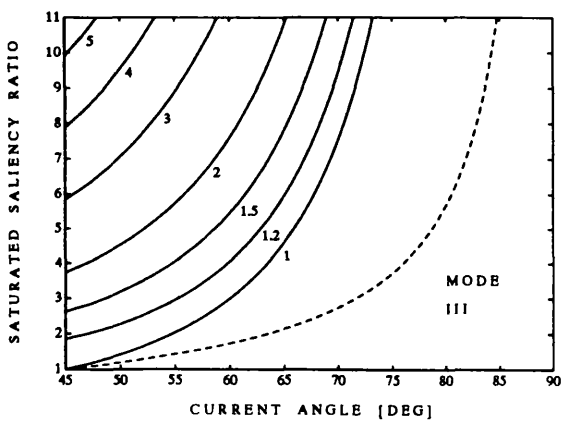

Figure 6: CPSR *for constant saturation model.*

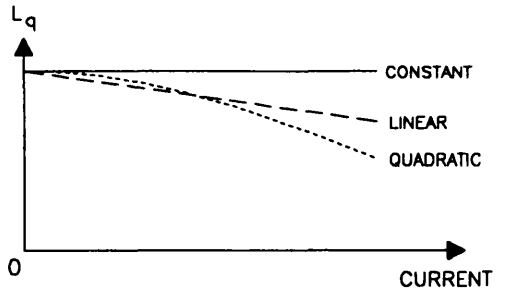

Figure 7: *Three saturation models.*

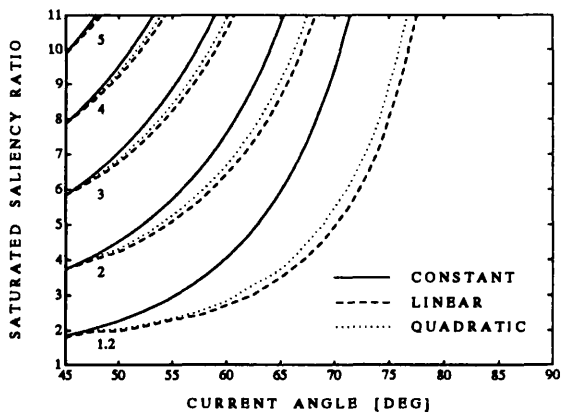

Figure 8: *Comparison of the* CPSR *predicted by the three saturation models for* SYNCHRELs.

It is however unrealistic to use a constant saturation model. Better approximations are the linear and quadratic saturation models shown in Fig. 7. Note that in these models the CPSR is always greater than unity as the γ_m constraint is not "artificially" imposed as it was in the constant saturation model. That is, the torque actually peaks at $\gamma = \gamma_m$ in these models (unlike the constant saturation model) and so the rate of change of torque with current angle is zero at this point. When field-weakening commences, and the speed rises, the torque remains momentarily constant and the output power *must* (at least momentarily) rise.

Fig. 8 compares the CPSR predicted by the constant, linear and quadratic saturation models. Note the divergence between the models as γ_m increases. The linear and quadratic models take into account the lessening of saturation during field-weakening and hence show a greater CPSR. The quadratic model predicts a slightly lower CPSR than the linear model as it saturates less due to the steepness of the quadratic saturation curve with increasing current. The small difference between the results of the linear and quadratic saturation models indicate that using more refined models are unlikely to yield substantially different results.

It should be noted that typical SYNCHRELs have maximum torque per ampere current angles in the range 55° to 65° and so the actual CPSR can be considerably lower than that predicted with an ideal model ($\gamma_m = 45°$).

3.3 : Iron Losses

The previous analysis neglected iron losses. These generally have more influence on the performance of SYNCHRELs than SPMs and this analysis will concentrate on SYNCHRELs.

Iron losses have two effects : they reduce the output power at base speed and increase γ_m [9]. More precisely the increase in γ_m is caused by a discrepancy between the *external* current angle ($\tan\gamma = -I_d/I_q$) and the *internal* (or magnetising) current angle ($\tan\gamma_i = -I_{dm}/I_{qm}$).

While γ_m can be significantly affected by iron losses, the *internal* maximum torque per ampere current angle γ_{mi} is relatively unaffected (for moderate levels of iron loss) as it is mainly dependent on the saturation characteristics of the motor. Iron losses reduce the magnetising current I_m which reduces saturation (see Fig. 5). This causes γ_{mi} to reduce slightly when iron losses are modelled and hence the saturated saliency ratio to increase slightly.

It can be shown using the same argument as for stator resistance, that the reduction in inverter utilisation due to iron losses does not affect the CPSR. Also, while iron loss increases γ_m, it does not cause substantial changes to γ_{mi} and it is γ_{mi} which mainly determines the CPSR. Thus to a first approximation, the CPSR of SYNCHRELs is unaffected by iron losses.

The effect of iron loss on γ_m and on the torque versus angle characteristic at rated current and speed is now examined and quantified.

From Eqns. 1 and 2, for a SYNCHREL with a high saliency and a low iron loss then :

$$I_{qm} \approx I_o \cos\gamma \tag{11}$$

$$I_{dm} \approx -I_o \sin\gamma + \left(\frac{wL_{qm}I_o}{R_c}\right)\cos\gamma \tag{12}$$

Also from Fig. 2 :

$$V_m \approx V_{dm} = -wL_{qm}I_o\cos\gamma \tag{13}$$

As iron losses are proportional to V_m^2, thus the losses will be largest at $\gamma = 0°$ and zero at $\gamma = 90°$. This is shown in Fig. 9.

Iron losses cause γ_i to be less than γ. In fact when $\gamma = 0°$, $\gamma_i < 0°$ and so the torque is negative. Defining $\Delta\gamma = \gamma - \gamma_i$ then from Eqn. 12 the zero torque point occurs when $I_{dm} = 0$ and $\gamma = \Delta\gamma_o$:

$$\Delta\gamma_o \approx \arctan\left(\frac{wL_{qm}}{R_c}\right) \tag{14}$$

This is illustrated in Fig. 9. In order to determine R_c it is sometimes convenient to measure the (negative) output power at $\gamma = 0°$. With $\gamma = 0°$, using Fig. 2 the iron losses are $P_{fe} = V_m^2/R_c$ while the useful input electrical power is $P_e \approx V_{qm}I_{qm}$. From Eqn. 13 it can be shown that $P_e/P_{fe} \approx 1/\xi_m$ and hence the mechanical output power $P_m = P_e - P_{fe}$ is given by :

$$P_m(\gamma = 0°) \approx P_{fe}(\gamma = 0°)\left[1 - \frac{1}{\xi_m}\right] \tag{15}$$

Thus the (negative) mechanical output power at $\gamma = 0°$ is equal to the iron loss if the saturated magnetising saliency ratio is high and for moderate values of iron loss.

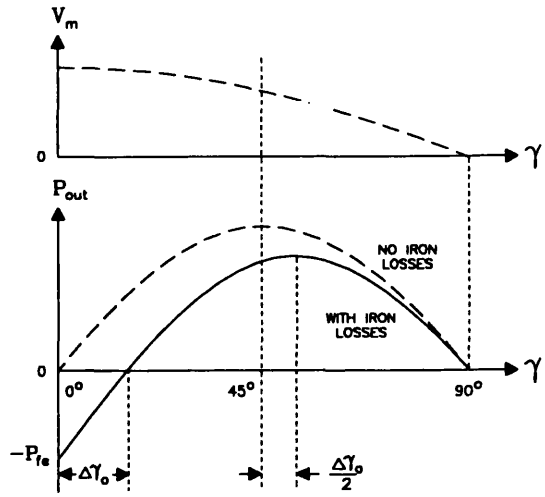

Figure 9: *Power versus current angle for a* SYNCHREL *operated at rated current and speed.*

From Fig. 9, for an infinitely salient SYNCHREL $\Delta\gamma$ is zero at 90° ($V_m = 0$) and approximately $\Delta\gamma_o$ at 0°. To a first approximation $\Delta\gamma$ decreases linearly from $\gamma = 0°$ to $\gamma = 90°$. Neglecting saturation $\gamma_{mi} = 45°$. γ_m will thus be shifted by about half of $\Delta\gamma_o$, that is $\gamma_m \approx \gamma_{mi} + \Delta\gamma_o/2$.

4 : VALIDATION OF RESULTS

A comparison was performed between the calculated and measured field-weakening characteristics of a SPM motor drive and two SYNCHREL motor drives.

The 2kW SPM motor was designed for servo applications and uses samarium-cobalt magnets. It has four poles and a rated speed of about 5000rpm. The tests were performed at approximately one quarter of rated voltage in order to keep the field-weakening characteristics within the 4000rpm dynamometer speed restriction. This gave it high copper losses ($R_{sn} = 0.153$pu) and low iron losses ($R_{cn} = 44$pu). It had a CPSR of about 2.

The 120W and 1kW SYNCHRELs are custom-built four-pole axially-laminated designs [12]. The 120W motor uses an induction motor stator, was operated at rated voltage ($V_o = 110V_{ll}$) and shows moderate saturation, high copper losses ($R_{sn} = 0.21$pu), moderate iron losses ($R_{cn} = 12.6$pu) and has a CPSR of about 2. The 1kW motor uses the same stator as the SPM motor, was operated at a reduced voltage, shows heavy saturation, high copper losses ($R_{sn} = 0.15$pu), moderate iron losses ($R_{cn} = 8.8$pu) and a low CPSR of about 1.3.

The SPM and SYNCHREL saturation characteristics were obtained from flux-linkage tests [12]. Care is required in measuring the d-axis SPM inductance as the pro-magnetising characteristic is substantially different from the de-magnetisation characteristic. The leakage inductance was included into the magnetising inductances for simplicity. The test results for the 2kW SPM design are shown in Fig. 10. Note that the q-axis characteristic is relatively symmetrical while the d-axis curve is "offset" due to the magnet flux producing a "DC bias".

Table 1: *Comparison of measured and calculated* SYNCHREL *results. The arrows indicate the value at that location is the same as that pointed to. The approximated* CPSR *for the three saturation models is from* γ_{mi} *and the approximated* κ *is from Eqns. 8 and 10.*

	Calculated From Equivalent Circuit Model							Approximations			
	ξ (sat)	γ_m	γ_{mi}	T_k Nm	w_k rpm	κ	CPSR	κ	CPSR cons	CPSR linear	CPSR quad
120W SYNCHREL											
measured		**56.5°**		**1.067**	**1580**	**0.545**	**2.13**				
$\xi_{unsat}, \gamma_m = 45°$	7.35	→	45°	1.348	1388	0.605	3.74		←	←	←
$\xi_{sat}, \gamma_m = 45°$	6.37	→	45°	1.141	1596	0.589	3.26		←	←	←
$\xi_{sat} + R_s + R_c$	6.37	48.3°	45.1°	1.048	1425	0.483	3.25	0.473	3.25	3.25	3.25
ξ	6.37	→	53.9°	1.088	1892	0.666	2.43		2.32	2.50	2.45
$\xi + R_s$	6.37	→	53.9°	↑	1604	0.564	↑	0.564	↑	↑	↑
$\xi + R_s + R_c$	6.44	55.9°	53.1°	1.012	1624	0.531	2.52	0.526	2.42	2.59	2.54
1kW SYNCHREL											
measured		**64.8°**		**3.28**	**1180**	**0.551**	**1.26**				
$\xi_{unsat}, \gamma_m = 45°$	8.46	→	45°	7.72	563	0.619	4.29		←	←	←
$\xi_{sat}, \gamma_m = 45°$	5.26	→	45°	4.41	895	0.563	2.73		←	←	←
$\xi_{sat} + R_s + R_c$	5.26	50.0°	45.2°	3.89	858	0.476	2.70	0.458	2.71	2.71	2.71
ξ	5.26	→	62.9°	3.58	1324	0.676	1.59		1.25	1.56	1.51
$\xi + R_s$	5.26	→	62.9°	↑	1179	0.602	↑	0.602	↑	↑	↑
$\xi + R_s + R_c$	5.40	66.2°	62.0°	3.26	1199	0.557	1.66	0.541	1.34	1.64	1.58

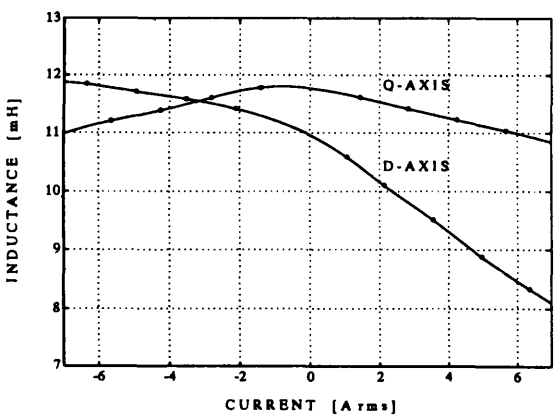

Figure 10: SPM *flux-linkage test results.*

Iron loss resistance estimates were obtained from the measured torque versus current angle characteristic at constant current and speed using Eqn. 15.

The field-weakening testing of the motors was performed using a custom-built 7.5kW, 10kHz IGBT inverter controlled by a hysteresis current controller. The current magnitude and angle were varied manually to determine the maximum torque at a given speed within the motor's voltage and current-limit constraints.

4.1 : Field-Weakening Characteristics

Table 1 shows a comparison between the measured, calculated and approximated performance of the two SYNCHREL designs.

The unsaturated ($\xi_{unsat}, \gamma_m = 45°$) and saturated ($\xi_{sat}, \gamma_m = 45°$) constant parameter models considerably overestimate the output torque and CPSR. Adding stator resistance and iron loss to the constant parameter saturated model ($\xi_{sat}+R_s+R_c$) shows that iron loss increases γ_m. As predicted, γ_{mi} and the CPSR are not significantly changed.

Modelling the saturation characteristics (ξ) considerably alters γ_{mi} and dramatically decreases the CPSR. The estimates produced by the three saturation models (constant, linear and quadratic) give a fair estimate of the CPSR. Note that as expected, the constant saturation model underestimates the CPSR obtained from the actual saturation characteristic, while the linear and quadratic saturation models give better estimates.

Adding stator resistance ($\xi + R_s$) and iron loss ($\xi + R_s + R_c$) to the saturation characteristic model shows again that iron loss affects γ_m. As indicated earlier, γ_{mi} actually decreases slightly and the saturated saliency increases slightly with iron loss as the magnetising current is reduced. This was not seen with the ($\xi_{sat} + R_s + R_c$) model as saturation was not modelled.

The full model ($\xi + R_s + R_c$) produces a more accurate estimate of the CPSR than the constant parameter models but still overestimates the actual CPSR by about 20–30%. This is probably due to the iron losses increasing more rapidly with speed than predicted by the constant iron loss resistance R_c model.

With regard to the inverter utilisation (κ), the full models show a good match with the measured characteristics. Note that κ shows only small variations with the different models as changes in the output torque (T_k) are partially compensated by changes in the knee-speed (ω_k). The approximate formula (Eqn. 10) shows a reasonable match with the full model.

The SPM characteristics in Table 2 show similar results. Using an unsaturated constant parameter, lossless model the CPSR is underestimated as L_d is underestimated (see

Table 2: *Comparison of measured and calculated* SPM *results.*

2kW SPM	ξ	γ_m	γ_{mi}	κ	CPSR
measured		**3.6°**		**0.736**	**1.98**
$\xi_{unsat}, \gamma_m = 45°$	1.08	←	2.6°	0.876	1.87
ξ	1.02	←	0.7°	0.876	2.01
$\xi + R_s$	1.02	←	0.7°	0.754	2.01
$\xi + R_s + R_c$	1.02	1.3°	0.8°	0.743	1.95

Fig. 10). Once the full saturation characteristic is modelled (ξ) the CPSR is closely predicted. As with SYNCHRELs, modelling iron losses increases γ_m while not significantly affecting γ_{mi}.

Unlike SYNCHRELs, the CPSR of SPMs appears to be sensitive to iron losses. The CPSR of the 2kW drive showed a significant change even with adding a small iron loss (R_{cn} = 44pu). Using a more reasonable (full voltage) iron loss resistance of R_{cn} = 15pu gave a 10% reduction in the CPSR compared to that with no iron losses. This effect will be investigated in a later paper. Note that this is still a small reduction compared to what saturation does to the CPSR of SYNCHRELs.

4.2 : Full Characteristics

The torque and power versus speed test results for the 2kW SPM and 120W SYNCHREL are shown in Figs. 11 and 12. Both drives showed operation in Mode I and II. The SYNCHREL reached Mode III operation at about 4100rpm. The effect of using a fixed current angle (ie. no field-weakening) was also measured.

The solid line shows the measured characteristics. With no field-weakening the output torque above knee-speed falls sharply while with field-weakening a CPSR of about 2 is achieved with both drives.

The dash-dot curve shows the calculated characteristic with an unsaturated constant parameter lossless model (ξ_{unsat}, γ_m = 45°). Comparing it with the measured characteristic shows the effect of stator resistance in reducing the voltage and hence power available in the field-weakening region. Note that in SYNCHRELs, saturation can substantially alter both the low speed and field-weakening characteristics, while in SPMs it tends to affect only the field-weakening characteristics.

The dotted curve is the calculated characteristic including saturation and stator resistance ($\xi + R_s$). This yields a better match to the measured characteristics.

Finally the dashed curve shows the effect of including iron loss ($\xi + R_s + R_c$) into the previous model. The small residual difference between this and the measured curve could be due to the iron loss increasing more rapidly with speed than predicted with the simple model, d-q cross-coupling or else windage and friction losses.

5 : CONCLUSIONS

This paper examined the effect of stator resistance, magnetic saturation and iron losses on the field-weakening performance of brushless synchronous AC motor drives. The field-weakening performance can be characterised by the rated output power and the constant power speed range (CPSR).

Saturation dramatically reduces the CPSR of synchronous reluctance motor drives by increasing the internal maximum torque per ampere current angle γ_{mi}. For drives showing heavy saturation, this can reduce the CPSR to half or even a third of that predicted using an unsaturated model.

Stator resistance and iron losses do not have much effect on the CPSR of surface permanent magnet or synchronous reluctance motor drives, however they do reduce the mechanical output power. With moderate values of iron loss, the two synchronous reluctance motor drives showed no significant change in CPSR while the surface permanent magnet motor drive showed a small (10%) reduction.

A full motor drive model incorporating saturation, stator resistance and iron loss was shown to predict accurately the measured field-weakening performance of a 2kW surface permanent magnet motor drive and a 120W synchronous reluctance motor drive.

ACKNOWLEDGEMENTS

The support of the Commonwealth Scholarship Commission in the United Kingdom and the Glasgow University SPEED Consortium is gratefully acknowledged. Thanks to P. Miller and R. Lagerquist for building the inverter/controller for the motors, D. Staton for designing the 120W rotor and J. Kelly for building the 120W and 1kW axially-laminated SYNCHREL rotors.

References

[1] W. L. Soong and T. J. E. Miller, "Theoretical limitations to the field-weakening performance of the five classes of brushless synchronous AC motor drive," in *Electrical Machines and Drives Conference*, Sep. 1993. to be published.

[2] T. Sebastian and G. R. Slemon, "Operating limits of inverter-driven permanent magnet motor drives," *IEEE Trans. Ind. Appl.*, vol. 23, pp. 327–333, Mar/Apr 1987.

[3] R. F. Schiferl and T. A. Lipo, "Power capability of salient pole permanent magnet synchronous motor in variable speed drive applications," *IEEE Trans. Ind. Appl.*, vol. 26, pp. 115–123, Jan/Feb 1990.

[4] S. Morimoto, Y. Takeda, T. Hirasa, and K. Taniguchi, "Expansion of operating limits for permanent magnet motor by current vector control considering inverter capacity," *IEEE Trans. Ind. Appl.*, vol. 26, pp. 866–871, Sep/Oct 1990.

[5] A. K. Adnanes, "Torque analysis of permanent magnet synchronous motors," in *Power Electronics Specialists Conference*, pp. 695–701, 1991.

[6] R. E. Betz, "Control of synchronous reluctance machines," in *Ind. Appl. Society Annual Meeting*, pp. 456–462, Sep. 1991.

[7] B. Sneyers, D. W. Novotny, and T. A. Lipo, "Field-weakening in buried permanent magnet AC motor drives," *IEEE Trans. Ind. Appl.*, vol. 21, pp. 398–407, Mar/Apr 1985.

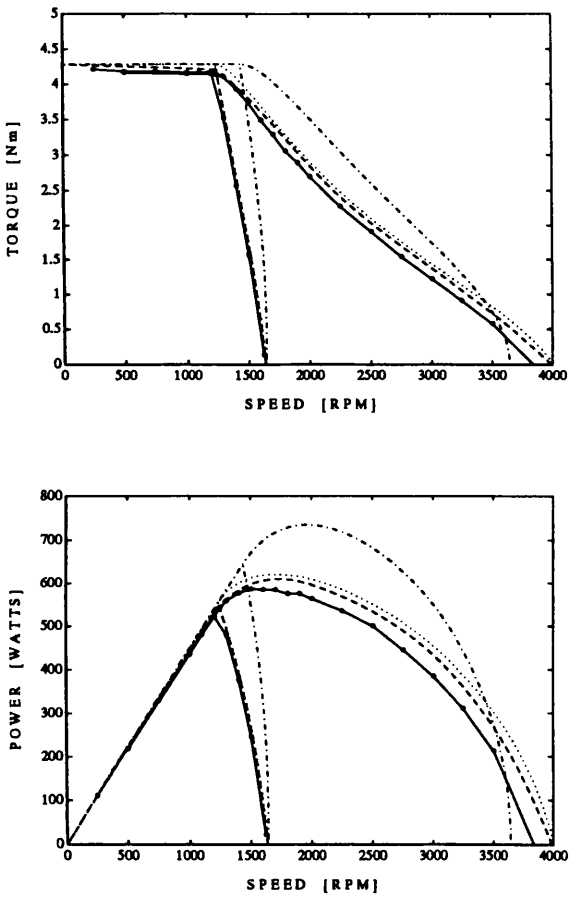

Figure 11: *2kW* SPM *torque and power versus speed results with and without field-weakening when operated at reduced voltage. Measured results (solid line), lossless linear unsaturated model (dash-dot line), model including saturation and stator resistance (dotted line) and full model (dashed line).*

[8] B. C. Mecrow and A. G. Jack, "Operation of highly-rated permanent magnet synchronous machines," in *Electrical Machines and Drives Conference*, pp. 26–30, Sep. 1991.

[9] L. Xu, X. Xu, T. A. Lipo, and D. W. Novotny, "Vector control of a synchronous reluctance motor including saturation and iron loss," *IEEE Trans. Ind. Appl.*, vol. 27, pp. 977–985, Sep/Oct 1991.

[10] R. E. Betz, M. Jovanovic, R. Lagerquist, and T. J. E. Miller, "Aspects of the control of synchronous reluctance machines including saturation and iron losses," in *Ind. Appl. Society Annual Meeting*, pp. 456–463, Oct. 1992.

[11] B. J. Chalmers, "Influence of saturation in brushless permanent-magnet motor drives," *Proc. IEE, Pt. B*, vol. 139, pp. 51–52, Jan. 1992.

[12] W. L. Soong, D. A. Staton, and T. J. E. Miller, "Validation of lumped-circuit and finite-element modelling of axially-laminated motors," in *Electrical Machines and Drives Conference*, Sep. 1993. to be published.

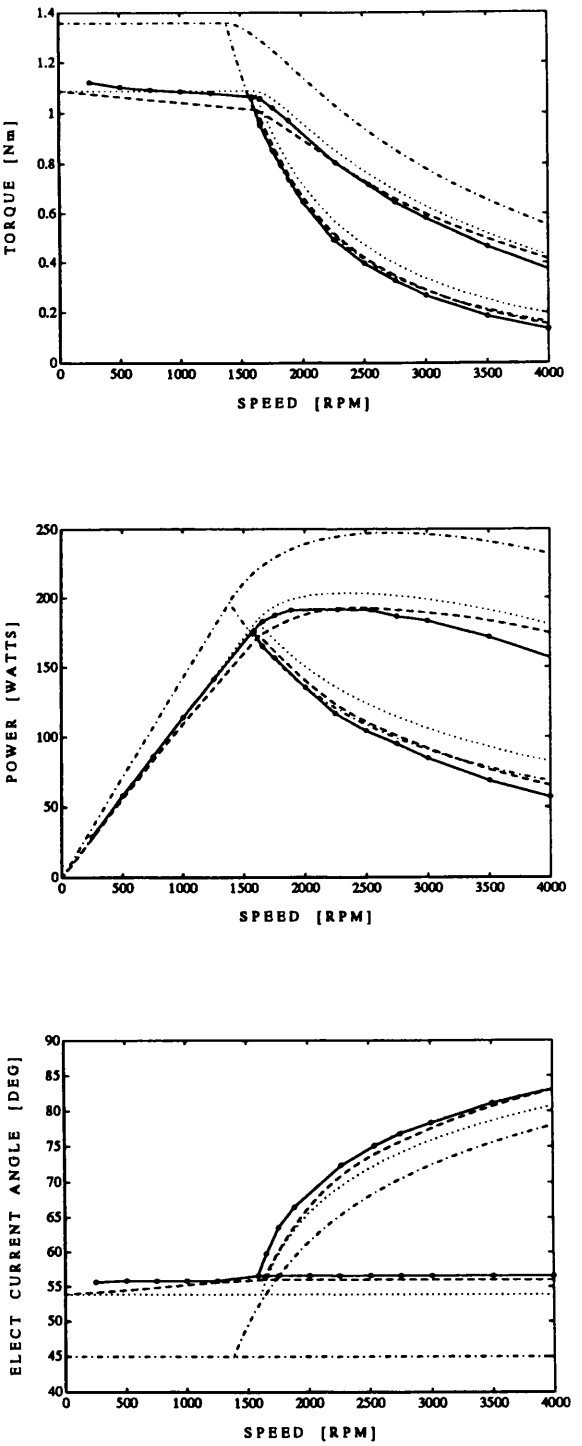

Figure 12: *120W* SYNCHREL *torque, power and current angle versus speed results with and without field-weakening. Measured results (solid line), lossless linear unsaturated model (dash-dot line), model including saturation and stator resistance (dotted line) and full model (dashed line).*

B.3 Modelling Paper

This paper entitled "Validation of Lumped-Circuit and Finite-Element Modelling of Axially-Laminated Brushless Motors" was presented at the Electrical Machines and Drives conference in Oxford in September 1993 (pages 85–90).

VALIDATION OF LUMPED-CIRCUIT AND FINITE-ELEMENT MODELLING OF AXIALLY-LAMINATED BRUSHLESS MOTORS

W L Soong, D A Staton and T J E Miller

SPEED Laboratory, Glasgow University, United Kingdom

ABSTRACT

The aim of this paper is to examine and validate the use of finite-element, analytical and lumped-circuit modelling for calculating the saturation curves and hence the operating characteristics of axially-laminated synchronous reluctance motors. Methods for measuring the saturation curves are also discussed. Comparisons are given with experimental results for a 120W motor.

1 : INTRODUCTION

Recently synchronous reluctance motors have undergone serious consideration for inverter-driven variable-speed applications [1,2]. An axially-laminated form of construction has been shown to be necessary to obtain the high output torque and saliency ratio required to make synchronous reluctance motors competitive with induction motors [1,2,3,4].

Synchronous reluctance motors can be characterised by their d-axis (unaligned) inductance L_d and q-axis (aligned) inductance L_q[1]. The torque per ampere is proportional to $(L_q - L_d)$ while the saliency ratio ($\xi = L_q/L_d$) determines many of the motor's operating characteristics such as field-weakening range, power-factor and sensitivity to parameter variations [5,6].

Finite-element, lumped-circuit and analytical methods have been used by earlier workers [1,7,8] to calculate the variation of L_d and L_q with current and hence predict the motor performance. There has been however no serious attempt to validate the accuracy of these techniques in predicting the actual saturation curves of axially-laminated motors and even less so to test their ability to predict the motor's steady-state characteristics accurately.

The d-axis magnetic path in axially-laminated designs is mostly air and shows little saturation at normal current levels. However in well designed motors the q-axis path shows significant saturation, mostly in the stator teeth. L_d and L_q can be obtained by :

direct measurement : This is clearly the most accurate method. For unsaturated inductances a simple AC reactance test can be used, however to obtain the saturation curve it is necessary to use a flux-linkage technique similar to that used for switched-reluctance motors [9].

PQ circle diagram : This is used for synchronous reluctance motors driven from a constant voltage source such as in high speed spindle drives [10]. The inductances are calculated by observing how the real and reactive components of the input VA alter as the machine's operating point is varied from motoring to generating [11]. It is not directly applicable to current-controlled inverters.

finite-element method : 3-D finite-element analysis should yield accurate results *if* accurate B-H characteristics are used. 2-D finite-element analysis can be used, but the results will need to be corrected for end-winding leakage inductance. The finite-element method is however too time consuming for everyday design.

analytical approximations : This can be used for predicting the unsaturated L_q. It can also be used for estimating L_d but this is more difficult as a significant part of L_d is formed by leakage inductances. It is also not possible to take into account saturation.

lumped-circuit : this method can offer moderate accuracy in predicting the saturated characteristics with a fast calculation period. It is particularly useful for an interactive motor design package.

This paper investigates the accuracy of the parameters obtained using finite-element and lumped-circuit techniques in predicting the operating characteristics of a 120W axially-laminated synchronous reluctance motor. Comparisons are given for torque, voltage and power-factor characteristics.

1.1 : Definition of Inductance

It is an inherent assumption in the use of the DQ equivalent circuit that the machine inductances vary sinusoidally with rotor angle [10].

Fig. 1 shows the test circuit which was used in the finite-element and lumped-circuit calculations, and in the experimental tests. The *actual* phase inductance is defined from V_A and I_A. The *weighted average* phase inductance is defined as 2/3 of the inductance calculated from the total motor flux-linkage (V_T and I_A). Using the definitions of L_d and L_q given in [12] it can be shown that for a machine with sinusoidally varying inductances, the actual and the weighted average techniques both give the same result, and that this is the synchronous inductance. In real machines with non-sinusoidal inductances, the two techniques yield different values and a comparison is given in [13]. In this paper the weighted average technique is used.

2 : THE EQUIVALENT CIRCUIT

Fig. 2 shows the steady-state equivalent circuit for a synchronous reluctance motor.

[1] This is opposite to the usual convention for synchronous reluctance motors, but is consistent with that used for modelling interior permanent magnet motors [5].

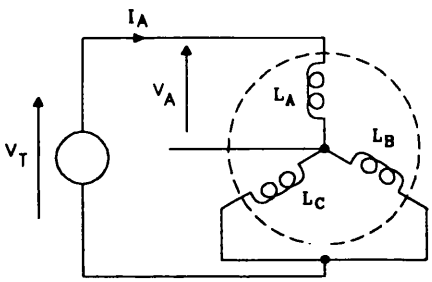

Figure 1: *Test circuit for measurement and calculation of the synchronous phase inductance.*

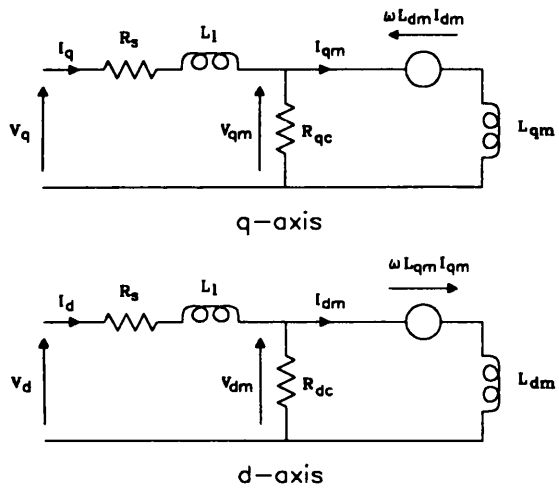

Figure 2: *Steady-state equivalent circuit for the synchronous reluctance motor [14].*

The saliency ratio is given by $\xi = L_q/L_d$ where $L_q = L_{qm} + L_l$ is the q-axis inductance and $L_d = L_{dm} + L_l$ is the d-axis inductance. L_l is the stator leakage inductance and L_{dm} and L_{qm} are the magnetising inductances. L_l consists of the stator slot-leakage and end-winding inductances.

This of course assumes that there is no cross-coupling between the axes. Cross-coupling is important in motors with a low saliency (ie. $\xi \leq 4$) as shown by Sneyers [15] and Mecrow [16] for interior permanent magnet motors. However cross-coupling is generally not significant in axially-laminated designs due to the high saliency ratios (6–10) and hence will be neglected in the remainder of this paper.

R_{qc} and R_{dc} represent the core loss resistances and are normally assumed to be equal [14].

3 : ANALYTICAL CALCULATIONS

3.1 : Q-Axis Inductance

In general $L_{qm} \gg L_l$, hence $L_q \approx L_{qm}$. The magnetising inductance L_m of a round rotor machine is [17] :

$$L_m = \frac{3\pi\mu_o N_s^2 l r_1}{8p^2 g''} \tag{1}$$

where N_s is the number of equivalent sine-distributed turns, l is the stack-length, r_1 is the airgap radius, p is the number of pole-pairs and g'' is the mechanical airgap extended by Carter's coefficient to take into account the rotor and stator slotting.

For a machine with a pole-arc of α electrical radians this gives [18] :

$$L_{qm} = \frac{\alpha + \sin\alpha}{\pi} L_m \tag{2}$$

3.2 : D-Axis Inductance

Various formulas have been proposed in the literature for estimating the d-axis magnetising inductance.

One technique is to use Eqn. 1 with a large airgap. Miller [19] roughly approximates the effective airgap for a four-pole machine as $(ar_1 + g)$. This gives a saliency ratio :

$$\xi = \frac{ar_1}{g} + 1 \tag{3}$$

where a is the ratio of insulation thickness w_{ins} to the sum of the insulation and lamination thicknesses $(w_{ins} + w_{lam})$.

Boldea [2] approximates the airgap permeance as a function of angular position and Vagati [21] performs a lumped-circuit analysis. They both show that :

$$\xi \propto \frac{r_1}{pg} \tag{4}$$

Platt [8] derives an approximate analytical solution as :

$$L_{dm} = \frac{3\pi^3(p-1)\mu_o N_s^2 l r_1}{64p^2 a r_1 + 8\pi^2 p^2 (p-1)g} \tag{5}$$

The technique proposed here is to consider the inductance of a cylindrical stator with a sine-distributed airgap winding and an ideal non-magnetic rotor. The magnetic field distribution for this situation is derived in [22]. From this it can be shown that the inductance is :

$$L_{dmi} = \frac{3\pi\mu_o N_s^2 l}{8p} \tag{6}$$

which is independent of the rotor diameter. This is similar to Eqn. 5 as $ar_1 \gg (p-1)g$.

Now if a large number of thin laminations separated by layers of insulation are placed in the rotor in such a way that the layers are always perpendicular to the flux lines, then the field distribution would be unchanged [19]. This would cause the inductance to increase to :

$$L_{dma} = \frac{3\pi\mu_o N_s^2 l}{8pa} \tag{7}$$

The *intrinsic* saliency ratio, ξ_i is the maximum possible saliency ratio for a given motor geometry and from Eqns. 1 and 6 is defined as :

$$\xi_i \triangleq \frac{L_m}{L_{dmi}} = \frac{r_1}{pg} \tag{8}$$

	#1	#2	#3	#4	#5
P_{out} [kW]	0.12	1.0	7.5	0.55	1.5
Poles	4	4	4	2	2
L_{stack} [mm]	32	76	202	60	80
D_{rotor} [mm]	57	59	127	60	80
Airgap [mm]	0.26	0.21	0.50	0.25	0.30
w_{lam} [mm]	0.30	0.30	0.50	0.50	0.50
w_{ins} [mm]	0.30	0.30	0.50	0.30	0.30
a	0.50	0.50	0.50	0.38	0.38
ξ_i	55	70	64	120	133
ξ_{mi}	27	35	32	45	50
ξ_{act}	7.4	8.2	13*	8.5	21
ξ_{act}/ξ_{mi}	0.27	0.23	0.41*	0.19	0.42
Reference	built by authors			[20,24]	

Table 1: *Performance of various axially-laminated designs. (* finite-element calculation)*

similarly the *intrinsic magnetising* saliency ratio ξ_{mi} is defined as :

$$\xi_{mi} \triangleq \frac{L_m}{L_{dma}} = \frac{ar_1}{pg} \tag{9}$$

This is a similar result to that obtained by other authors (Eqns. 3 and 4). It sets an upper limit to the saliency ratio achievable with a given motor geometry.

The *actual magnetising* saliency ratio, defined as $\xi_m \triangleq L_{qm}/L_{dm}$ is lower than ξ_{mi} due to the finite rotor pole arc, the extension of the effective airgap due to rotor and stator slotting, and the distortion of the d-axis field distribution due to the rotor laminations.

The measured unsaturated saliency ratio ξ_{act}, is lower again due to the swamping effect of the stator leakage inductance. This consists of the slot-leakage and end-winding inductances and can be estimated using the same techniques as for induction machines [23].

Table 1 shows the parameters of five axially-laminated synchronous reluctance motors. It shows that the measured unsaturated saliency ratio is generally in the range $0.2\xi_{mi} < \xi < 0.4\xi_{mi}$.

4 : FINITE-ELEMENT ANALYSIS

A four pole, 120W axially-laminated motor (design #1 in Table 1) was modelled. This uses a standard 24 slot induction motor stator with a single-layer, equi-turn consequent pole, concentric winding. Due to the symmetry in the motor only an eighth of it was modelled (see Fig. 3). Each rotor pole consists of 26 laminations and 25 insulation layers and is clamped to the square section shaft by a brass pole-piece and three non-magnetic stainless-steel bolts. Grain-oriented material was used for its good magnetic properties and low iron losses.

2-D finite-element analysis with a correction factor for end-winding inductance (see Table 2) was used. Care is required in modelling axially-laminated rotors due to the fine structure at the rotor surface. A large number of nodes is required in this region in order to calculate accurately the unsaturated q-axis inductance. At high currents, saturation of the iron paths mean that the modelling of the airgap region is less critical.

Finite-element results concerning the effect of replacing the rotor or stator steel with "ideal" material are shown in Fig. 4. From the small change in the results when using real or ideal rotor steel it is clear that the majority of the saturation in the motor occurs in the stator. This is because of the use of grain-oriented steel in the rotor and also due to the greater iron cross-sectional area in the rotor compared to the stator teeth. The latter point is partly offset by the area of the rotor laminations taken up by the bolts.

5 : LUMPED-CIRCUIT ANALYSIS

A general purpose non-linear lumped-circuit solver was written using Matlab [25]. The q-axis case for the 120W motor was analysed using a simple three mesh circuit and assuming the rotor was infinitely permeable (see Fig. 3).

The airgap reluctances R_G were calculated using the extended airgap to take into account rotor and stator slotting. The tooth reluctances R_T were taken to be only that of the straight section of the tooth. Finally the back-iron reluctances R_B consisted of a width given by the minimum back-iron depth plus one third of the slot bottom fillet radius and a length equal to the slot pitch

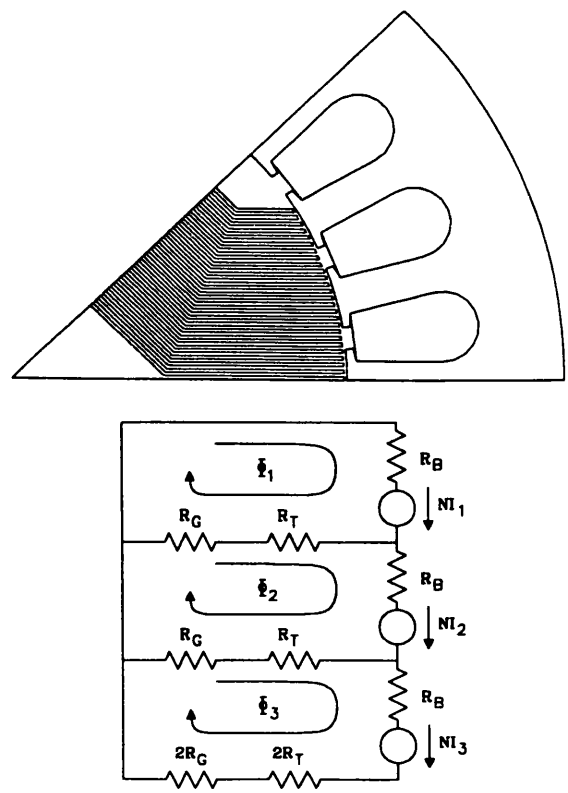

Figure 3: *120W rotor cross-section and lumped-circuit model (q-axis case).*

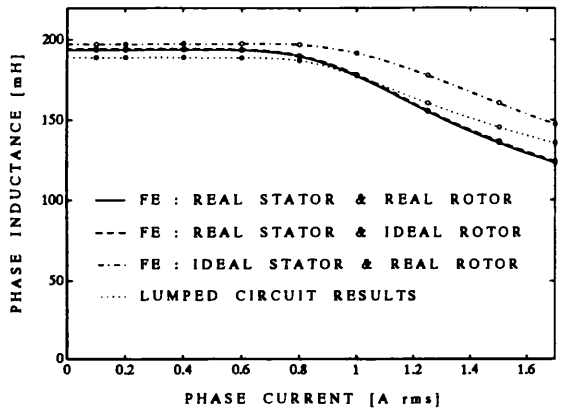

Figure 4: *Effect of using ideal stator and rotor steel.*

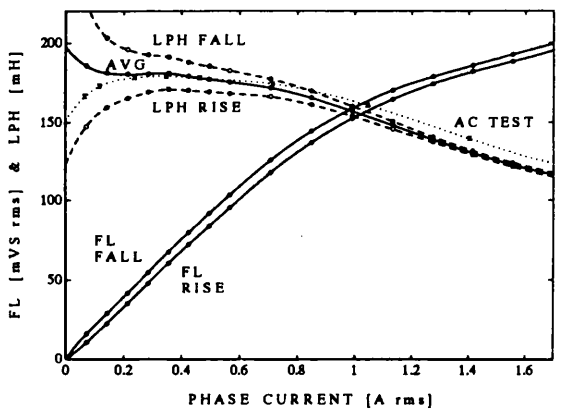

Figure 5: *Experimental results from AC and flux-linkage tests.*

measured midway in the thinnest section of the back-iron.

Fig. 4 shows the curve calculated with cubic spline interpolated iron characteristics. Given the simplicity of the calculations, the results show a reasonable match with the finite-element results.

6 : MEASURED RESULTS AND DISCUSSION

6.1 : Measurement of Saturation Curves

The simplest method is to apply a variable-voltage 50Hz AC supply to the motor as shown in Fig. 1 and use an AC power analyser to measured the input *reactance* and hence inductance of the motor (see dotted line in Fig. 5). It gives accurate results for the unsaturated inductance but overestimates the saturated values due to its "averaging" nature. The error due to iron loss under AC excitation (see Fig. 2) is usually less than 1%. If desired this can be corrected using the measured AC input resistance which due to the iron losses will be substantially greater than the DC resistance.

The flux-linkage method is a more accurate means for

Inductance mH	Actual	Fin. Elmt	Lump Cct.	Analytical
L_{dmi}	—	4.82	—	4.85
$L_{dmi} + L_{slot}$	—	9.2	—	9.8
$L_{dmi} + L_{slot} + L_{end}$	16.0	—	—	—
L_{end} (from above)	—	6.8	—	6.2
L_d	24.4	24.3*	—	20.9*
L_q (unsat)	181	200*	195*	197*

Table 2: *Comparison of unsaturated inductances. The * indicates the values have been corrected for the endwinding inductance.*

obtaining the saturation characteristics as it gives the instantaneous flux-linkage versus current characteristic [9]. The test involves calculating the flux-linkage :

$$\lambda(t) = \int [v(t) - i(t)R]\, dt \qquad (10)$$

as an applied square-wave voltage input ramps the current up from zero to some maximum value and then ramps it down to zero again. The flux-linkage versus current characteristic and the calculated inductance $L(t) = \lambda(t)/i(t)$ obtained are shown in Fig. 5. Iron losses mean that the rising and falling flux-linkage curves form a "hysteresis" loop and it is necessary to average the two curves to obtain accurate results. The resultant inductance characteristic (marked "AVG" in Fig. 5) corresponds well with the unsaturated inductance calculated with the AC test.

At low currents the inductance falls due to the low permeability of the stator and rotor iron at low flux levels. This is shown by the AC test results. The errors in the inductance calculated from the flux-linkage method are large at low currents and hence these points are omitted from the curve used in the calculations shown in Fig. 6.

Table 2 compares the measured unsaturated inductances with that calculated using finite-element, analytical and lumped-circuit techniques. Finite-element analysis using a smooth stator and sine-distributed airgap winding was used to obtain a value for L_{dmi}. This corresponded well with the analytical prediction. Next a slotted stator and the actual winding was modelled to introduce slot-leakage L_{slot}. The difference between these values and that measured for the stator without a rotor is mainly due to end-winding inductance L_{end} which is relatively large in this motor due to the short stack length. The measured d-axis inductance with the rotor inserted corresponds well to the value from finite-element analysis which has been corrected for the end-winding inductance. The analytical prediction is about 14% low which is reasonable considering its simplicity.

Table 2 and Fig. 6 compare the calculated and measured L_q saturation curves. The finite-element, analytical and lumped-circuit results are consistent but they significantly overestimate the measured inductance (by about 10%).

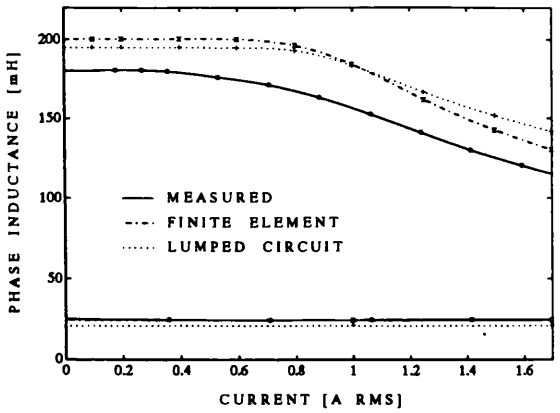

Figure 6: *Inductances versus current (corrected for endwinding inductance).*

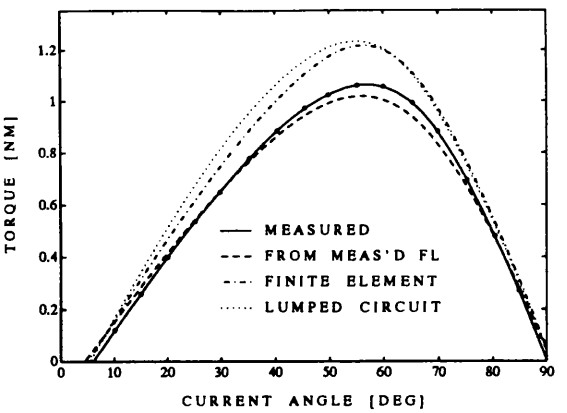

Figure 7: *Torque versus current angle.*

6.2 : Comparison of Predicted Characteristics

Figs. 7–9 shows comparisons between the calculated and measured characteristics for the 120W axially-laminated motor at rated speed (1500 rpm) and rated phase current (1.7A).

The calculated curves were obtained by solving the equivalent circuit shown in Fig. 2 taking into account the nonlinear saturation characteristics (see Fig. 6) with the approximations that the two iron loss resistances are equal and of constant value and with the leakage inductance combined into the magnetising inductances. The iron loss resistance was calculated at $\gamma = 0°$ from the experimental measurements.

The measured flux-linkage curves accurately predict the motor's torque, voltage, and power-factor characteristics. Note how iron losses reduce the output torque at low current angles, but do not significantly affect the torque at high current angles.

The finite-element and lumped-circuit results overestimate L_q and hence the torque and fundamental phase voltage. The power-factor appear to be relatively insensitive to errors in L_q. The maximum efficiency for motors of this size is low due to the high stator copper losses.

Table 3 compares the manufacturer's ratings for the induction motor against the measured performance of the synchronous reluctance motor. It shows a significant improvement in performance. Though the synchronous reluctance motor does use a smaller airgap, finite-element analysis has shown that the performance is not substantially affected with the larger airgap because at rated current most of the saturation occurs in the stator.

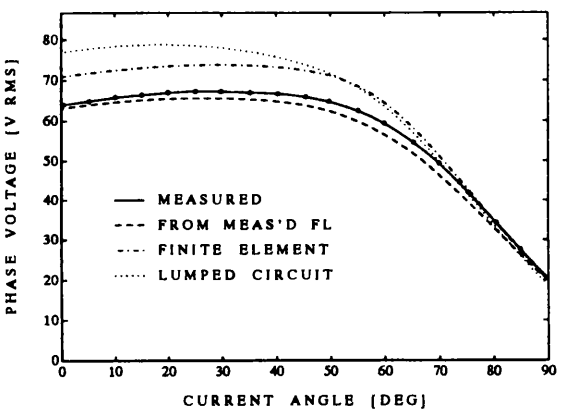

Figure 8: *Fundamental phase voltage versus current angle.*

7 : CONCLUSIONS

The intrinsic magnetising saliency ratio $\xi_{mi} = ar_1/pg$, is the maximum saliency ratio theoretically possible with a given motor geometry. Practical motors generally achieve unsaturated saliency ratios of between 20–40% of the this, depending on their design.

The performance of the 120W axially-laminated motor

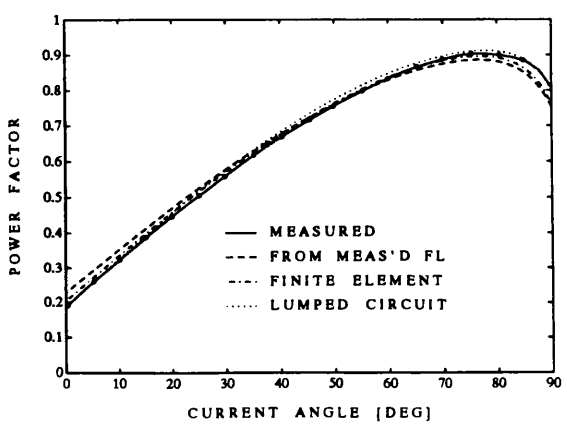

Figure 9: *Power-factor versus current angle.*

Parameter	IM	Synchrel
Mean Airgap (mm)	0.305	0.265
Rated Line Voltage (Vrms)	110	110
Rated Phase Current (Arms)	1.7	1.7
Rated Speed (rpm)	1360	1580
Output Torque (Nm)	0.84	1.07
Power Output (W)	120	165
Efficiency (%)	61	66
Power Factor	0.62	0.82
Apparent Efficiency	0.38	0.54

Table 3: *Comparison between the induction motor and* SYNCHREL *in the same stator.*

considered is limited by saturation in the stator. Hence simple lumped-circuit models which only model stator saturation allow rapid calculation of the machine's saturation characteristics with reasonable accuracy.

Analytical, lumped-circuit and finite-element methods gave consistent predictions of the motor's saturation characteristics.

Experimental measurement of the saturation characteristics can be obtained from AC reactance or flux-linkage tests. The latter gives a more accurate result. The measured saturation characteristics have been shown to predict the motor's performance accurately.

The 10% discrepancy between the calculated and measured saturation characteristics is significant but has not been explained. This will be investigated in a later paper.

ACKNOWLEDGEMENTS

The support of the Commonwealth Scholarship Commission and the Glasgow University SPEED Consortium is gratefully acknowledged. Thanks to P. Miller and R. Lagerquist for building the inverter/controller and to J. Kelly for building the rotor.

References

[1] T. A. Lipo, A. Vagati, L. Malesani, and T. Fukao, eds., *Synchronous Reluctance Machines - A Viable Alternative for AC Drives*, Ind. Appl. Society Annual Meeting Tutorial, Oct. 1992.

[2] I. Boldea and S. Nasar, "Emerging electric machines with axially laminated anisotropic rotors : a review," *Electrical Machines and Power Systems*, vol. 19, pp. 673–704, 1991.

[3] A. Fratta and A. Vagati, "Synchronous reluctance vs induction motor : a comparison," in *Intelligent Motion Conference Proceedings*, pp. 179–186, Apr. 1992.

[4] D. A. Staton, T. J. E. Miller, and S. E. Wood, "Optimisation of the synchronous reluctance motor," in *Electrical Machines and Drives Conference*, pp. 156–160, Sep. 1991.

[5] W. L. Soong and T. J. E. Miller, "Theoretical limitations to the field-weakening performance of the five classes of brushless synchronous AC motor drive," in *Electrical Machines and Drives Conference*, Sep. 1993. to be published.

[6] R. E. Betz, "Control of synchronous reluctance machines," in *Ind. Appl. Society Annual Meeting*, pp. 456–462, Sep. 1991.

[7] A. Fratta and A. Vagati, "Axially-laminated reluctance motor : an analytical approach to the magnetic behaviour," in *Int. Conf. Electric Machines*, pp. 1–6, 1988.

[8] D. Platt, "Reluctance motor with strong rotor anisotropy," *IEEE Trans. Ind. Appl.*, vol. 28, pp. 652–658, May/June 1992.

[9] C. Cossar and T. J. E. Miller, "Electromagnetic testing of switched reluctance motor," in *Int. Conf. Electric Machines*, pp. 470–474, Sep. 1992.

[10] A. Chiba, F. Nakamura, and T. Fukao, "Inductances of cageless reluctance-synchronous machines having nonsinusoidal space distributions," in *Ind. Appl. Society Annual Meeting*, pp. 314–319, 1989.

[11] A. A. Fock and P. M. Hart, "New method for measuring Xd and Xq based on the P–Q diagram," *Proc. IEE, Pt. B*, vol. 131, pp. 259–262, 1984.

[12] A. E. Fitzgerald and C. K. Kingsley, *Electric Machinery*. McGraw Hill, second ed., 1961.

[13] D. A. Staton, W. L. Soong, C. Cossar, and T. J. E. Miller, "Unified theory of torque production in switched and synchronous reluctance motors," in *Ind. Appl. Society Annual Meeting*, Oct. 1993. abstract submitted.

[14] R. E. Betz, M. Jovanovic, R. Lagerquist, and T. J. E. Miller, "Aspects of the control of synchronous reluctance machines including saturation and iron losses," in *Ind. Appl. Society Annual Meeting*, pp. 456–463, Oct. 1992.

[15] B. Sneyers, D. W. Novotny, and T. A. Lipo, "Field-weakening in buried permanent magnet AC motor drives," *IEEE Trans. Ind. Appl.*, vol. 21, pp. 398–407, Mar./Apr. 1985.

[16] B. C. Mecrow and A. G. Jack, "Operation of highly-rated permanent magnet synchronous machines," in *Electrical Machines and Drives Conference*, pp. 26–30, Sep. 1991.

[17] T. J. E. Miller, *Brushless Permanent Magnet and Reluctance Motor Drives*. Oxford University Press, 1989.

[18] P. J. Lawrenson and L. A. Agu, "Theory and performance of polyphase reluctance machines," *Proc. IEE, Pt. B*, vol. 111, pp. 1435–1445, Aug. 1964.

[19] T. J. E. Miller, A. Hutton, C. Cossar, and D. A. Staton, "Design of a synchronous reluctance motor drive," *IEEE Trans. Ind. Appl.*, vol. 27, pp. 741–749, July/Aug. 1991.

[20] I. Boldea, Z. X. Fu, and S. A. Nasar, "Performance evaluation of axially-laminated (ALA) rotor reluctance synchronous motors," in *Ind. Appl. Society Annual Meeting*, pp. 212–218, Oct. 1992.

[21] A. Vagati, G. Franceschini, I. Marongiu, and G. P. Troglia, "Design criteria of high performance synchronous reluctance motors," in *Ind. Appl. Society Annual Meeting*, pp. 66–73, Oct. 1992.

[22] A. Hughes and T. J. E. Miller, "Analysis of fields and inductances in air-cored and iron-cored synchronous machines," *Proc. IEE, Pt. B*, vol. 124, pp. 121–126, Feb. 1977.

[23] P. L. Alger, *Induction Machines*. Gordon and Breach, 1970.

[24] I. Boldea, N. Muntean, S. Deaconu, S. A. Nasar, and Z. Fu, "Distributed anisotropy rotor synchronous (DARSYN) drives - motor indentification and performance," in *Int. Conf. Electric Machines*, pp. 542–546, 1992.

[25] *Matlab User's Guide*. The MathWorks Inc., Jan. 1990.

B.4 Design and Test Paper

This paper entitled "Design of a New Axially-Laminated Interior Permanent Magnet Motor" was presented at the IEEE Industry Applications Society Annual Meeting in Toronto in October 1993 (volume 1, pages 27–36). It won the Electrical Machines Committee first paper prize.

Design of a New Axially-Laminated Interior Permanent Magnet Motor

W L Soong, D A Staton and T J E Miller

SPEED Laboratory, Glasgow University, United Kingdom

Abstract — The design of an axially-laminated interior permanent magnet motor drive showing a constant power speed range exceeding 7.5:1 is described. The rotor consists of alternating layers of laminations and rubber-bonded ferrite magnet sheet. A 7.5kW synchronous reluctance and a 7.5kW interior permanent magnet axially-laminated motor were built and experimental results are presented showing the enhanced field-weakening range.

I. Introduction

Applications such as machine tools and traction require motor drives with a wide constant power speed range (>4:1). Presently vector-controlled induction motors are widely used. This paper examines an alternative drive based on an axially-laminated interior permanent magnet motor. This offers a wider field-weakening range, better inverter utilisation, simpler control due to its synchronous nature and higher efficiency due to the elimination of rotor copper losses.

An earlier paper [1] investigated the field-weakening performance of the three main types of brushless synchronous AC motor drive : the surface permanent magnet, the synchronous reluctance and the interior permanent magnet motor drive (see Fig. 1).

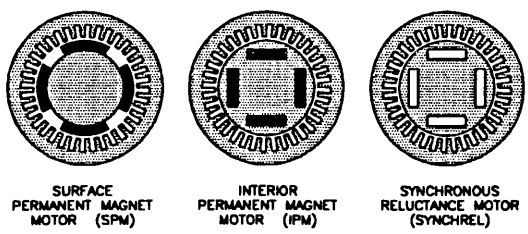

Figure 1: *Motor cross-sections.*

This showed that for all three drives there is a fundamental tradeoff between the field-weakening and the low speed performance. The "optimum" field-weakening characteristic cannot match that produced by an ideal motor drive but can approach it. This "optimal" characteristic can be achieved theoretically by :

- synchronous reluctance motors with an infinite saliency ratio,
- surface permanent magnet motors with an unusually high value of synchronous inductance or ...
- interior permanent magnet motors where the fundamental flux along the magnet axis can be reduced to zero by rated stator current in that axis.

Of the three options, the first is impossible, the second is possible but generally requires the addition of external inductors [2], leaving only the latter option as being practical.

Sneyers, Maggetto and Van Eck [3] and Jahns [4] first recognised the suitability of the interior permanent magnet motor for field-weakening applications.

Schiferl and Lipo [5] showed that the "optimal" field-weakening performance was achieved when the permanent magnet flux Ψ_m, the least inductive axis inductance L_d and the rated current I_o were related by :

$$\Psi_m = L_d I_o \tag{1}$$

Fratta, Vagati and Villata [6] showed that improving the saliency ratio $\xi = L_q/L_d$ of an interior permanent magnet motor would reduce L_d and hence the required Ψ_m. This would reduce the magnet requirements, the induced voltage at high speeds and the required demagnetising current under light loads at high speeds. They designed and built a multiple-barrier (radially-laminated) design based on ferrite magnets.

Lipo [7] suggested that an axially-laminated interior permanent magnet motor could be constructed by sandwiching bar magnets between the laminations. The new design uses this idea with rubber-bonded magnet sheet.

The highest saliency ratio synchronous reluctance motors are obtained with axially-laminated designs [8] which can offer practical saliency ratios in the range 6–20 [9]. In axially-laminated motors the magnet requirement is low enough to allow the use of rubber-bonded ferrite magnets. This is a flexible, isotropic, low-cost material available in thin sheets (0.4–1mm) and is normally used in applications such as magnetic "L" plates for cars and refrigerator door seals. In the motor design, the flexibility is important as the magnets are sandwiched between magnetic laminations which have sharp bends in a four pole motor. Compared to sintered ferrite magnets (let alone rare-earth magnets) its magnetic properties are poor, but prove to be all that it required for this application.

Axially-laminated interior permanent magnet motors designed for good field-weakening performance are predominantly reluctance machines. Thus this paper first examines the optimisation of the performance of the axially-laminated synchronous reluctance motor drive. The design of the interior permanent magnet version is similar except some compromises in the reluctance performance are necessary to ensure good back-emf waveforms and suitable demagnetisation limits. A 7.5kW synchronous reluctance motor and a 7.5kW interior

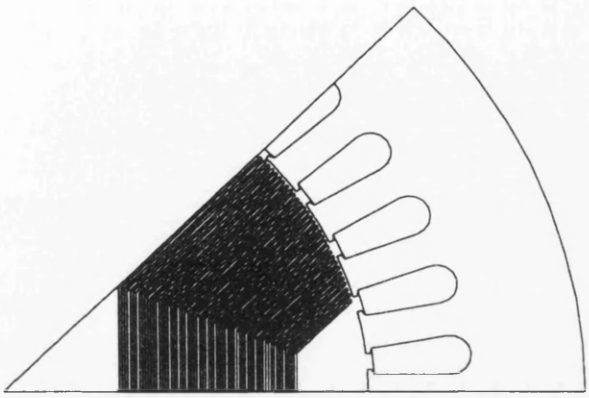

Figure 2: *Cross-section of 7.5kW synchronous reluctance and interior permanent magnet motor.*

permanent magnet motor were built and experimental results are presented.

II. Synchronous Reluctance Motor Design

A commerical induction motor stator was used in this design to allow a direct comparison with the induction motor performance. An induction motor based on this stator is actually capable of 11kW at rated speed, but is derated to 7.5kW for a 10:1 constant torque speed range with a shaft-mounted fan.

A cross-section of the stator is shown in Fig. 2. Each pole consists of thin interleaved layers of insulation and lamination material, topped with a metal pole-piece. It is bolted onto the square cross-section shaft with six non-magnetic, stainless steel bolts (Fig. 3). The rotor is assembled (Fig. 4) and then turned and ground down to the required diameter. The finished rotor is shown in Fig. 5. The photographs show the synchronous reluctance rotor however the interior permanent magnet rotor is nearly identical.

The saliency ratio ξ is an important performance parameter of synchronous reluctance motors, with the performance improving monotonically with increasing saliency ratio. It has been shown by Betz [10], that this determines the machine's power-factor, sensitivity to parameter variations and field-weakening performance. In particular, the ideal constant power speed range is approximately half the saliency ratio. Thus to achieve a 4:1 constant power speed range, a saliency ratio of about 8 is theoretically required.

A useful design equation for axially-laminated synchronous reluctance motors is that for the maximum possible saliency ratio (ξ_{mi}) [9] for a given geometry :

$$\xi_{mi} = \frac{ar_1}{pg} \tag{2}$$

where a is the ratio of the insulation thickness to the lamination plus insulation thickness, r_1 is the airgap radius, p is the number of pole-pairs and g is the radial airgap. For the 7.5kW induction motor stator with a 0.5mm airgap, $\xi_{mi} = 32$.

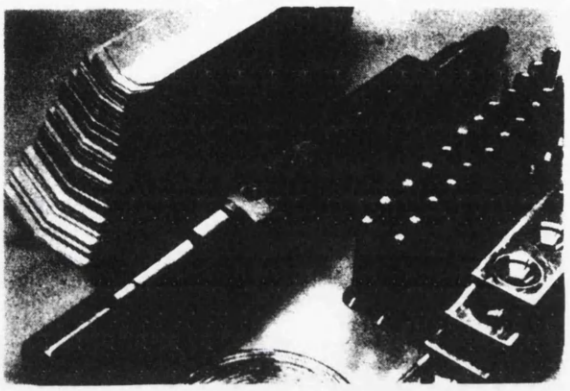

Figure 3: *7.5kW rotor components before assembly.*

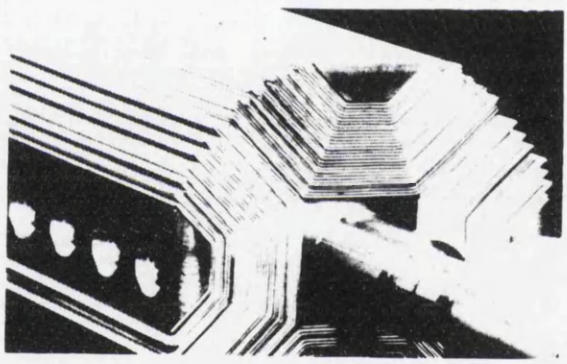

Figure 4: *Assembled 7.5kW axially-laminated rotor before turning and grinding operations.*

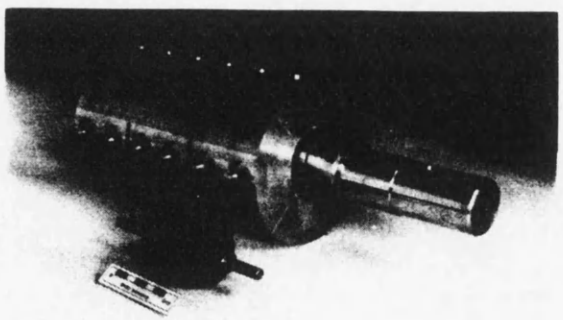

Figure 5: *Experimental 7.5kW axially-laminated motor with 50W prototype version shown for comparison. The scale in front is 5cm long.*

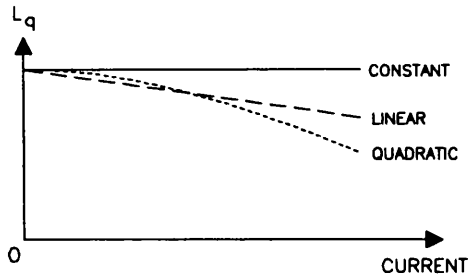

Figure 6: *Three saturation models.*

The actual saliency ratio is considerably lower than this due to practical factors such as Carter's coefficient, the finite pole-arc and stator leakage inductance. The measured unsaturated saliency ratio ξ is generally in the range $0.2\xi_{mi} < \xi < 0.4\xi_{mi}$ [9]. For the 7.5kW synchronous reluctance motor, this range corresponds to $6.4 < \xi < 12.8$ which matches well with the measured unsaturated saliency ratio of 11.5.

The actual constant power speed range is generally much lower than that predicted by $\xi/2$. This was investigated in depth in [11] and it was found that it is mostly due to magnetic saturation. To a first approximation it was found that iron losses and stator resistance have little effect on the constant power speed range, though they do reduce the output power capability.

Saturation has two effects : it reduces the saturated saliency ratio, and it increases the current angle at which maximum torque is obtained (γ_m) beyond the ideal value of 45°. In order to calculate the effect of saturation, it is necessary to make some assumptions about the shape of the saturation characteristic. Fig. 6 shows three simple saturation models.

Fig. 7 shows a contour plot of the constant power speed range against γ_m and the saturated saliency ratio for the three saturation models [11]. Practical designs generally have values of γ_m in the range 55°–65° and hence saturation can dramatically reduce the achievable constant power speed range. For the 7.5kW design, the saturated saliency ratio was 9.6 and the maximum torque per ampere angle was 60°. Thus the ideal constant power speed range was $\xi/2 = 4.8$, but the measured value was only 2.5. This corresponds well with that predicted by Fig. 7.

The major design decisions for an axially-laminated synchronous reluctance motor are : pole number, pole-piece material, airgap size and lamination to barrier ratio.

A. Pole Number

Most axially-laminated designs are four pole, though two pole [12] and six pole [13] designs have built. The two pole designs offer the highest saliency (21 has been achieved) and the simplest rotor design (no bending required). The main drawback is that there is no room for a shaft to run through the rotor. In [12] this was overcome for two small motors (0.55kW and 1.5kW) by glueing endplates to the rotor stack. This is

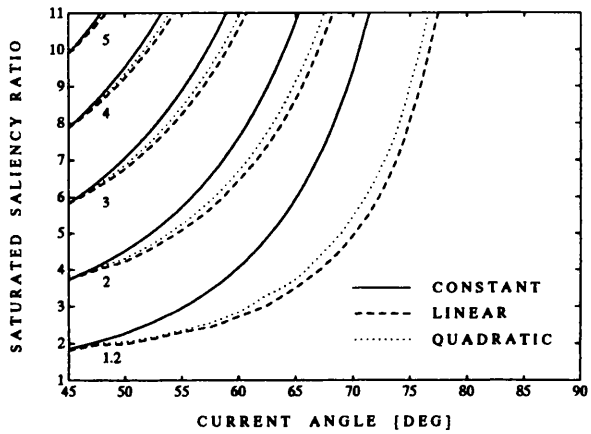

Figure 7: *Contour plot of the constant power speed range against the maximum torque per ampere current angle and the saturated saliency ratio for the three saturation models.*

however impractical for larger motors.

A four pole design allows the shaft to run through the rotor and is commonly used [7, 8]. Six pole designs can be built but are more complex and have a poorer saliency ratio (from (2), theoretically two thirds of that for the four pole design). However the incremental performance improvement with increasing saliency ratio diminishes rapidly once $\xi > 8$ [10]. Thus in large motors, with correspondingly large values of ξ_{mi}, six or eight pole designs may yield better performance because the shorter flux paths and reduced back-iron thickness reduces the saturation, offsetting the reduced saliency ratio.

As mentioned above, the four pole 7.5kW synchronous reluctance design with a 0.5mm airgap had an unsaturated saliency of 11.5. A six pole 7.5kW motor design would thus yield too low a saliency ratio for good performance.

B. Pole-Piece Material and Bolts

The final design used non-magnetic pole-pieces and required six 10mm diameter bolts per pole to give it a maximum safe operating speed of 3000rpm. The bolt holes locally reduce the effective rotor magnetic cross-section by 30% and this degrades the saturation characteristic. Fig. 8 and Table 1 shows the effect of using magnetic pole-pieces and of removing the bolts.

Magnetic pole-pieces increase the output torque by 9%, decrease the saliency ratio by 15% and reduce the constant power speed range by 2.5%.

From the performance of the motor with no bolts, it can be seen that their use reduces the output torque by 14% and the constant power speed range (CPSR) by 40%. Note that L_d is unaffected and that the saturated saliency ratio is similar to the final design due to the lower γ_m. This highlights the sensitivity of the constant power speed range to γ_m.

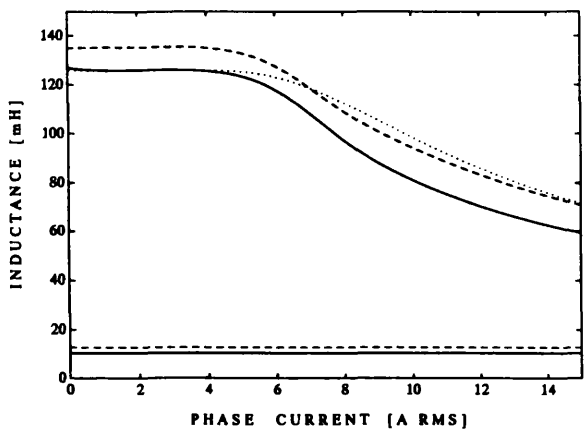

Figure 8: *Calculated inductance characteristics for the 7.5kW synchronous reluctance motor. The final design (solid line), with magnetic pole-pieces (dashed line) and with no bolts (dotted line).*

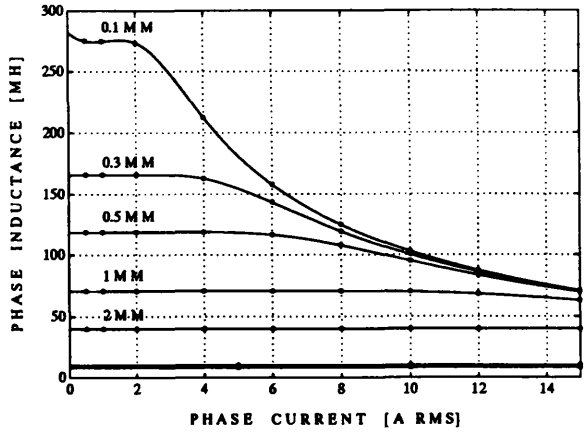

Figure 9: *Calculated flux-linkage characteristics for a 7.5kW synchronous reluctance motor with different airgaps.*

Table 1: *Calculated performance of the final design compared with that obtained with magnetic pole-pieces and no bolts.*

Property	Final Design	Mag. Polepieces	No Bolts
Torque [Nm]	54.6	59.2	62.3
ξ (unsat)	12.3	10.7	12.2
ξ (sat)	10.7	9.2	10.8
CPSR	2.44	2.38	3.43
γ_m	62.9°	61.2°	56.6°

C. Airgap Size

Fig. 9 shows the calculated flux-linkage characteristics for the 7.5kW synchronous reluctance motor with a range of airgaps. The operating characteristics of the designs were calculated from these and the normalised results are shown in Fig. 10 as a function of the *inverse airgap* ($1/g$). The unsaturated saliency ratio (UNSAT) and the saturated saliency ratio (SAT) are normalised against the saturated saliency ratio at the nominal airgap (0.5mm). The torque and constant power speed range are also normalised against their respective values at this value of airgap. The inverter utilisation κ (KAPPA) is the ratio of the rated output power of the motor to the inverter VA rating [11].

Starting from $1/g = 0.5\text{mm}^{-1}$, all the characteristics improve with increasing $1/g$. Note that as $1/g$ approaches infinity, all the parameters except the unsaturated saliency ratio asymptote towards constant values. Thus, decreasing the airgap past a certain point will not yield significant improvement in performance.

The constant power speed range differs from the other characteristics in that it peaks between $0.5 < g < 2$mm. This is

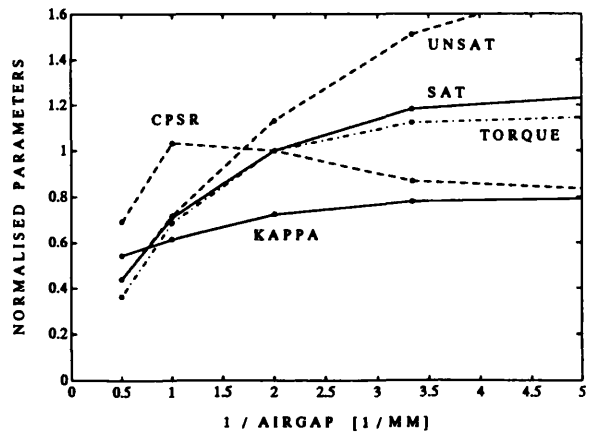

Figure 10: *Effect of airgap size on the calculated performance characteristics for a 7.5kW synchronous reluctance motor.*

associated with the increase of both the saturated saliency ratio and the maximum torque per ampere current angle with decreasing airgap size.

D. Lamination to Barrier Ratio

This is measured by the parameter a, which is the ratio of the insulation thickness to the combined insulation and lamination thickness. We have generally used $a = 0.5$ in our designs however Boldea [14] recommends using values in the range 0.33–

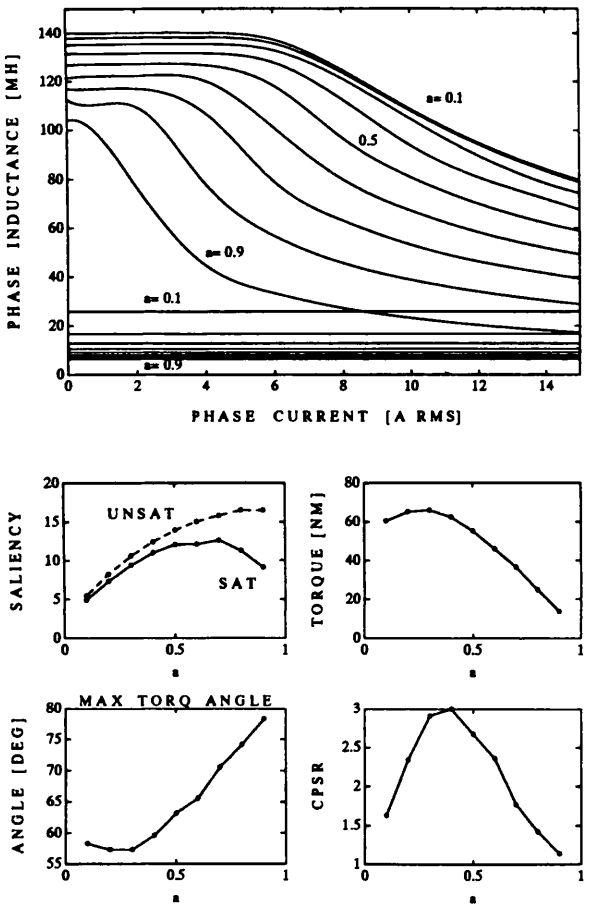

Figure 11: *Effect of the lamination to barrier ratio on the calculated performance characteristics of the 7.5kW synchronous reluctance motor. Top : flux-linkage characteristics. Bottom : calculated performance.*

0.40, with the upper limit due to rotor saturation. Lipo [7] suggests a value of about 1/3 in order to reduce rotor iron loss.

To investigate this further, finite-element analysis was used to calculate the performance characteristics of the 7.5kW motor with different values of a. The results are shown in Fig. 11.

From (2) the saliency ratio should be proportional to a. This is true for low values of a, however for larger values, Carter's coefficient reduces the unsaturated saliency ratio and heavy saturation brings down the saturated saliency ratio. This is reflected in the maximum torque per ampere current angle plot. The torque peaks at about $a = 0.3$ and the constant power speed range (CPSR) peaks at about $a = 0.4$. Note that these results are sensitive to how much of the rotor cross-section is lost due to the bolt holes.

The value of $a = 0.5$ used in the final design is not optimal, but gives reasonable performance.

III. Axially-Laminated IPM Design

A major problem with synchronous reluctance motors with regard to field-weakening performance is the limited achievable constant power speed range. The 7.5kW design achieved about 2.5, and the previous section has shown that it would be difficult to improve this by more than about 50%.

However by adding just sufficient permanent magnet material to the motor, an interior permanent magnet axially-laminated motor with an extremely wide constant power speed range can theoretically be obtained [5, 6, 7].

The theoretical field-weakening performance of such drives was investigated in an earlier paper [1]. The top graph in Fig. 12 uses a lossless linear model to show the effect on the constant power speed range of adding permanent magnets to the motor. Note that with no magnet flux, the constant power speed range is approximately half the saliency ratio. The normalised magnet flux-linkage is the ratio of the magnet back-emf voltage to the supply voltage at rated speed (for a lossless linear motor).

Note that for a given saliency ratio, adding magnet material to a synchronous reluctance motor first improves the constant power speed range until it is infinitely wide, then causes it to decrease to unity. Optimum designs described by (1) lies on the right-hand side of the infinite constant power speed range zone as these offer the highest inverter utilisation [1]. The graph also illustrates the point made in the introduction that a high saliency ratio design reduces the magnet requirements and the back-emf at high speed.

In designing the interior permanent magnet motor only sufficient magnet material should be added to yield optimum performance.

A larger airgap (0.92mm) was used in the interior permanent magnet motor design to produce a comparable torque to the synchronous reluctance motor and not exceed the dynamometer capacity. This also allowed the investigation of the effect of increasing the airgap on the inductance characteristics.

The main design decisions for an axially-laminated interior permanent magnet motor are : pole-piece material, magnet type and demagnetisation withstand. Each of these will now be examined.

A. Pole-Piece Material

Finite-element analysis was used to investigate the effect of using magnetic and non-magnetic pole-pieces on the motor back-emf shape and magnitude. Fig. 13 shows the calculated airgap flux-density distribution and the line-to-line voltage of the motor for the two cases, when using rubber-bonded ferrite magnets. Note the large distortion caused to the airgap flux distribution by using non-magnetic pole-pieces.

Magnetic pole-pieces increase the fundamental voltage by 13% and result in a far more sinusoidal airgap flux density distribution and hence back-emf waveform. The latter point is

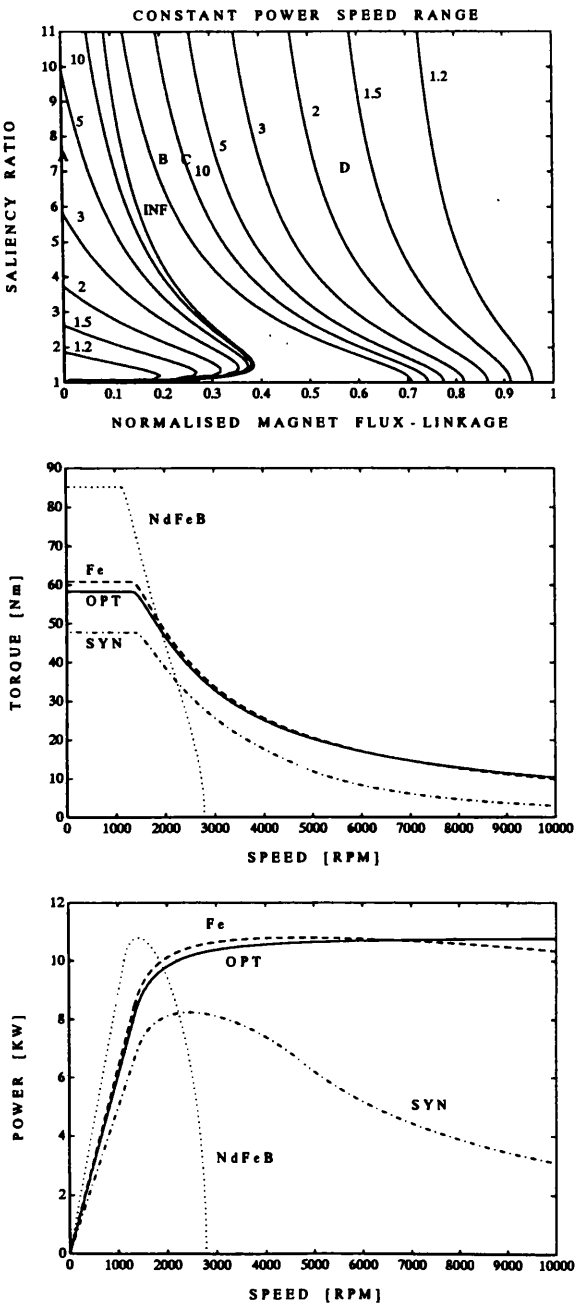

Figure 12: *Top : contour plot of the constant power speed range against the saliency ratio and the normalised magnet flux-linkage. Middle and bottom : calculated field-weakening performance curves for a purely synchronous reluctance design (SYN), an optimal design (OPT), a design using rubber-bonded ferrite magnets (Fe) and a design using rubber-bonded NdFeB magnets (NdFeB).*

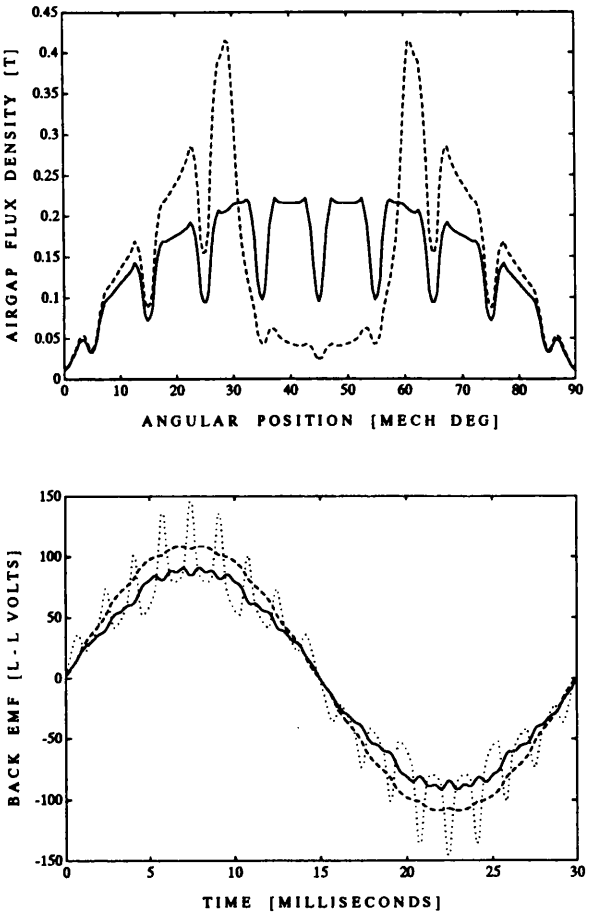

Figure 13: *Calculated airgap flux distribution (top) with magnetic (solid line) and non-magnetic (dashed line) pole-pieces. Back-emf waveforms at 1000rpm (bottom) : calculated with magnetic (dashed line) and non-magnetic (dotted line) pole-pieces and measured waveform with magnetic pole-pieces (solid line).*

important in order to reduce harmonic iron losses, especially in the field-weakening region [5]. Thus magnetic pole-pieces were used despite the small loss in the saliency ratio predicted in the previous section.

Fig. 13 also shows the measured back-emf waveform. The shape of the waveform is predicted accurately and the discrepancy in the amplitude is due to problems with fully magnetising the magnetic sheet (described later).

Table 2: *Typical flexible magnetic sheet properties. Courtesy of Anchor Magnets, Lucas AEC and Cookson Technology.*

Property	Ferrite	NdFeB
Remanent Flux Density B_r [T]	0.165	0.4–0.5
Coercivity H_c [kA/m]	110	
Intrinsic Coercivity H_{ci} [kA/m]	180	700–1000
Recoil Permeability μ_{rec}	1.10	1.06
Density ρ [kg/m^3]	3600	5000
Max. Continuous Temp. [°C]	80	60–100
Max. Intermittent Temp. [°C]	110	
Temp. Coeff. of B_r [%/°C]	-0.2	-0.1
Temp. Coeff. of H_{ci} [%/°C]	0.4	-0.6
Magnet Thickness [mm]	$\geq$ 0.4	$\geq$ 0.4

B. Magnet Selection

The axially-laminated interior permanent magnet motor design requires magnets with the following properties : available in thin sheets ($\leq$0.5mm), flexible enough to be bent through 45° in a radius of a few millimetres, high coercivity, high maximum operating temperature and low-cost.

The only flexible magnet sheet presently available commercially in quantity is rubber-bonded ferrite, though flexible NdFeB magnet sheet is under development. Typical properties of these two materials are summarised in Table 2.

The optimum field-weakening criteria (1) gives the optimum value of magnet flux-linkage. Finite-element calculations corrected for end-winding inductance [9] gives $L_d = 11.5$mH (the measured value was 12.0mH). This gives the optimum magnet flux-linkage Ψ_{opt} as :

$$\Psi_{opt} = L_d I_o = 11.5\text{mH} \times 15\text{Arms} = 0.173\text{Vs} \qquad (3)$$

From Fig. 13, flexible ferrite magnets give $\Psi_m = 0.214$Vs. Thus this material would give slightly more than the optimal flux-density. A problem with this material is its poor demagnetisation characteristics.

Neglecting saturation, with NdFeB magnets of remanent flux density $B_r = 0.45$T (see Table 2), the magnet flux would be $\Psi_m = 0.584$Vs. This is excessive and could be reduced to Ψ_{opt} by replacing most of the magnet material with normal insulation material. This would also reduce the amount of the (expensive) magnet required. NdFeB magnets have excellent demagnetisation characteristics (see Table 2) which would be essential in a commerical motor.

Fig. 12 shows the effect on the calculated field-weakening characteristics of adding magnet material to the motor. The performance of a pure synchronous reluctance motor with a 0.92mm airgap (point A in the contour plot) is compared against that with the optimal magnet flux (point B), rubber-bonded ferrite magnets (point C) and NdFeB magnets (point D). Note that point B should ideally lie exactly on the right-hand side of infinite constant power speed range band as it is an optimal field-weakening design. It does not because the model used to calculate the characteristics takes saturation into account while the contour plot is calculated for a constant parameter model.

The synchronous reluctance motor shows a constant power speed range of 3.2. Adding the optimal magnet flux improves the output torque and produces a motor with the optimal field-weakening performance. That is, with constant power up to infinite speeds. The ferrite magnet motor has a slight excess of flux, this gives slightly more torque at low speed, but a reduction in the constant power speed range from infinity to 13. Using NdFeB magnets greatly enhances the low speed torque at the price of a poor field-weakening performance. Thus ferrite magnets offer the best performance and were used in the final design.

The rubber-bonded ferrite magnet sheet is normally supplied magnetised in a multi-pole fashion on one surface. Thus it was necessary to remagnetise them through the thickness. This was performed by passing it through a field of about 1.4T. Note that the magnets could probably be magnetised *in situ* if desired, though for the prototype the magnets were magnetised before assembly. A difficulty found with this technique was that low operating point of the sheet material in free air caused partial demagnetisation. This meant the actual magnet flux-linkage was lower than predicted (actually 0.174Vs) and was nearly exactly equal to the optimal value.

The maximum continuous operating temperature of both the ferrite and NdFeB flexible sheet magnets is limited by the binders used. Present materials are limited to 60–100°C. This not however an intrinsic limit and if there is a sufficiently large market, alternative binders could be found.

C. Demagnetisation Withstand

An important design consideration is demagnetisation withstand. This is because from (1), in an optimal field-weakening design the total effective flux in the magnet axis is reduced to zero by rated stator current in that axis. Note that does not actually require the flux in the magnets to be reduced to zero because a substantial proportion of L_d (about 40% in the 7.5kW design) consists of slot-leakage and end-winding inductance which does not produce airgap flux. Nevertheless the magnet operating point is low under these conditions.

The measured demagnetisation curve of the flexible ferrite magnet sheet is shown in Fig. 14. Due to the "softness" of the characteristic, care is required to prevent irreversible demagnetisation of the magnets. Finite-element analysis showed that with rated current in the least inductive axis (the worst case) that the magnetic field in the magnets was in range 0.04–0.08T. This will not cause irreversible demagnetisation as it is above the knee in the characteristic.

IV. Experimental Results

The 7.5kW axially-laminated interior permanent magnet and synchronous reluctance motors were built. Their design characteristics are summarised in Table 3.

The inductance characteristics (see Fig. 15) were measured using the instantaneous flux-linkage method described in [9]. Conventional 50Hz AC impedance tests were found to give poor results due to the large iron losses produced by the flux oscillations in the rotor. Note that under normal field-oriented control, the flux in the rotor is substantially constant and so these losses will not appear.

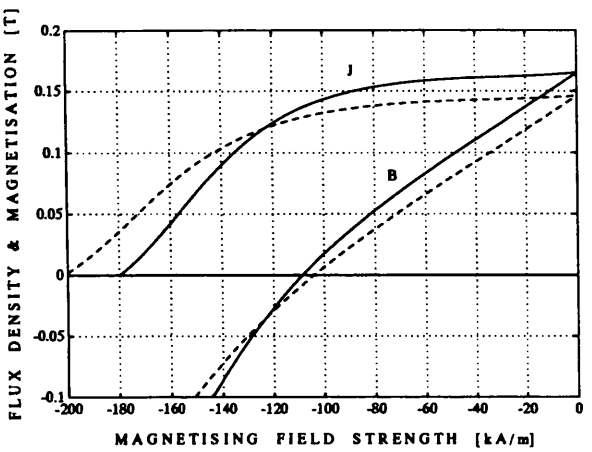

Figure 14: *Magnetic properties of rubber-bonded ferrite sheet. The solid line is the measured characteristic (courtesy of Lucas AEC) at 20°C and the dashed line is the calculated characteristic at 80°C.*

The measured inductance characteristics correspond well with the finite-element predictions. The interior permanent magnet motor shows much less saturation than the synchronous reluctance motor due to the larger airgap. This can be clearly seen from Table 3 where the interior permanent magnet motor's unsaturated saliency ratio is 6.7 and the saturated value is 6.3. The use of iron pole-pieces causes the d-axis inductance of the interior permanent magnet motor to be slightly greater than that of the synchronous reluctance motor as predicted earlier.

Running tests were performed on a fully-instrumented 50Nm dynamometer using a vector-controlled induction motor as a load. A 7.5kW, 10kHz IGBT inverter and an analog hysteresis current loop was used to control the test motor.

Fig. 15 shows the effect of varying the current angle for operation at rated current at 500rpm. The finite-element inductance predictions (with the measured magnet flux-linkage) give a good approximation to the performance though the calculated characteristics from the measured inductance results are generally better as would be expected. Note the reduction in the terminal voltage as the current angle is increased towards 90°. This is the key to the field-weakening operation.

A comparison between the calculated and measured field-weakening characteristics at rated current and one third of rated voltage is shown in Fig. 16. The reduced voltage was used to allow the field-weakening region to be characterised without overstressing the rotor mechanically. Note that to a first approximation, the constant power speed range is independent of the supply voltage [1].

Ideally the induction motor has a constant power speed range of about 2.5. This is the ratio of the breakdown torque to the rated torque [15]. The synchronous reluctance motor

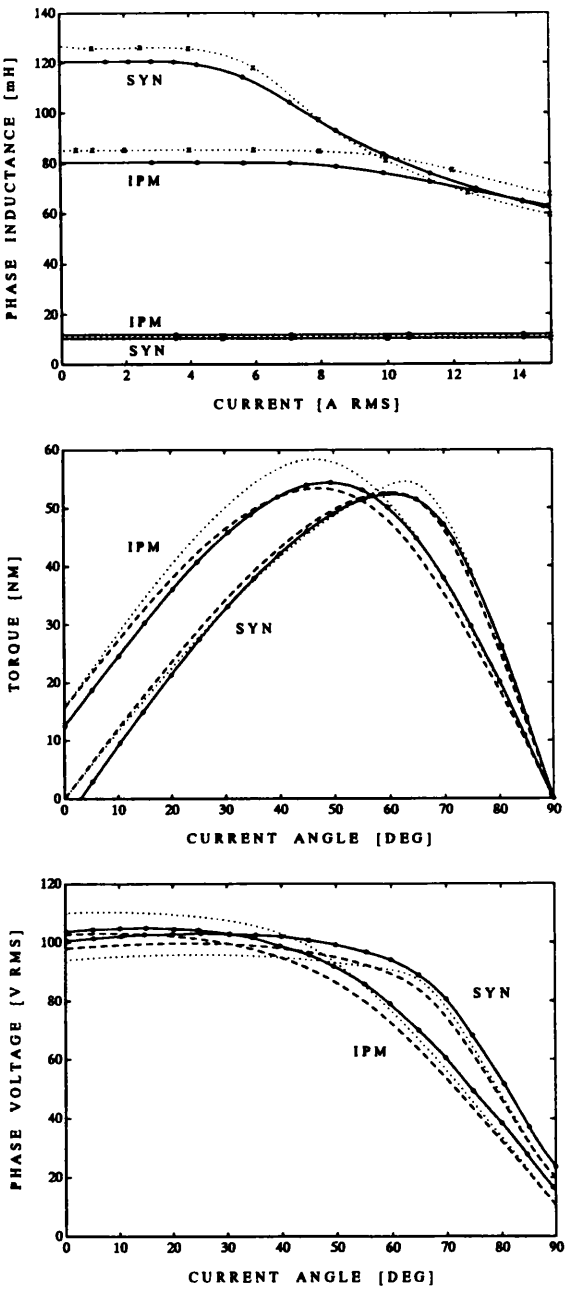

Figure 15: *Inductance, torque and fundamental voltage characteristics of the 7.5kW synchronous reluctance (SYN) and interior permanent magnet motor (IPM). The torque and voltage characteristics are measured at 500rpm and 15A. Measured (solid), calculated from the measured inductance characteristics (dashed) and finite-element predictions (dotted).*

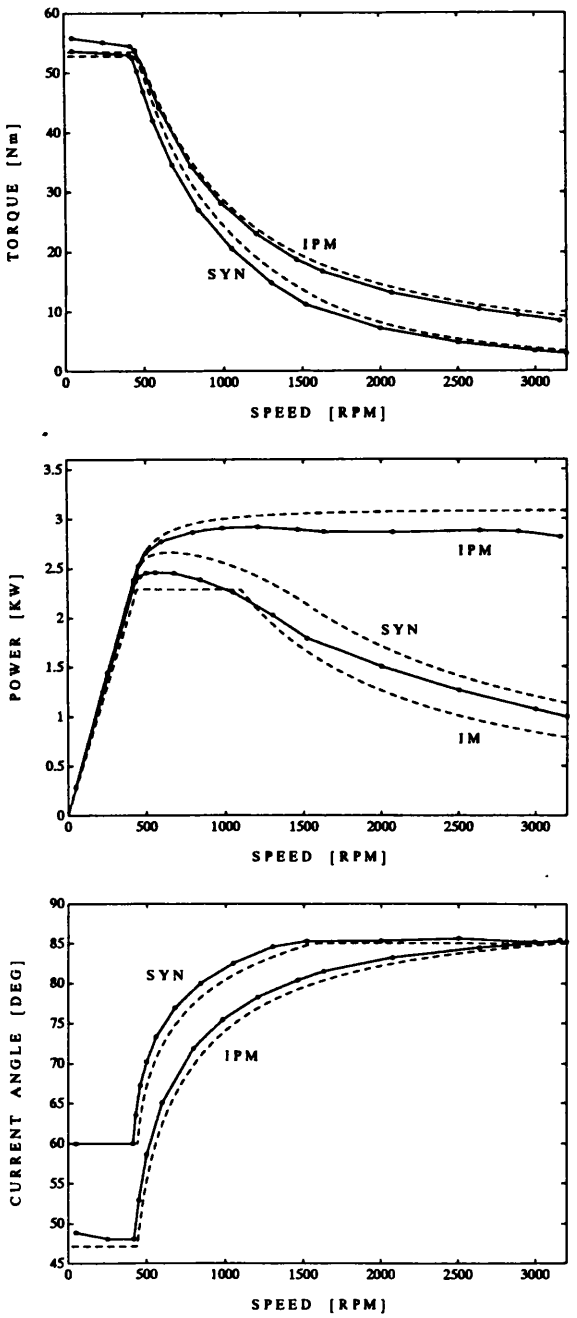

Figure 16: *Field-weakening characteristics at rated current and one third of rated voltage. Measured results (solid lines) and calculated results (dashed lines). The calculated characteristic of the induction motor is given for comparison.*

Table 3: *Comparison of motors in same stator. The induction motor power-factor is low as the motor is actually capable of 11kW, but is derated to 7.5kW for a 10:1 constant torque speed range with a shaft-mounted fan.*

Parameter	IM	SYNCHREL	IPM
Airgap [mm]	0.48	0.517	0.917
Stator Inner Dia. [mm]	127	127	127
Stack Length [mm]	202	202	202
Poles	4	4	4
Lamination Thick. [mm]		0.50	0.50
Ins./Magnet Thick. [mm]		0.50	0.50
Rotor Layers		62	62
Pole Arc [elec deg]		131	131
Pole Pieces		brass	iron
Magnet Flux [Vs rms]	0	0	0.174
Unsat. ξ		11.5	6.7
Sat. ξ		9.6	6.3
Rated Line Voltage V_o [V]	415	415	415
Rated Current I_o [A]	15	15	15
γ_m [deg]		64.1	48.1
Knee Speed ω_k [rpm]	1460	1442	1396
Rated Torque T_k [Nm]	50	49.6	53.1
Rated Output Power P_k [kW]	7.5	7.48	7.76
Efficiency η [%]	87.5	85.5	89.5
Power Factor $\cos\phi$	0.72	0.813	0.804
Inverter Utilisation $\kappa = \eta\cos\phi$	0.63	0.696	0.720
CPSR	2.5	2.5	$\geq$ 7.5

has a measured constant power speed range of also about 2.5. As predicted by the model, the interior permanent magnet motor drive shows an excellent field-weakening characteristic. The base speed is about 420rpm at which the output power is about 2.4kW. The highest measured speed was 3160rpm, constrained by mechanical limitations in the prototype motor. This corresponds to a 7.5:1 constant power speed range, and at the highest speed the output power was still over 2.8kW. Thus the actual constant power speed range is probably greater than 10:1 and may even reach 15:1.

The calculated characteristics were based on the measured inductance and magnet flux-linkage and did not take into account iron losses and friction and windage. This causes the discrepancy between the measured and calculated power output curves. Note that the interior permanent magnet motor appears to have lower iron losses than the synchronous reluctance motor.

The required control characteristics are predicted accurately as shown by the current angle versus speed graph in Fig. 16. The synchronous reluctance motor enters the purely voltage-limited or inverse power region (Mode III) [1] at about 1500rpm. The interior permanent magnet motor remains in the voltage-and-current-limited region (Mode II) throughout the measured speed range.

A comparison of the measured torque ripple performance of the 7.5kW axially-laminated synchronous reluctance motor against that of a 7.5kW single-barrier synchronous reluctance design [16] is given in Fig. 17. Note the axially-laminated design has approximately half the torque ripple of the single-barrier design. The torque ripple at full load is approximately

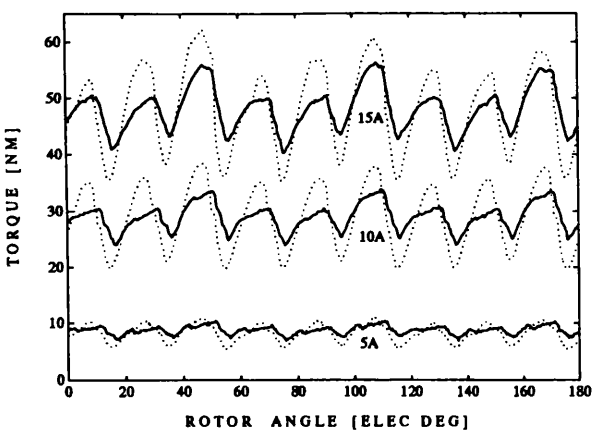

Figure 17: *Measured torque ripple for 7.5kW axially-laminated (solid line) and single-barrier (dotted line) synchronous reluctance motor at three levels of current ($\gamma = 45°$).*

20%. The large torque ripple even with the axially-laminated rotor construction is due to the simple single-layer stator winding.

A comparison of the measured performance of the motors at rated speed is shown in Table 3. Note the axially-laminated interior permanent magnet motor shows an improved efficiency and inverter utilisation compared to the induction motor.

V. Conclusions

This paper described the design of an axially-laminated interior permanent magnet motor drive optimised for its field-weakening performance. A 7.5kW motor was built based on low-cost, flexible rubber-bonded ferrite magnet sheet. It achieved an extremely wide constant power speed range of greater than 7.5:1, in contrast to the 2.5:1 obtained both with an axially-laminated synchronous reluctance motor and a standard induction motor. The excellent field-weakening performance makes this type of motor a serious contender for applications such as machine tool main spindle drives and traction.

Acknowledgments

The support of the Commonwealth Scholarship Commission of the United Kingdom and the Glasgow University SPEED Consortium is gratefully acknowledged. Thanks to P. Miller and R. Lagerquist for building the inverter/controller, J. Kelly and W. McDougall for constructing the rotors, H. Stanbury and J. Cawley of Orb Electrical Steels for providing the lamination material, J. Taylor of Lucas AEC for testing the ferrite magnet material and S. Jeffrey of Cookson Technology Centre for the data on the flexible NdFeB magnet properties.

References

[1] W. L. Soong and T. J. E. Miller, "Theoretical limitations to the field-weakening performance of the five classes of brushless synchronous AC motor drive," in *Electrical Machines and Drives Conference*, Sep. 1993. In press.

[2] T. Sebastian and G. R. Slemon, "Operating limits of inverter-driven permanent magnet motor drives," *IEEE Trans. Ind. Appl.*, vol. 23, pp. 327–333, Mar/Apr 1987.

[3] B. Sneyers, G. Maggetto, and J. L. Van Eck, "Inverter fed PM synchronous motor for road electric traction," in *Proc. Int. Conf. Electrical Machines*, pp. 550–553, Sep. 1982.

[4] T. M. Jahns, "Flux-weakening regime operation of an interior permanent magnet synchronous motor drive," *IEEE Trans. Ind. Appl.*, vol. 23, pp. 681–689, Jul/Aug 1987.

[5] R. F. Schiferl and T. A. Lipo, "Power capability of salient pole permanent magnet synchronous motor in variable speed drive applications," *IEEE Trans. Ind. Appl.*, vol. 26, pp. 115–123, Jan/Feb 1990.

[6] A. Fratta, A. Vagati, and F. Villata, "Design criteria of an IPM machine suitable for field-weakened operation," in *Proc. Int. Conf. Electrical Machines*, pp. 1059–1065, 1990.

[7] T. A. Lipo, A. Vagati, L. Malesani, and T. Fukao, eds., *Synchronous Reluctance Machines - A Viable Alternative for AC Drives*, Ind. Appl. Society Annual Meeting Tutorial, Oct. 1992.

[8] D. A. Staton, T. J. E. Miller, and S. E. Wood, "Optimisation of the synchronous reluctance motor," in *Electrical Machines and Drives Conference*, pp. 156–160, Sep. 1991.

[9] W. L. Soong, D. A. Staton, and T. J. E. Miller, "Validation of lumped-circuit and finite-element modelling of axially-laminated motors," in *Electrical Machines and Drives Conference*, Sep. 1993. In press.

[10] R. E. Betz, "Control of synchronous reluctance machines," in *Ind. Appl. Society Annual Meeting*, pp. 456–462, Sep. 1991.

[11] W. L. Soong and T. J. E. Miller, "Practical field-weakening operation of the five classes of brushless synchronous motor drives," in *European Power Electronics Conference*, Sep. 1993. In press.

[12] I. Boldea, N. Muntean, S. Deaconu, S. A. Nasar, and Z. Fu, "Distributed anisotropy rotor synchronous (DARSYN) drives - motor indentification and performance," in *Proc. Int. Conf. Electrical Machines*, pp. 542–546, 1992.

[13] A. El-Antably and T. L. Hudson, "The design and steady-state performance of a high-efficiency reluctance motor," in *Ind. Appl. Society Annual Meeting*, pp. 770–776, 1985.

[14] I. Boldea and S. Nasar, "Emerging electric machines with axially laminated anisotropic rotors : a review," *Electrical Machines and Power Systems*, vol. 19, pp. 673–704, 1991.

[15] A. J. Humphrey, "Constant horsepower operation of induction motors," *IEEE Trans. Ind. Gen. Appl.*, vol. 5, pp. 552–557, Sep/Oct 1969.

[16] D. A. Staton, W. L. Soong, and T. J. E. Miller, "Unified theory of torque production in switched reluctance and synchronous reluctance motors," in *Ind. Appl. Society Annual Meeting*, Oct. 1993. In press.

Appendix C

General-Purpose FE Script File

This is a listing of the script file written by myself and Dr. Dave Staton for Vector Field's 2D finite-element analysis program "Opera". It creates a finite-element mesh for axially-laminated motors from the standard stator geometry parameters (number of slots, tooth angle, slot depth etc.) and the rotor parameters (number of layers, thickness of layers etc.).

```
////////////////////////////////////////////////////////////////////////////
/                                OP7_C_D3.COMI                             /
////////////////////////////////////////////////////////////////////////////

/ Brook Crompton : D132MKE frame size, 8 inch stack length, 4 pole
/ axially laminated rotor

/=========================================================================

$comi mode=cont
unit mm dens=amm2

/**** INPUT BH DATA
bhdata 4
   load ../../M800
q
bhdata 5
   load ../../M750
q
bhdata 7
   load ../../M750
   $do #i 1 24
     r #i b*0.7 h*0.4*2/3
   $end do
q
bhdata 6
   load ../../RUBM
q

/***** SET ELEMENT TYPE
/set elem=quad

/***** SET UP USEFUL CONVERSION FACTORS
$cons #rad pi/180
$cons #deg 180/pi
$cons #xmin 0
$cons #xmax 200
$cons #ymin 0
$cons #ymax 100

/***** SET UP SCALING FOR OUTLINE PLOT *****
reco xmin=#xmin ymin=#ymin xmax=#xmax ymax=#ymax label=no


/$$$$$$$$$$$$$$$$$$$$$$$$$$$$$$$$$$$$$$$$$$$$$$$$$$$$$$$$$$$$$$$$$$$$$$$$$$
/$$$$$$$$$$$$$$$$$$$$$$$$$$ IMPORTANT SETTINGS $$$$$$$$$$$$$$$$$$$$$$$$$$$$
/$$$$$$$$$$$$$$$$$$$$$$$$$$$$$$$$$$$$$$$$$$$$$$$$$$$$$$$$$$$$$$$$$$$$$$$$$

/ case = d-axis
/ non-lamination layers = insulation
/ polepiece = non-magnetic
/ shaft = magnetic


/***** Rotp Minimum Angle By Which Rotor can be Rotated
/           ie. Airgap Element Spacing in degrees
/  needs to be comparable to lamination angular span at airgap
/***** Rang = angle by which rotor is rotated in mechanical degrees
/***** Cang = angle by which current phasor leads rotor q-axis in
/*****               electrical degrees
/***** curr = rms phase current in amperes
/***** turn = number of conductors per coil

/************ material types are : 0=air, 5=rotor steel, 6=magnet, 7=diluted
/***** Fmat - material type number for first layer (closest to shaft)
/***** Smat - material type number for second layer
/***** Sma2 - material type number for steel near bolt hole
/***** Mpp  - material type number for polepiece
/***** Msh  - material type number for shaft
```

```
/***** Mden  measure of the density of nodes in rotor lamination
/            in nodes per mm, adjust to give just under maximum number of
/       elements
/***** AGap - radial airgap in mm
/***** muS  - linear permeability of stator steel
/***** mu1  - linear permeability of first rotor material
/***** mu2  - linear permeability of second rotor material
/***** muP  - linear permeability of polepieces
/***** muH  - linear permeability of shaft

/************ set $qxs=1 if q-axis or 0 if d-axis case, do not change $Rang
/$cons $qxs  0
/******************** value of insulation to lamination ratio
$cons $aaaa 0.5

$cons $Rotp 1/5
$cons $Cang 0
$cons $Rang 0
$cons $curr 1.0
$cons $Turn 19
$cons $Fmat 0
$cons $Smat 5
$cons $Sma2 7
$cons $Mpp  0
$cons $Msh  5
$cons $Mden 1.5
$cons $AGap 0.517
$cons $muS   1000000
$cons $mu1   1
$cons $mu2   1000000
$cons $muP   1
$cons $muH   1000000


/$$$$$$$$$$$$$$$$$$$$$$$$$$$$$$$$$$$$$$$$$$$$$$$$$$$$$$$$$$$$$$$$$$$$$$$$$$$$$$$
/$$$$$$$$$$$$$$$$$$$$$$$$$$$$$$ CREATE STATOR $$$$$$$$$$$$$$$$$$$$$$$$$$$$$$$$
/$$$$$$$$$$$$$$$$$$$$$$$$$$$$$$$$$$$$$$$$$$$$$$$$$$$$$$$$$$$$$$$$$$$$$$$$$$$$

/=========================================================================
/***** STATOR CONSTANTS ***** from Brook Crompton DRW 8050Y36/23, 6/1/81
/***** Nslt - Number of slots in full motor
/***** Nmod - Number of HALF slots modelled
/***** Rad1 - Stator Inner Radius
/***** Rad2 - Stator Outer Radius, Diameter of Outer Frame/2
/***** Th1  - Half slot pitch (Radians)
/***** Thid - Half slot pitch (Degrees)
/***** Tw   - Tooth Thickness, Assumes parallel sided teeth
/***** Fill - Slot Bottom curve section radius, (fillet)
/***** Sd   - Slot depth, top of tooth to bottom of slot
/***** So   - Slot Opening
/***** Sod  - Slot Opening Depth
/***** Tang - angle of backside of tooth, 0 = hammerhead shape
/***** Std  - Slot Tang Depth (Fslot+Eslot)
/***** Sreg - Number of regions in half a slot (10)
/***** NSrg - total number of stator regions including stator airgap layer

$cons $Nslt   36
$cons $Nmod   9
$cons $Rad1   127.0/2
$cons $Rad2   203.9/2
$cons $Th1    pi/$Nslt
$cons $Thid   pi/$Nslt*$deg
$cons $Tw     6.35
$cons $Fill   7.30/2
$cons $Sd     17.78+0.762
$cons $So     2.92
$cons $Sod    0.762
/**** APPROXIMATELY CALCULATE STD see Finite-Element I, pg 29 from Tang
$cons $Tang   20*$Rad
$cons $Std    (($Rad1+$Sod)*tan($Th1)-$Tw/2-$So/2)*tan($Tang)+$Sod
```

```
$cons $Sreg   10

$cons $Sr1    $Rad1
$cons $Sr2    $Rad1
$cons $Sr3    $Rad1
$cons $Sr4    $Rad1+$Std
$cons $Sr5    $Rad1+($Std+$Sd)/2
$cons $Sr6    $Rad1+$Sd
$cons $Sr7    $Rad2
$cons $Sr8    $Rad2
$cons $Sx9    $Sr6-$Fill-$Fill*sin($Th1)
$cons $Sx10   $Sr5
$cons $Sx11   $Rad1+$Sod
$cons $Sx12   $Sr4
$cons $Sx13   $Sr5
$cons $Sx14   $Sx9
$cons $Sx15   $Sr6

$cons $St1    $Th1d
$cons $St2    asin($So/(2*$Rad1))*$deg
$cons $St3    0
$cons $St4    0
$cons $St5    0
$cons $St6    0
$cons $St7    0
$cons $St8    $Th1d
$cons $Sy9    $Sx9*tan($Th1)
$cons $Sy10   $Sx10*tan($Th1)
$cons $Sy11   $So/2
$cons $Sy12   $Sx12*tan($Th1)-($Tw/2)/cos($Th1)
$cons $Sy13   $Sx13*tan($Th1)-($Tw/2)/cos($Th1)
$cons $Sy14   $Sx14*tan($Th1)-($Tw/2)/cos($Th1)
$cons $Sy15   $Sy14-$Fill/cos($Th1)

$cons $Sn1    1/$Rotp
$cons $Sn2    2/3/$Rotp
$cons $Sn3    2
$cons $Sn4    2
$cons $Sn5    2
$cons $Sn6    4
$cons $Sn7    1
$cons $Sn8    4
$cons $Sn9    1
$cons $Sn10   3
$cons $Sn11   3
$cons $Sn12   3
$cons $Sn13   3
$cons $Sn14   3
$cons $Sn15   3
$cons $Sn16   3
$cons $Sn17   1
$cons $Sn18   1
$cons $Sn19   2
$cons $Sn20   4
$cons $Sn21   1
$cons $Sn22   4
$cons $Sn23   3
$cons $Sn24   1

$cons $Bsp1   0.3
$cons $Bsn1   0.7
$cons $Bsp2   0.3
$cons $Bsn2   0.7
$cons $Bsp3   0.15
$cons $Bsn3   0.85


/=================================================================
/*** CREATE REGIONS
```

```
/region # 1
draw poly mate=4 perm=$muS
     pola $Sr6   $St6
/**** This converts the flat bottom to round bottom
/     cart $Sx15  $Sy15  n=$Sn21  c=0.0      b=0.5   f=N0
     pola $Sr8   $St8   n=$Sn22  c=0.0      b=$Bsp3   f=N0
     pola $Sr7   $St7   n=$Sn7   c=1/$Rad2  b=0.5   f=V
     fini               n=$Sn6   c=0.0      b=$Bsn3   f=N0
q

/region # 2
draw poly mate=4 perm=$muS
     pola $Sr8   $St8
/ flat bottom to round bottom
/     cart $Sx15  $Sy15  n=$Sn22  c=0.0      b=0.5   f=N0
     pola $Sr6   $St6   n=$Sn22  c=0.0      b=$Bsn3    f=N0
     cart $Sx14  $Sy14  n=$Sn20  c=-1/$Fill b=0.5    f=N0
     cart $Sx9   $Sy9   n=$Sn23  c=0.0      b=0.5
     fini               n=$Sn8   c=0.0      b=$Bsp3
q

/region # 3
draw poly mate=4 perm=$muS
     cart $Sx9   $Sy9
     cart $Sx14  $Sy14  n=$Sn23  c=0.0      b=0.5  f=N0
     cart $Sx13  $Sy13  n=$Sn18  c=0.0      b=0.5
     cart $Sx10  $Sy10  n=$Sn24  c=0.0      b=0.5
     fini               n=$Sn9   c=0.0      b=0.5
q

/region # 4
draw poly mate=4 perm=$muS
     pola $Sr1   $St1
     cart $Sx10  $Sy10  n=$Sn10  c=0.0      b=$Bsp1   f=N0
     cart $Sx13  $Sy13  n=$Sn24  c=0.0      b=0.5
     cart $Sx12  $Sy12  n=$Sn16  c=0.0      b=$Bsn1
     fini               n=$Sn11  c=0.0      b=$Bsp2
q

/region # 5
draw poly mate=4 perm=$muS
     pola $Sr1   $St1
     cart $Sx12  $Sy12  n=$Sn11  c=0.0      b=$Bsn1  f=N0
     cart $Sx11  $Sy11  n=$Sn12  c=0.0      b=0.5
     pola $Sr2   $St2   n=$Sn13  c=0.0      b=0.5
     fini               n=$Sn1   c=-1/$Rad1 b=0.5
q

/region # 6
draw poly mate=0 perm=1
     pola $Sr2   $St2
     cart $Sx11  $Sy11  n=$Sn13  c=0.0      b=0.5   f=N0
     pola $Sr4   $St4   n=$Sn14  c=0.0      b=0.5
     pola $Sr3   $St3   n=$Sn3   c=0.0      b=0.7
     fini               n=$Sn2   c=-1/$Rad1 b=0.7
q

/region # 7
draw poly mate=0 perm=1
     pola $Sr4   $St4
     cart $Sx11  $Sy11  n=$Sn14  c=0.0      b=0.5   f=N0
     cart $Sx12  $Sy12  n=$Sn12  c=0.0      b=0.5
     fini               n=$Sn15  c=0.0      b=0.5
q

/region # 8
draw poly mate=1 perm=1
     pola $Sr4   $St4
     cart $Sx12  $Sy12  n=$Sn15  c=0.0      b=0.5   f=N0
     cart $Sx13  $Sy13  n=$Sn16  c=0.0      b=$Bsp1
```

```
     pola $Sr5   $St5   n=$Sn17  c=0.0      b=0.5
     fini               n=$Sn4   c=0.0      b=$Bsn1
q

/region # 9
draw poly mate=1 perm=1
     pola $Sr5   $St5
     cart $Sx13  $Sy13  n=$Sn17  c=0.0      b=0.5   f=NO
     cart $Sx14  $Sy14  n=$Sn18  c=0.0      b=0.5
     fini               n=$Sn19  c=0.0      b=0.5
q

/region # 10
draw poly mate=1 perm=1
     pola $Sr5   $St5
     cart $Sx14  $Sy14  n=$Sn19   c=0.0      b=0.5   f=NO
/    cart $Sx15  $Sy15  n=$Sn20  c=1/$Fill   b=0.5
/    pola $Sr6   $St6   n=$Sn21  c=0.0       b=0.5
     pola $Sr6   $St6   n=$Sn20  c=1/$Fill   b=0.5
     fini               n=$Sn5   c=0.0       b=0.5
q


/***** CONVERT SOME FOURSIDED POLYGONS TO QUADRILATERALS TO REDUCE
/***** RISK OF ERRORS IN MESH GENERATION
/***** if slot shape is changed from square to round, this needs to
/***** be changed
conv reg1=2 reg2=5 shap=q

/***** REFLECT HALF SLOT BY (SLOT PITCH / 4)
/***** $Thi  = Half slot pitch (Radians)
/***** $Thid = Half slot pitch (Degrees)
/***** reg2  = $Sreg
copy reg1=1 reg2=10 t=$Thid/2
eras reg1=1 reg2=10
reco

/***** MIRROR HALF SLOT TO CREATE FULL SLOT PITCH
copy 1 10 t=$Thid

/***** CREATE EIGHTH MOTOR BY MULTIPLE ROTATIONS
/***** reg2 = 2*$Sreg
$do #i 1 3 1
copy 1 20 t=#i*$Thid*2 MIRR=no
$end do

/above line creates regions 1 to 60, need to create last
copy reg1=71 reg2=80 t=40 mirr=yes


/=============================================================================
/***** SET UP THE RELEVANT CURRENT DENSITY LEVELS IN THE SLOTS

/***** Rang = angle by which rotor is rotated in mechanical degrees
/***** Cang = angle by which current phasor leads rotor q-axis in
/*****            electrical degrees
/***** Aoff = angle by which rotor d-axis is offset from stator +ve
/*****            x-axis in electrical degrees
/***** curr = rms phase current in amperes
/***** turn = number of conductors per coil

$cons $Aoff 0
$cons $AmpA sqrt(2)*$curr*cos(2*$Rang*$Rad+$Cang*$Rad+$Aoff*$Rad+0*$Rad)
$cons $AmpB sqrt(2)*$curr*cos(2*$Rang*$Rad+$Cang*$Rad+$Aoff*$Rad-240*$Rad)
$cons $AmpC sqrt(2)*$curr*cos(2*$Rang*$Rad+$Cang*$Rad+$Aoff*$Rad-120*$Rad)


/***** SINGLE LAYER WINDING, EQUAL CONCENTRIC
/***** reg1 = 8 + Count*$Sreg  (Count = 0 to $Nslt-1)
```

```
/calculate total area of half slot, note that must use some operation
/  using "area" in order to set its value
modi reg1=8  reg2=8  dens=area
$cons $a8  area
modi reg1=9  reg2=9  dens=area
$cons $a9  area
modi reg1=10 reg2=10 dens=area
$cons $a10 area
$cons $atot $a8+$a9+$a10

modi reg1=8   reg2=10  dens=-$Turn/2*$AmpB/$atot
modi reg1=18  reg2=20  dens=-$Turn/2*$AmpB/$atot
modi reg1=28  reg2=30  dens=-$Turn/2*$AmpB/$atot
modi reg1=38  reg2=40  dens=-$Turn/2*$AmpB/$atot
modi reg1=48  reg2=50  dens=-$Turn/2*$AmpB/$atot
modi reg1=58  reg2=60  dens=-$Turn/2*$AmpB/$atot

modi reg1=68  reg2=70  dens=$Turn/2*$AmpA/$atot
modi reg1=78  reg2=80  dens=$Turn/2*$AmpA/$atot
modi reg1=88  reg2=90  dens=$Turn/2*$AmpA/$atot


/=============================================================================
/***** SET UP THE BOUNDARY CONDITIONS ON THE STATOR

/***** On the x>0 axis modify regions 2,3,4
/***** On the x<0 axis modify regions 2 + (Nmod-1)*Sreg
/*****                               3 + (Nmod-1)*Sreg
/*****                               4 + (Nmod-1)*Sreg

modi reg1=2   reg2=3   f4=V
modi reg1=4   reg2=4   f1=V

modi reg1=81  reg2=81  f3=DV
modi reg1=86  reg2=86  f3=DV
modi reg1=88  reg2=88  f4=DV
modi reg1=90  reg2=90  f3=DV


/$$$$$$$$$$$$$$$$$$$$$$$$$$$$$$$$$$$$$$$$$$$$$$$$$$$$$$$$$$$$$$$$$$$$$$$$$$$
/$$$$$$$$$$$$$$$$$$$$$$$$ CREATE STATOR AIRGAP $$$$$$$$$$$$$$$$$$$$$$$$$$$$
/$$$$$$$$$$$$$$$$$$$$$$$$$$$$$$$$$$$$$$$$$$$$$$$$$$$$$$$$$$$$$$$$$$$$$$$$$$$

/***** There are 4 layers in the gap.
/***** Sgr and Sgt define the polar coordinates of the 3 nodes on the
/***** stator surface over the 1st half slot slot pitch
/***** AGap airgap (radial) : set upstairs
/***** Rad1 Stator Inner Radius (defined above)
/***** Rad3 Rotor Outer Radius
/***** Rgm  Centre of Airgap Radius
/***** Rgs  Airgap Layer Closer to Stator
/***** Rgr  Airgap Layer Closer to Rotor

$cons $Rad3 $Rad1-$AGap
$cons $Lg   $Rad1-$Rad3
$cons $Rgm  $Rad3+0.30*$Lg
$cons $Rgs  $Rad3+0.60*$Lg
$cons $Rgr  $Rad3+0.15*$Lg

$cons $Sgr1 $Rad1
$cons $Sgr2 $Rad1
$cons $Sgr3 $Rad1
$cons $Sgr4 $Rgs
$cons $Sgr5 $Rgs

$cons $Sgt1 0
$cons $Sgt2 $Th1d-$St2
$cons $Sgt3 $Th1d
$cons $Sgt4 $Th1d
```

```
$cons #Sgt5 0

$cons #Sgn1 #Thid/#Rotp/2-mod(#Thid/#Rotp/2;1)


/***** Define Stator Airgap Region (region number is #Nmod*#Sreg+1 )
draw poly mate=0 perm=1
     pola #Sgr1  #Sgt1
     pola #Sgr2  #Sgt2  n=#Sn1   c=-1/#Sgr1 b=0.5   f=NO
     pola #Sgr3  #Sgt3  n=#Sn2   c=-1/#Sgr2 b=0.3
     pola #Sgr4  #Sgt4  n=1      c=0.0      b=0.5
     pola #Sgr5  #Sgt5  n=#Sgn1  c=1/#Sgr5      b=0.5
     fini               n=1      c=0.0      b=0.5
q


/***** MIRROR HALF SLOT STATOR AIRGAP TO CREATE FULL SLOT PITCH
copy reg1=%int(#Sreg*#Nmod+1) reg2=%int(#Sreg*#Nmod+1) t=#Thid   MIRR=yes


/***** CREATE EIGHTH MOTOR STATOR AIRGAP BY MULTIPLE ROTATIONS
/***** reg2 = 2*#Sreg
$do #i 1 3 1
copy  %int(#Nmod*#Sreg+1) %int(#Nmod*#Sreg+2) t=#i*#Thid*2 MIRR=no
$end do

copy reg1=%int(#Nmod*(#Sreg+1)-1) reg2=%int(#Nmod*(#Sreg+1)-1) t=40 mirr=yes

/***** set up boundary conditions on stator airgap
/ reg1= #Nmod*(#Sreg+1) : no need as this is the default condition
/ reg1= #Nmod*#Sreg+1
/ erase reg1=%int(#Nmod*(#Sreg+1)) reg2=%int(#Nmod*(#Sreg+1))
erase reg1=%int(#Nmod*#Sreg+1)   reg2=%int(#Nmod*#Sreg+1)

draw poly mate=0 perm=1
     pola #Sgr1  #Sgt1
     pola #Sgr2  #Sgt2  n=#Sn1   c=-1/#Sgr1 b=0.5   f=NO
     pola #Sgr3  #Sgt3  n=#Sn2   c=-1/#Sgr2 b=0.3
     pola #Sgr4  #Sgt4  n=1      c=0.0      b=0.5
     pola #Sgr5  #Sgt5  n=#Sgn1  c=1/#Sgr5      b=0.5
     fini               n=1      c=0.0      b=0.5   f=V
q



/$$$$$$$$$$$$$$$$$$$$$$$$$$$$$$$$$$$$$$$$$$$$$$$$$$$$$$$$$$$$$$$$$$$$$$$$$$$$$$$
/$$$$$$$$$$$$$$$$$$$$$$$$$$$$$$$$ CREATE ROTOR $$$$$$$$$$$$$$$$$$$$$$$$$$$$$$$$
/$$$$$$$$$$$$$$$$$$$$$$$$$$$$$$$$$$$$$$$$$$$$$$$$$$$$$$$$$$$$$$$$$$$$$$$$$$$$$$$

/***** Lshf - edge length of square shaft
/***** Tlam - thickness of lamination
/***** Tins - thickness of insulation material
/***** Nlay - number of layers of material
/***** Icur - variable for current rotor layer being calculated

/***** Fmat - material type number for first layer (defined in header)
/***** Smat - material type number for second layer (defined in header)
/***** Mpp  - material type number for polepiece (defined in header)

$cons #Lshf 40
$cons #Tlam #aaaa
$cons #Tins 1-#aaaa
$cons #Nlay 62
$cons #Icur 1


/=================================================================
/***** DEFINE ROTOR POINTS
```

```
$para $Rr1  $Lshf/2+(($Icur-1)/2)*($Tlam+$Tins)
$para $Rr2  $Rr1+$Tlam
$cons $K1   $Lshf/sqrt(2)
$cons $K2   tan(22.5*$rad)
$para $Rx3  $K1+$K2*(($Icur-1)/2*($Tlam+$Tins)+$Tlam)
$para $Rx4  $Rx3-$K2*$Tlam
$para $Rr5  $Rad3
$para $Rr6  $Rad3
$para $Rr7  $Rad3
$para $Rx8  $K1+$K2*($Icur+1)/2*($Tlam+$Tins)
$para $Rr9  $Lshf/2+($Icur+1)/2*($Tlam+$Tins)
$para $Rr10 $Rgr
$para $Rr11 $Rgr
$para $Rr12 $Rgr

$para $Rt1  45
$para $Rt2  45
$para $Ry3  (($Icur-1)/2)*($Tlam+$Tins)+$Tlam
$para $Ry4  (($Icur-1)/2)*($Tlam+$Tins)
$para $Rt5  asin($Ry4/$Rr5)*$deg
$para $Rt6  asin($Ry3/$Rr6)*$deg
$para $Ry8  ($Icur+1)/2*($Tlam+$Tins)
$para $Rt7  asin($Ry8/$Rr7)*$deg
$para $Rt9  45
$para $Rt10 $Rt5-$Rotp/2+$Rotp-mod($Rt5+$Rotp/2;$Rotp)
$para $Rt11 $Rt6-$Rotp/2+$Rotp-mod($Rt6+$Rotp/2;$Rotp)
$para $Rt12 $Rt7-$Rotp/2+$Rotp-mod($Rt7+$Rotp/2;$Rotp)


/=====================================================================
/***** SET NUMBER OF NODES
/***** Mden  measure of the density of nodes in rotor lamination
/           in nodes per mm  (set at head of file)
/***** Rden  density of nodes at outside of rotor in nodes per degree
$cons $Rden 1/$Rotp

$para $Rx1  $Rr1*cos($Rt1*$rad)
$para $Ry1  $Rr1*sin($Rt1*$rad)

$para $Rx2  $Rr2*cos($Rt2*$rad)
$para $Ry2  $Rr2*sin($Rt2*$rad)

$para $Rx5  $Rr5*cos($Rt5*$rad)
$para $Ry5  $Rr5*sin($Rt5*$rad)

$para $Rx6  $Rr6*cos($Rt6*$rad)
$para $Ry6  $Rr6*sin($Rt6*$rad)

$para $Rx7  $Rr7*cos($Rt7*$rad)
$para $Ry7  $Rr7*sin($Rt7*$rad)

$para $Rx9  $Rr9*cos($Rt9*$rad)
$para $Ry9  $Rr9*sin($Rt9*$rad)

$para $Rn1  1
$para $Rn2  sqrt(($Rx2-$Rx3)**2+($Ry2-$Ry3)**2)*$Mden
$para $Rn3  1
$para $Rn4  sqrt(($Rx1-$Rx4)**2+($Ry1-$Ry4)**2)*$Mden
/*** Fix Rn5 to allow more nodes on airgap
/ para $Rn5  sqrt(($Rx4-$Rx5)**2+($Ry4-$Ry5)**2)*$Mden
$para  $Rn5 14
/ change to 1 as rotor has 62 layers so no need to use finer subdivision
/ for motors with fewer layers the original function may need to be used
/para $Rn6  ($Rt6-$Rt5)*$Rden
$para $Rn6  $aaaa*10
/*** Fix Rn7 to allow more nodes on airgap
/ para $Rn7  sqrt(($Rx3-$Rx6)**2+($Ry3-$Ry6)**2)*$Mden
$para $Rn7 14
$para $Rn8  1
$para $Rn9  sqrt(($Rx9-$Rx8)**2+($Ry9-$Ry8)**2)*$Mden
```

```
/ *** Fix Rn10 to allow more nodes on airgap
/para $Rn10 sqrt(($Rx7-$Rx8)**2+($Ry7-$Ry8)**2)*$Mden
$para $Rn10 14
/ see note for $Rn6
/para $Rn11 ($Rt7-$Rt6)*$Rden
$para $Rn11 (1-$aaaa)*10
$para $Rn12 1
$para $Rn13 $Rn4/2
$para $Rn14 $Rn4/2
$para $Rn15 ($Rad3-$Rr2)*$Mden/2
$para $Rn16 (45-$Rt6)*$Rden*2
$para $Rn17 1
$para $Rn18 2*($Rt11-$Rt10)/$Rotp
$para $Rn19 1
$para $Rn20 2*($Rt12-$Rt11)/$Rotp
$para $Rn21 1

/**** set bias towards airgap
$cons $Rbp 0.0000001
$cons $Rbn 1-$Rbp

/*** set bias towards outside
$cons $Rbp1 0.3
$cons $Rbn1 0.7


/=====================================================================
/ ***** DRAW ROTOR LAYERS

/-------------------------- Q-AXIS
$IF $qxs NE 0

/*(1)*
$do $Icur 1 $Nlay 2
draw poly mate=$Fmat  phas=45-$Rang perm=$mu1
     pola $Rr1   $Rt1
     pola $Rr2   $Rt2  n=$Rn1   c=0.0      b=0.5   f=NO
     cart $Rx3   $Ry3  n=$Rn2   c=0.0      b=$Rbn1
     cart $Rx4   $Ry4  n=$Rn3   c=0.0      b=0.5
     fini              n=$Rn4   c=0.0      b=$Rbp1
q
$end do

/*(2)* to set boundary conditions on first element
$do $Icur 1 1
draw poly mate=$Fmat  phas=90-$Rang  perm=$mu1
     cart $Rx3   $Ry3
     pola $Rr6   $Rt6  n=$Rn7   c=0.0      b=$Rbn  f=NO
     pola $Rr5   $Rt5  n=$Rn6   c=1/$Rr5   b=0.5
     cart $Rx4   $Ry4  n=$Rn5   c=0.0      b=$Rbp  f=V
     fini              n=$Rn3   c=0.0      b=0.5   f=NO
q
$end do

$do $Icur 3 $Nlay 2
draw poly mate=$Fmat  phas=90-$Rang  perm=$mu1
     cart $Rx3   $Ry3
     pola $Rr6   $Rt6  n=$Rn7   c=0.0      b=$Rbn  f=NO
     pola $Rr5   $Rt5  n=$Rn6   c=1/$Rr5   b=0.5
     cart $Rx4   $Ry4  n=$Rn5   c=0.0      b=$Rbp
     fini              n=$Rn3   c=0.0      b=0.5
q
$end do


/*(3)*
$do $Icur 1 1
draw poly mate=0 perm=1
     pola $Rr5   $Rt5
     pola $Rr6   $Rt6  n=$Rn6   c=-1/$Rr6  b=0.5   f=NO
```

```
     pola $Rri1  $Rt11 n=$Rn19  c=0        b=0.5
     pola $Rr10  $Rt10 n=$Rn18  c=1/$Rr10  b=0.5
     fini              n=$Rn17  c=0.0      b=0.5   F=V
q
$end do

$do $Icur 3 $Nlay 2
draw poly mate=0 perm=1
     pola $Rr5   $Rt5
     pola $Rr6   $Rt6  n=$Rn6   c=-1/$Rr6  b=0.5   f=NO
     pola $Rri1  $Rt11 n=$Rn19  c=0        b=0.5
     pola $Rr10  $Rt10 n=$Rn18  c=1/$Rr10  b=0.5
     fini              n=$Rn17  c=0.0      b=0.5
q
$end do

/*(4)*
$do $Icur 1 $Nlay-1 2
draw poly mate=$Sma2   phas=45-$Rang perm=$mu2
     pola $Rr2   $Rt2
     pola $Rr9   $Rt9  n=$Rn8   c=0.0      b=0.5   f=NO
     cart $Rx8   $Ry8  n=$Rn9   c=0.0      b=$Rbn1
     cart $Rx3   $Ry3  n=$Rn12  c=0.0      b=0.5
     fini              n=$Rn2   c=0.0      b=$Rbp1
q
$end do

/*(5)*
$do $Icur 1 $Nlay-1 2
draw poly mate=$Smat    phas=90-$Rang perm=$mu2
     cart $Rx8   $Ry8
     pola $Rr7   $Rt7  n=$Rn10  c=0.0      b=$Rbn  f=NO
     pola $Rr6   $Rt6  n=$Rn11  c=1/$Rr5   b=0.5
     cart $Rx3   $Ry3  n=$Rn7   c=0.0      b=$Rbp
     fini              n=$Rn12  c=0.0      b=0.5
q
$end do

/*(6)*
$do $Icur 1 $Nlay-1 2
draw poly mate=0 perm=1
     pola $Rr6   $Rt6
     pola $Rr7   $Rt7  n=$Rn11  c=-1/$Rr7  b=0.5   f=NO
     pola $Rri2  $Rt12 n=$Rn21  c=0        b=0.5
     pola $Rri1  $Rt11 n=$Rn20  c=1/$Rri1  b=0.5
     fini              n=$Rn19  c=0.0      b=0.5
q
$end do

/---------------------- D-AXIS
$ else

/*(1)*
$do $Icur 1 $Nlay 2
draw poly mate=$Fmat  phas=45-$Rang perm=$mu1
     pola $Rri   $Rt1
     pola $Rr2   $Rt2  n=$Rn1   c=0.0      b=0.5   f=V
     cart $Rx3   $Ry3  n=$Rn2   c=0.0      b=$Rbn1 f=no
     cart $Rx4   $Ry4  n=$Rn3   c=0.0      b=0.5
     fini              n=$Rn4   c=0.0      b=$Rbp1
q
$end do

/*(2)*
$do $Icur 1 $Nlay 2
draw poly mate=$Fmat  phas=90-$Rang  perm=$mu1
     cart $Rx3   $Ry3
     pola $Rr6   $Rt6  n=$Rn7   c=0.0      b=$Rbn  f=NO
     pola $Rr5   $Rt5  n=$Rn6   c=1/$Rr5   b=0.5
     cart $Rx4   $Ry4  n=$Rn5   c=0.0      b=$Rbp
```

```
     fini              n=$Rn3   c=0.0      b=0.5
q
$end do


/*(3)*
$do $Icur 1 $Nlay 2
draw poly mate=0 perm=1
     pola $Rr5   $Rt5
     pola $Rr6   $Rt6  n=$Rn6   c=-1/$Rr6  b=0.5   f=NO
     pola $Rri1  $Rti1 n=$Rn19  c=0        b=0.5
     pola $Rr10  $Rt10 n=$Rn18  c=1/$Rr10  b=0.5
     fini              n=$Rn17  c=0.0      b=0.5
q
$end do

/*(4)*
$do $Icur 1 $Nlay-1 2
draw poly mate=$Sma2   phas=45-$Rang perm=$mu2
     pola $Rr2   $Rt2
     pola $Rr9   $Rt9  n=$Rn8   c=0.0      b=0.5   f=V
     cart $Rx8   $Ry8  n=$Rn9   c=0.0      b=$Rbn1 f=no
     cart $Rx3   $Ry3  n=$Rn12  c=0.0      b=0.5
     fini              n=$Rn2   c=0.0      b=$Rbp1
q
$end do

/*(5)*
$do $Icur 1 $Nlay-1 2
draw poly mate=$Smat    phas=90-$Rang perm=$mu2
     cart $Rx8   $Ry8
     pola $Rr7   $Rt7  n=$Rn10  c=0.0      b=$Rbn  f=NO
     pola $Rr6   $Rt6  n=$Rn11  c=1/$Rr5   b=0.5
     cart $Rx3   $Ry3  n=$Rn7   c=0.0      b=$Rbp
     fini              n=$Rn12  c=0.0      b=0.5
q
$end do

/*(6)*
$do $Icur 1 $Nlay-1 2
draw poly mate=0 perm=1
     pola $Rr6   $Rt6
     pola $Rr7   $Rt7  n=$Rn11  c=-1/$Rr7  b=0.5   f=NO
     pola $Rr12  $Rt12 n=$Rn21  c=0        b=0.5
     pola $Rri1  $Rti1 n=$Rn20  c=1/$Rri1  b=0.5
     fini              n=$Rn19  c=0.0      b=0.5
q
$end do

$ end if


/****** CONVERT FOUR SIDED POLYGONS TO QUADRILATERALS
/**** reg1= $Nmod*($Sreg+1)+1 = 199
/**** reg2= $Nmod*($Sreg+1)+($Nlay*3)=384
conv reg1=199  reg2=384  shap=q



/=====================================================================
/***** CREATE ROTOR SHAFT AND POLE PIECE

$if $qxs NE 0

/create shaft
$para $Icur  1
draw poly mate=$Msh  perm=$muH
     pola $Rr1   $Rt1
     cart $Rx4   $Ry4  n=$Rn4   c=0.0      b=$Rbn1 f=no
```

```
     cart 0      0     n=$Rn13  c=0.0      b=0.5   f=V
     fini              n=$Rn14  c=0.0      b=0.5   f=no
q

/create polepiece
$para $Icur  $Nlay+1
draw poly mate=$Mpp perm=$muP
     pola $Rr5   $Rt5
     cart $Rx4   $Ry4  n=$Rn5   c=0.0      b=$Rbp  f=NO
     pola $Rr1   $Rt1  n=$Rn4   c=0.0      b=$Rbp1
     pola $Rad3  45    n=$Rn15  c=0.0      b=0.5
     fini              n=$Rn16  c=1/$Rad3  b=0.5
q

/create polepiece airgap
draw poly mate=0  perm=1
     pola $Rr5   $Rt5
     pola $Rad3  45    n=$Rn16  c=-1/$Rad3 b=0.5   f=NO
     pola $Rgr   45    n=1      c=0.0      b=0.5
     pola $Rgr   $Rt10 n=2*(45-$Rt10)/$Rotp  c=1/$Rgr   b=0.5
     fini              n=1      c=0.0      b=0.5
q

/---- d-axis
$ else

/create shaft
$para $Icur  1
draw poly mate=$Msh  perm=$muH
     pola $Rr1   $Rt1
     cart $Rx4   $Ry4  n=$Rn4   c=0.0      b=$Rbn1 f=no
     cart 0      0     n=$Rn13  c=0.0      b=0.5   f=no
     fini              n=$Rn14  c=0.0      b=0.5   f=V
q

/create polepiece
$para $Icur  $Nlay+1
draw poly mate=$Mpp perm=$muP
     pola $Rr5   $Rt5
     cart $Rx4   $Ry4  n=$Rn5   c=0.0      b=$Rbp  f=NO
     pola $Rr1   $Rt1  n=$Rn4   c=0.0      b=$Rbp1
     pola $Rad3  45    n=$Rn15  c=0.0      b=0.5   f=V
     fini              n=$Rn16  c=1/$Rad3  b=0.5   f=no
q

/create polepiece airgap
draw poly mate=0  perm=1
     pola $Rr5   $Rt5
     pola $Rad3  45    n=$Rn16  c=-1/$Rad3 b=0.5   f=NO
     pola $Rgr   45    n=1      c=0.0      b=0.5   f=V
     pola $Rgr   $Rt10 n=2*(45-$Rt10)/$Rotp  c=1/$Rgr   b=0.5  f=NO
     fini              n=1      c=0.0      b=0.5
q


$ end if


/***** CONVERT POLEPIECE AIRGAP TO QUADRILATERAL
/**** reg1=  $Nmod*($Sreg+1)+($Nlay*3) + 3 =387

conv reg1=387 reg2=387 shap=q


/$$$$$$$$$$$$$$$$$$$$$$$$$$$$$$$$$$$$$$$$$$$$$$$$$$$$$$$$$$$$$$$$$$$$$$$$$$$$$$$
/$$$$$$$$$$$$$$$$$$$$$$$$ CREATE AIRGAP ELEMENTS $$$$$$$$$$$$$$$$$$$$$$$$$$$$$$
/$$$$$$$$$$$$$$$$$$$$$$$$$$$$$$$$$$$$$$$$$$$$$$$$$$$$$$$$$$$$$$$$$$$$$$$$$$$$


/=================================================================
```

```
/ DEFINE COORDINATES

$cons $Gn3 %int(($Hmod*$Th1d-$Rang)/($Th1d/$Sgn1)+0.5)
$cons $Gn4 $Hmod*$Sgn1-$Gn3

$cons $Gr1  $Rgm
$cons $Gr2  $Rgr
$cons $Gr3  $Rgr
$cons $Gr4  $Rgm
$cons $Gr5  $Rgs
$cons $Gr6  $Rgs
$cons $Gr7  $Rgm
$cons $Gr8  $Rgr
$cons $Gr9  $Rgm
$cons $Gr10 $Rgs

$cons $Gt1  -$Rang
$cons $Gt2  -$Rang
$cons $Gt3  0
$cons $Gt4  0
$cons $Gt5  0
/$cons $Gt6  45-$Rang
$cons $Gt6 $Gn3*$Th1d/$Sgn1
$cons $Gt7  45-$Rang
$cons $Gt8  45-$Rang
$cons $Gt9  45
$cons $Gt10 45

$cons $Gn1  $Rang/$Rotp
$cons $Gn2  (45-$Rang)/$Rotp
/ if 1/$Rotp is odd, must be use an integral number of elements per half slot
/ this integer is defined in stator airgap as $Sgn1

/=================================================================
/ DRAW REGIONS

$if $qxs NE 0

/*(5)* airgap region # 2
draw poly mate=0 perm=1
     pola $Gr4   $Gt4
     pola $Gr3   $Gt3   n=1     c=0.0     b=0.5   f=V
     pola $Gr8   $Gt8   n=2*$Gn2  c=-1/$Gr3 b=0.5   f=NO
     pola $Gr7   $Gt7   n=1     c=0.0     b=0.5   f=No
     fini               n=$Gn2  c=1/$Gr4  b=0.5   f=NO
q

/*(6)* airgap region # 3
draw poly mate=0 perm=1
     pola $Gr5   $Gt5
     pola $Gr4   $Gt4   n=1     c=0.0     b=0.5   f=V
     pola $Gr7   $Gt7   n=$Gn2  c=-1/$Gr7 b=0.5   f=NO
     pola $Gr6   $Gt6   n=1     c=0.0     b=0.5   f=NO
     fini               n=$Gn3  c=1/$Gr6  b=0.5   f=NO
q

$else

/*(5)* airgap region # 2
draw poly mate=0 perm=1
     pola $Gr4   $Gt4
     pola $Gr3   $Gt3   n=1     c=0.0     b=0.5   f=NO
     pola $Gr8   $Gt8   n=2*$Gn2  c=-1/$Gr3 b=0.5   f=NO
     pola $Gr7   $Gt7   n=1     c=0.0     b=0.5   f=V
     fini               n=$Gn2  c=1/$Gr4  b=0.5   f=NO
q

/*(6)* airgap region # 3
draw poly mate=0 perm=1
     pola $Gr5   $Gt5
```

```
     pola $Gr4   $Gt4   n=1     c=0.0     b=0.5   f=no
     pola $Gr7   $Gt7   n=$Gn2  c=-1/$Gr7 b=0.5   f=NO
     pola $Gr6   $Gt6   n=1     c=0.0     b=0.5   f=V
     fini               n=$Gn3  c=1/$Gr6  b=0.5   f=NO
q

$ end if

/=========================================================================
/*****  Convert Airgap to Quadrilaterals

/***** reg1= $Nslt*($Sreg+1)+2*(($Nlay*3)+3) +1
/***** reg2= reg1+ number of airgap regions -1
conv reg1=%int($Nmod*($Sreg+1)+(($Nlay*3)+3)+1)   |
     reg2=%int($Nmod*($Sreg+1)+(($Nlay*3)+3)+2) shap=q


/*************************************************************************
/**** flip rotor if d-axis
$if $qxs EQ 0
$cons $star $Nmod*($Sreg+1)+1
$cons $fin  $Nmod*($Sreg+1)+($Nlay*3)+3+2
copy reg1=%int($star) reg2=%int($fin) t=22.5 mirr=yes
eras reg1=%int($star) reg2=%int($fin)
$end if
```

Appendix D

PC-AXL Design Program

This is a prototype analysis program for axially-laminated motors. It is written in Matlab [37] and is based on the highly successful computer-aided-design (CAD) programs PC-SRD, PC-BDC and PC-DCM produced by the SPEED Laboratory [97].

It reads in a "design" file containing the dimensional information about the motor. An example of this is given in Sec. D.1. The design program consists of two parts. The program `draw.m` (see Sec. D.3) draws a radial and axial cross-section of the rotor. This is useful for sizing the relative proportions of the motor by eye. Examples of the graphics output are shown in Figs. 5.4 and 5.5.

The second program `calc.m` (see Sec. D.4) calculates the unsaturated inductances and the performance of the motor. It is based on the analytical formulas given in Sec. 4.2. A sample output listing is given in Sec. D.2. Presently only a single-layer consequent pole winding is modelled, though other types could be added later. A glossary of the parameters used in the programs is given in Sec. D.5. This section also includes diagrams showing the definitions of the parameters.

A lumped-circuit solver which can interface to PC-AXL is given in App. E.

D.1 Example.m

```
clear
Title= '1ikW Axially-Laminated Synchrel';

inch= 25.4;

% Stator Dimensional Data : assumes round bottomed slots
%        with parallel sided teeth
NPhase= 3;              % number of phases
StatOD= 203.9;          % stator outer diameter [mm]
StatID= 127.0;          % stator inside diameter [mm]
NSlot= 36;              % number of stator slots
StackL= 202.4;          % motor stack length [mm]
SlotOp= 2.92;           % stator slot openings [mm]
TAng= 20;               % tang angle [deg]
TangD= 0.762;           % tang depth [mm]
SlotD= 18.54;           % slot depth measured from airgap [mm]
ToothW= 6.35;           % width of parallel sided teeth [mm]

% Rotor Dimensional Data : axially-laminated construction
NPolePair= 2;           % number of polepairs
Gap= 0.50;              % airgap in mm
ShaftSq= 40;            % edge length of square shaft in mm
NLayer= 62;             % number of layers
TLam= 0.5;              % thickness of lamination in mm
TIns= 0.5;              % thickness of insulation in mm
                        % material types 0=air 1=iron
MatFL= 0;               % first layer material type
MatPP= 0;               % polepiece material type

% Rotor Mechanical Data
NBolt=6;                % number of bolts per pole piece
BoltD= 10;              % bolt diameter in mm
BoltL= 53;              % length of bolt in mm
BoltCl= 3;              % radial clearance from bolt head to airgap
BoltSp= 35;             % spacing between bolts in mm
BoltTD= 1;              % radial thread depth of bolt in mm
DLam= 7800;             % kilograms per cubic metre
BoltYS= 230;            % yield stress of bolt in MPa of stainless steel
ShaftYS= 300;           % yield stress of shaft in MPa of mild steel

% Winding Type : assumes simple equal turn concentric winding
WindingType= 'equal turn, concentric, single layer, integral SPP';
Delta=1;                % delta or star connected
                        % if star then delta=1 else delta=3;
Skew= 0;                % skew in slot pitches
NCoil= 18;              % number of coils
TC= 19;                 % turns per coil
WDia= 0.850;            % wire diameter in mm
NSH= 4;                 % number of strands per conductor
XLend= 0.5;             % end-turn leakage adjustment factor

% Control Data
Io= 15;                 % rated current per phase [Arms]
KDisp= 10;              % dissipation of stator [W/m2/degC]
Wrpm= 1500;             % rated speed [rpm]
Gamma_deg=55;           % maximum-torque-per-ampere angle
```

D.2 Sample Output

```
*******************************************************************************
PC-AXL : AXIALLY-LAMINATED MOTOR DESIGN PROGRAM
31-Aug-93 : Title : 11kW Axially-Laminated Synchrel

STATOR DIMENSIONS ------------------------------------------------------------
NumPhases       3          PolePair        2
Stator ID  127.00 mm       Stator OD  203.90 mm       Stack Len   202.4 mm
Slots          36          Slot Open    2.92 mm       Slot Depth  18.54 mm
Tooth Wdth   6.35 mm       Tooth Angle    20 mDeg     Tang Depth   0.76 mm
Slot Area  106.96 mm^2     Disp Area  0.1950 m^2

ROTOR DIMENSIONS -------------------------------------------------------------
Airgap      0.500 mm       1st Layer      Ins         Pole Piece     Ins
NLayers        62          Lam Thk      0.500 mm      Ins Thk      0.500 mm
Shaft Edge  40.00 mm       Lam Area     1.969 m^2     PoleArc      117.9 eDeg

MECHANICAL QUANTITIES --------------------------------------------------------
NBolts/pole     6          Bolt Diam.   10.0 mm       Bolt Length  53.0 mm
Bolt Clear   3.00 mm       Bolt Sepn    35.00 mm      Thread Dpth  1.00 mm
Bolt Yield    230 MPa      Shaft Yield   300 MPa      Fe rho       7800 kg/m^3
Shft BoltL  13.00 mm       ShftBltClr   2.00 mm       MinBoltCl    2.20 mm
F/Blt tens 11.561 kN       F/Blt Bshr 18.787 kN       F/Blt Sshr 30.631 kN
Fail Speed   5.93 krpm     Inertia  0.039065 kgm^2     Bolt Loss   0.296

WINDING INFORMATION ----------------------------------------------------------
Winding Type : equal turn, concentric, single layer, integral SPP
WindType      star
Num Coils       18         Turn/Coil       19         Strd/Cond        4
WDiam        0.850 mm      Skew             0 slots   CS/Slot          1
MLT stack  404.80 mm       MLT end    359.11 mm       MLT total  763.91 mm
Kdi : dist  0.960          Kci : chord 1.000          Ksi : skew  1.000
Kwi : total 0.960          Nph             114 turns  Rph (20C)   0.661 ohm
SlotArea   106.96 mm^2     SlotFill     0.403
XLend        0.500

ANALYTICAL UNSATURATED INDUCTANCES -------------------------------------------
Kc stator    1.211         Kc rotor     1.083         Kc total     1.312
Ps0          0.600         Ps1          0.261         Ps2          0.093
Ps3          1.142         Ps total     2.096         Lslot        2.310 mH
Lend         1.221 mH      a            0.500         Lleak        3.531 mH
Lm         140.20 mH       Lmq        131.27 mH       Lq         134.80 mH
Ldi          2.908 mH      Lmd          5.816 mH      Ld           9.346 mH
Xi intr     63.50          Xi mag       22.57         Xi act       14.42

CONTROL INFORMATION ----------------------------------------------------------
Io         15.000 Arms     PLoss      0.4465 kW       KDisp       10.00 W/m2/C
Trise      229.01 degC     Gamma       55.00 eDeg     Vph        373.731 Vrms
Tmech      79.578 Nm       Pmech     12.5000 kW       kVA in     16.8179 kVA
PF          0.770          efficiency  0.966         AppPF        0.743

END OF OUTPUT
```

D.3 Draw.m

```
% pc_axl file : draw3.m
% last revised :

if (exist('out.met')==2)
   !erase out.met
end

% 1 : DEFINE PARAMETERS ----------------------------------------
% these must be read in before hand


% 2 : INITIAL CALCULATIONS -------------------------------------
PlotAspectRatio=1.377;    % aspect ratio of plots
rad= pi ./ 180;           % conversion from degrees to radians
deg= 1 ./ rad;            % conversion from radians to degrees
krpm= 1 ./ ( 2 .* pi ) .* 60 ./ 1000;   % rad/s -> krpm

Rr= StatID./2-Gap;           % rotor outer radius in mm


% 3 : CALCULATE ROTOR POINTS -----------------------------------
% this generates plotting arrays of points A, B, C and D which
% define vertices of the laminations

% create an array of the indices of each lamination layers
N= [ (2-MatFL) : 2 : NLayer ];

% calculate the number of lamination and insulator layers below
NLamBelow= fix( (N+MatFL-1)./2 );  % fix rounds to int towards zero
NInsBelow= N - NLamBelow -1;

% calculate bottom left corner of lamination relative to top right
% shaft edge
deltaY= TLam .* NLamBelow + TIns .* NInsBelow;
deltaX= deltaY .* tan(22.5 .* rad);  % argument must be in radians

% calculate bottom left corner in absolute coordinates
Xa= ShaftSq./2 - deltaX;
Ya= ShaftSq./2 + deltaY;

% calculate top left corner position
Xd= Xa - TLam .* tan(22.5 .* rad);
Yd= Ya + TLam;

% calculate coordinates of bottom right corner
Xb= (1 ./ sqrt(2) ) .* ( sqrt(Rr.^2-deltaY.^2) - deltaY );
Yb= sqrt(Rr.^2-Xb.^2);

% calculate coordinates of top right corner
deltaY= deltaY+TLam;
Xc= (1 ./ sqrt(2) ) .* ( sqrt(Rr.^2-deltaY.^2) - deltaY );
Yc= sqrt(Rr.^2-Xc.^2);


% 4 : DRAW ROTOR -----------------------------------------------

% ----- generate appropriate axes
% use a square graph
axis('square');
Ymax= Rr .* 1.1;          % make it slightly bigger than rotor
Xmax= Ymax ;              % the plot has an aspect ratio

axis([-Xmax Xmax -Ymax Ymax]);

% ----- draw square shaft
sq= ShaftSq./2;
```

```
X= [ -sq  sq  sq -sq -sq ];
Y= [ -sq -sq  sq  sq -sq ];

plot(X,Y,'-');

% ----- freeze screen
title('Cross-Sectional View of Rotor');
hold on;

% ----- draw top quarter
Xtq= [ Xa ; Xb ; Xc ; Xd ; -Xd ; -Xc ; -Xb ; -Xa ; Xa ];
Ytq= [ Ya ; Yb ; Yc ; Yd ;  Yd ;  Yc ;  Yb ;  Ya ; Ya ];

plot(Xtq,Ytq,'-');

% ----- draw bottom quarter
X=  Xtq;
Y= -Ytq;                    % reverse Y

plot(X,Y,'-');

% ----- draw right quarter
X= Ytq;
Y= Xtq;

plot(X,Y,'-');

% ----- draw left quarter
X= -Ytq;
Y=  Xtq;
plot(X,Y,'-');

hold off;


% 5 : CALCULATE AND DRAW POLEPIECES ----------------------------

% calculate coordinates of pole piece
N= NLayer;                % take topmost layer

% calculate the number of lamination and insulator layers
% INCLUDING THIS LAYER
NLamBelow= fix( (N+MatFL)./2 );  % fix rounds to int towards zero
NInsBelow= N - NLamBelow;

% calculate top left corner of layer relative to top right
% shaft edge
deltaY= TLam .* NLamBelow + TIns .* NInsBelow;
deltaX= deltaY .* tan(22.5 .* rad);  % argument must be in radians

% calculate top left corner in absolute coordinates
Xe= ShaftSq./2 - deltaX;
Ye= ShaftSq./2 + deltaY;

% calculate coordinates of top right corner
Xf= (1 ./ sqrt(2) ) .* ( sqrt(Rr.^2-deltaY.^2) - deltaY );
Yf= sqrt(Rr.^2-Xf.^2);


% 6 : DRAW POLE-PIECES -----------------------------------------

hold on;

% generate a smooth circular polepiece by interpolation
X= linspace(Xf,-Xf,10);   % interpolate between endpoints
Y= sqrt(Rr.^2-X.^2);      % points lie on circumference

% generate outline of top polepiece
Xt= [ Xe  X  -Xe  Xe];
Yt= [ Ye  Y   Ye  Ye];
```

```
% plot vectors
plot(Xt,Yt,'-');

% ----- draw bottom quarter
X=  Xt;
Y= -Yt;
plot(X,Y,'-');

% ----- draw right quarter
X= Yt;
Y= Xt;
plot(X,Y,'-');

% ----- draw left quarter
X= -Yt;
Y=  Xt;
plot(X,Y,'-');

hold off;
meta out

pause;
axis('normal');

% 7 : DRAW LENGTHWISE VIEW ------------------------------------

% ----- generate appropriate axes
Ymax= max(Rr,StackL ./2 ./PlotAspectRatio) .* 1.2;   % fit into plot
Xmax= Ymax .* PlotAspectRatio;      % the plot has an aspect ratio

axis([-Xmax Xmax -Ymax Ymax]);

% ----- draw rotor outline
x=StackL./2;
y=Rr;
X= [ -x  x  x -x -x ];
Y= [ -y -y  y  y -y ];
plot(X,Y,'-');

% ----- freeze screen
title('LengthWise View of Rotor');
hold on;

% ----- draw shaft outline
x= StackL./2;
y= ShaftSq./2;
X= [ -x  x  x -x -x ];
Y= [ -y -y  y  y -y ];
plot(X,Y,'--');

% ----- draw shaft centreline
X= [ -Xmax  Xmax ];
Y= [     0     0 ];
plot(X,Y,'-.');

% ----- draw polepiece outline
x=StackL./2;

% calculate coordinates of pole piece
NLamBelow= fix( (NLayer+MatFL)./2 );
NInsBelow= NLayer - NLamBelow;
deltaY= TLam .* NLamBelow + TIns .* NInsBelow;
y= ShaftSq./2 + deltaY;

X= [ -x  x  x -x -x ];
Y= [ -y -y  y  y -y ];
plot(X,Y,'--');

% ----- draw bolts
```

```
% absolute position of rightmost bolt
FirstBolt= StackL./2 - (StackL-(NBolt-1).*BoltSp)./2;

% location of each bolt
Offset= linspace(-FirstBolt,FirstBolt,NBolt);

% local coordinates of one bolt
BoltHead= 2 .* BoltD;      % size of head
BoltAngle= 90 .* rad;              % angle subtended by head
HeadLength= (BoltHead-BoltD)./ 2 .* tan(BoltAngle./2);
x1= BoltD./2;
x2= BoltHead ./2;
y1= Rr-BoltCl;             % top of bolt
y2= Rr-BoltCl-HeadLength;  % bottom of head
y3= Rr-BoltCl-BoltL;  % bottom of bolt

X_= [ -x1  x1  x1  x2 -x2 -x1 -x1 ];
Y_= [  y3  y3  y2  y1  y1  y2  y3 ];

% extend to all bolt using matrix operations
X= ( ones(Offset') * X_ )';
Y= ( ones(Offset') * Y_ )';

Offset= ones(X_') * Offset;

X= X+Offset;

plot(X,Y,'--');
plot(X,-Y,'--');

% ----- unfreeze screen
hold off;
meta out1
pause
```

D.4 Calc.m

```
% pc_axl file : calc5.m
% last revised : 7/2/93

% 1 : DEFINE PARAMETERS ----------------------------------------
% these must be read in beforehand

% 2 : INITIAL CALCULATIONS -------------------------------------
rad= pi ./ 180;           % conversion from degrees to radians
deg= 1 ./ rad;            % conversion from radians to degrees
krpm= 1 ./ ( 2 .* pi ) .* 60 ./ 1000;   % rad/s -> krpm

Ri= StatID./2;            % stator inner diameter in mm
Rr= Ri-Gap;               % rotor outer radius in mm
mH= 1000;                 % conversion from H to mH
kW= 0.001;                % conversion from W to kW

CopperResistivity= 0.01724e-6;    % ohms per metre at 20C

% 3 : CALCULATE LAMINATION AREA REQUIRED -----------------------
% calculate total surface area of lamination required

% create an array of the indices of each lamination layers
N= [ (2-MatFL) : 2 : NLayer ];

% calculate the number of lamination and insulator layers below
NLamBelow= fix( (N+MatFL-1)./2 );  % fix rounds to int towards zero
NInsBelow= N - NLamBelow -1;

% calculate bottom left corner of lamination relative to top right
% shaft edge
deltaY= TLam .* NLamBelow + TIns .* NInsBelow;
deltaX= deltaY .* tan(22.5 .* rad);  % argument must be in radians

% calculate bottom left corner in absolute coordinates
Xa= ShaftSq./2 - deltaX;
Ya= ShaftSq./2 + deltaY;

% calculate coordinates of bottom right corner
Xb= ( 1 ./ sqrt(2) ) .* ( sqrt(Rr.^2-deltaY.^2) - deltaY );
Yb= sqrt(Rr.^2-Xb.^2);

% calculate length of lamination (bottom edge)
LamLength= 2 .* ( Xa + sqrt( (Yb-Ya).^2 + (Xb-Xa).^2 ) );

% calculate total lamination area in metres squared
LamArea= NPolePair .* 2 .* sum(LamLength) .* StackL ./ 1e6;


% 4 : CALCULATE BOLT STRESSES ----------------------------------

% ----- calculate maximum allowable bolt forces

% length of bolt which is in shaft is
BoltLS= ShaftSq./2-(Rr-BoltCl-BoltL);

% calculate ShfBltClear which is the clearance between the bolts
% in the shaft
ShfBltClear= ShaftSq ./2 - BoltLS - BoltD ./2 ;

% calculate the minimum clearance between bolt head and airgap
MinBoltCl= BoltCl - (Rr-sqrt(Rr.^2-BoltD.^2));

% diameter definitions
DMinor=BoltD-2*BoltTD;
DMajor=BoltD;

% tensile failure of bolt in Newtons
```

```
FBolt1= (pi./4)*(DMinor^2)*BoltYS;

% shear failure of thread in bolt in Newtons
FBolt2= (pi./4)*(DMinor)*BoltLS*BoltYS;

% shear failure of thread in shaft in Newtons
FBolt3= (pi./4)*(DMajor)*BoltLS*ShaftYS;

% locate minimum quantity
FBoltMax= min(FBolt1,min(FBolt2,FBolt3));


% ----- calculate forces on pole piece

ForcePerOmegaSquared= (StackL./1000) ./ NBolt * DLam ...
       .* ((Rr./1000).^3-(ShaftSq./2000).^3) .* 2 ./ 3 ./ sqrt(2);

% corresponding maximum speed in krpm
UltimateMaxSpeed= sqrt( FBoltMax ./ ForcePerOmegaSquared ) .* krpm;


% 5 : CALCULATE LOSS OF LAMINATION AREA DUE TO BOLTS ----------
% ratio of total lamination axial length loss due to bolt
% holes

BoltAreaLoss= NBolt.*BoltD./StackL;


% 6 : CALCULATE WINDING FACTORS ------------------------------

% calculate fundamental winding factors, assume a single layer
% coil with an integral number of slots per pole per phase
% equal turn concentric winding

% fundamental distribution factor
q= NSlot ./ ( 2 .* NPolePair) ./ NPhase;
SlotPAngM= 2 .*  pi ./ NSlot;
SlotPAngE= SlotPAngM .* NPolePair;
Kd1= sin(SlotPAngE.*q./2)./q./sin(SlotPAngE./2);

% fundamental chording factor : for this simple winding is unity
Kc1= 1;

% fundamental skew factor :
%      Skew= skew in slot pitches
ElecSkew= Skew .* SlotPAngE;
if (Skew==0)
   Ks1=1;
else
   Ks1= sin(ElecSkew)./ElecSkew;
end

% total fundamental winding factor
Kw1= Kd1 .* Kc1 .* Ks1;

% number of coil sides per slot
CoilSidesPerSlot= NCoil .* 2 ./ NSlot;

% total number of series connected turns
Nph= NCoil .* TC ./ NPhase;

% effective number of sine distributed turns
Nse= (4 ./ pi) .* Kw1 .* Nph;


% 7 : CALCULATE EFFECTIVE AIRGAP -----------------------------
% take into account the stator and rotor slotting

% rotor Carter's coefficient : "open" slots
Kcr= carter(TLam,TIns,Gap,'op');
```

```
% stator Carter's coefficient : for semi-closed slots
SlotP= 2 .* pi .* R1 ./ NSlot;
Kcs= carter(SlotP-SlotOp,SlotOp,Gap,'sc');

% effective airgap
EffGap= Gap .* Kcr .* Kcs;


% 8 : CALCULATE ALIGNED MAGNETISING INDUCTANCE ------------------

% inductance of motor with 180 degrees pole pitch
mu_o= 4 .* pi .* 1e-7;
Lm= 3 .* pi .* mu_o .* Nse.^2 .* StackL .* (Rr+Gap./2) ./ ...
    ( 8 .* NPolePair.^2 .* EffGap ) .* 1e-3 ./ Delta;

% actual pole-arc
NLam= fix( (NLayer+MatFL)./2 );   % number of laminations layers
NIns= NLayer-NLam;                % number of insulation layers
StackThickness= NLam .* TLam + NIns .* TIns;
if MatPP==0
   ElecPoleArc= 2 .* NPolePair .* asin(StackThickness./Rr);
else % effectively round rotor
   ElecPoleArc= pi;
end
% inductance of motor with a limited pole-arc
Lmq= Lm .* (ElecPoleArc+sin(ElecPoleArc))./pi;


% 9 : CALCULATE UNALIGNED MAGNETISING INDUCTANCE ---------------

% intrinsic unaligned inductance
Ldi= 3 .* pi .* mu_o .* Nse.^2 .* StackL ./ ( 8 .* NPolePair) ...
       .* 1e-3 ./ Delta;

% add effect of iron in rotor
a= TIns ./ ( TLam + TIns);
Lmd= Ldi./a;

% 10 : CALCULATE SALIENCY RATIO ------------------------------

% intrinsic saliency ratio
Xi_i= StatID ./ ( 2 .* NPolePair .* Gap);

% actual saliency ratio
Xi_m= Lmq ./Lmd;

% 11 : SLOT DIMENSIONS ---------------------------------------

% calculate the length of the back section of the stator tooth
TangD1= ( (R1+TangD) .* tan(SlotPAngM./2) ...
          - SlotOp./2 -ToothW./2 ) .* tan(TAng.*rad);

% calculate other slot dimensions
l_1= TangD;
l_2= TangD1;
l_3= SlotD-l_1-l_2;
w_1= SlotOp;
w_2= 2 .* (R1+TangD+TangD1) .* tan(SlotPAngM./2) - ToothW;
w_3= 2 .* (R1+SlotD) .* tan(SlotPAngM./2) - ToothW;

% the radial position of the centre of the slot bottom curvature
% is
SlotCentreOfCurvature= (R1+SlotD+ToothW./2)./(1+sin(SlotPAngM./2));

% the radius of curvature of the slot bottom is
SlotCurv= R1+SlotD-SlotCentreOfCurvature;

% calculate slot area
% w_4 is the full slot width at the centre of slot curvature
```

```
w_4= 2 .* SlotCentreOfCurvature .* tan(SlotPAngM./2) - ToothW;
SlotArea= 0.50 .* (pi+SlotPAngM) .* SlotCurv.^2 + ...
          (w_2+w_4).*(l_3-SlotCurv)./2;

% 12 : SLOT LEAKAGE INDUCTANCE ------------------------------

% calculate slot permeance components

% a: the slot opening
R_a= SlotOp./2;
R_b= SlotP - R_a;
P_s0= (1 ./ pi) .* log(R_b./R_a);

P_s1= l_1 ./ w_1;

% b : the back of the tooth
P_s2= l_2 ./ (w_2 - w_1) .* log ( w_2 ./ w_1 );

% c : the main part of the tooth
Beta= w_2 ./ w_3;
P_s3= l_3 ./ w_3 .* ( 4 .* Beta.^2 - Beta.^4 - 4 .* log(Beta) - 3)./ ...
      (4 .* (1-Beta) .* (1-Beta.^2).^2);

% sum up components
P_s= P_s0+P_s1+P_s2+P_s3;

% the leakage inductance per phase is
Lslot= 4 .* Nph.^2 .* NPhase .* mu_o .* StackL .* P_s ./ NSlot ..
       .* 1e-3 ./ Delta;

% 13 : STATOR RESISTANCE ------------------------------------

% the mean diameter of the endwindings is
Dend= NPhase .* q ./ NSlot .* pi .* 2 .* (Ri+SlotD./2);

% the mean length per turn is composed of the straight (useful)
% section in the stator (MLT_stack) and the useless section in
% the endwinding (MLT_end)
MLT_end= pi .* Dend;
MLT_stack= 2 .* StackL;
MLT= MLT_end + MLT_stack;

% the total length of conductors is
Lcu= NCoil .* TC ./ NPhase .* MLT;

% the cross-sectional area of copper is
CSA_cu= NSH .* pi .* WDia.^2 ./4;

% the phase resistance is
Rph= CopperResistivity .* (Lcu .* 1e-3) ./ (CSA_cu .* 1e-6) ./ Delta;


% 14 : SLOT FILL --------------------------------------------

AreaCopperInSlot= 2 .* NCoil ./ NSlot .* TC .* NSH ...
                  .* pi .* WDia.^2 ./4 ;
SlotFill= AreaCopperInSlot ./ SlotArea;


% 15 : END-WINDING INDUCTANCE -------------------------------

% the radius of the wire is
Rw= WDia ./2;

% the inductance of one turn of diameter D and wire radius Rw is
L_OneTurn= mu_o .* (Dend.*1e-3) ./ 2 ...
         .* ( (1 + Rw.^2 ./ 2 ./ Dend.^2 ) .* log( 4 .*Dend./Rw ) ...
              + (Rw./Dend).^2 ./6 - 1.75);

% the number of turns per pole-pair per phase is
```

```
N_end= NCoil .* TC ./ (NPhase .* NPolePair);

% the total endwinding inductance is
Lend= L_OneTurn .* NPolePair .* N_end.^2 ./ Delta .* XLend;


% 16 : THERMAL DISSIPATION ------------------------------------

% assume the total loss is simply the copper loss
PLoss= NPhase .* Io.^2 .* Rph;

% the outside surface area of the motor in metre^2 is approximately
ADisp= (pi .* StatOD .* StackL + pi .* StatOD.^2 ./ 2) ./ 1e6;

% the approximate temperature rise is
TRise= PLoss ./ ( KDisp .* ADisp);


% 17 : CALCULATE TOTAL INDUCTANCES ----------------------------

% calculate the total inductances by adding the leakage
% inductances to the magnetising inductances.

Ld= Lmd + Lend + Lslot;
Lq= Lmq + Lend + Lslot;
Xi= Lq ./ Ld;


% 18 : CHARACTERISTICS ----------------------------------------

% calculate the required voltage to drive rated current into the
% machine at the maximum torque per ampere angle.  Neglecting
% saturation this is 45 degrees

% set the current angle
gamma_m= Gamma_deg .* rad;

% calculate the operating speed in rad/s electrical
We= Wrpm ./ 60 .* 2 .* pi .* NPolePair;

Vd= -We .* Lq .* Io .* cos(gamma_m) - Io .* Rph .* sin(gamma_m);
Vq= -We .* Ld .* Io .* sin(gamma_m) + Io .* Rph .* cos(gamma_m);

% the required phase voltage is
Vph= sqrt(Vd.^2 + Vq.^2);

% the output torque is
Torque= NPhase .* NPolePair ...
        .* (0.5) .* (Lq-Ld) .* Io.^2 .* sin( 2 .* gamma_m);

% the output power is
Pmech= Torque .* We ./ NPolePair;

% the input power is (only resistive losses considered)
Pin= Pmech + NPhase .* Io.^2 .* Rph;

% the input kVA is
kVA= 3 .* Vph .* Io;

% the input power factor is
PowerFactor= Pin ./ kVA;

% the efficiency
Efficiency= Pmech ./ Pin;

% the apparent power factor is
ApparentPowerFactor= PowerFactor .* Efficiency;


% 19 : ROTOR INERTIA ------------------------------------------
```

```
% the moment of inertia of the rotor assuming it to be a uniform
% cylinder of density equal to the iron in kgm^2 is
Jrotor= 0.5 .* pi .* StackL .* DLam .* Rr.^4 .* 1e-15;


% 20 : DISPLAY RESULTS ----------------------------------------
clc
home

fprintf('*************************************************************')
fprintf('**********************\n')
fprintf('PC-AXL : AXIALLY-LAMINATED MOTOR DESIGN PROGRAM\n')
fprintf(date)
fprintf(' : Title : ')
fprintf(Title)
fprintf('\n')
fprintf('\n')
fprintf('STATOR DIMENSIONS ------------------------------------')
fprintf('--------------------\n')
fprintf('NumPhases   %5.0f          ',NPhase)
fprintf('PolePair    %5.0f\n',NPolePair)
fprintf('Stator ID  %6.2f mm       ',StatID)
fprintf('Stator OD  %6.2f mm       ',StatOD)
fprintf('Stack Len   %5.1f mm\n',StackL)
fprintf('Slots       %5.0f          ',NSlot)
fprintf('Slot Open  %6.2f mm       ',SlotOp)
fprintf('Slot Depth %6.2f mm\n',SlotD)
fprintf('Tooth Wdth %6.2f mm       ',ToothW)
fprintf('Tooth Angle %5.0f mDeg    ',TAng)
fprintf('Tang Depth %6.2f mm\n',TangD)
fprintf('Slot Area  %6.2f mm^2     ',SlotArea)
fprintf('Disp Area  %6.4f m^2\n',ADisp)

fprintf('\n')
fprintf('ROTOR DIMENSIONS -------------------------------------')
fprintf('--------------------\n')
fprintf('Airgap      %5.3f mm       ',Gap)
fprintf('1st Layer     ');
if (MatFL==0)
   fprintf('Ins          ');
else
   fprintf('Lam          ');
end
fprintf('Pole Piece   ');
if (MatPP==0)
   fprintf(' Ins        ');
else
   fprintf('Iron        ');
end
fprintf('\n')

fprintf('NLayers     %5.0f          ',NLayer)
fprintf('Lam Thk    %6.3f mm       ',TLam)
fprintf('Ins Thk    %6.3f mm\n',TIns)
fprintf('Shaft Edge %6.2f mm       ',ShaftSq)
fprintf('Lam Area   %6.3f m^2      ',LamArea)
fprintf('PoleArc     %5.1f eDeg\n',ElecPoleArc.*deg)

fprintf('\n')

fprintf('MECHANICAL QUANTITIES --------------------------------')
fprintf('--------------------\n')
fprintf('NBolts/pole %5.0f          ',NBolt)
fprintf('Bolt Diam.  %5.1f mm       ',BoltD)
fprintf('Bolt Length %5.1f mm\n',BoltL)
fprintf('Bolt Clear  %5.2f mm       ',BoltCl)
fprintf('Bolt Sepn   %5.2f mm       ',BoltSp)
fprintf('Thread Dpth  %4.2f mm\n',BoltTD)
fprintf('Bolt Yield   %4.0f MPa     ',BoltYS);
```

```
fprintf('Shaft Yield  %4.0f MPa     ',ShaftYS);
fprintf('Fe rho       %5.0f kg/m^3 \n',DLam)
fprintf('Shft BoltL   %5.2f mm      ',BoltLS)
fprintf('ShftBltClr   %5.2f mm      ',ShfBltClear)
fprintf('MinBoltCl    %5.2f mm\n',MinBoltCl)
fprintf('F/Blt tens %6.3f kN      ',FBolt1./1000)
fprintf('F/Blt Bshr %6.3f kN      ',FBolt2./1000)
fprintf('F/Blt Sshr %6.3f kN\n',FBolt3./1000)
fprintf('Fail Speed  %5.2f krpm    ',UltimateMaxSpeed)
fprintf('Inertia  %8.6f kgm^2   ',Jrotor)
fprintf('Bolt Loss   %5.3f\n ',BoltAreaLoss)

pause

fprintf('\n')
fprintf('WINDING INFORMATION ----------------------------------')
fprintf('--------------------\n')
fprintf('Winding Type : ')
fprintf(WindingType)
fprintf('\n')
if (Delta==1)
fprintf('WindType     star\n',NCoil)
end
if (Delta==3)
fprintf('WindType    delta\n',NCoil)
end
if ((Delta~=1) & (Delta~=3))
fprintf('BAD WINDING TYPE : check input file! \n',NCoil)
end

fprintf('Num Coils   %5.0f          ',NCoil)
fprintf('Turn/Coil   %5.0f          ',TC)
fprintf('Strd/Cond   %5.0f\n',NSH)
fprintf('WDiam       %5.3f mm       ',WDia)
fprintf('Skew        %5.0f slots    ',Skew)
fprintf('CS/Slot     %5.0f \n',CoilSidesPerSlot)
fprintf('MLT stack %7.2f mm       ',MLT_stack)
fprintf('MLT end   %7.2f mm       ',MLT_end)
fprintf('MLT total %7.2f mm\n',MLT)
fprintf('Kdi : dist  %5.3f          ',Kdi)
fprintf('Kci : chord %5.3f          ',Kci)
fprintf('Ksi : skew  %5.3f\n',Ksi)
fprintf('Kwi : total %5.3f          ',Kwi)
fprintf('Nph         %5.0f turns    ',Nph)
fprintf('Rph (20C) %7.3f ohm\n',Rph)
fprintf('SlotArea    %6.2f mm^2     ',SlotArea)
fprintf('SlotFill    %5.3f\n',SlotFill)
fprintf('XLend       %5.3f\n',XLend)


fprintf('\n')
fprintf('ANALYTICAL UNSATURATED INDUCTANCES --------------------')
fprintf('--------------------\n')

fprintf('Kc stator   %5.3f          ',Kcs)
fprintf('Kc rotor    %5.3f          ',Kcr)
fprintf('Kc total    %5.3f\n',Kcs.*Kcr)

fprintf('Ps0         %5.3f          ',P_s0)
fprintf('Psi         %5.3f          ',P_si)
fprintf('Ps2         %5.3f\n',P_s2)

fprintf('Ps3         %5.3f          ',P_s3)
fprintf('Ps total    %5.3f          ',P_s)
fprintf('Lslot     %7.3f mH\n',Lslot.*mH)
fprintf('Lend      %7.3f mH       ',Lend.*mH)
fprintf('a           %5.3f          ',a)
fprintf('Lleak      %6.3f mH\n',(Lend+Lslot).*mH)

fprintf('Lm          %6.2f mH       ',Lm.*mH)
```

```
fprintf('Lmq        %6.2f mH      ',Lmq.*mH)
fprintf('Lq         %6.2f mH\n',Lq.*mH)

fprintf('Ldi        %6.3f mH      ',Ldi.*mH)
fprintf('Lmd        %6.3f mH      ',Lmd.*mH)
fprintf('Ld         %6.3f mH\n',Ld.*mH)

fprintf('Xi intr    %6.2f         ',Xi_i)
fprintf('Xi mag     %6.2f         ',Xi_m)
fprintf('Xi act     %6.2f\n',Xi)

pause

fprintf('\n')
fprintf('CONTROL INFORMATION ----------------------------------')
fprintf('--------------------\n')
fprintf('Io          %6.3f Arms    ',Io)
fprintf('PLoss     %7.4f kW      ',PLoss.*kW)
fprintf('KDisp       %5.2f W/m2/C\n',KDisp)
fprintf('Trise     %7.2f degC    ',TRise)
fprintf('Gamma      %6.2f eDeg    ',Gamma_deg)
fprintf('Vph       %7.3f Vrms\n',Vph)
fprintf('Tmech     %7.3f Nm      ',Torque)
fprintf('Pmech     %7.4f kW      ',Pmech.*kW)
fprintf('kVA in    %7.4f kVA \n',kVA.*kW)
fprintf('PF          %5.3f         ',PowerFactor)
fprintf('efficiency  %5.3f         ',Efficiency)
fprintf('AppPF       %5.3f\n',ApparentPowerFactor)

fprintf('\n');
fprintf('END OF OUTPUT\n');

pause
```

D.5 Glossary of Symbols

a	ratio of rotor which is insulation $w_{ins}/(w_{ins} + w_{lam})$	
ACu	area of copper conductors used	[m^2]
ADisp	area available for heat dissipation	[m^2]
ALam	total area of rotor laminations required	[m^2]
ASlot	total slot area	[m^2]
BoltCl	bolt clearance, head to airgap	[m]
BoltD	bolt diameter	[m]
BoltL	bolt length	[m]
BoltLS	bolt length in shaft	[m]
BoltLoss	percentage of rotor length covered by bolts	
BoltSp	spacing between adjacent bolts	[m]
BoltTD	radial bolt thread depth	[m]
BoltYS	yield stress of bolt material	[MPa]
DLam	density of lamination material	[kgm^{-3}]
FBolt	force on each bolt at rated speed	[N]
FBoltMax	strength of bolt	[N]
Gap	radial airgap	[m]
Io	rated stator current	[Arms]
Jrot	moment of inertia of rotor	[kgm^2]
KDisp	thermal dissipation of motor frame	[$W/m^2/°C$]
Kc1	fundamental chording factor	
Kd1	fundamental distribution winding factor	
Ks1	fundamental skew winding factor	
Kw1	total fundamental winding factor	
Kcr	rotor Carter's coefficient	
Kcs	stator Carter's coefficient	
Kct	total stator and rotor Carter's coefficient	
Lm	phase inductance of smooth round rotor machine	[H]
Lmd	d-axis magnetising inductance	[H]
Ld	total d-axis inductance	[H]
Ldi	intrinsic d-axis magnetising inductance	[H]
Lmq	q-axis magnetising inductance	[H]
Lq	total q-axis inductance	[H]
Lslot	stator slot leakage inductance	[H]

Lend	stator endwinding leakage inductance	[H]
MatFL	material type of first layer, 0 = air, 1 = iron	
MatPP	material type of pole piece, 0 = air, 1 = iron	
MLT	mean length of stator winding	[m]
NBolt	number of bolts per pole	
NCoil	number of coils in motor	
NLayer	number of rotor layers per pole	
Nph	number of series turns per stator phase	
NPhase	number of phases	
NPolePair	number of pole pairs	
NSH	number of strands in hand	
NSlot	number of stator slots	
PoleArc	rotor pole arc	[edeg]
q	number of slots per pole per phase	
R1	Stator Inner Radius	[m]
Rph	phase resistance	[ohms]
Rr	Rotor Radius	[m]
ShaftSq	edge length of square shaft	[m]
ShaftYS	yield stress of shaft material	[MPa]
SlotArea	area of slot available for winding	$[m^2]$
SlotD	stator slot depth	[m]
SlotOp	stator slot opening	[m]
SlotP	slot pitch	[m]
SlotPAngM	slot pitch angle, mechanical	[mdeg]
SlotPAngE	slot pitch angle, electrical	[edeg]
SlotSp	width of stator slot winding retainer	[m]
StackL	rotor and stator stack length	[m]
StatID	stator inside diameter	[m]
StatOD	stator outside diameter	[m]
TangD	depth of stator tooth tang	[m]
TAng	angle of stator tooth tang	[mdeg]
TC	turns per coil	
TIns	thickness of rotor insulation material	[m]
TLam	thickness of rotor lamination material	[m]
ToothW	width of stator tooth, parallel	[m]
TRise	estimated winding temperature rise	[°C]
WDia	bare copper, wire diameter	[m]

Wrpm	mechanical speed	[rpm]
We	electrical speed	[e rad/s]
Wm	mechanical speed	[m rad/s]
Xi	saliency ratio : Lq/Ld	
Xi_i	intrinsic saliency ratio of machine	
Xi_m	magnetising saliency ratio : Lmq/Lmd	

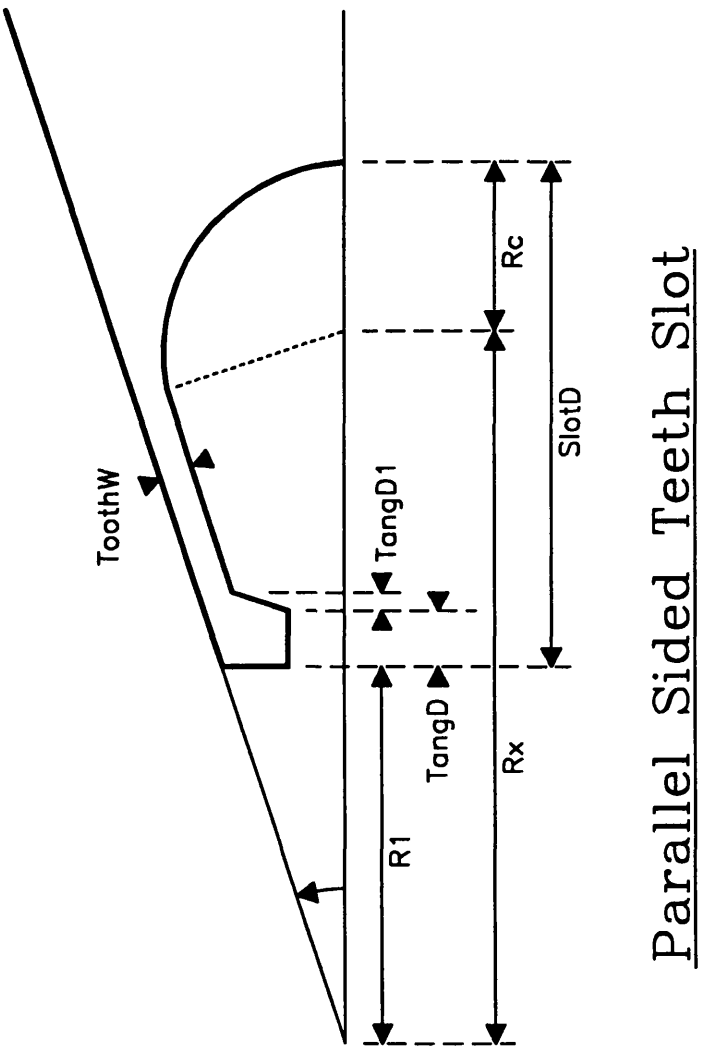

Figure D.1: *Slot dimensions.*

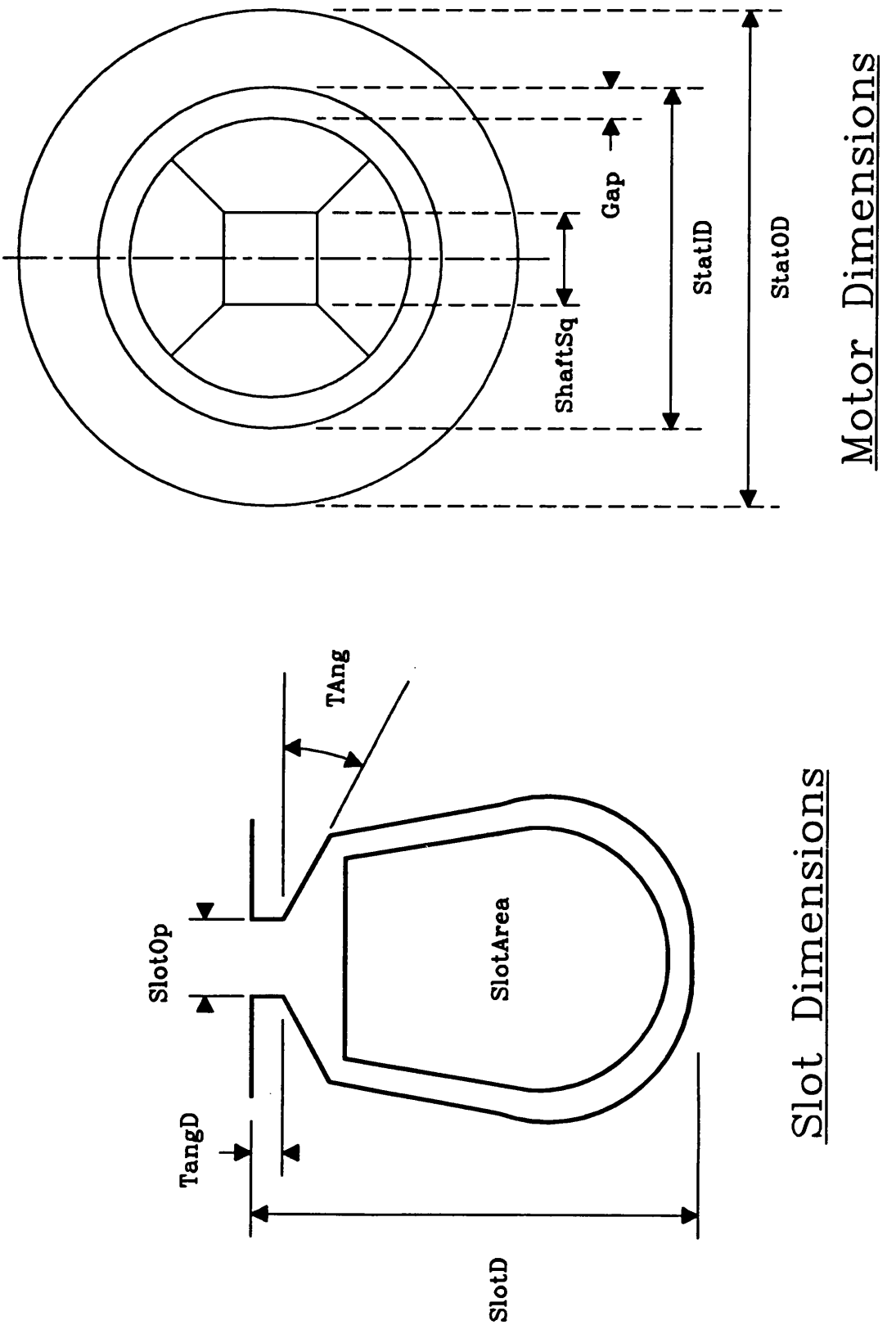

Figure D.2: *Slot and radial view dimensions.*

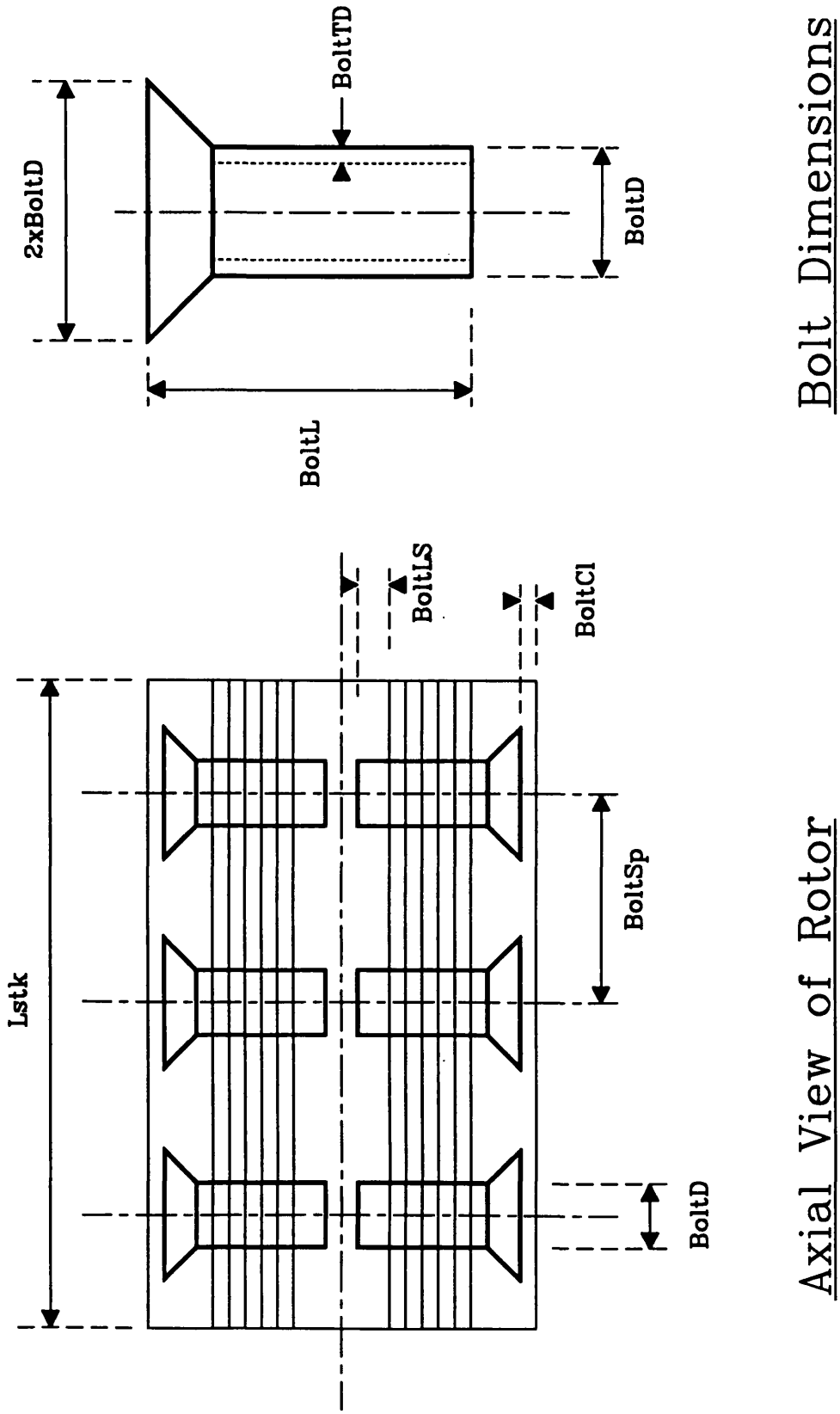

Figure D.3: *Bolt and axial view dimensions.*

Appendix E

Lumped-Circuit Analysis Program

This is a general-purpose lumped-circuit program for solving non-linear magnetic circuits. It is written in Matlab [37]. Its operation is described in Sec. 4.3. A brief description of the variables used and the analysis programs are given in Sec. E.1. This is followed by listings of all the Matlab subroutines.

It has been used in conjunction with the PC-AXL (described in App. D) to analyse the saturation characteristics of the 120W axially-laminated motor (see Chapter 4). More work is required in order to make the interface between PC-AXL and the lumped-circuit solver transparent to the user.

E.1 Read.me

```
%%%%%%%%%%%%%%%%%%%%%%%%%%%%% INPUTS %%%%%%%%%%%%%%%%%%%%%%%%%%%%%%%%

-----------------------------------------------------------------
Sizes :

indicates sizes of matrices used in problem

Sizes(1)= number of materials used (B)
Sizes(2)= number of reluctances used (M)
Sizes(3)= number of independent circuits or fluxes (N)

-----------------------------------------------------------------
SourceList

This is a n x 2 matrix of the form :
     LoopNumber     SourceValue
where LoopNumber indicates which mesh loop the source is in and
SourceValue is its value.  This is positive if the source is
aiding current flow in that loop and negative if it is retarding
it.  The LoopNumbers can be in any order and there can be more
than source in each loop.

-----------------------------------------------------------------
Material Types

This consists of a vector Ur with values 1..6 corresponding to
linear materials.  Materials 7, 8 and 9 are non linear materials
which are strings storing function names whose input is H is A/m
and which return the relevant value of B in T.

1 : air : Uri=1
2 : linear : Ur2=
3 : linear : Ur3=
4
5
6
7 : uses cubic spline interpolant stored in RotorSteel
8 : uses cubic spline interpolant stored in StatorSteel


-----------------------------------------------------------------
ReluctList

is an ( M x 4 ) matrix describing each of the "M" lumped circuit
reluctances.  It is of the form

Num LPath     Area MatType

where
     Num : is the reference number associated with the reluctance
          this must start from 1, 2 ... M
     PathL is length of path in [mm]
     Area is area of path in [mm2]
     MatType is material type code, integer from 1..B


-----------------------------------------------------------------
ConnList :

is a linear list of elements each which consists of an equal
length string of the form :
'm,n,a,b,c   '
where m and n are the row and column number and a, b ,c etc are
positive integers referring to elements of ReluctList.  The
matrix elements can be listed in any order.  There must be at
least one reluctance list element in each list.
```

```
Only elements in the upper diagonal matrix should be listed, eg.
m<=n.  The lower diagonal will be created automatically.


%%%%%%%%%%%%%%%%%%%% INTERMEDIATE VARIABLES %%%%%%%%%%%%%%%%%%%%

----------------------------------------------------------------
Sources

This is a n x 1 matrix of sources.

creator : GenSrc

----------------------------------------------------------------
RelElements

This is a m x 1 matrix of reluctances.  In general these are non-
linear functions of the flux in each element.  Thus their values
must be successively refined.

creator : GenRel (first estimate)

----------------------------------------------------------------
ConnRel

is an (n^2) x m  matrix which allows the creation of the
reluctance matrix RelMatrix.  It describes how each element of
RelMatrix is a linear combination of elements in RelElements.
RelMatrix is formed by reshaping (and transposing) the product of
ConnRel x RelElements.

creator : GenCnR

----------------------------------------------------------------
RelMatrix

is a n x n square matrix whose size is determined by InitFlux and
whose elements contain the present estimates of the values of the
reluctances.

creator : solver

----------------------------------------------------------------
ConnFlux

is rectangular matrix of elements of values 1,0,-1.  It is used
to calculate the flux in each reluctance by the equation
Flux= ConnFlux * InitFlux
It is generated externally from ConnList.

----------------------------------------------------------------
RelFlux

is the flux in each reluctance
               Flux= ConnFlux * Flux

%%%%%%%%%%%%%%%%%%%%%%%%%%%% FUNCTIONS %%%%%%%%%%%%%%%%%%%%%%%%%%%%

----------------------------------------------------------------
GenRel

input : RelList, Ur, StatorSteel, RotorSteel
output : RelElements

This function returns the linear value of reluctances in the
matrix RelElements.  For non-linear values of reluctance it
calculates the the value of reluctance at a fixed value of MMF
chosen to be low enough such that the material will be in its
linear region.
```

```
------------------------------------------------------------------
GenSrc

input : SourceList
output : Sources

This reads in the SourceList and creates the output matrix
Sources.

errors :
1) checks to make sure at least one source is defined.


------------------------------------------------------------------
GenCnR

INPUT : ConnList
OUTPUT : ConnRel

This reads the ConnList and creates ConnRel.

METHOD :

1) initializes ConnRel as a zero matrix of size (n^2) x m

2) reads in strings from ConnList one at a time, disassembles
them into vectors.  Performs error checking on vectors (see
below).  If OK sets appropriate elements in ConnList.


ERRORS :
1) checks that each (row,col) index is within the size bounds and
     that the reluctance index number exists.
2) checks that there is at least one reluctance reference in each
     row of ConnList
3) checks that there are no references to reluctances in the
     lower diagonal
4) checks that there are no duplicate references to the same row
     and column

------------------------------------------------------------------
GenCFlx

INPUT : ConnList
OUTPUT : ConnFlux


SUMMARY:

This reads ConnList and creates ConnFlux

It assumes GenCnR has already been run and has picked up any of
the above errors in ConnList.


METHOD :

1) initialise ConnFlux as a zero matrix of size m x n

2) read row in one at a time
     assume row is  m, n , a , b, c ... z

3) for each reluctance i=a..z
     if ConnFlux(i,m)==0
          if "i"th row of ConnFlux are all zeros
               ConnFlux(i,m)=1
          else
               ConnFlux(i,m)=-1
     if ConnFlux(i,n)==0
          if "i"th row of ConnFlux are all zeros
```

```
            ConnFlux(i,n)=1
        else
            ConnFlux(i,n)=-1

4) repeat for all rows

5) check at end that sum of each row is either 0 or 1
   and that the sum of the absolute value of each row is either 1
     or 2.


ERRORS :

1) it checks to make sure each element in RelElements is referred
to at least once

2) checks to make sure that reluctances are not referenced by more
than two loops.


-----------------------------------------------------------------
UpdateR

input : RelList, Ur, StatorSteel, RotorSteel, RelFlux, RelElements
output : RelElements

This program updates the values of RelElements using RelFlux.

For each element in RelList it calculates the value of B in the
element and the required H. From the old value of reluctance it
then calculates the MMF across the element in the last solution.
It then calculates the reluctance of the element at this value of
MMF and updates the reluctance.


-----------------------------------------------------------------
Solver

input : Sizes, SourceList, Ur, RotorSteel, StatorSteel,
          ConnList, ReluctList
output : mesh fluxes

This program uses the preceeding programs to solve for the fluxes
in the problem.  It iterates until each element of the solution
changes by less than 0.1% relative to itself in three iterations.
```

E.2 Example.m

```
%%%%%%%%%%%%%%%%%%%%%%%%%%%%%%%%%%%%%%%%%%%%%%%%%%%%%%%%%%%%%%%%%%%%%%%
% SYSTEM DEFINITION

kw120          % example PC-AXL dimension data input file
calc           % PC-AXL calculation program

%-------------------------------------------------------------
% SIZES OF MATRICES

% number of material types
Sizes(1)= 2;

% number of reluctances
Sizes(2)= 9;

% number of fluxes or independent circuits
Sizes(3)= 3;


%-------------------------------------------------------------
% SOURCELIST : define sources

TurnsPerCoil= 92;
RMSCurrent= 1.7      % current in amps
Current= sqrt(2) .* RMSCurrent;
MI_Aphase= TurnsPerCoil .* Current;
MI_Bphase= MI_Aphase ./ 2;

SourceList= ...
[ 1   MI_Aphase ;
  2   MI_Bphase ;
  3   MI_Bphase ];


%-------------------------------------------------------------
% MATERIAL TYPES

Ur(1)= 1;
Ur(2)= 10000;

load new800.bh
new800hb= spline(new800(:,2),new800(:,1));
new800bh= spline(new800(:,1),new800(:,2));

RotorSteelHB= new800hb;
StatorSteelHB= new800hb;
RotorSteelBH= new800bh;
StatorSteelBH= new800bh;

%-------------------------------------------------------------
%%%%%% Define Main Dimensions in [millimetres]
% The following parameters are defined/calculated in calc
% StatID          : stator inside diameter [mm]
% Gap             : mechanical airgap [mm]
% SlotP           : slot pitch at the stator inside D[mm]
% StackL          : stack length [mm]
% ToothW          : tooth width [mm]
% SlotD           : total depth of slot [mm]
% SlotCurv        : radius of curvature of slot bottom [mm]
% TangD           : depth of tang [mm]
% TangDi          : depth of tang back angle [mm]

%%%%%% GENERATE LIST OF RELUCTANCES
% three columns : Length : area : Material Code
% see diagram in notes for numbering
% material 1 : air
% material 2 : steel, assume infinite permeability
```

```
GapArea= SlotP .* StackL;
StatorMaterial= 7;
ToothArea= ToothW .* StackL;
ToothL= SlotD-SlotCurv-TangD-TangDi;  % straight length of tooth
MinBackIron= StatOD./2-(Ri+SlotD);
BackIronL= 2 .* pi .* (StatOD-MinBackIron) ./ 2 ./ NSlot;
BackIronArea= (MinBackIron+SlotCurv./3).*StackL;

% This factor takes care of a finite polearc for two slot per
% per motors with polearcs between 90 to 150 degrees
XPArc= (ElecPoleArc-pi./2)./(pi./3);

ReluctList=  ...
[ 1 EffGap          GapArea.*XPArc  1              ;
        2       ToothL          ToothArea       StatorMaterial ;
        3       BackIronL       BackIronArea    StatorMaterial ;
        4       EffGap          GapArea         1              ;
        5       ToothL          ToothArea       StatorMaterial ;
        6       BackIronL       BackIronArea    StatorMaterial ;
        7       EffGap          GapArea./2      1              ;
        8       ToothL          ToothArea./2    StatorMaterial ;
        9       BackIronL       BackIronArea    StatorMaterial ];


%%%%%%%%%%%%%%%%%%%%%%%%%%%%%%%%%%%%%%%%%%%%%%%%%%%%%%%%%%%%%%%%%%%%%%%%%%%
% CONNECTIVITY LIST
% format= 'row,column, list of reluctances'

ConnList = ...
[  '1,1, 1,2,3          ';
           '1,2, 1,2            ';
           '2,2, 1,2,4,5,6      ';
           '2,3, 4,5            ';
           '3,3, 4,5,7,8,9      ']

%%%%%%%%%%%%%%%%%%%%%%%%%%%%%%%%%%%%%%%%%%%%%%%%%%%%%%%%%%%%%%%%%%%%%%%%%%%
solver

%%%%%%%%%%%%%%%%%%%%%%%%%%%%%%%%%%%%%%%%%%%%%%%%%%%%%%%%%%%%%%%%%%%%%%%%%%%
% calculate inductances
L_Aphase= 8 .* TurnsPerCoil .* NewFlux(1) ./ Current
L_Bphase= 8 .* TurnsPerCoil .* (NewFlux(2)+NewFlux(3)) ./ Current
L_Av= (2 ./ 3) .* (L_Aphase+L_Bphase./2)
```

E.3 Solver.m

```
%%%%%%%%%%%%%%%%%%%%%%%%%%%%%%%%%%%%%%%%%%%%%%%%%%%%%%%%%%%%%%%%%%%%%%%%%%%%
% 1 : INITIALISATION

M= Sizes(2); % number of reluctances
N= Sizes(3);    % number of loops

% create sourcelist
Sources= gensrc(Sizes,SourceList);

% create connection matrix
ConnRel= gencnr(Sizes,ConnList);

% create flux matrix
ConnFlux= gencflx(Sizes,ConnList);

% calculate initial values for reluctance
RelElements= genrel(Sizes,ReluctList,Ur,StatorSteel,RotorSteel);


%%%%%%%%%%%%%%%%%%%%%%%%%%%%%%%%%%%%%%%%%%%%%%%%%%%%%%%%%%%%%%%%%%%%%%%%%%%%
% 2 :

% initialise solver
OldFlux= ones(M,1);
good=0;
MaxCount= 100;
count=0;

while ((~good)&(count<=MaxCount))

   fprintf('Solving Equations\n')
   % create reluctance matrix
   RelMatrix= reshape(ConnRel*RelElements,M,M);

   % create upper diagonal part
   RelMatrix= RelMatrix + RelMatrix'.*(1-eye(length(RelMatrix)));

   % solve for new fluxes
   NewFlux= inv(RelMatrix) * Sources;

   % solve for flux in each reluctance
   RelFlux= ConnFlux*NewFlux;

   % update reluctances
   NewRelElements=updateR(RelElements,RelFlux,ReluctList, ...
Ur,StatorSteel,RotorSteel);
   RelElements= NewRelElements;


   % calculate error
   Error= NewFlux-OldFlux;
   RelError= Error./NewFlux
   Tolerance= 1e-3;

   good= all(abs(RelError)<Tolerance);
   OldFlux= NewFlux;
   count= count+1;

 end

i
NewFlux
fprintf('Finished.\n')
```

E.4 Gensrc.m

```
function Sources=gensrc(Sizes,SourceList)
% lumped circuit operation file : gensrc.m
% reads SourceList and creates Sources
% see read.me
% last revised 4/12/92

fprintf('Creating Source Vector ...\n')

% initialise Sources
Sources= zeros(Sizes(3),1);

% size of sourcelist
Index= SourceList(:,1);
Value= SourceList(:,2);

% set values, this must be done sequentially as Index may contain
% identical values
for i=1:length(Index)
Sources(Index(i))= Sources(Index(i))+Value(i);
end

% check at least one non-zero source has been set
result= sum(abs(Sources));

if (result<eps)
  fprintf('     WARNING : GenSrc : no sources have been set\n')
end
```

E.5 Gencnr.m

```
function ConnRel=gencnr(Size,ConnList)
% lumped circuit operation file : gencnr.m
% creates connection matrix for reluctances
% see read.me
% last revised 4/12/92

fprintf('Forming Connection Matrix ...\n')

% initialise matrix
M= Size(2); % number of reluctances used
N= Size(3); % number of independent circuit loops
ConnRel= zeros(N.^2,M);

% find size of list
[listsize cols]= size(ConnList);

% operate on each row sequentially

for i=1:listsize

   % extract information from string into a vector
   op= ['list = [',ConnList(i,:),'];'];
   eval(op);

   % extract the row and column number and then delete them from list
   row_no= list(1);
   col_no= list(2);
   list(1)= [];
   list(1)= [];

   % check row for correctness
   good= (length(list)>0)&(all(list<=M))&(all(list)>=0) ...
        &(row_no>0)&(row_no<=N)&(col_no>0)&(col_no<=N);

   % list is now an array of reluctance indices which make up the
   % lumped circuit reluctance under consideration, add them together

   if (good)

      ConnRelRow= (row_no-1).*N+col_no;

      % check that row has not already been referred to
      if (sum(abs(ConnRel(ConnRelRow,:)))~=0)
         fprintf('     WARNING : GenCnr : multiple reference in')
         fprintf(' ConnList row %3.0f \n',i)
      end

      % if along main diagonal they should be positive else negative
      if (row_no==col_no)
         ConnRel(ConnRelRow,list)= ones(list);
      else
         ConnRel(ConnRelRow,list)= -ones(list);
      end

      % check that no references in list were repeated
      % if this is the case, the number of non-zero elements in
      % the row in ConnRel will be less than the length of list
      repeat= (sum(abs(ConnRel(ConnRelRow,:)))~=length(list));
      if repeat
         fprintf('     WARNING : GenCnr : repeated references in row')
         fprintf(' ConnList row %3.0f \n',i)
      end

      % check reference is not in lower diagonal
      if (row_no>col_no)
         fprintf('     WARNING : GenCnr : lower diagonal references in')
         fprintf(' ConnList row %3.0f \n',i)
```

```
      end

   else % if bad
      fprintf('     WARNING : GenCnR : syntax error in ConnList')
      fprintf(' row %3.0f \n',i)
   end

end  % of for each row of ConnList

% check that each reluctance element is referred to at least once
UnRefRel= ~all(sum(abs(ConnRel))>0);
if UnRefRel
   fprintf('     WARNING : GenCnr : Unreferenced reluctances found.')
   indices = find(sum(abs(ConnRel))==0)
end
```

E.6 Gencflx.m

```
function ConnFlux=gencflx(Sizes,ConnList)
% lumped circuit operation file : gencflx
% reads SourceList and creates Sources
% see read.me
% last revised 4/12/92

fprintf('Creating Flux Matrix ...\n')

%%%%%%%%%%%%%%%%%%%%%%%%%%%%%%%%%%%%%%%%%%%%%%%%%%%%%%%%%%%%%%%%%%%%%%%%%%%
% This program takes the connectivity list ConnList and
% generates the flux connectivity matrix ConnFlux which allows
% simple calculation of the flux in each reluctance knowing the
% flux in each circuit loop.

%%%%%%%%%%%%%%%%%%%%%%%%%%%%%%%%%%%%%%%%%%%%%%%%%%%%%%%%%%%%%%%%%%%%%%%%%%%
% SET UP

% disassemble sizes
NumMaterials = Sizes(1);
NumReluctances = Sizes(2);
NumFluxes = Sizes(3);

% initialise ConnFlux matrix
ConnFlux= zeros(NumReluctances,NumFluxes);

%%%%%%%%%%%%%%%%%%%%%%%%%%%%%%%%%%%%%%%%%%%%%%%%%%%%%%%%%%%%%%%%%%%%%%%%%%%
% WORK THROUGH CONNECTION LIST SETTING APPROPRIATE ELEMENTS IN
% RELMATRIX

[listsize cols]= size(ConnList);

for i=1:listsize

   % extract information from string into a vector
   op= ['list = [',ConnList(i,:),'];'];
   eval(op);

   % extract the row and column number and then delete them from list
   row_no= list(1);
   col_no= list(2);
   list(1)= [];
   list(1)= [];

   % list : is now an array of reluctance indices which make up the
   %  lumped circuit reluctance under consideration.
   % col_no : describes which flux loop is under consideration
   % check if element is already non-zero, if so do nothing
   % else if zero, check if any other elements in row have been set
   % if yes, set element to -1, else set to 1

   % set corresponding element in ConnFlux to 1
   for i=1:length(list)

      row= list(i);

      if (ConnFlux(row,row_no)==0)
         if any(ConnFlux(row,:)~=0)
            ConnFlux(row,row_no)=-1;
         else
            ConnFlux(row,row_no)=1;
         end
      end

      if (ConnFlux(row,col_no)==0)
         if any(ConnFlux(row,:)~=0)
            ConnFlux(row,col_no)=-1;
         else
```

```
            ConnFlux(row,col_no)=1;
          end
       end

   end

end  % of for each row of ConnList


%%%%%%%%%%%%%%%%%%%%%%%%%%%%%%%%%%%%%%%%%%%%%%%%%%%%%%%%%%%%%%%%%%%%%%%%%%%
% ERROR CHECKING

% check that each reluctance has been referred to either once or
% twice but not more

Check1= sum(ConnFlux');
Check2= sum(abs(ConnFlux'));

error= (Check1<0)|(Check1>1)|(Check2<1)|(Check2>2);
if any(error~=0)
   fprintf('     WARNING : GenCFlx : error in reluctance reference.\n')
   indices= find(error~=0)
end
```

E.7 Genrel.m

```
function RelElements=genrel(Sizes,RelList,Ur,StatorSteel,RotorSteel)
% lumped circuit operation file : genrel.m
% creates initial values for reluctances
% see read.me
% last revised 4/12/92

fprintf('Calculating Linear Values for Reluctances ...\n')

% initialise Sources
RelElements= zeros(Sizes(2),1);

% dissect RelList
Index= RelList(:,1);
Path= RelList(:,2)./1e3;  % convert to metres
Area= RelList(:,3)./1e6;  % convert to metres squared
Material = RelList(:,4);

% define Uo
Uo= 4 * pi * 1e-7;

% mmf at which reluctance of non-linear materials is calculate
deltaH= 50;

% for each element
for i=1:length(Index)
   if (Material(i)<=6)
      % material is linear with relative permeability Ur
      RelElements(i)=Path(i)./(Area(i).*Uo.*Ur(Material(i)));
   end

   if (Material(i)==7)
      U=ppval(RotorSteel,deltaH)./deltaH;
      RelElements(i)=Path(i)./(Area(i).*U);
   end

   if (Material(i)==8)
      U=ppval(StatorSteel,deltaH)./deltaH;
      RelElements(i)=Path(i)./(Area(i).*U);
   end


end % of for
```

E.8 Updater.m

```
function RelElements= updateR(RelElements,RelFlux,RelList, ...
Ur,StatorSteel,RotorSteel)
% lumped circuit operation file : updateR.m
% revises estimate for RelElements based on fluxes
% see read.me
% last revised 4/12/92

% dissect RelList
Index= RelList(:,1);
Path= RelList(:,2)./1e3;  % convert to metres
Area= RelList(:,3)./1e6;  % convert to metres squared
Material = RelList(:,4);

% find the mmf across each reluctance
mmf= abs(RelElements .* RelFlux);

% convert mmf to a H
H= mmf ./ Path;
Uo= 4 .* pi .* 1e-7;

% calculate B for each H
B=zeros(H);
for i=1:length(H)

   if (Material(i)<=6)
      B(i)= Uo .* Ur(Material(i)) .* H(i);
   end

   if (Material(i)==7)
      B(i)=ppval(StatorSteel,H(i));
   end

   if (Material(i)==8)
      B(i)=ppval(RotorSteel,H(i));
   end

   if ((~(Material(i)<=6))&(~(Material(i)==7))&(~(Material(i)==8)))
      fprintf('Unknown Material Type ...\n')
   end

end


% calculate reluctance
Flux= B .* Area;
RelElements= mmf ./ Flux;
```

References

[1] T. Kenjo, *Electric Motors and Their Controls.* Oxford University Press, 1991.

[2] T. M. Jahns, "Flux-weakening regime operation of an interior permanent magnet synchronous motor drive," *IEEE Trans. Ind. Appl.*, vol. 23, pp. 681–689, Jul./Aug. 1987.

[3] T. Sebastian and G. R. Slemon, "Operating limits of inverter-driven permanent magnet motor drives," *IEEE Trans. Ind. Appl.*, vol. 23, pp. 327–333, Mar./Apr. 1987.

[4] R. F. Schiferl and T. A. Lipo, "Power capability of salient pole permanent magnet synchronous motor in variable speed drive applications," *IEEE Trans. Ind. Appl.*, vol. 26, pp. 115–123, Jan./Feb. 1990.

[5] A. K. Adnanes, "Torque analysis of permanent magnet synchronous motors," in *Power Electronics Specialists Conference*, pp. 695–701, 1991.

[6] R. E. Betz, "Control of synchronous reluctance machines," in *Ind. Appl. Society Annual Meeting*, pp. 456–462, Sep. 1991.

[7] T. A. Lipo, A. Vagati, L. Malesani, and T. Fukao, eds., *Synchronous Reluctance Machines – A Viable Alternative for AC Drives*, Ind. Appl. Society Annual Meeting Tutorial, Oct. 1992.

[8] B. V. Murty and L. J. Jacovides, "A critical evaluation of AC motor drives for traction," in *Proceedings of the Intersociety Energy Conversion Engineering Conference*, pp. 1.729–1.737, Aug. 1985.

[9] Hoover Ltd., "Washing machines,". Notes from a lecture at Glasgow University presented in December, 1992 by a representative of Hoover Ltd.

[10] J. M. D. Murphy and F. G. Turnbull, *Power Electronic Control of AC Motors.* Pergamon Press, 1988.

[11] A. K. Adnanes, *High Efficiency, High Performance Permanent Magnet Synchronous Motor Drives.* PhD thesis, The Norwegien Institute of Technology, Sep. 1991.

[12] T. J. E. Miller, *Brushless Permanent Magnet and Reluctance Motor Drives.* Oxford University Press, 1989.

[13] A. Hughes, *Electric Motors and Drives.* Heinemann Newnes, 1990.

[14] A. E. Fitzgerald, C. K. Kingsley, and S. D. Umans, *Electric Machinery.* McGraw Hill, fifth ed., 1990.

[15] F. F. Nouvion, "Three-phase motors in electric rail traction," *IEEE Trans. Ind. Appl.*, vol. 20, pp. 1152–1170, Sep./Oct. 1984.

[16] W. Sokolowski, "Series-wound motors : small, potent, popular," *Power Transmission Design*, pp. 53–55, July 1988.

[17] N. Schofield, P. H. Mellor, and D. Howe, "Field-weakening of brushless permanent magnet motors," in *Proc. Int. Conf. Electrical Machines*, pp. 269–272, 1992.

[18] T. M. Jahns, "Torque production in permanent-magnet synchronous motor drives with rectangular current excitation," *IEEE Trans. Ind. Appl.*, vol. 20, pp. 803–813, Jul./Aug. 1984.

[19] P. Pillay, "Modelling, performance and design of sinusoidal- and rectangular-fed permanent magnet motor drives," in *Performance and Design of the Permanent Magnet AC Motor Drives*, (P. Pillay, ed.), ch. 5, Ind. Appl. Society Annual Meeting Tutorial, Sep. 1991.

[20] J. K. Kostko, "Polyphase reaction synchronous motors," *Journal of the AIEE*, vol. 42, pp. 1162–1168, 1923.

[21] D. A. Staton, T. J. E. Miller, and S. E. Wood, "Optimisation of the synchronous reluctance motor," in *Electrical Machines and Drives Conference*, pp. 156–160, Sep. 1991.

[22] T. M. Jahns, G. B. Kliman, and T. W. Neumann, "Interior PM synchronous motors for adjustable-speed drives," *IEEE Trans. Ind. Appl.*, vol. 22, pp. 738–747, Jul./Aug. 1986.

[23] C. F. Geraldi, "Higher performance from brushless spindle motors with magnetic flux control (G.F.C.)," in *Ind. Appl. Society Annual Meeting*, pp. 1395–9, Oct. 1991.

[24] A. J. Humphrey, "Constant horsepower operation of induction motors," *IEEE Trans. Ind. Gen. Appl.*, vol. 5, pp. 552–557, Sep./Oct. 1969.

[25] A. Boglietti, P. Ferraris, M. Lazzari, and F. Profumo, "A new design criteria for spindles induction motors controlled by field-oriented technique," in *Proc. Int. Conf. Electrical Machines*, pp. 356–360, Sep. 1992.

[26] T. Kume, T. Iwakane, T. Sawa, T. Yoshida, and I. Nagai, "A wide constant power range vector-controlled AC motor drive using winding changeover technique," *IEEE Trans. Ind. Appl.*, vol. 27, pp. 934–939, Sep./Oct. 1991.

[27] "Electric vehicles," *IEEE Spectrum*, Nov. 1992.

[28] H. Hakata, R. Kurosawa, S. Tatara, C. P. Lemone, and H. Hosoda, "Application strategies for AC rolling mill drives," in *Ind. Appl. Society Annual Meeting*, pp. 1141–1147, Oct. 1991.

[29] T. Nakano, H. Ohsawa, and K. Endoh, "A high-performance cycloconverter-fed synchronous machine drive system," *IEEE Trans. Ind. Appl.*, vol. 20, pp. 1278–1284, Sep./Oct. 194.

[30] B. Sneyers, D. W. Novotny, and T. A. Lipo, "Field-weakening in buried permanent magnet AC motor drives," *IEEE Trans. Ind. Appl.*, vol. 21, pp. 398–407, Mar./Apr. 1985.

[31] M. R. Harris, P. J. Lawrenson, and J. M. Stephenson, *Per-Unit Systems.* Cambridge University Press, 1970.

[32] W. Leonhard, *Control of Electrical Drives.* Springer-Verlag, 1990.

[33] A. K. Adnanes and T. M. Undeland, "Optimum torque performance in PMSM drives above rated speed," in *Ind. Appl. Society Annual Meeting*, pp. 169–175, Oct. 1991.

[34] S. Morimoto, Y. Takeda, T. Hirasa, and K. Taniguchi, "Expansion of operating limits for permanent magnet motor by current vector control considering inverter capacity," *IEEE Trans. Ind. Appl.*, vol. 26, pp. 866–871, Sep./Oct. 1990.

[35] S. Morimoto, Y. Takeda, and T. Hirasa, "Flux-weakening control method for surface permanent magnet synchronous motor," in *IPEC*, pp. 942–949, 1990.

[36] I. Boldea, Z. X. Fu, and S. A. Nasar, "High-performance reluctance generator," *Proc. IEE, Pt. B*, vol. 140, pp. 124–130, March 1993.

[37] *Matlab User's Guide.* The MathWorks Inc., Jan. 1990.

[38] B. J. Chalmers, "Influence of saturation in brushless permanent-magnet motor drives," *Proc. IEE, Pt. B*, vol. 139, pp. 51–52, Jan. 1992.

[39] A. Fratta, A. Vagati, and F. Villata, "Design criteria of an IPM machine suitable for field-weakened operation," in *Proc. Int. Conf. Electrical Machines*, pp. 1059–1065, 1990.

[40] *Brushless DC/AC Servomotors.* SEM Ltd., Kangley Bridge, London.

[41] *Brushless DC Servomotors.* SEM Ltd., Kangley Bridge, London.

[42] *FT Series AC Servomotors.* AEG Ltd.

[43] J. Faucher, M. Lajoie-Mazenc, and A. Chayegani, "Characterization of a closed-loop controlled current-fed reluctance machine taking into account saturation," *IEEE Trans. Ind. Appl.*, vol. 15, pp. 482–488, Sep./Oct. 1979.

[44] M. J. Kamper and R. A. Trubenbach, "Vector control and performance of a reluctance synchronous machine with a flux barrier rotor," in *Proc. Int. Conf. Electrical Machines*, pp. 547–551, Sep. 1992.

[45] S. Morimoto, K. Hatanaka, Y. Tong, Y. Takeda, and T. Hirasa, "High performance servo drive system of salient pole permanent magnet synchronous motor," in *Ind. Appl. Society Annual Meeting*, pp. 463–468, Oct. 1991.

[46] B. K. Bose, "A high-performance inverter-fed drive system of an interior permanent magnet synchronous machine," *IEEE Trans. Ind. Appl.*, vol. 24, pp. 987–997, Nov./Dec. 1988.

[47] B. C. Mecrow and A. G. Jack, "Operation of highly-rated permanent magnet synchronous machines," in *Electrical Machines and Drives Conference*, pp. 26–30, Sep. 1991.

[48] I. Boldea, N. Muntean, S. Deaconu, S. A. Nasar, and Z. Fu, "Distributed anisotropy rotor synchronous (DARSYN) drives - motor indentification and performance," in *Proc. Int. Conf. Electrical Machines*, pp. 542–546, 1992.

[49] L. Xu, X. Xu, T. A. Lipo, and D. W. Novotny, "Vector control of a synchronous reluctance motor including saturation and iron loss," *IEEE Trans. Ind. Appl.*, vol. 27, pp. 977–985, Sep./Oct. 1991.

[50] D. Platt, "Reluctance motor with strong rotor anisotropy," *IEEE Trans. Ind. Appl.*, vol. 28, pp. 652–658, May./Jun. 1992.

[51] W. Fong and J. S. C. Htsui, "New type of reluctance motor," *Proc. IEE, Pt. B*, vol. 117, pp. 545–551, March 1970.

[52] W. L. Soong, D. A. Staton, and T. J. E. Miller, "Validation of lumped-circuit and finite-element modelling of axially-laminated motors," in *Electrical Machines and Drives Conference*, pp. 85–90, Sep. 1993.

[53] W. L. Soong, D. A. Staton, and T. J. E. Miller, "Design of a new axially-laminated interior permanent magnet motor," in *Ind. Appl. Society Annual Meeting*, pp. 27–36, Oct. 1993.

[54] A. Fratta, R. Grassi, and A. Vagati, "High performance spindle drives adopting IPM synchronous machines : theoretical goals and a practical solution," in *European Power Electronics Conference*, pp. 476–481, 1991.

[55] T. J. E. Miller, "Methods for testing permanent magnet polyphase AC motors," *IEEE Trans. Ind. Appl.*, pp. 494–499, 1981.

[56] R. F. Schiferl and T. A. Lipo, "Core loss in buried permanent magnet synchronous motors," *IEEE Trans. Energy Conv.*, vol. 4, pp. 279–284, June 1989.

[57] F. Parasiliti and P. Poffet, "A model for saturation effects in high-field permanent magnet motors," *IEEE Trans. Energy Conv.*, vol. 4, pp. 487–494, Sep. 1989.

[58] M. G. Say, *The Performance and Design of Alternating Current Machines.* Pitman, 1958.

[59] I. Marongiu and A. Vagati, "Improved modelling of a distributed anisotropy synchronous reluctance machine," in *Ind. Appl. Society Annual Meeting*, pp. 359–364, Oct. 1991.

[60] A. Boglietti, P. Ferraris, M. Lazzari, and F. Profumo, "About the design of very high frequency induction motors for spindle applications," in *Ind. Appl. Society Annual Meeting*, pp. 25–32, Oct. 1992.

[61] A. Chiba and T. Fukao, "A closed-loop operation of super high-speed reluctance motor for quick torque response," *IEEE Trans. Ind. Appl.*, vol. 28, pp. 600–606, May./Jun. 1992.

[62] R. E. Betz, M. Jovanovic, R. Lagerquist, and T. J. E. Miller, "Aspects of the control of synchronous reluctance machines including saturation and iron losses," in *Ind. Appl. Society Annual Meeting*, pp. 456–463, Oct. 1992.

[63] T. J. E. Miller, A. Hutton, C. Cossar, and D. A. Staton, "Design of a synchronous reluctance motor drive," *IEEE Trans. Ind. Appl.*, vol. 27, pp. 741–749, Jul./Aug. 1991.

[64] I. Boldea and S. Nasar, "Emerging electric machines with axially laminated anisotropic rotors : a review," *Electrical Machines and Power Systems*, vol. 19, pp. 673–704, 1991.

[65] A. Fratta and A. Vagati, "Synchronous reluctance vs induction motor : a comparison," in *Intelligent Motion Conference Proceedings*, pp. 179–186, Apr. 1992.

[66] A. E. Fitzgerald and C. K. Kingsley, *Electric Machinery.* McGraw Hill, second ed., 1961.

[67] D. A. Staton, W. L. Soong, C. Cossar, and T. J. E. Miller, "Unified theory of torque production in switched and synchronous reluctance motors," in *Electrical Machines and Drives Conference*, pp. 67–72, Sep. 1993.

[68] A. Chiba, F. Nakamura, and T. Fukao, "Inductances of cageless reluctance-synchronous machines having nonsinusoidal space distributions," in *Ind. Appl. Society Annual Meeting*, pp. 314–319, 1989.

[69] D. A. Staton, W. L. Soong, and T. J. E. Miller, "Unified theory of torque production in switched reluctance and synchronous reluctance motors," in *Ind. Appl. Society Annual Meeting*, pp. 185–193, Oct. 1993.

[70] P. A. Ward, *Analysis and Design of Ferrite Permanent-Magnet D.C. Motors.* PhD thesis, University of Sheffield, Feb. 1974.

[71] T. A. Lipo, "Synchronous reluctance machines – a viable alternative for AC drives," *Electrical Machines and Power Systems*, vol. 19, pp. 659–671, 1991.

[72] A. Vagati, G. Franceschini, I. Marongiu, and G. P. Troglia, "Design criteria of high performance synchronous reluctance motors," in *Ind. Appl. Society Annual Meeting*, pp. 66–73, Oct. 1992.

[73] A. Hughes and T. J. E. Miller, "Analysis of fields and inductances in air-cored and iron-cored synchronous machines," *Proc. IEE, Pt. B*, vol. 124, pp. 121–126, Feb. 1977.

[74] I. Boldea, Z. X. Fu, and S. A. Nasar, "Performance evaluation of axially-laminated (ALA) rotor reluctance synchronous motors," in *Ind. Appl. Society Annual Meeting*, pp. 212–218, Oct. 1992.

[75] P. L. Alger, *Induction Machines.* Gordon and Breach, 1970.

[76] D. A. Staton, *CAD of Permanent Magnet DC Motors for Industrial Drives.* PhD thesis, University of Sheffield, Aug. 1978.

[77] A. Vagati, "Design of synchronous reluctance motors," in *Synchronous Reluctance Machines – A Viable Alternative for AC Drives*, ch. 2, Ind. Appl. Society Annual Meeting Tutorial, Oct. 1992.

[78] T. J. E. Miller, *Switched Reluctance Motors and their Control.* Oxford University Press, 1993.

[79] D. A. Lowther and P. P. Silvester, *Computer-Aided Design in Magnetics.* Springer-Verlag, 1985.

[80] *PE2D User's Guide.* Vector Fields, 1991.

[81] D. A. Staton, T. J. E. Miller, and S. E. Wood, "Maximising the saliency ratio of synchronous reluctanc motors," in *Proc. IEE, Pt. B*, pp. 249–259, July 1993.

[82] E. A. Klingshirn, "Dc standstill torque used to measure L_q of reluctance and synchronous machines," *IEEE Trans. Power App. Syst.*, vol. 97, pp. 1862–1869, Sep./Oct. 1978.

[83] H. C. Lovatt and J. M. Stephenson, "Measurement of magnetic characteristics of switched-reluctance motors," in *Proc. Int. Conf. Electrical Machines*, pp. 465–469, Sep. 1992.

[84] T. J. E. Miller, *Switched Reluctance Motors and their Controls.* Hillsboro, Ohio: Magna Physics Corp, 1992.

[85] C. Cossar and T. J. E. Miller, "Electromagnetic testing of switched reluctance motor," in *Proc. Int. Conf. Electrical Machines*, pp. 470–474, Sep. 1992.

[86] *Maintenance-free AC Main Spindle Drives.* Mannesmann Rexroth, IE 71 602/12.85 ed.

[87] *Brushless Spindle Servomotors LV.* GEC Alsthom Parvex Ltd.

[88] A. G. Jack, B. C. Mecrow, and A. J. Mitcham, "Design and initial test results from a permanent magnet synchronous motor for a vehicle drive," in *Proc. Int. Conf. Electrical Machines*, pp. 751–755, 1992.

[89] T. A. Lipo, "Performance of synchronous reluctance motor drives," in *Synchronous Reluctance Machines – A Viable Alternative for AC Drives*, ch. 1, Ind. Appl. Society Annual Meeting Tutorial, Oct. 1992.

[90] A. J. O. Cruickshank, A. F. Anderson, and R. W. Menzies, "Theory and performance of reluctance machines with axially-laminated anisotropic rotors," *Proc. IEE, Pt. B*, vol. 118, pp. 887–894, July 1971.

[91] A. El-Antably and T. L. Hudson, "The design and steady-state performance of a high-efficiency reluctance motor," in *Ind. Appl. Society Annual Meeting*, pp. 770–776, 1985.

[92] D. J. Bak, "Rotor design minimizes magnetic leakage," *Design News*, no. 5-21-84, pp. 110–111, 1984.

[93] S. E. Wood and D. Greenwood, "Force ventilated motors - advantages in fixed and variable speed applications," in *Electrical Machines and Drives Conference*, pp. 276–280, Sep. 1991.

[94] *Catalogue 3, Cast Iron TEFV Motors.* Brook Crompton, Huddersfield, HD1 3LJ, England.

[95] R. M. Tennant, ed., *Science Data Book.* Oliver and Boyd, 1989.

[96] J. Faupel and F. Fisher, *Engineering Design.* Wiley, 1981.

[97] T. J. E. Miller, D. A. Staton, and M. McGilp, *PC-BDC User Manual.* SPEED Laboratory, 1993.

[98] R. Lagerquist, I. Boldea, and T. J. E. Miller, "Sensorless control of the synchronous reluctance motor," in *Ind. Appl. Society Annual Meeting*, pp. 427–436, 1993.

[99] D. A. Staton and T. J. E. Miller, "Validation of PC-CAD using a precision dynamometer," in *Proc. Int. Conf. Electrical Machines*, pp. 1221–1225, 1992.

[100] R. Lagerquist, R. E. Betz, and T. J. E. Miller, "DSP96002 based high performance digital vector controller synchronous reluctance motor," in *Proc. Int. Conf. Electrical Machines*, pp. 903–907, Sep. 1992.

[101] *GTR Module (IGBT) Databook.* 1991.

[102] S. Dewar, "Design in IGBTs – motor drive applications," in *GTR Module IGBT Application Notes*, pp. 62–72, Toshiba, 1991.

[103] P. Horowitz and W. Hill, *The Art of Electronics.* Cambridge University Press, 1990.